Vortex magnétiques couplés dans des oscillateurs à transfert de spin : de l'excitation résonante à la synchronisation mutuelle

Romain Lebrun

NNT=2015SACLS233

THESE DE DOCTORAT
DE L'UNIVERSITE PARIS-SACLAY,
préparée à l'Université Paris Sud

ÉCOLE DOCTORALE N°564
Physique en Ile-de-France

Spécialité de doctorat : Physique

Par

Romain Lebrun

Coupled vortex dynamics in spin-torque oscillators: From resonant excitation to mutual synchronization

Thèse présentée et soutenue à Palaiseau, le 11 Décembre 2015 :

Composition du Jury :

Catherine Gourdon	Directeur de recherche, INSP Paris	Présidente
Johan Akerman	Professeur, Université de Gothenburg	Rapporteur
Ursula Ebels	Ingénieur Chercheur, CEA Grenoble	Rapporteur
Dafine Ravelosona	Directeur de recherche, Université Paris Saclay	Examinateur
Olivier Fruchart	Directeur de recherche, Institut Neel	Examinateur
Vincent Cros	Directeur de recherche, Université Paris Saclay	Directeur de thèse

Remerciements

Cette thèse est le fruit d'un long voyage de trois ans au sein de l'$UM\phi$. Loin d'un long travail en solitaire, cela fut pour moi une excellente expérience de recherche (et humaine) collective du début à la fin. J'y ai embarqué un peu par hasard en Juin 2012 suite à 2h de discussions matinales avec Vincent qui a immédiatement su me passionner pour les oscillateurs à transfert de spin. Je tiens ainsi tout particulièrement à te remercier Vincent pour ces trois excellentes années à travailler ensemble, pour la liberté que tu laisses à tes thésards, pour l'écoute que tu as toujours eu lors des nombreux passages que j'ai pu faire entre mon bureau et la salle de manip, et pour tes conseils aussi bien sur les oscillations des vortex magnétiques que sur les oscillations de moral de tes thésards.

Remonter le fil des choix qui m'ont amené à faire une thèse en nanomagnétisme serait compliqué. Toutefois, les cours de Stéphane Mangin à l'Ecole des Mines de Nancy y ont sans aucun doute fortement contribué, et sa proposition de stage pour un été à San Diego au sein du groupe d'Eric Fullerton n'y est probablement pas non plus étrangère. Mes 6 mois de stage au CEA avec J-B. Moussy n'ont fait que confirmer le début de cette histoire entre moi et le spin des électrons.

Je veux remercier plein de personnes pour ces 3 années de thèse, et en premier lieu les différents groupes avec qui j'ai collaboré durant ma thèse. Tout d'abord, cette thèse n'aurait été possible sans le nombre record et la très grande qualité des échantillons fabriqués par l'équipe de Shinji Yuasa au Japon. Je tiens tout particulièrement à remercier Hitoshi Kubota pour son accueil lors de mon séjour à AIST. Par ailleurs, mon initiation à l'électronique de spin n'aurait pas eu la même saveur sans les nombreuses discussions animées (souvent enflammées) qui ont eu lieu au SPEC avec Abbas, Olivier et Grégoire durant les premiers mois de ma thèse. Cette thèse n'aurait aussi pas non plus été la même sans ces allers retours à Louvain La Neuve où Flavio m'a au moins autant initié aux simulations micromagnétiques qu'aux spécialités culinaires belges (mitraillette en tête !).

Ce manuscrit n'évoque pas la face cachée, mais essentielle, du monde de la recherche qu'est l'enseignement qui lui est souvent lié. Je tiens donc aussi à remercier tous ceux avec qui j'ai

enseigné durant ces trois années, Anne-Laure, Yannick, Anniina, Carine et Manue qui m'a fait découvrir la physique de la matière molle, et me passionner pour la chute des gouttes.

Et puis cette thèse n'aurait pas eu la même saveur sans ce grand paquebot qu'est l'"$UM\phi$. Je tiens tout d'abord à remercier toute l'équipe "STNO". Merci aux pionniers : Olivier, Benoit, Antoine et Nicolas L. qui ont fait vivre ce sujet depuis presque 10 ans à l'"$UM\phi$, et qui m'ont transmis le flambeau par leurs thèses et leurs nombreuses présentations qui restent aujourd'hui inspirantes. Merci Julie pour le temps passé à m'expliquer le formalisme des vortex et de l'équation de Thiele, et pour ta passion communicative des dispositifs bio-inspirés (et qui m'a couté quelques semaines de rédaction au mois d'aout). Merci Paolo pour m'avoir appris à boire 3 cafés en 30 sec à défaut de m'avoir transmis ta passion pour Python, grâce à toi les vortex sortiront peut être un jour de notre laboratoire. Un grand merci Alex pour la relecture de cette thèse entre deux changements de couches, et Eva pour m'avoir supporté autant que je t'ai supporté. Ces longues discussions avec vous sur les vortex magnétiques (et sur tout et n'importe quoi) risquent de me manquer, préparez-vous donc à m'accueillir en Suisse ou au Portugal. Thank you Sumito for all your "Maybe not" and all your tofu's stories. Bon courage à ceux qui continuent et qui pourraient bientôt renommer cette équipe "STNO based bio-inspired devices" (heureusement que Sam fait de la résistancee) : Matthieu, Jacob et en particulier Miguel pour la reprise du flambeau dans la section basket du CEA, et Philippe pour ces quelques mois à maniper ensemble.

Et puis l'"$UM\phi$, c'est tout sauf un ensemble d'équipes de recherche cloisonnées. J'ai ainsi eu la chance de passer ces années de thèse avec de nombreuses personnes déconcertées par ces générations de thésards fadas de vortex magnétiques. Merci "Tangui" Steven pour ces 3 ans et demi de co-bureau (et ces 4 déménagements !), pour tes gaffes inoubliables et nos nombreuses conf' (et post-conf, des soirées de San Sebastian à celles d'Hawai). Merci Martin et ses bouclettes pour m'avoir presque réappris à suivre la L1, Olivier pour nos débats économiques (et nos engueulades dans un certain taxi new-yorkais), Soren pour le verre d'eau de Louis Neel, Joao pour tes restos portugais sur Gentilly, Alice et Constance pour ces deux semaines inoubliables à Hawaï, David et Michel pour vos talents de chanteur, Sophie et Regina pour les pauses cafés improvisées dans votre bureau, Carlos pour me faire redécouvrir Nancy à défaut de m'avoir appris à danser la salsa. Merci aussi à tous les permanents qui sont pour certains là depuis plus de 20 ans mais qui sont bien plus que les meubles de ce labo. Merci Madjid pour tes conseils aussi bien en physique que pour les sushis, Richard pour m'avoir fait découvrir ce labo, Nicolas R. pour m'avoir fait éviter de nombreuses crises de nerf sur la cableuse, Pierre pour m'avoir obtenu ce monitorat au sein des méandres de l'Université, Vincent G. pour notre unique séance de badminton, Karim pour tes vannes 24h/24. Et merci à tous les autres, que j'oublie surement, et qui ont fait ou qui font encore l'âme de ce labo.

Merci à toute l'équipe qui gère formidablement ce laboratoire au quotidien. Anne et Christine, vous avez toujours su trouver des solutions à mes problèmes administratifs de dernière minute. Votre patience et votre efficacité sont incroyables, l'administratif et la paperasse commencent (presque) à me faire moins peur. Merci aux deux Fred, pour vos conseils et pour être attentif au suivi des thésards du labo sans forcément beaucoup les cotoyer.

Et puis merci à tous mes amis qui ont fini par comprendre que je n'étais pas un magnétiseur, en particulier Gabriel et Pauline pour avoir suivi ma thèse au point de prendre des notes pendant ma soutenance, Jules pour ces 2 ans de coloc et pour tes drosophiles que tu ramènes jusqu'à l'appart, Gouss pour ton aide LatEx (et pour tes fameux lentilles-saucisses), Bruno pour m'avoir suivi jusqu'au Japon, Nicolas pour tes' "bons" plans sur Massy-Palaiseau, Claire pour ta venue inattendue lors de ma soutenance et tes appels à tout heure. Merci à mon frère et à mon père pour avoir soutenu et supporté depuis 26 ans, je n'en serai pas là sans vous. Et merci à toi de m'avoir supporté quasi-quotidiennement durant cette dernière année de thèse, aussi bien à Gentilly que par téléphone pendant ton road-trip européen, et de me faire sourire dès que je te vois. Je ne souhaite qu'une chose, c'est que tout cela continue..

Contents

Introduction

The discovery of the giant magnetoresistance in 1988 is considered as the birth date of a new and dynamic research field called spintronics. The rich physics associated with spin transport has created a breakthrough for the future of nano-electronics. Giant magnetoresistance (GMR) based sensors have enhanced the data storage density by several orders of magnitude and this trend will continue to be pursued with the oncoming non-volatile magnetic recording random-access memories (MRAMs). In the magnetism roadmap, spin-torque oscillators (STOs) are candidates for future generation of spintronic based rf-devices.

The concept of a spin torque oscillator originates with the discovery of the spin transfer torque. The transfer of spin between a spin-polarized current and the magnetic moments of a ferromagnet can compensate the magnetic damping and thus lead to sustained oscillations of the magnetization. Combined with the magnetoresistive effect, it leads to a device called a spin-torque oscillator that convert a dc-current into voltage oscillations. These new and promising oscillators present a large accordability, are radiation hardened, compatible with CMOS technologies and can operate in a frequency range from 100 MHz to 65 GHz. Thus, a new generation of rf-devices, from frequency synthetizer to frequency detector, based on STO has been predicted.

Intense studies have developed since their first observation in 2003 but at the beginning of my PhD one major issue of spin-torque oscillators remained their poor spectral coherence. Different strategies have been considered to decrease the linewidths of STOs: (i) the development of magnetic materials with a low damping and large spin-polarization, (ii) the study of collective mode dynamics in hybridized magnetic systems (iii) the stabilization of the STO dynamics with a reference external signal (iv) the synchronization of multiple STOs to enhance both their power and spectral coherence. In my thesis, I investigated these different approaches to overcome the issue of phase noise in STOs. With this in mind, I concentrated my efforts on vortex based STOs which present higher spectral coherences than other kinds of STOs. A first part of my work consisted in identifying, experimentally and analytically, the different mechanisms that can drive and stabilize the dynamics of a vortex based STO. From this work, I could think up and study different concepts of spintronic rf-devices based on vortex STOs from rf-synthetizers to bio-inspired networks.

My thesis consists of three parts. The first part includes a short description of the physical concepts that will be addressed in this thesis and then introduces the concept of spin-torque oscillators. In chapter 1, I present the physical mechanisms involved in their operation, i.e. the magnetoresistance, the spin-transfer torque and the magnetization dynamics. I chapter 2 I introduce the properties of vortex based STOs. I present the characteristics of an isolated magnetic vortex and then describe the sustained dynamics of a vortex gyrotropic mode excited by a spin polarized current. Following the works done by N. Locatelli during his thesis, I extend

my study to the case of double vortex based STOs and highlight the potential of mode coupling for STOs.

In the second part, I investigate the dynamics of a double vortex based STO in the autonomous and non-autonomous regime. The experimental measurements have been performed on hybrid magnetic tunnel junctions that combine a Cu based double vortex spin-valve above a magnetic tunnel junction with a synthetic antiferromagnet (SAF) polarizer as presented in the appendix A. In chapter 3, I demonstrate that the coupled mode dynamics are strongly affected by the vortex core configuration. A better spectral coherence is reported in anti-parallel vortex core configuration (APc) compared to parallel core configuration (Pc). I associate this feature to the dipolar repulsion between the two vortex cores and correlate it to a lower critical current and a higher effective damping in the APc configuration. I thus demonstrate that mode coupling can be used to improve the rf-properties of the vortex gyrotropic mode. In chapter 4, I present the different non-autonomous regimes of a vortex based STO and experimentally investigate the injection locking and the resonant excitation driven by an rf-current. I first demonstrate that the locked state is mainly driven by a strong in-plane Field-like torque in our magnetic tunnel junctions (MTJs), leading to a record thermal stability for a spin-torque oscillator. In this "pure" phase locked state, I prove the absence of phase slips, i.e desynchronization/resynchronization events, that are detrimental for the stability of the spin-torque oscillator. Then I extend my study on the case of a damped oscillator resonantly excited by an rf-current at a fraction of the eigenfrequency. For the first time, a phenomenon of superharmonic resonance in an STO is reported. There, I discuss the origin of the excitation mechanism, either "normal" and/or parametric resonances. In chapter 5, I highlight the limits of the single mode approach in our double vortex based STO. In a regime of strong interaction between the two coupled modes, one can no longer consider that one mode is excited by spin-transfer force while the other is damped. Thus, I show that the mode interaction can lead to exotic new phenomena in STOs, such as "self-resonance" and chaotic behaviors, in both the autonomous and non-autonomous regimes.

In the last part, I propose three different concepts of STO based rf-devices. First, I present in chapter 6 a preliminary study towards the development of an on-chip STO based phase locked loop. I analytically highlight the correlation between the locking process of such a phase locked loop and the one of a modulated STO. In chapter 7, I first theoretically study the spindiode excitation in a vortex based STO. By taking advantage of the large Field-like torque in our MTJs, a new rf detection scheme based on the resonant and reversible expulsion of the vortex core is proposed. This novel detection scheme is shown to be more efficient than the state of the art Schottky diode. Finally, in chapter 8 I show the first experimental observation of the electrical synchronization of two STOs. I study the properties of the synchronized state depending on the relative parameters of each STO and on the phase shift between them. In

the best locking conditions, I succeed to observe, as theoretically predicted, a quantitative enhancement of the output power by a factor 4 and of the spectral coherence by a factor 2.

Part I

Introduction on spin-torque oscillators

Chapter 1

From spin-polarized current to spin-torque oscillators

1.1 Physical phenomena under investigation

1.1.1 Electronic transport in ferromagnets

Among all elements, $3d$ transition metals and $4f$ rare earths are the two main classes of materials with ferromagnetic properties at room temperature. Transition metals like Co, Fe, Ni and their alloys have the advantage of combining ferromagnetic properties with excellent transport properties which makes them key components in the field of spintronics research. $4f$ rare earths have localized conduction electrons that are weakly sensitive to the environment. Furthermore they have a much higher resistivity than the $3d$ transition metals and a high magnetic anisotropy so that they are more found in the development of permanent magnets.

At the Fermi energy, $3d$ transition metals have an electronic configuration with two electronic shells: the $4s$ shell is filled and the $3d$ shell is partially filled as represented in Fig. 1.1. The $4s$ shell has as many conduction electrons with an up spin and a down spin. Thus the $4s$ shell only contributes to the transport properties of the materials and not to its ferromagnetic properties[1]. On the contrary, the $3d$ is half-filled and the exchange interaction between neighbouring electrons favors the alignment of the spins. At the Fermi level, the reduction of exchange energy associated with two parallel spins is higher than the increase of kinetic energy (Stoner criteria). This favors the spins to align in one preferential direction and induces an energy splitting of the $3d$ conduction shell into two sub-shells associated with each direction of spin as represented

[1] In reality, $4s$ bands have also a non zero spin-polarization at the Fermi level due to hybridization with the d bands but it is much smaller than the $3d$ bands.

in Fig. 1.1. At the Fermi level, a $3d$ transition metal has two different density of states, one for each direction of spin ($\uparrow$ and $\downarrow$) which defines a preferential spin orientation leading to a ferromagnetic ordering.

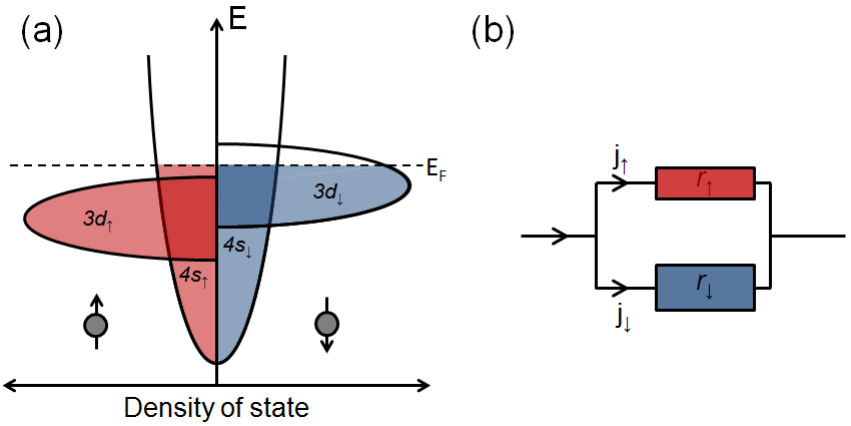

FIGURE 1.1: (a) Bandshell structure of a soft ferromagnet transition metal with E_F the Fermi leve (b) Equivalent circuit in the two current model

Magnetic alloys made of transition metals have also been developed to enhance the net magnetic moment of $3d$ transition metals. The evolution of the net magnetic moment by atom with the number of valence electron follows a "Slater-Pauling" curve (see Fig 1.2). In Ni alloys, such as NiFe that we investigate in this work, the $3d_\uparrow$ shell is full and only the number of electron with $\downarrow$ spin decreases. In the alloy, the increase of net magnetic moment corresponds to the number of $\downarrow$ electrons that has been removed.

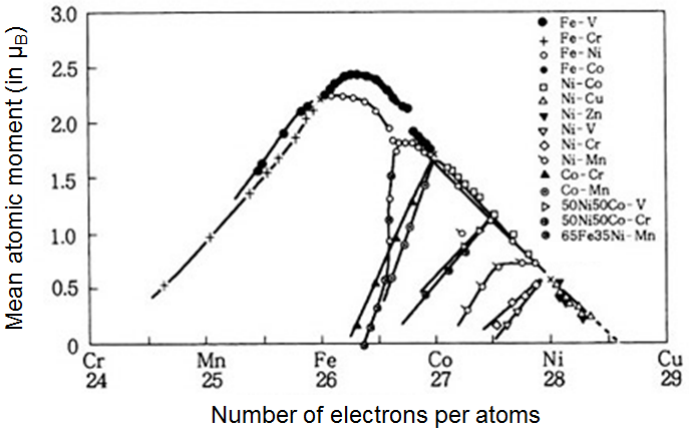

FIGURE 1.2: Slater-Pauli curve of transition metal alloys

A ferromagnetic alloy with a Fermi level above the $3d_\uparrow$ sub-shell can thus be obtained. Thus, the $4s_\uparrow$ electrons, more delocalized and responsible of the transport properties (higher DOS at Fermi level), do not scatter through the localized state of the $3d_\uparrow$ sub-shell. On the contrary, the $4s_\downarrow$ electrons can diffuse through the $3d_\downarrow$ sub-shell. This results in different transport

properties for the two directions of spin, i.e to a lower resistivity $r_\uparrow$ for the $\uparrow$ electrons than the resistivity $r_\downarrow$ for $\downarrow$ electrons [1].

1.1.2 Giant magnetoresistance (GMR) effect and spin-polarization of the current

1.1.3 Principle of the GMR

The giant magnetoresistance discovered by A. Fert and P. Grünberg [2, 3] can easily be described in a two channel model. The effect of magnetoresistance takes place in ferromagnetic / non-magnetic / ferromagnetic multilayers, i.e. in a system called a spin-valve. Two kinds of spin-valves can be distinguished depending on the direction of the injected current, either in the plane (CIP) of the multilayers as it was first observed, or perpendicular to the plane (CPP) of the multilayers.

In this thesis, we focus on the CPP configuration. In the first FM, the electrons with majority spins, i.e with spins parallel to the local magnetization, are less scattered. Then we assume that the spin of electrons is conserved during the transport in the non-magnetic layer. This hypothesis is valid if the NM layer is thinner than the spin diffusion length (mean distance between two collisions leading to a spin flip). Indeed, due to spin-accumulation the current remains spin-polarized in the NM layer over the spin-diffusion length in CPP configuration and not only over the mean free path (mean distance between two diffusive events) as in CIP configuration. In the second FM layer, the transport of electrons is again facilitated for the spins parallel to the local magnetization. Taking into account the transport in the two FM layers, we can model a resistance equivalent to the spin-valve for each magnetic configuration, respectively R_P and R_{AP} for parallel (P) or antiparallel (AP) magnetizations in the two ferromagnetic layers as shown in Fig. 1.3.

For two non-collinear ferromagnetic layers, the expression of the spin valve-resistance R depends on the magneto-resistance ratio (GMR) and on the angle θ between the magnetic layers [4]:

$$R = R_p \left[1 + \frac{GMR}{2}(1 - \cos(\theta))\right] \text{ with } GMR = \frac{R_{AP} - R_P}{R_P} \tag{1.1}$$

In all metallic spin-valves, the GMR ratio is generally between 1 and 10 % at room temperature with the largest ratio in Heusler alloys [5]. Much larger ratio up to a few hundred percents are obtained in MTJ junctions [6] with an insulating non-magnetic spacer.

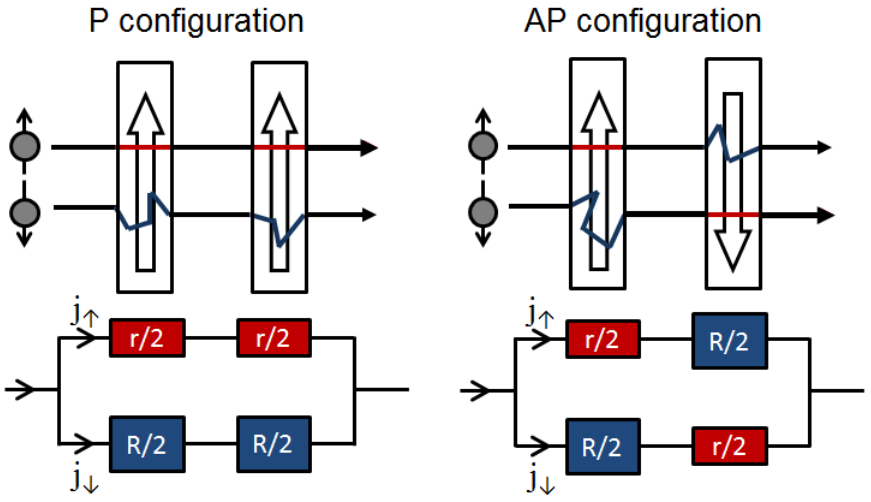

FIGURE 1.3: Two current model for a spin-valve FM/NM/FM in parallel (P) and antiparallel (AP) configuration. When a dc-current goes through a ferromagnetic layer, the electrons with a spin parallel to the magnetization sense a lower resistance than the electrons with a spin anti-parallel to the local magnetization

1.1.4 Transport in magnetic tunnel junctions (MTJs)

The two current approach does not permit to estimate the current spin-polarization for GMR or MTJ junctions. More complex models have been developed to investigate in more details the spin-polarized transport properties: the Valet-Fert model [7] for GMR spin-valves, the Julliere model [8] and then the Slonczewski model [9] for MTJ junctions. For a MTJ junction such as will be presented later in this thesis, the Slonczewski model allows to solve the Schrödinger equation for two identical ferromagnetic electrodes, modelled with parabolic and shifted densities of states for the majority and minority spins, and separated by a rectangular potential barrier in the free electrons approximation. By considering that only the $\overrightarrow{k}$ vectors normal to the surface ($\overrightarrow{k_{//}} = 0$) participate to the transport of electrons, the tunneling conductance dependency with the magnetization angle between the two electrodes θ is expressed as:

$$G(\theta) = G_0 \left[1 + P_{eff}^2 \cos(\theta)\right] \text{ with } P_{eff} = \frac{k_\uparrow - k_\downarrow}{k_\uparrow + k_\downarrow} \frac{\kappa^2 - k_\downarrow k_\uparrow}{\kappa^2 + k_\downarrow k_\uparrow} \tag{1.2}$$

The effective spin polarization, P_{eff}, depends on both the wave vectors of minority $k_\uparrow$ and majority $k_\uparrow$ spins in the ferromagnetic electrodes and on the attenuation constant of the wave functions inside the tunnel barrier κ. The attenuation constant κ depends on the height and on the width of the barrier. Thus the spin-polarization is hence not a property of the ferromagnetic metal but of the ferromagnet/insulator bilayer. From these expressions, the TMR ratio can be written as:

$$TMR = \frac{2P_{eff}^2}{1 - P_{eff}^2} \tag{1.3}$$

The first MTJs were developed with amorphous alumina barriers [10–12]. In 2004, Yuasa et al. [6] and Parkin et al. [13] respectively demonstrated on epitaxial MgO junctions with Fe and CoFe electrodes that the TMR ratio does not only depend the weight and width of the barrier but also on the crystalline orientation and on the nature of the barrier (epitaxial or amorphous). The crystalline structure of the barrier introduces a filtering mechanism as predicted by Zhang and Butler [14]. The Bloch states in the ferromagnets couple at the interface with the evanescent states of the insulating layer. Using crystalline MgO barrier, the minority electrons have faster decay rates as their Bloch states are coupled with evanescent wave functions that attenuate much faster in the barrier. Consequently, the effective polarization is higher in crystalline MTJs.

1.1.5 Transfer of spin angular momentum

1.1.5.1 Spin-transfer torques: Slonczewski and Field-like torques

In 1996, J. Slonczewski [9] and L. Berger [15] introduced the concept of spin-transfer (ST) by demonstrating theoretically that a spin-polarized current can excite spin-waves and even reverse the magnetization of a magnetic layer in a thin FM1/NM/FM2 spin-valve.

In CPP configuration, a dc-current I_{dc} is injected perpendicularly to the structure. The first ferromagnetic layer is thick so that it plays the role of a fixed polarizing layer. The second ferromagnetic layer is thin and thus its magnetization is free and sensitive to the effect of an injected spin-current. The two magnetic layers are separated by a thin non-magnetic metal or an insulator. The magnetization of the two ferromagnetic layers make a small angle θ (see Fig. 1.4). The injected current first gets spin-polarized along $\overrightarrow{M_1}$ and then is injected into the spacer and eventually crosses the second magnetic layer FM1. The spin current has a component transverse to $\overrightarrow{M_2}$ and proportional to θ. When the current crosses the thin layer, the spins align rapidly along $\overrightarrow{M_2}$ and their transerve components are transfered to $\overrightarrow{M_2}$. This transverse component, proportional to $|\Delta\overrightarrow{m_\perp}|$ acts as a torque $\overrightarrow{\Gamma}$ on $\overrightarrow{M_2}$:

$$\overrightarrow{\Gamma} = \frac{1}{\gamma_0}\frac{I_{dc}}{e}P_i g\mu_B(\overrightarrow{m_2} \times (\overrightarrow{m_2} \times \overrightarrow{m_1})) \text{ and } \left|\overrightarrow{m_2} \times (\overrightarrow{m_2} \times \overrightarrow{m_1})\right| = \sin(\theta) \tag{1.4}$$

with P_i the spin-polarization at the NM/FM2 interface, γ_0 the gyromagnetic ratio, e the elementary charge, g the Landé factor (equal to 2 for an electron), μ_B the Bohr magneton, $\overrightarrow{m_1}$

and $\overrightarrow{m_2}$ the unit vectors parallel to $\overrightarrow{M_1}$ and $\overrightarrow{M_2}$. It can also be noted that the torque depends on the sign of the current direction.

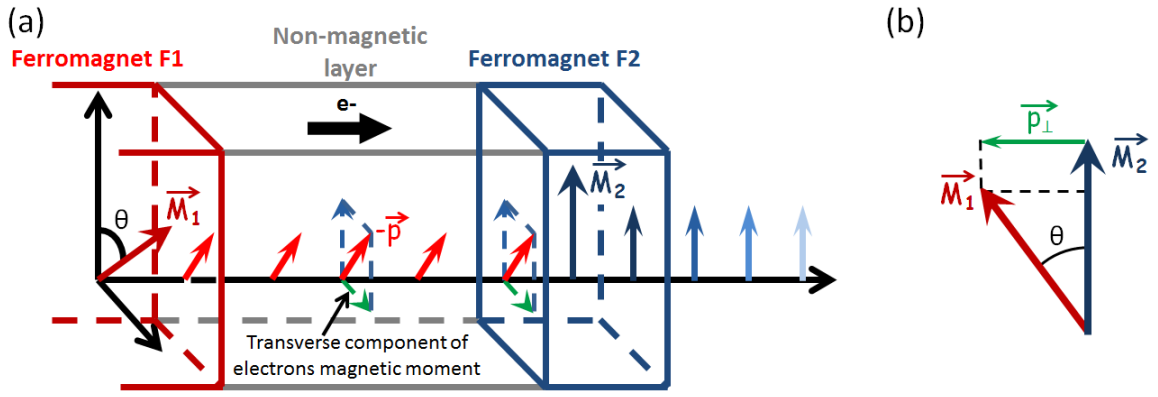

FIGURE 1.4: (a) Principle of spin-transfer torque in a FM1/NM/FM2 spin-valve (b) The transverse component of the spin-polarized current is transfer to the magnetization

Several studies later confirmed [16, 17] that the ST torque is an interfacial phenomenon and that the transverse spin-current component is absorbed over a few atomic planes. If we consider an interface between a ferromagnetic metal and a non-magnetic layer, an incident spin-current $\overrightarrow{I}_{inc}$ is either transmitted $\overrightarrow{I}_{trans}$ or reflected $\overrightarrow{I}_{ref}$. Locally, the torque exerted on the local spins (or magnetic moment of the free layer) is equal to :

$$\overrightarrow{\tau} = \overrightarrow{I}_{trans} + \overrightarrow{I}_{ref} - \overrightarrow{I}_{inc} \tag{1.5}$$

Again, only the transverse component of the spin-current is absorbed and acts as a torque on the magnetization. Three absorption mechanisms drive the effect of spin transfer:

1. First, the difference between $\overrightarrow{I}_{inc\perp}$ and $\overrightarrow{I}_{ref\perp} - \overrightarrow{I}_{trans\perp}$ leads to a non-zero torque.
2. In the ferromagnetic free layer, the spins precess around the exchange field with a random phase. Above the phase coherence length (around 1 nm), one can consider that $\overrightarrow{I}_{trans\perp} = 0$. Thus, the spin transfer torque can be written as $\overrightarrow{\tau} = \overrightarrow{I}_{inc\perp} + \overrightarrow{I}_{ref\perp}$.
3. In metallic systems, the transmitted and reflected conduction electrons have random phases as represented in Fig. 1.5. Thus their average contribution on all the $\overrightarrow{k_{\parallel}}$ vectors is zero. In this case, the torque exerted by a current polarized along $\vec{p}$ on the local magnetization $\overrightarrow{m}$ is called the Slonczewski torque and it can be described as :

$$\overrightarrow{\tau_{Slonc}} = \tau_{Slonc}\overrightarrow{m} \times (\overrightarrow{m} \times \overrightarrow{p}) \text{ with } \tau_{Slonc} = -\frac{I_{dc}P\gamma\hbar}{2LM_s\mu_0 e} \tag{1.6}$$

with M_s and L the respective saturation magnetization and thickness of the magnetic layer, μ_0 the vacuum permeability, γ the gyromagnetic ratio and e the electron charge. In magnetic tunnel junctions, mainly the wave vectors around $\overrightarrow{k_{\parallel}} = 0$ are transfered. The phase coherence of the reflected wave vectors is thus higher and $\overrightarrow{I_{ref\perp}}$ is non-zero. This effect gives rise to a second spin transfer torque that acts like a field and is called the Field-like torque:

$$\overrightarrow{\tau_{FL}} = \tau_{FL}\overrightarrow{m} \times \overrightarrow{p} \tag{1.7}$$

with τ_{FL} the Field-like torque efficiency. Its amplitude varies from 0.1-0.4 the Slonczewski efficiency in MTJs [18–21]. The origin of this torque remain in debate and different mechanisms have been proposed to explain it such as interlayer exchange coupling [22] or spin relaxation process [14]. In this thesis, we will show that in vortex based systems, the contribution of the Field-like torque can be large compared to the Slonczewski torque due to the different symmetries of the two torques. We will especially highlight the crucial role of the Field-like torque in the non-autonomous regime of a vortex based STO.

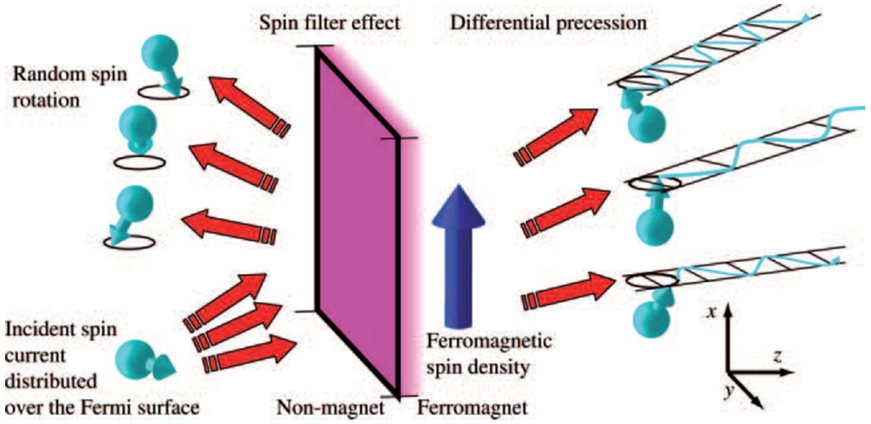

FIGURE 1.5: Mechanisms contributing to absorption of incident transverse spin current. Electrons incident (*lower left*) from the nonmagnet are distributed over a distribution of states represented by three different incident directions. All of these electrons are in the same spin state, which is transverse to the ferromagnetic spin density (*blue arrow*). The reflected electron spins have predominantly minority character and their transverse components are distributed over many directions (random spin rotation). The transmitted electron spins precess as they go into the ferromagnet because the wavevectors for the majority and minority components are different. Electrons with different initial conditions precess at different rates, leading to classical dephasing. Extracted from [23]

1.1.5.2 Spin-orbit torques

More recently, new type of spin-torques arising from spin-orbit interactions have been identified (Spin Hall effect, Rashba Edelstein effect). These spin-orbit interactions are intrinsic in magnetic materials with large spin orbit coupling like the $4f$ rare earths or extrinsic in magnetic materials containing impurities with a high spin-orbit coupling. Recently, they have

been rather studied as interfacial effects between a ferromagnetic material and a non magnetic metal with a strong spin-orbit (SO) coupling. The main idea is that a charge current injected in the non-magnetic metal with a SO coupling could lead to the generation of either a pure spin-current or/and a spin-accumulation at the FM/NM inferface. A spin-accumulation and spin-current are not fundamentally decorrelated. However one should consider that the Spin-Hall effect mainly leads to the generation of a spin-current[2] (scattering of spin up and down) [24, 25] while the Rashba effect leads to spin-accumulation through spin-filtering (k filtering at the interface) [26, 27]. It must be noted that spin-orbit torques in bilayers can be observed only if the conductivity of the NM metal is larger than that of the ferromagnetic layer.

Both a interfacial pure spin current ("Slonczewski like effect") or a spin-accumulation ("Field-like effect") will act on the local magnetization and can thus be associated with a spin-orbit torque $\overrightarrow{\tau}_{SO}$. The efficiency of the different spin-orbit torques remains under debate in many of metals with a strong SO [28]. However all the studies agree that the spin-orbit interaction is generally proportional to Z^4 and so focus on metals with a high atomic number Z like Pt, Pd, Ta, Au or W. One main advantage of these spin-orbit torques is that no charge current flows in the ferromagnetic layer which permits to avoid detrimental phenomena like Joule heating.

1.2 Magnetization oscillations due to spin-current injection

1.2.1 Magnetization dynamics with the Landau-Lifschitz-Gilbert equation

In a FM1/NM/FM2 trilayer, the spin torques modify the magnetization direction of the free layer $\overrightarrow{m_2}$. The dynamics of uniform magnetization (macro-spin model) is described by the phenomenological Landau-Lifschitz-Gilbert equation (LLG) [29] in which the spin torques are included (see also Fig. 1.6):

$$\frac{d\overrightarrow{m_2}}{dt} = -\gamma\overrightarrow{m_2} \times \overrightarrow{H}_{eff} + \alpha\overrightarrow{m_2} \times \frac{d\overrightarrow{m_2}}{dt} + \tau_{Slonc}\overrightarrow{m_2} \times (\overrightarrow{m_2} \times \overrightarrow{p}) + \tau_{FL}\overrightarrow{m_2} \times \overrightarrow{p} \qquad (1.8)$$

The first term describes the magnetization precession around the effective field $\overrightarrow{H_{eff}}$ that takes into account the contributions of the external field, the anisotropy field and the coupling fields (γ is the electron gyromagnetic ratio). The second term corresponds to the damping term. The last two terms correspond to the Slonczewski and Field-like spin-transfer torque with τ_{Slonc} and τ_{FL}, their relative efficiencies, and p the direction of spin polarization. In our study, we will consider only the "classical" Slonczewski and Field-like torques.[3]

[2] It also leads to a small spin-accumulation and to a corresponding diffusive spin-current.
[3] The spin orbit torques are negligible in our studied samples.

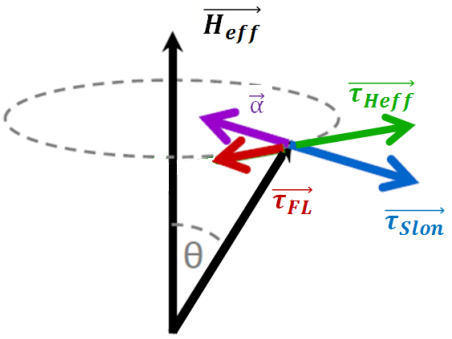

FIGURE 1.6: Scheme of the different torques acting on the local magnetization. $\vec{\alpha}$, $\tau_{\vec{H_{eff}}}$, $\tau_{\vec{FL}}$, $\tau_{\vec{SL}}$ correspond to the torques respectively associated with the effective field, the damping term and the two spin-transfer components.

From the LLG equation, we can then define the effective damping (in first approximation, we neglect the the Field-like torque and the nonlinear damping term):

$$\tilde{\alpha} = \alpha + \frac{I_{dc} P \gamma \hbar}{2 L M_s \mu_0 e} \tag{1.9}$$

We notice that the spin-transfer torque acts as an extra- or anti-damping torque depending on the dc-current sign. When the spin-transfer torque and the damping term cancel each other out, the effective damping term is zero. Depending on the shape of the energy potential, it can either switch the magnetization or trigger sustained oscillations of the magnetization which leads to the concept of spin-torque oscillator.

1.2.2 Principle of the spin-torque oscillator

In spin-valve multilayers (GMR or TMR junctions), sustained oscillations of the magnetization at the eigenfrequency of the excited magnetic free layer can be excited through the spin-transfer torques generated by the dc-current. The magnetoresistance (MR) effect converts the oscillations of magnetization in voltage oscillations, which can then be detected using a spectrum analyzer or an high frequency oscilloscope. Thus spin-torque oscillators (STO) convert a dc-current into voltage oscillations at the device terminals as represented in Fig. 1.7.

The main features of a spin-torque oscillator are the following: its frequency, its emitted power, its spectral coherence and its tunability. The frequency of a STO can go from 100 MHz for a magnetic free layer in the vortex configuration up to 70 GHz for perpendicularly magnetized free layer [30]. The power is proportional to the square of the voltage and so to the square of the dynamical part of the MR ratio. In magnetic tunnel junctions, the output emitted power can thus reach a few microwatts while the power of GMR based STO remains below 1 nW even for Heusler alloys with large spin polarizations [31]. However in a MTJ the applied voltage, and

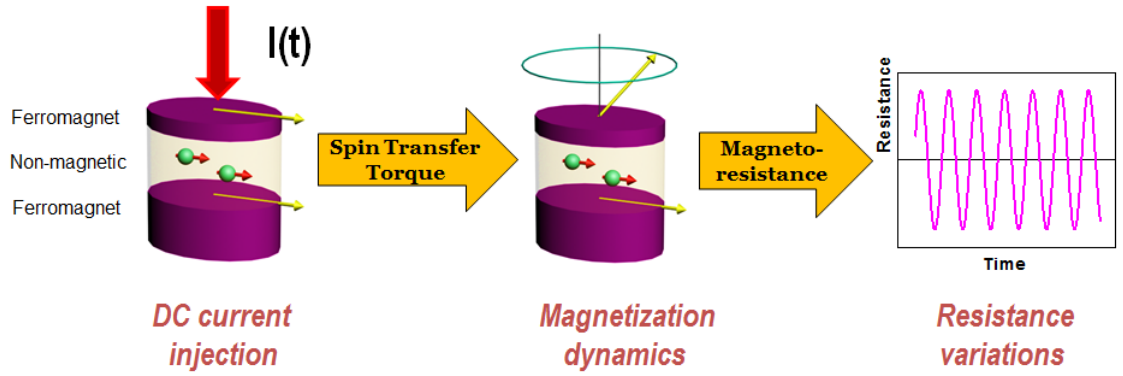

FIGURE 1.7: Principle of a spin-torque oscillator. The dc-current gets spin-polarized in the first ferromagnetic layer. The spin polarized current then exerts a torque on the local magnetization of the second ferromagnetic layer, which can induce sustained oscillations of the magnetization. The magnetization oscillations are converted in voltage oscillations through the GMR effect.

so the amplitude of oscillations, is limited by the breakdown voltage of MTJs (< 1 V). This restrains the STO frequency tunability that is determined by its amplitude of oscillations as in any nonlinear system. To lower the critical current required to obtain sustained oscillations, the choice of magnetic material is crucial as it determines both the damping parameter and the anisotropy of the system. Generally soft ferromagnetic materials like Co, Fe, Ni and their alloys are used as they have low anisotropies, relatively low damping parameters (α between 0.005-0.03) and also relatively large spin-polarization ($P = 0.1 - 0.4$).

1.2.3 Different families of spin-torque oscillators

The first spin-torque oscillators have been measured in 2003 by Kiselev et al. [32] in confined nanodots with an in-planely magnetized free layer. Then, Rippard et al. [33] demonstrated that point contact based STOs with similar magnetic configuration could reach higher frequency of oscillations. These first results were observed in GMR based STOs and the output emitted power was below 1 nW. In 2006, a record 10 nW emitted power was reported for a MTJ based STO [34]. Until now, MTJ based STOs have been limited to confined nanodots and to the recent sombrero shape STOs [35]. The geometry of point contact, where the free magnetic free is spatially extended, is currently limited in output power as realizing MTJ based nanocontacts is a real challenge.

In these first results, the STOs had an in-plane magnetized free layer. Later on, other types of spin-torque oscillators have been reported like the vortex based STO in 2007 [36] and the bullet mode STO in 2010 [37]. With the stabilization of skyrmions at room temperature [38], skyrmion based STOs are anticipated [39] and might present a higher thermal stability than other STOs. Up today, vortex based STOs present the lowest linewidths given that the vortex

gyrotropic mode is much lower in energy than the other vortex modes and involves larger magnetic volume than other type of STOs.

In these different families of STOs, one key issue for applications is to avoid the use of magnetic field. In the last few years, different tricks have been proposed to tackle this issue. For STOs with an in-plane free layer, Houssamedine et al. [40] and Devolder at al. [41] respectively proposed to use a perpendicular polarizer or an in-plane polarizer shifted by 90° compared to the free layer. In vortex based STOs, Khvalkovskiy et al. from CNRS/Thales [42] first proposed to use a second vortex as a spin-polarizer. N. Locatelli et al. [43] reported on such double vortex systems record quality factor, up to 16 000. Recently, Dussaux et al. [44] showed that a single vortex based STO with a perpendicular polarizer can also permit to observe sustained oscillations at zero applied field. All in all, vortex based STOs present major advantages for rf-applications: they present the best spectral coherence and they can easily operate at zero applied field.

More generally, one common characteristic of all types of spin-torque oscillators is their strong nonlinear behavior that couples their amplitude of oscillations to their frequency. This nonlinear behavior strongly enhances the STO agility but also leads to a detrimental loss of spectral coherence. Understanding and controlling the non-linear behavior of spin-torque oscillators is thus a crucial concern that can be addressed in the "auto-oscillator model" [45].

1.2.4 Nonlinear behavior and auto-oscillator framework

To model the STO behavior, Slavin et al. [45] proposed a general formalism that can describe the dynamics of any nonlinear oscillator (STO, voltage control oscillator, pendulum etc). This model, called "the auto-oscillator model", permits to predict the necessary conditions to establish a regime of self-sustained oscillations and to evaluate the effect of thermal noise on the sustained regime. Furthermore, it can also predict the conditions for synchronizing the oscillations with an external periodic signal. In the last few years, different analytical, experimental and micromagnetic studies have demonstrated that the dynamics of STOs can be well described by this theoretical model. In this section, we present the main ingredients of this model that we will use to discuss our experiments in different chapters of the manuscript. In chapter 4, we will adapt this model to the vortex based STO locked with an external current and highlight how the locking process can be precisely tuned through the spin-transfer locking forces.

1.2.4.1 Auto-oscillator equation

The auto-oscillator model describes in a complex form the dynamics of a single excited mode. In a STO, the hypothesis of a single mode excited by spin-transfer torque is quite strong as we will see in this manuscript. However this model is widely used as it fits well with the experimental results even when several weakly coupled modes are excited. In this framework, an excited mode is modelled by a variable $c(t) = \sqrt{q(t)} \exp i\Phi(t)$ with $q(t) = |c(t)|^2$ and $\Phi(t) = arg[c(t)]$ its respective power and phase. The mode dynamics are then described by the following equation :

$$\frac{dc}{dt} + i\omega(|c|^2)c(t) + [\Gamma_+(q) - \Gamma_-(q)]c(t) = f(t) \tag{1.10}$$

with ω the oscillator resonance frequency, Γ_+ the intrinsic damping for energy dissipation, Γ_- the negative damping corresponding to the action of the energy source, and $f(t)$ the driving term which model the interaction with external signal or thermal fluctuations. For spin-torque oscillator, the intrinsic positive damping is defined by the Gilbert damping. The negative damping corresponds to the effect of the spin torque and is thus proportional to the applied current I. All the system parameters generally depend on the auto-oscillation power $p = |c|^2$ so that the spin-torque auto-oscillator is a nonlinear system.

1.2.4.2 Self-sustained regime

The dynamics of an isolated ($f(t) = 0$) auto-oscillator equation can be described by its phase $\Phi(t)$ and amplitude $q(t)$ dynamics:

$$\begin{cases} \frac{dq}{dt} + 2[\Gamma_+ - \Gamma_-]q(t) = 0 \\ \frac{d\Phi}{dt}\sqrt{q(t)} + \omega(q)\sqrt{q(t)} = 0 \end{cases} \tag{1.11}$$

This system has a stationary solution $c_0(t) = \sqrt{q_0} \exp i\Phi_0(t)$ with a non-zero power if $\Gamma_+(0) > \Gamma_-(0)$. Thus the condition $\Gamma_+(0) = \Gamma_-(0)$ determines the threshold for sustained oscillations (see Fig. 1.8). The stable solution is then determined by the condition $\Gamma_+(q_0) = \Gamma_-(q_0)$ where the negative damping exactly compensates the positive damping, i.e where the effective damping is equal to zero. Generally, the negative and positive damping respectively increases and decreases with p_0 so that the system has a unique and stable solution.

The stationary power p_0 and the frequency of oscillation ω are expressed as [45]:

$$\begin{cases} p_0 = \frac{\zeta-1}{\zeta+Q} \\ \omega = \omega_0 + N\frac{\zeta-1}{\zeta+Q} \end{cases} \tag{1.12}$$

with $\zeta = I/I_{th}$ the dimensionless supercriticality parameter, Q the nonlinear positive damping parameter ($\Gamma_+ = \Gamma_G(1+Qp)$), ω_0 the oscillator's intrinsic frequency and $N = d\omega/dp$ the nonlinear frequency shift which links the power to the phase of the oscillator. The stationary power is thus equal to zero at the threshold current and increases with the supercriticality. One should notice that a modification of power creates a change of the oscillating frequency (see Fig. 1.8).

To determine the stability of this solution, we linearize Eq. 1.11 around $p = p_0$. Thus we determine the damping rate Γ_p for small power deviations δp:

$$\Gamma_p = (\frac{d\Gamma_+(p)}{dp} - \frac{d\Gamma_-(p)}{dp})p_0 \tag{1.13}$$

The stationary solution is thus stable only if $\Gamma_p > 0$, i.e $\frac{d\Gamma_+(p)}{dp} > \frac{d\Gamma_-(p)}{dp}$ which is the case of a spin-torque oscillator [45]. For an STO, the damping rate is expressed as:

$$\Gamma_p = (\zeta - 1)\Gamma_G \tag{1.14}$$

with Γ_G the linear contribution of the positive damping. One can notice that we find again that Γ_p is positive only for $\zeta > 1$, i.e. in the regime of self-sustained oscillations.

Contrary to most oscillators in nature, the nonlinear frequency shift N of a STO is generally large. This means that the phase of a STO is strongly coupled to its amplitude and so that STOs are highly nonlinear oscillators. A relevant parameter to describe the impact of this coupling on the STO dynamics will be the nonlinear dimensionless parameter ν:

$$\nu = \frac{Np_0}{\Gamma_p} \tag{1.15}$$

In a spin torque oscillator, ν is generally large ($\nu >> 1$). This parameter ν will be particularly crucial to understand the non-autonomous regimes of a STO or the dynamics of a STO under thermal fluctuations as we will see in this manuscript.

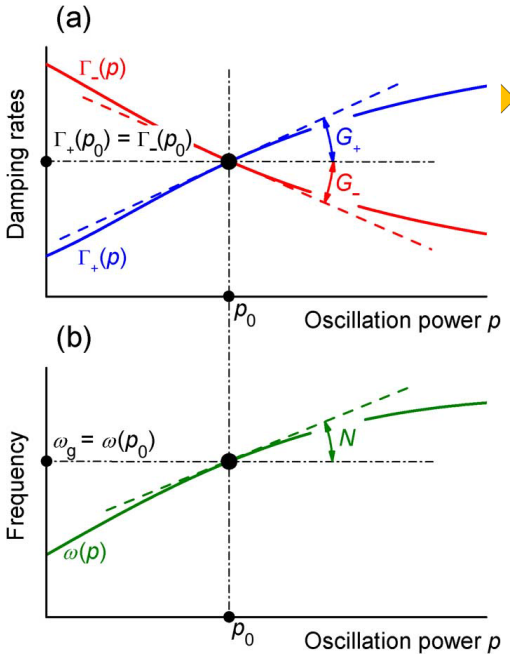

FIGURE 1.8: Dependences of the damping rates and oscillation frequency on the oscillation power p. Intersection of the curves Γ_+ and Γ_- determines the free-running operation point of the oscillator with the power p_0 and free-running generation frequency ω_0. The slopes of the damping rates and the frequency at the free-running operation point define the nonlinear positive and negative damping coefficients and the nonlinear frequency shift coefficient N. Extracted from [45].

1.2.4.3 Effect of thermal fluctuations on the auto-oscillator's dynamics

The small size of a spin torque nano-oscillator makes them really sensitive to noise as the energy of the thermal fluctuations are of the same order as the energy of the system at room temperature. In the presence of thermal noise, the auto-oscillator complex variable $c(t)$ is no longer monochromatic. Thus the frequency spectrum of the auto-oscillator is no longer a Dirac peak but has a finite linewidth $\Delta\omega$. Generally the thermal noise $f_b(t)$ can be considered as a white Gaussian stochastic process.

The linearized equation of motion of the spin-torque oscillator under the influence of noise is expressed as:

$$\begin{cases} \frac{d\delta q}{dt} + 2\pi f_p \delta q(t) = 2\sqrt{q_0} g_b(t) \\ \frac{d\delta\Phi}{dt} + \omega_{STO}(|q|^2) = \frac{1}{\sqrt{q_0}} h_b(t) \end{cases} \tag{1.16}$$

with $g_b(t) = Re[f_b(t)\exp(-i\Phi(t))]$ and $h_b(t) = Im[f_b(t)\exp(-i\Phi(t))]$, and ω_{STO} the STO frequency. The amplitude dynamics is driven by a retroaction process, due to the retroaction force $2\pi f_p \delta q(t)$ with $f_p = \Gamma_p/\pi$, which is not the case of its phase that diffuses during time. Thus the oscillator linewidth will mainly be determined by the phase dynamics [45, 46].

From the fluctuation-dissipation theorem, it is also possible to calculate the diffusion constant Δf_0 associated with the thermal noise [46]:

$$\Delta f_0 = \Gamma_+(q_0)\frac{k_bT}{E(q_0)} \tag{1.17}$$

with Γ_+ the intrinsic damping, k_bT the thermal energy, E the energy of the system. Given the absence of a phase retroaction, the linewidth of a linear oscillator ($\nu = 0$) is thus directly equal to Δf_0. For a nonlinear spin-torque oscillator, the linewidth Δf strongly depends on the amplitude/phase coupling as demonstrated by J. V. Kim et al. [46]:

$$\Delta f = (1+\nu^2)\Delta f_0 \tag{1.18}$$

The strong impact of the amplitude/phase coupling on the linewidth contributes a lot to the quite poor spectral coherence of STOs.

To analyze more in details the spectral coherence of a STO, one should not only focus on its linewidth but also on the spectral densities of amplitude and phase noises which represent the repartition of power around the oscillating frequency. Indeed depending on the type of rf-applications, the noise requirements are at a different frequency offset, i.e. more or less closer to the oscillator frequency carrier f_0. By solving the linearized equation of motion of the spin-torque oscillator in the Fourier domain (see Eq. 1.19), we can establish the expressions of the amplitude and phase noise spectral densities:

$$\begin{cases} S_{\delta p} = \frac{\Delta f_0}{\pi}\frac{1}{f^2+f_p^2} \\ S_{\delta\Phi} = \frac{\Delta f_0}{\pi f^2} + \frac{\nu^2 f_p^2}{f^2}S_{\delta p} = \frac{\Delta f_0}{\pi f^2}\left(1+\nu^2\frac{f_p^2}{f^2+f_p^2}\right) \end{cases} \tag{1.19}$$

Through time domains measurements, M. Quinsat et al. [47] and E. Grimaldi et al. [48] respectively demonstrated the validity of these equations on uniformely magnetized STOs and vortex based STOs. In Fig. 1.9, we notice that (f_p, Δf_0 and ν) are the three parameters that drive the oscillator response to thermal fluctuations. It can be seen that the amplitude-phase coupling increases by 14 dB ($10\log(1+\nu^2)$) the phase noise level for frequency offset lower than f_p.

1.2.4.4 Enhancement of the spectral coherence in the self-sustained regime

Controlling and understanding the three parameters, i.e f_p, Δf_0 and ν, that drive the oscillator dynamics is thus a crucial issue to enhance the spectral coherence of a STO. In this perspective, different approaches can be considered:

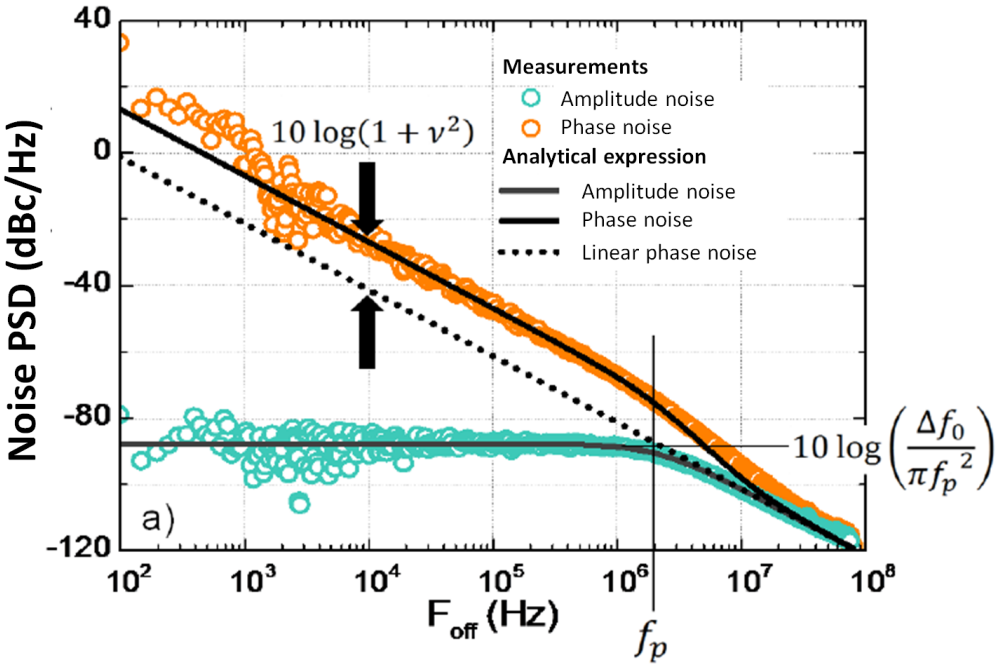

FIGURE 1.9: Experimental measurements of the power spectral density of phase (orange dots) and amplitude (green dots). The dot and solid lines respectively correspond to the theoretical linear phase noise and total phase noise. Adapted from [48].

1. The reduction of the linear linewidth Δf_0: Vortex based STOs are particularly promising as their dynamics involve larger oscillations of magnetization than uniformely magnetized STOs, which increase their energy $E(q)$ and reduce Δf_0. Vortex based STO thus present lower linewidth than uniformly magnetized STOs (300 kHz [36] compared to 20 MHz [49] in NiFe based junctions).

2. The development of magnetic materials with lower damping constant α than the generally used NiFe: For example, FeB junctions are particularly promising with a damping constant α two times lower than permalloy (0.005 for FeB [50], 0.01 for NiFe junctions).

3. The control of the nonlinear dimensionless parameter ν: A large ν increases the oscillator frequency tunability with current but also increases the oscillator linewidth through the amplitude/phase coupling. A optimal tradeoff between these two requirements is thus be needed. As demonstrated by Houssameddine [49], interlayer mode coupling can be an option to control the oscillator nonlinear behavior. In Chapter 3, we will discuss this option in double vortex based STOs. Vortex based STOs have an intrinsic advantage, compared to other STOs, which is the fact that their frequency tunability with current is decorrelated from their nonlinear behavior. Indeed, thanks to the Oersted field (that modifies the vortex confinement) they can have a high frequency tunability with the dc-current for either large or low N parameter.

1.2.4.5 Auto-oscillator in the non-autonomous regime

Controlling an oscillator with an external oscillating signal f_{ext} offers multiple options to improve its dynamics. Depending on the type of excitations, the STO is in different non-autonomous regime (injection locking [51–58], mutual synchronization[45, 59, 60], parametric [61, 62] or resonant excitation [53], frequency modulation [63–65] etc..).

Similarly to the autonomous regime, experimental and theoretical studies [45, 56, 66–68] have reported the strong influence of the oscillator's nonlinear behavior on the non-autonomous regimes (locking bandwidths [45], spectral coherence [66, 69], transient regime [56, 70] among others).

Most of these experimental studies have focused on the non-autonomous regimes driven by oscillating magnetic signal (either generated by a rf-source or a second STO) such as spin-waves [59, 60, 65, 71] or dipolar [53, 61, 69, 72]/exchange [73] interactions. Different parameters have been identified as crucial to control these types of locking mechanism such as the field symmetry [61, 62] and the attenuation length of spin-waves [74].

In parallel, most of the possibilities offered by the different spin-transfer torques to lock a STO remain to be explored. In chapters 4 and 7, we will demonstrate that the specific locking process of a vortex based STO involves two different components of spin-transfer torques: the Slonczewski torque and the Field-Like torque. In particular, we will show in chapter 8 that the Field-like torque driven synchronization permits to achieve mutual synchronization of STOs driven by the self-emitted currents. Spin-orbit torques should offer similar perspectives to control the non-autonomous regime of STOs.

1.3 Potential spintronics rf-devices based on spin-transfer nano-oscillators

In this section, we present the different technologies that could take advantages of spin torque oscillators. Beyond their small size and low power consumption, STOs are tunable oscillators, compatibles with CMOS technologies and radiation hard [75].

1.3.1 RF emitters and amplifiers

1.3.1.1 Frequency tunable oscillators

Within the family of rf-applications, the first application that we think about is the frequency generator. Information and communications technologies face a growing demand on oscillators that can generate rf-signals from a few kHz to hundreds of GHz. The state of the art spin torque oscillators cover a large range of frequencies from 100 MHz to 65 GHz [30], and antiferromagnet based STOs are expected to reach the THz [76]. Depending on the targeted applications, the required characteristics can vary from a highly coherent and stable oscillator like quartz oscillators to a frequency tunable oscillator like a voltage control oscillator (VCO). The characteristics of STOs fit more with the second family given their nonlinear behavior. Their high agility combined with their low size and tolerance to radiations are particularly well adapted for rf-applications such as mobile and satellite telecommunications. Indeed, the widely used VCOs consists of RLC resonator with diode varactor. Thus its size is generally above the micrometer and limited by the size of the inductance and the capacitance. The STO has the great advantage to be much smaller (around 100 nm^2). Nevertheless their phase noise remains much larger than the conventional VCO (-90 dBC/Hz against -120 dBc/Hz at 1 MHz offset frequency).

One approach is to stabilize the sSTO through a phase locked loop circuit with a quartz as reference oscillator. The STO frequency is divided and its phase continuously compared to the quartz phase. An error signal generates a current feedback to correct the oscillator phase. This option should enhance the oscillator spectral coherence close to the coherence of the quartz oscillator but it will strongly enhance the dimension of the total device. However this type of circuit has its interest for satellite applications which requires radiation hard oscillators like STOs. In Chap. 6, we will present some promising developments towards the integration of STO based phase locked loop in conventional electrical circuits.

Another approach is to take advantage of the large frequency agility of STOs. Indeed, their agility constant is determined by the oscillator effective damping which is about ten times their period of oscillation [68, 77], i.e. of only a few nanoseconds. Thus Choi et al. [78] experimentally demonstrated that STOs can transmit information through discrete amplitude changes of their carrier signal with a modulation current, i.e. with “an amplitude-shift keying (ASK)” technique (see Fig. 1.10). In their experiment, they encode the information with a binary signal, i.e a pair of discrete amplitudes, and their encoding rate is about 200 kHz. They anticipate that better STOs [79] could operate at a much faster rate, up to 1.5 GHz, for an estimated 12.5 dB signal to noise ratio. After amplification the encoded signal is emitted with an rf antenna and transmitted over a 1 m distance before being detected by a second antenna.

The detected signal is then demodulated with an envelope detector to recover the initial signal. These preliminary results are really promising as they used STOs that are far from the current state of the art [80].

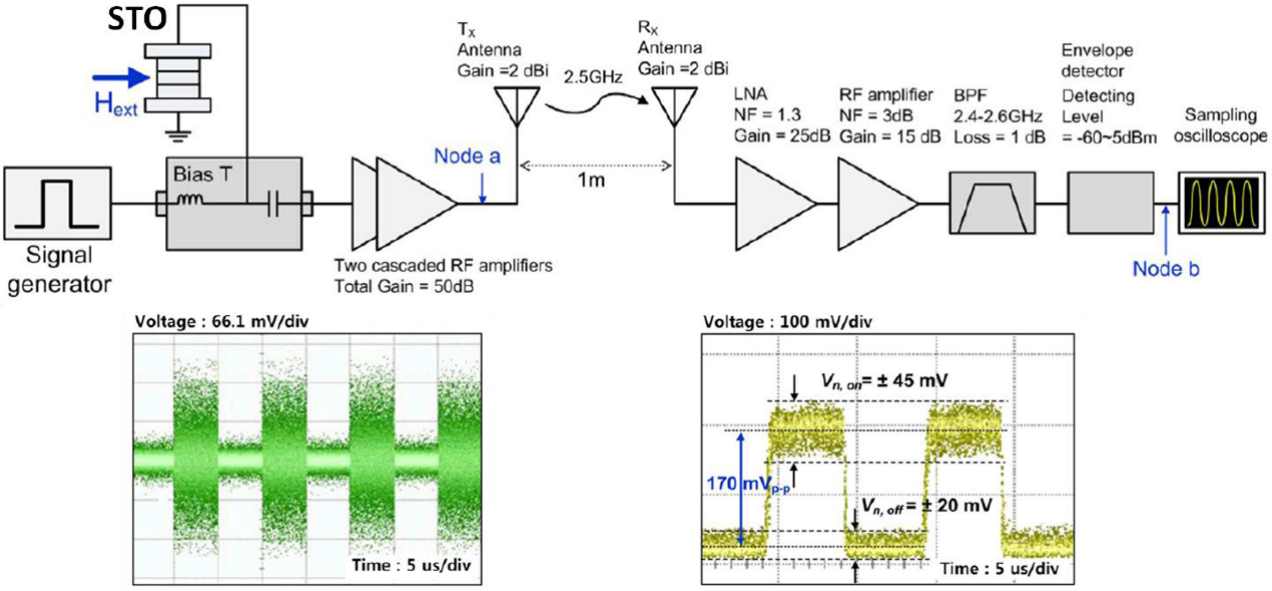

FIGURE 1.10: (Top) Schematic of the STNO–based binary amplitude-shift keying transmitter (Bottom) Measured time trace of the modulated signal when the pulse frequency is 100 kHz at nodes a and b. Adapted from [78]

A third option is to synchronize an array of N-STOs to increase the total output emitted power by a factor N^2 and the spectral coherence by a factor N [81]. However as the number of synchronized STOs increases, the array will loose its agility, except for vortices thanks to the influence of the Oersted field. Thus a precise trade-off is needed between the targeted coherence, power and the agility to evaluate the optimal number of synchronized STOs. Anyway, the synchronization of multiple STOs is expected for more than ten years [60, 82] and has not been successful for more than N=4 [73] through exchange coupling which is not really suitable for applications. The most promising type of coupling is the electrical synchronization of STOs that had been theoretically largely studied [66, 83–86] but never experimentally observed until now (see Chap. 8), mainly due to technical (low output power [83]) and intrinsic (coupling mechanism [84]) limitations.

1.3.1.2 RF-amplifiers

In 2006, Slavin et al. [87] proposed the concept of a microwave-frequency selective amplifier based on an array of STOs. Indeed, a damped STO can be resonantly excited by an rf-current or field either around its eigenfrequency f_0 ("normal" resonance [53, 58, 88]) or twice $2f_0$ (parametric resonance [61, 62, 89]). Thus the STO retransmit a copy of the injected rf-signal but the output power of a single STO need to be strongly enhanced to get an amplified copy.

For an array of N-STOs, locked to the injected rf-current, the power is enhanced by a factor N^2 which is potentially larger than the power of the injected rf-current. Furthermore, the frequency of the device can be tuned by the dc-current. Thus arrays of STOs have all the characteristics required for an rf-amplifier. One should also notice that the parametric phenomenon is well known to act as a low noise amplifier [87].

1.3.2 Frequency detector

1.3.2.1 Spin-diode detectors and filters

The state of the art for microwave detection is the Schottky diode. The diode rectifies the incident rf-signal and sends it to a bypass capacitor that then delivers an amplitude proportional to the input power level (square-law). The sensitivity of the diode can be controlled with a dc-current that changes the functioning point to enhance the conduction. However most of the commercial Schottky diodes work at zero electric field to reduce the power consumption. The commercial Schottky diode based detector currently uses semiconductor materials (GaAs, Si etc..) which make them really sensitive to thermal fluctuations and radiation. Another limitation is their large size as the detection circuit has to contain a Schottky diode but also an RF choke and a bypass capacitor to return a dc-current and fix the detection bandwidth.

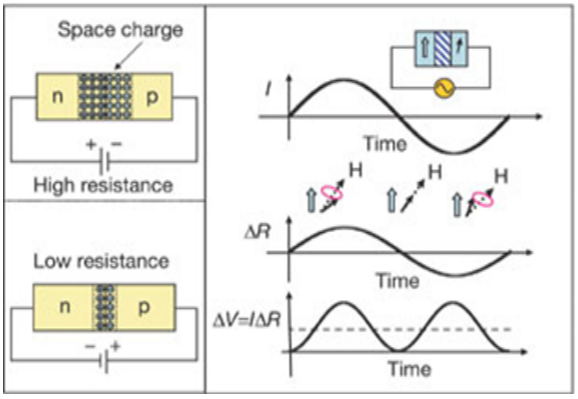

FIGURE 1.11: Comparison of the the semiconductor p–n diode (left panel) and the spin-torque diode (right panel). In the semi-conductor diode, if positive voltage is applied to the n side, the space charge region around the p–n junction is enlarged, and the resistance is high. For the opposite polarity, the space charge region is shrunk and the resistance is low. In the case of the spin-torque diode, the free-layer magnetization oscillates owing to the current-induced torque. The bottom trace in the right panel of a shows the schematic variation of the product of the current and the change in resistance and its average value that is non-zero. Adapted from [90]

Thus the small size of spin-torque oscillators and their potential use on a large range of temperature make them promising candidates for rf-detection applications. Indeed Tulapurkar et al. [90] demonstrated in 2005 that spin-diode rectification could be observed with a spin-torque oscillator excited by an rf-current. The spin-transfer torque associated with the spin-polarized

rf-current makes the magnetic moment oscillate when its frequency is close to the eigenfrequency of the magnetic layer. The generated oscillations of magnetoresistance are proportional to the injected rf-current and either in-phase or out-phase with it. The multiplication of the injected rf-current with the oscillations of magnetoresistance generates a rectified voltage proportional to I_{rf}^2 (see Fig. 1.11). Similarly to the Schottky diode, the spin-diode effect follows a power square law. Recent studies on the out-of-plane modes of uniformely magnetized STOs have reported a maximum effective sensitivity of 12,000 V/W [91], exceeding that of semiconductor diode detectors (3,800 V/W [92]).

To go beyond these already record sensitivies, one perspective is to detect with an array of STOs that react at close frequencies. Depending on the circuit geometry (phase shifter) or on the STO configuration (direction of the spin-transfer torques, see Chap. 7), the array can either act as a band-pass or band-stop filter around the central frequency of the array. If N STOs are simultaneously excited by the rf-current, the detected signal is enhanced by a factor N^2. Moreover, if the N STOs are synchronized, the bandwidth selectivity of the filter is expected to increase by a factor N (see Fig. 1.12) as it is the case for its spectral coherence in the autonomous regime.

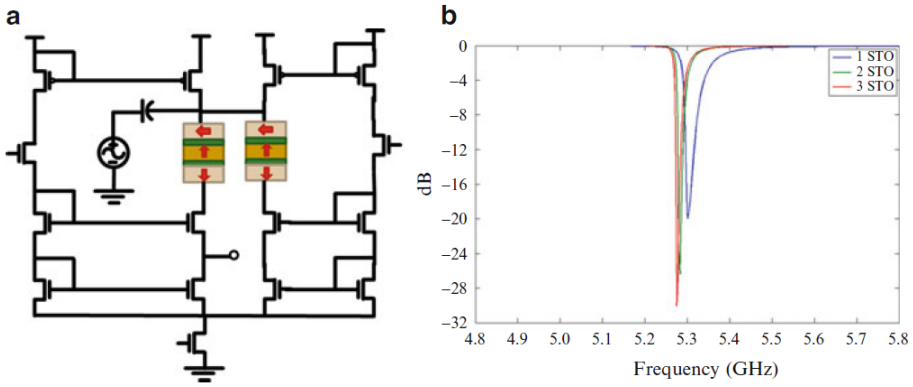

FIGURE 1.12: (a) A bandstop filter based on coupled STOs. The external circuit permit to fix with precision the frequency of oscillation and is adapted to reduce the losses (b) Frequency response of a filter depending on the number of coupled STOs. Adapted from [93]

Another alternative approach to enhance the detection sensitivy is to correlate the detection scheme with a magnetic switching. Indeed, a spin-polarized rf-current can resonantly excite a magnetic layer and induce its switching [94]. In such case, the rectified signal will be enhanced as a magnetic switching is associated with a change of resistance scalable with the TMR. In Chap. 7, we report a record effective sensitivity of 40000 V/W in vortex based STOs by resonantly expulsing the vortex core with an rf-current. A similar detection scheme have recently been reported by B. Fang et al. [95] on uniformly magnetized STOs.

With this large effective sensitivity, the response of the STO detector is no longer a problem. A similar detection scheme can thus be used to develop another kind of STO array that cover

a large band of frequencies as targeted for mobile telecommunications. Each STO of the array will be patterned to have its own eigenfrequency so that we have multiple detection channels and the size of the circuit remains in the range of the μm^2. This makes this kind of network particularly suitable and promising for radio frequency telecommunications where a size reduction and larger frequency bands are targeted.

1.3.2.2 Hard disk read head

In the competitive sectors of data storage, strong efforts are continuously made to reduce the size and enhance the storage capacity of hard disk. The latest generations of hard disk present a storage density of hundreds Gbit/in^2 and the next step is now to reach the Tbit/in^2. Different technologies are under development to reach this aim like the Shingle Magnetic Recording [96] or the Bit Patterned Media [97] that could store information bit of around 20-30 nm.

To encode or read so small a bit, data read heads of similar size are necessary. In commercial HDD, the read head consists of highly sensitive magnetic tunnel junctions with a free and fixed layer. As seen in Fig. 1.13, the resistance state of the junction indicates the magnetic state of the magnetic bit below the read head as the free layer switches in the field direction parallel to the bit. This current technology is limited both by the signal to noise ratio as the read head size decreases and by the relaxation time of the free layer which limits the reading rate below 1 Gbit/s.

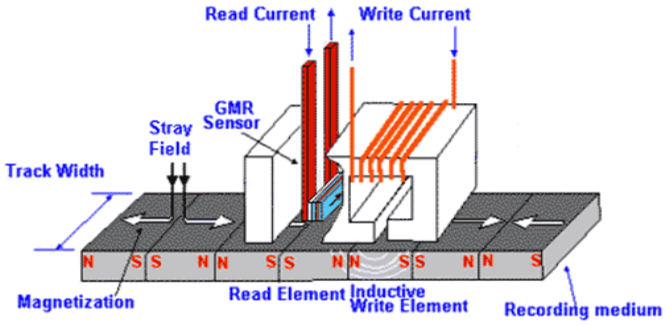

FIGURE 1.13: Principle of a GMR read hear. Extracted from a MRSEC lecture

One solution proposed by Toshiba researchers is to develop a 30 nm STO based read head with an oscillating free layer instead of a fixed one. The reading is driven by the stray field of the magnetic bit which acts as a modulating field that modifies the STO frequency. By demodulating the signal, the changes in frequency are converted into a DC voltage signal. The reading rate is therefore determined by the nonlinear behavior of the spin-torque oscillator through its effective relaxation time, i.e its effective damping f_p, which is of only a few nanoseconds. Thus such a technology could lead to a reading rate of a few Gbit/s. Nevertheless, the oscillator

noise remains currently too large for real applications. Different solutions are currently under investigation to face with this issue such as employing a delay detection method [98], using the parametric effect and phase locked loop driven STOs [87] or through the development of new materials.

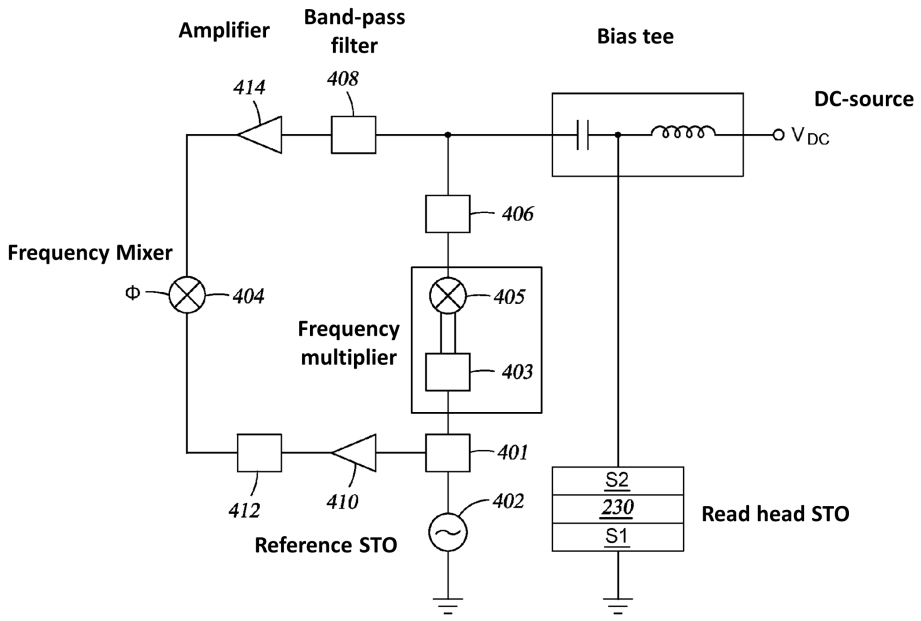

FIGURE 1.14: STO read head coupled to an injection locking circuit. The signal from the local reference oscillator locked in a PLL is divided in two part. One is sent to a frequency multiplier to generate a $2f_0$ ac-signal isolated with a band-pass filter and that injection locks with the STO read head. The second part is sent to a frequency mixer that allows the detection of the STO signal filtered with a bandpass filter. Adapted from [99]

In Fig. 1.14, we present the principle of the parametrically locked STO read head with a reference signal supplied by a STO stabilized in phase locked loop (PLL) as proposed by Braganca et al. [99]. The STO read head oscillates at f_0 and can parametrically synchronize with a reference ac-signal emitted at $2f_0$. This reference signal can be a second STO that also oscillates at f_0 and which is stabilized in a phase locked loop. By using a frequency mixer, a signal at $2f_0$ is generated and used to lock the first STO. In this locked regime, the STO read head has a much better SNR and its output power is enhanced. Furthermore, Muduli et al. [100] and Iacocca et al. [101] respectively demonstrated experimentally and theoretically the stability of such a regime by studying the modulation regime of a synchronized STO. In the device proposed by HGST researchers [99], the ac-reference signal and the output signal are decorrelated (one at f_0, the other at $2f_0$). The detection scheme is thus performed through the demodulation of the STO read head signal with the reference signal of the second STO (see Fig. 1.14).

1.3.3 Heterodyne and self-homodyne frequency mixers

A heterodyne frequency mixer is a electrical device that can create two new signals ($f_1 - f_2$ and $f_1 + f_2$) from two input signals (f_1 and f_2). The widely used applications with this type of device is the superheterodyne receiver which lowers the frequency of a receiving signal to facilitate its post-process. The frequency is lower by mixing the receiving signal with a second signal generated by a local oscillator. Generally the output signal is filtered with a low pass filter to only keep the lowest frequency. Such detection circuits are widely used to demodulate a signal and recreate a copy of the original signal. Spin torque oscillators have been considered to combine both functions of a heterodyne frequency mixer [102] and thus to form a self-homodyne frequency mixer. Indeed it is possible to modulate the emitted signal of a STO due to its highly nonlinear behavior. Thus a STO is a local oscillator that can also effectuate a mixing function.

In 2007, A. Yamaguchi et al. [103] demonstrated that a ferromagnetic nanowire can demodulate the modulated amplitude of a rf signal whose carrier frequency corresponds to the resonant frequency of the nanowire. Spin-torque nano-oscillators are expected to perform a similar function but with much larger demodulating ratio and higher SNR as we mentioned. A STO could replace the envelope detector used in the study of Choi et al. [78] (see Fig. 1.10) leading to a full spintronic transmitting and receiving chain.

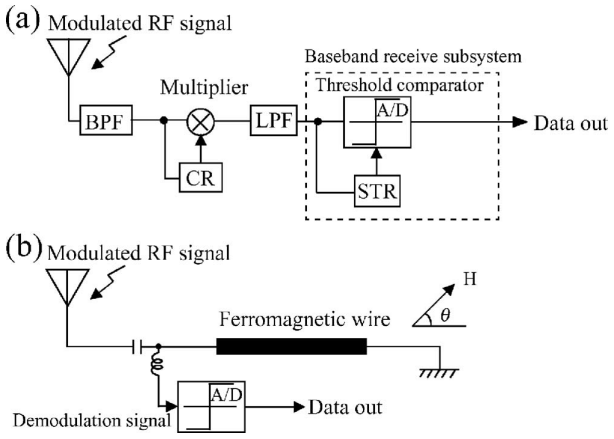

FIGURE 1.15: (a) Block diagram of a general rf signal demodulator. BPF: bandpass filter, LPF: low-pass filter, CR: carrier recovery circuit, STR: symbol timing recovery circuit, and A/D: threshold comparator analog-to-digital converter. (b) Block diagram of an equivalent demodulator using a single ferromagnetic wire. Extracted from [103].

1.3.4 Oscillator networks for non-conventional and bio-inspired rf-applications

Besides the constant research for miniaturization, there are various classes of problems related to brain functions like image and voice recognition that computers handle only with complex Boolean algorithms at the cost of a large power consumption. In this section, we expend

upon different considered approaches to use STOs in associative memories that can handle non-boolean logic.

1.3.4.1 The brain architecture

Non-Boolean methods have been proposed to change the computing paradigm and to mimic the best known non-Boolean system, i.e the human brain. The brain is made up of neurons that are massively interconnected in parallel through synapses to form neural networks. Its properties make the brain much more efficient for recognition/learning and less power consuming than a supercomputer (10 MJ per day compared to 10^5 MJ).

The basic unit of the brain is the neuron, an electrically excitable cell that processes and transmits information (the "neuron doctrin" [104]). Each neuron has its own function and can only be activated by specific and defined inputs. The neuron activity is defined by "an integrate and fire" model. The neuron potential integrates the received electrical pulses. When the neuron potential overtakes a threshold value, the neuron fires and emits an electrical pulse (or eventually a train of pulses).

The neuron activity is controlled by its external connections through synapses. A synapse is a structure that connects two neurons and controls the transport of neurotransmitters (either electrical or chemical) between them (see Fig. 1.16). The synaptic plasticity, i.e the dependance of the transmission rate with the history of the external inputs, is controlled by the pre- and post-synaptic activity of the neurons. Synapses thus play a key role in the memory function. Some synapses connect with a neuron to itself to form an autapse.

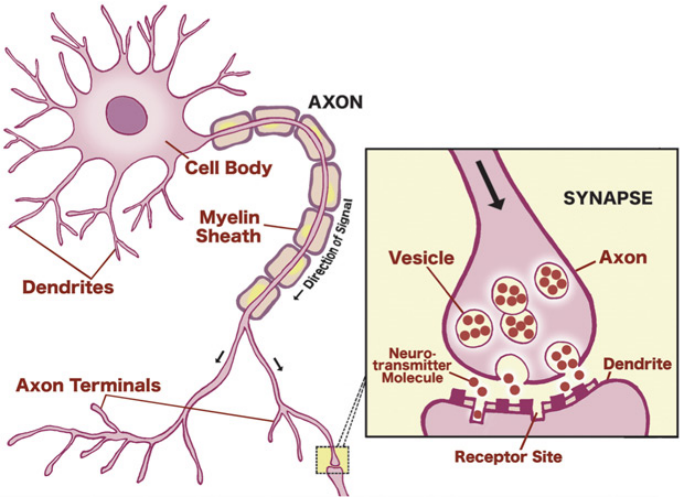

FIGURE 1.16: Principle of communication between neurons. Extracted from www.educarer.org

Depending on the learning inputs, a neural network change its connecting weights and thus adapts its activity. The network activity can be described as an energy function that minimizes

to a stable state through the evolution of the network interconnections. It should be noted that the learning process can either be supervised or not depending on the type of network.

1.3.4.2 Spin-torque based neural networks

Studies about neural networks have flourished in the 70s and 80s but have dropped off since then. Over the past decade, there has been a renewed interest with the development of new techniques that allow to the observation of neural activities [105, 106]. Another perspective to study and mimic neural network is to develop bio-inspired networks. A first example of effective associative memories based on classical electronic components (micro-controllers and a potentiometer) has been proposed and demonstrated by Pershin et al. [107].

Indeed, neurons can be modeled as nonlinear oscillators. They adjusts their firing rate depending on the signal of excitation. Thus a network of coupled neurons can synchronize or not depending on the coupling weights mediated through synapses. A network of non-linear spin-torque oscillators can present similar properties. Spin-torque oscillators also have the advantage of presenting intrinsically different ways to tune their coupling weight through their non-linear behavior ν or their frequency detuning. Nevertheless it may be difficult to individually control with precision these parameters in large arrays of oscillators. Another possibility is to tune externally the coupling constant of two STOs. This can be realized in the case of electrically coupled STOs. Indeed we can easily add between them an electrical component that acts like a synapse.

A synapse can be modelled by a memristive device that confers the property of dynamical learning to the total network. A memristive device, also called a memristor, is a non-volatile and multi-state memory that adapts its memory state to the input activity. Such devices represent a promising alternative to the binary information storage. Recently, we demonstrated at CNRS/Thales the concept of a spin-torque memristor [18] that could be combined with STOs to form a neural network as represented in Fig. 1.17. For a system of two STOs coupled through a memristor, the impedance mismatch between the STO and the memristor could thus drive and modify the coupling constant. In such a case, each STO is not only connected to its neighbour but also to itself due to the reflection at the memristor interface.

Other promising architectures of neural networks based on STOs and without memristor devices have also been proposed [108]. Generally, the patterns are either store in the phases of the STOs or in the frequency detunings between the different STOs. The difficulties to measure the STO phase and to achieve phase synchronization make the second option more promising for large networks. To stabilize and drive the network, Bourianoff et al. [108] proposed for example to use STO based phase locked loops that we will present in Chapter 6.

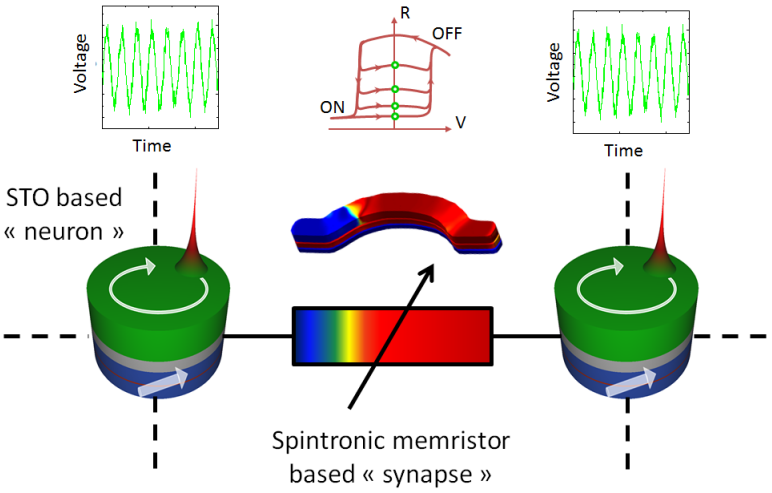

FIGURE 1.17: Principle of a spintronic network with STO based neurons and spintronic memristor based sinapses

Chapter 2

Vortex based spin-torque oscillators : "From single vortex to double vortices"

For this thesis, we study the dynamics of vortex based STOs in confined nanodots. In this chapter, we present the main properties of the vortex magnetization distribution and describe how external parameters such as field or current can modify this distribution. We describe the dynamics of the lowest mode in energy of a magnetic vortex configuration, i.e the gyrotropic mode of the vortex core, in the framework of the Thiele equation. The gyrotropic mode is generally the only mode observed in vortex based STOs given that it is far in frequency from the other modes and the symmetry of the spin-transfer torque. We thus discuss the different spin transfer forces that can excite self-sustained oscillations of the gyrotropic mode. Finally, we extend our study to the case of coupled vortices. Indeed, different studies reported [43, 49, 101, 109] that mode coupling could be used to tune the properties of a STO. Here we present the theoretical expectations for a double vortex based STO that we will investigate experimentally in the next chapters. In this system, the coupling between the two vortices leads to an hybridization of the vortex gyrotropic modes. There we highlight that the STO's properties can be controlled by changing the relative configurations (chirality and polarity) of the two vortices.

2.1 The magnetic vortex

The magnetization distribution of a ferromagnetic configuration is defined by the balance between magnetostatic, exchange and anisotropic energies. In circular, but not only, ferromagnetic dot, a non-uniform magnetization state can be stable for a certain aspect ratio between

the radius and the thickness of the magnetic film. This non-uniformed magnetic state, with zero mean magnetization, is called "magnetic vortex".

2.1.1 Properties of a magnetic vortex

2.1.1.1 Stability domain

The stability diagram of a ferromagnetic nanodot depends on the radius R, on the thickness L and on the exchange length $L_e = \sqrt{\frac{2A}{\mu_0 M_s^2}}$ of the magnetic material (with A the exchange constant) as shown in Fig. 2.1. To stabilize a magnetic vortex, the radius R and the thickness L have to be large to respectively minimize the effect of the exchange energy and to avoid an in-plane magnetization.

In the region of vortex stability, the magnetization distribution is composed of two parts. A spatially extended region, called the "vortex body", where the magnetization is circular and contained in the disk plane. This planar component of the magnetization is orthoradial (colinear to the border of the disk), minimizing the stray field. In the center of the vortex body is a second region, spacially restricted (about twice the exchange length L_E 10 nm), where the magnetization is out of plane and is called the vortex core.

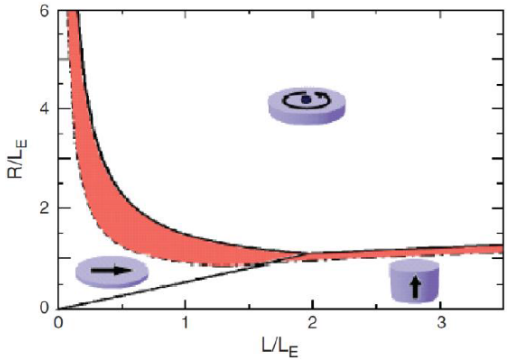

FIGURE 2.1: Phase diagram of the magnetization distribution in a ferromagnetic cylindric dot with an exchange length L_E, a radius R and a thickness L. The three stable magnetic states are: the vortex, the quasi-uniform distribution in-plane or out of plane. Full line determined stability regions. A metastable zone, called the corail zone, is represented in red and delimined by full and dot lines. Extracted from [110]

Two parameters characterize a magnetic vortex: the vortex polarity P, which corresponds to the direction of the vortex core (either up +1 or down -1), and the vortex chirality C, which corresponds to the coiling of the magnetization in the vortex body (either clockwise +1 or anticlockwise -1)

2.1.1.2 Static properties of a vortex

2.1.1.2.1 Centered vortex

Usov et al. [111] first used the variational method to obtain the magnetization distribution of a centered vortex in a dot. They minimized the exchange energy to obtain the shape of the vortex core, and then the total free energy (i.e exchange, magnetostatic and anisotropy energies) to obtain its size. Supported by micromagnetic simulations, Feldtkeller et al.[112] demonstrated that the vortex core distribution was more precisely described (see Fig. 2.2) by a Gaussian distribution (Eq. 2.1). In spherical coordinates, the total magnetization distribution is then written as (see Fig. 2.3):

$$\begin{cases} m_\rho = 0 \\ m_\chi = C \ \left(1 - \cos^2\left(\Theta(\rho)\right)\right) \\ m_z = \cos\left(\Theta(\rho)\right) = P \ exp\left(-ln2(\frac{2\rho}{b})^2\right) \end{cases} \tag{2.1}$$

with $\Theta(\rho)$ the angle between the local magnetization $\overrightarrow{m}$ and $\overrightarrow{m_z}$

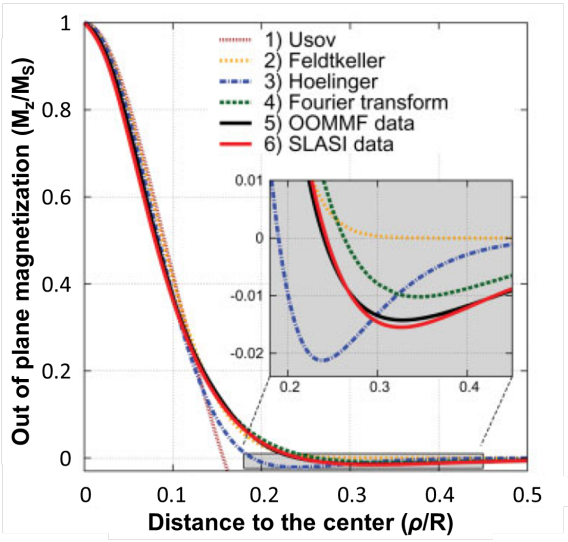

FIGURE 2.2: Out of plane magnetization. Dot lines corresponds to different analytical models: (1) Usov, (2) Feldtkeller (gaussian), (3) Hollinger, (4) Fourier transform. Filled lines correspond to micromagnetic simulations: (5) OOMMF software, (6) SLASI software for a disk with a 100 nm radius and 20 nm thickness. Adapted from [113]

Among the different models presented in Fig. 2.2, the Feldtkeller's model gives the most precise description of the magnetization of the vortex core. A precise description of the magnetic distribution of the vortex core is particularly useful to understand the dynamical properties of a vortex based STO [48, 114] given that the core is the main contribution to the effective damping of a magnetic vortex.

2.1.1.2.2 Off-centered vortex

To describe the vortex dynamics, it is necessary to model the magnetization distribution of the vortex when it is out of its equilibrium position. We can assume that the perpendicular magnetization is not affected by the vortex dynamics. However, in a dynamical regime the in-plane magnetization cannot be considered as orthoradial in each point. A model, called the Two Vortex Ansatz (TVA), was proposed to take this deformation into account and to avoid the formation of charge surface at the edges of the cylinder. Two rigid vortices are considered, one at the vortex position $\overrightarrow{X_c}(\rho_c, \chi_c)$ and a second ghost vortex at the position $\overrightarrow{X_c*}\left(\frac{R^2}{\rho_c}, \chi_c\right)$. The magnetization distribution $\overrightarrow{m}$ at the coordinates (ρ,χ) can then be described by the angles (Θ,Φ) as:

$$\begin{cases} \cos\left(\Theta(\overrightarrow{r})\right) = P\ exp\left(-ln2\left(\frac{2\left\|\overrightarrow{r}-\overrightarrow{X}\right\|}{b}\right)^2\right) \\ \Phi = \arg\left(\overrightarrow{r}-\overrightarrow{X_c}\right) + \arg\left(\overrightarrow{r}-\overrightarrow{X_c*}\right) - \pi - \chi_c + C\frac{\pi}{2} \end{cases} \tag{2.2}$$

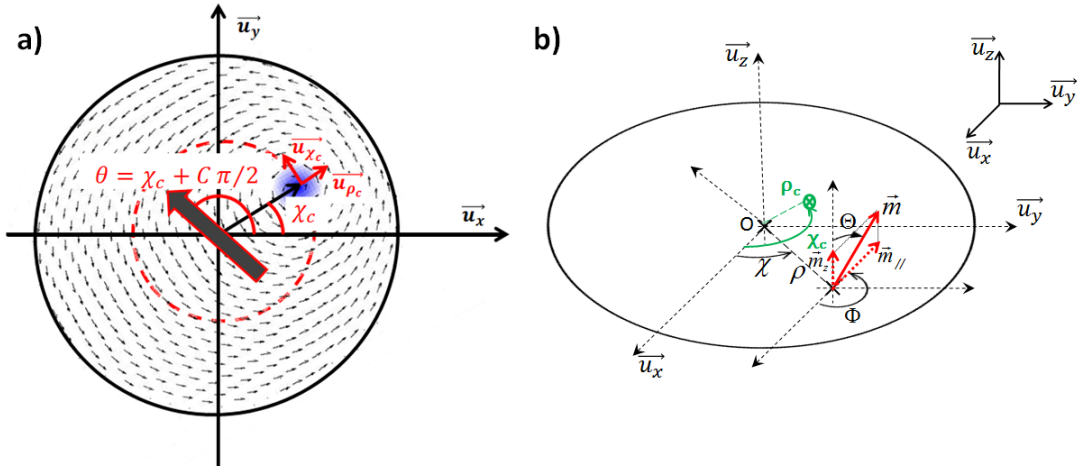

FIGURE 2.3: (a) Polar coordinates of the off-centered vortex. $\theta = \chi + C\pi/2$ is the angle defined by the net inplane magnetization (with C the vortex chirality). The net inplane magnetization, equivalent to the total vortex inplane magnetization, is represented by the grey arrow. (b) Spheric coordinates used to describe the local vortex magnetization. The vortex core has the coordinates (ρ_c, χ_c). The in-plane magnetization $\vec{m}_{//}$ at the coordinate (ρ,χ) is characterized by the angle Φ. The out-of-plane magnetization is characterized by the angle Θ.

This description will allow us to determine the instantaneous net inplane magnetization (vortex equivalent inplane magnetization) during the vortex oscillations.

2.1.1.2.3 Net in-plane magnetization of a vortex

Determing the net in-plane magnetization is crucial to understand the characteristics of the signal emitted by a STO. Indeed, the output power of a STO depends on the oscillations of resistance due to the effect of magnetoresistance which is defined by the respective orientations of the polarizer and the free layer. Thus for a vortex based STO with an in-plane fixed polarizer, the dynamics of the net in-plane magnetization directly determine the properties of the emitted signal. In Chap. 4, we will highlight that the phase of a vortex based STO is a crucial parameter for phase locked multiple STOs, and that this parameter is directly proportional to the angle defined by the net in-plane magnetization and the fixed polarizer.

To study the net in-plane magnetization, we thus use the works of K. Y. Guslienko et al. [115] that demonstrated for small displacements ($\rho_c < 0.6R$) that the net in-plane magnetization can be expressed as:

$$\overrightarrow{M_{//}} = \frac{2CM_s}{3R}\overrightarrow{X_c} \times \overrightarrow{e_z} = \frac{2CM_s}{3R}\rho(\sin(\chi_c)\overrightarrow{u_x} - \cos(\chi_c)\overrightarrow{u_y}) \tag{2.3}$$

with M_s the saturation magnetization,R the dot radius, C the vortex chirality, $\overrightarrow{X_c}$=(ρ,χ_c) the position of the vortex core with ρ the distance of the vortex core from the dot center and χ_c the angle defined by ($\overrightarrow{u_x}$;$\overrightarrow{0X_c}$ as represented in Fig. 2.3).

2.1.1.3 Effect of current on the vortex stability

To reach the autonomous regime of a vortex based STO, we need to supply the STO with a dc-current that can also modify the vortex configuration. Indeed, the dc-current generates an orthoradial magnetic field called the Oersted field. Within a dot, its amplitude increases as a function of the distance ρ from the dot center:

$$\overrightarrow{H_{oe}} = \frac{C_{oe}}{2\pi R^2}|I|\rho\ \overrightarrow{e_\chi} \text{ for } \rho < R \tag{2.4}$$

with C_{oe} the chirality of Oersted field defined by the direction of the current I.

The chirality of the Oersted field either stabilizes (if parallel) or destabilizes (if antiparallel) the chirality of the vortex. For large enough dc current, the vortex chirality can be reversed by a dc-current with an Oersted field opposite to its chirality. Experimentally, this will allow us to control the vortex chirality by changing the sign of the applied dc-current.

2.1.1.4 Effect of a magnetic field on the vortex shape and stability

2.1.1.4.1 For an in-plane field

When an in-plane field is applied, the vortex core moves from the center of the dot due to the Zeeman torque so that the vortex aligns its net in-plane magnetization parallel to the field. In the framework of the two vortex ansatz, this displacement is perpendicular to the field and proportional both to the field and the dot ratio $\beta = \frac{L}{R}$:

$$\overrightarrow{X} = \frac{5\beta RC}{2\pi M_s} \overrightarrow{e_z} \times \overrightarrow{H} \tag{2.5}$$

When the vortex core comes close to the border of the dot (at H_{an} in Fig. 2.4), it becomes unstable and the disk enters the uniformly magnetized configuration. By decreasing the field, the vortex can be nucleate again. However it happens only at a field lower H_n than H_{an}. An hysteretic behavior is thus observed in the annihilation/nucleation process of the vortex with a magnetic field. The transition between the uniformed state and the vortex state happens through a metastable state, generally a C state (vortex without a core) as seen in Fig. 2.4.b.

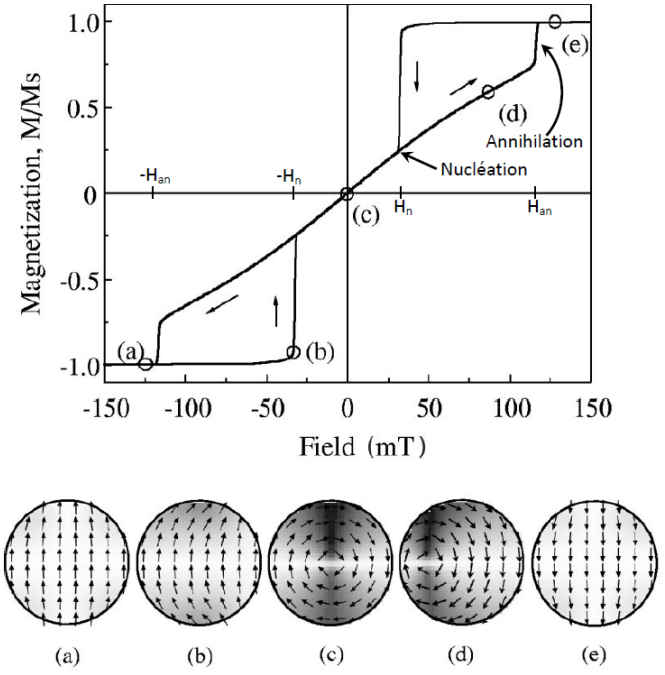

FIGURE 2.4: Hysteresis loop and modification of the magnetization due to the nucleation, displacement and annihilation of a magnetic vortex. The figure has been obtained from micromagnetic simulations on a nanodisk with $R = 0.1\ \mu m$ and $L = 30nm$. (Adapted from [116])

2.1.1.4.2 For an out of plane field

A perpendicular field H_{perp} does not modify the equilibrium position of the vortex but its magnetization distribution. In a first approximation, the magnetization in the vortex body linearly goes out of plane as a function of the perpendicular field $m_{z(body)} = \frac{H_{perp}}{H_s}$.

2.1.2 Thiele formalism: A model equation to describe the vortex dynamics

The Thiele model provides a general analytical approach to describe the translational motion of a magnetic soliton in an infinite environment. A wave which propagates without deformation in a nonlinear and dispersive environment is called a soliton. The Thiele approach is thus consistent with the gyrotropic motion of a vortex in an extensive film. The vortex dynamics is thus described by the following Thiele equation:

$$\vec{G} \times \dot{\vec{X}} - \frac{\partial E}{\partial \vec{X}} - D(\vec{X})\dot{\vec{X}} + \vec{F}_{STT}(\vec{X}) = \vec{0} \tag{2.6}$$

In a first approach, it is also possible to assume that the gyrotropic mode of a vortex confined in a dot corresponds to the translational motion of the core as shown in Fig. 2.5. In this section, we present, in the framework of the Thiele equation, the terms associated to the vortex gyrotropic motion, excluding the spin transfer contribution $\vec{F}_{STT}$ that plays the role of an anti-damping term which will be discussed in Sec. 2.2.

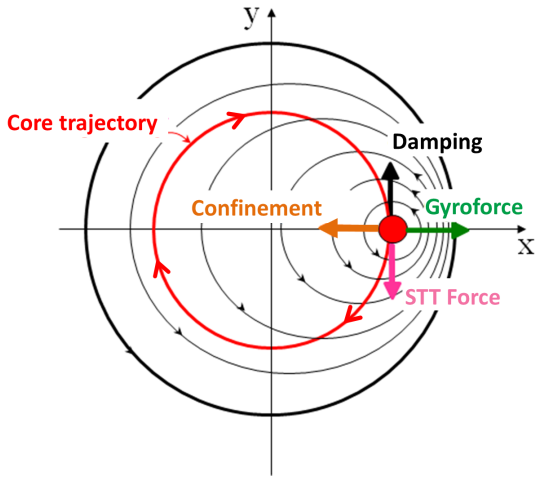

FIGURE 2.5: Schematic representation of the different forces acting on the vortex core in the Thiele framework

2.1.2.1 The gyroforce vector $\vec{G}$

The first term of the Thiele equation is the conservative gyroforce $\overrightarrow{G} \times \frac{d\overrightarrow{X}}{dt}$. The gyrovector is associated to the cross product of magnetization gradients that is non zero only within the vortex core. This force is responsible for the rotational motion of the vortex core around the center of the dot. The expression of the gyroforce is given by:

$$\overrightarrow{G} = -2\pi PL\frac{M_s}{\gamma}\overrightarrow{e_z} = -PG\overrightarrow{e_z} \tag{2.7}$$

with $G = 2\pi L\frac{M_s}{\gamma}$, γ the gyromagnetic ratio and P the polarity of the vortex. The gyrovector tends to increase the vortex core displacement as the vortex speed is increased.

2.1.2.2 The confinement force

The confinement force derives from the gradient of the potential energy $\frac{\partial E}{\partial \overrightarrow{X}}$. The potential energy is the sum of the magnetostatic energy and of the Zeeman energy. When the vortex core is shifted from the dot center, the creation of a non-zero net in-plane magnetization increases the magnetostatic energy. Thus the confinement force acts to return the vortex core to the dot center and to lower the total energy of the system. The confinement force expression has been calculated by Gaididei et al. [113]:

$$\overrightarrow{F_{ms}} = \kappa\rho\overrightarrow{u_\rho} = k_{ms}\rho(1 + \frac{1}{4}(\frac{\rho_c}{R})^2)\overrightarrow{u_\rho} \text{ with } k_{ms} = \frac{10}{9}\mu_0 M_s^2\frac{L^2}{R} \tag{2.8}$$

The Zeeman energy contributes to the total confinement in presence of an external field or an external current that generates an Oersted field. The Zeeman term can be expressed as:

$$\overrightarrow{F_{oe}} = Ck_{oe}J\rho(1 - \frac{1}{2}(\frac{\rho_c}{R})^2)\overrightarrow{u_\rho} \text{ with } k_{oe} = 0.85\mu_0 M_s LR \tag{2.9}$$

with C the vortex chirality relatively to the Oersted field

2.1.2.3 The damping force

Usov et al. [111] first established an analytical expression for the damping constant, and showed the large contribution of the vortex core in the relaxation process. Subsequently, A. Khvalkovskiy et al. [117] proposed a new approach, based on the energy dissipation of the vortex dynamics, to calculate the damping term. This model, more accurate than the Thiele

formalism, uses the two vortex ansatz (TVA) and permits the description of not only the translational but also circular motions:

$$D(\rho_c) = 2\pi\alpha L \left(\eta + \eta' \left(\frac{\rho_c}{R}\right)^2\right) \frac{M_S}{\gamma} \tag{2.10}$$

with $\eta = \ln(R/2b) - \frac{1}{4}$ the linear damping contribution and $\eta' = 2/3$ the nonlinear damping contribution.

2.1.2.4 Damped oscillations of the vortex eigenfrequency

From the Thiele equation, we can establish the gyrotropic trajectory of the damped oscillations of a magnetic vortex. In the hypothesis of small amplitudes of oscillations, the vortex core will have a damped circulary trajectory, i.e a spiral trajectory around the equilibrium position. The sense of gyration of the vortex core is defined by the vortex polarity [115, 118]. The eigenfrequency of the gyrotropic mode ω can be expressed, at the first order, as:

$$\omega = \frac{\kappa}{G} = \frac{k_{ms} + CJk_{oe}}{G} \tag{2.11}$$

The eigenfrequency ω is proportional to the aspect ratio of the vortex layer L/R through the first confinement term k_{ms}/G, and to R through the second term associated with the Oersted field generated by the dc-current. The frequency tunability with the dc-current is thus controlled by the Oersted field and not only by the nonlinearities of the system through the amplitude of the gyration radius [45, 119]. The Oersted field offers here a crucial and interesting way to tune the frequency of vortex based spin-torque oscillators as we will see in the next chapters.

2.1.2.5 Evolution of the Thiele equation with the perpendicular field

As we have seen in Sec. 2.1.1.4.2, the magnetization distribution of the vortex is modified in presence of a magnetic field. The shape of the energy potential changes and so does the eigenfrequency of the system. G. de Loubens et al.[118] demonstrated that the vortex frequency is expressed as $\omega(H_\perp) = (k_{ms}(H_\perp) + Jk_{oe}(H_\perp))/G(H_\perp)$ with the gyrovector and the confinement terms which respectively decreases and increases as a function of the applied field:

$$\begin{aligned} G(H_\perp) &= G(0)(1 - P\cos\Theta_0) \\ k_{ms}(H_\perp) &= k_{ms}(0)\sin^2\Theta_0 \\ k_{Oe}(H_\perp) &= k_{Oe}(0)\sin\Theta_0 \end{aligned} \tag{2.12}$$

with $\cos\Theta_0 = H_{perp}/H_s$ and $\sin\Theta_0$ the perpendicular and planar magnetization components. Then we notice that the vortex frequency increases (decreases) with the applied perpendicular field when the vortex core is parallel (anti-parallel) to the field. The perpendicular field will thus offer another tool to tune the frequency of a vortex based STO.

2.2 Spin transfer excitation of vortex based oscillator in confined nanodots

Tsoi et al. [120] first shed light on the strong potential of spin currents to excite magnetic modes in thin magnetic films. Here we describe the different spin transfer (ST) forces that can excite the gyrotropic mode of a magnetic vortex. Either resonant or self-oscillating behavior can be observed depending on both the symmetry of the system and on the characteristics of the applied current (rf or ac, spin polarization).

2.2.1 For a spin-polarized current with a perpendicular component:

It has first been demonstrated that a perpendicularly spin polarized current could excite the gyrotropic mode of a magnetic vortex confined in a nanodot through the corresponding Slonczewski ST torque. The threshold current J_c needed to establish a sustained regime is then :

$$J_c = \frac{\alpha\eta k_{ms}}{\kappa_\perp - \alpha\eta k_{oe}} \text{ with } \kappa_\perp = \frac{a_J M_s \pi L}{\gamma} \tag{2.13}$$

where a_J is the ST torque efficiency, M_s is the magnetization saturation, γ the gyromagnetic ratio and L the thickness of the free layer. Depending on the current sign, the ST torque either acts as an extra- or an anti-damping term. Sustained oscillations of the magnetization can be observed only when the condition $Jpp_z > 0$ is fulfilled with J the current flow defined as positive for electron flowing from the vortex free layer to the polarizer, p_z the perpendicular polarization of current and p the vortex core direction.

Experimentally vortex based STO excited by a perpendicularly spin-polarized current have first been realized in spin-valves [121, 122] and then in magnetic tunnel junctions [119] with

a vortex based magnetic free layer and an in-plane magnetized layer as a polarizer (often the top layer of a synthetic antiferromagnet). In presence of an in-plane polarizer tilted by an out-of-plane field and for a sufficiently large dc-current, a self-oscillating state of the vortex core can be observed.

To avoid the use of magnetic field, it has recently been demonstrated that self-sustained oscillations can be obtained at zero field on similar systems by adding on top of the vortex layer an additional spin-valve with a perpendicularly magnetized layer that directly plays the role of a perpendicular polarizer [44, 48].

2.2.2 Through a uniformly in-plane spin-polarized current:

Contrary to the previous case, we cannot excite sustained oscillations of the vortex core with a uniform dc-current distribution in a system with an ideal in-plane polarizer. For a non-uniform distribution of the dc-current, Martin et al. [89] demonstrated that sustained oscillations could be observed at zero field but no other groups have reported similar results. Indeed, the ST forces associated to an in-plane polarizer, i.e the Slonczewski and Field-like in-plane ST torques, do not have the required symmetry to maintain the circular trajectory of a gyrotropic motion:

$$\begin{array}{ll} \overrightarrow{F_{SL}} = \Lambda_{SL} J \left[\cos(\theta(t))\overrightarrow{u_\chi} + \sin(\theta(t))\overrightarrow{u_\rho}\right] & \text{the Slonczewski inplane force} \\ \overrightarrow{F_{FL}} = \Lambda_{FL} J \left[\sin(\theta(t))\overrightarrow{u_\chi} - \cos(\theta(t))\overrightarrow{u_\rho}\right] & \text{the field-like inplane force} \end{array} \tag{2.14}$$

with $\Lambda_{SL} = C\pi M_s L b a_J p_{x,y}$ and $\Lambda_{FL} = 2/3 C\pi M_s L R a_J \xi_{FL} p_z$ the respective efficiency of the two ST torques, b, the diameter of the vortex core, ξ_{FL} the Field-like torque efficiency, $p_{x,y}$ and p_z the in-plane and perpendicular spin-polarization, J the current density, $\overrightarrow{u_\chi}$ and $\overrightarrow{u_\rho}$ the polar vectors defined by the position of the vortex core (see Fig. 2.3), and $\theta(t)$ the angle determined by the net inplane magnetization relatively to the direction of the inplane polarizer (which is thus the phase of the STO).

The expression of the two torques, Slonczewski and Field-like, depend on the phase of the vortex core and they are respectively oriented along $\overrightarrow{u_x}$ and $\overrightarrow{u_y}$. For a circular trajectory and a dc-current, they thus both act like in-plane fields that can only slightly shift the vortex core from the center of the dot.

Nevertheless, in presence of an alternating current applied at the vortex eigenfrequency, the averages of these torques during a period of oscillations are non-zero. In this case, the spin transfer torques do not compensate the damping term but can induce resonant phenomena that are crucial for synchronization and spin-diode effects as we will develop in Chap. 4 and 7.

2.2.3 Through a circularly polarized current:

One original approach to induce a self-sustained gyrotropic motion has been proposed by Khvalkovskiy et al.[42]. They demonstrated that the Slonczewski force associated with a circularly polarized current could excite the gyrotropic mode of a vortex confined in a nanodot. In this case, the spin transfer force takes the following form:

$$\overrightarrow{F_{STT}} = -\frac{a_j J M_s L \pi b}{\gamma} PCC_{pol} \begin{cases} \frac{1}{b}\left(\overrightarrow{e_z} \times \overrightarrow{X}\right) \text{ si } \left\|\overrightarrow{X}\right\| < b \\ \overrightarrow{e_\chi} \text{ si } \left\|\overrightarrow{X}\right\| > b \end{cases} \tag{2.15}$$

The ST force is thus linear at small gyration radii and saturates for orbits larger than the vortex core b.

The spin transfer and damping forces both depend on the vortex polarity so that the vortex core does not influence the conditions of excitation. To observe sustained oscillations, the sign of the ST force, relative to the damping force, must fulfill the condition $JCC_{pol} < 0$ and is thus determined by the relative orientation of the vortex chirality and of the polarizer circulation, and the current sign $JCC_{pol} < 0$.

Experimentally Locatelli et al. [43] demonstrated that sustained oscillations of the gyrotropic mode could be observed with such circular spin polarization in a double vortex based spin-valve nanopillar. Depending on the sign of the applied dc current, one vortex layer is excited by spin transfer while the second one is damped by spin-transfer. A second but negligible ST force arises from the perpendicular polarization of the vortex core [43, 123]. In the first studies, it was considered that one of the two vortices acts as a quasi-static circular polarizer. However, we will see that the coupling between the two vortices plays a crucial role in these systems so that coupled modes can be excited by ST and simultaneously observed in the two vortex layers.

2.3 Double vortex based spin transfer nano-oscillators and their characteristics:

Numerous studies [36, 48, 119, 121] have shown the high spectral coherence of vortex based STOs, with Q > 1000, compared to other kinds of STNOs. However the key features of single vortex based STOs are still far from rf-applications requirements.

Within the family of vortex oscillators, record quality factor (Q > 15 000 by Locatelli et al. [43]) has been reported on double-vortex based STOs at zero applied field. Only recently have

similar quality factors (Q > 6400) been reported for a single vortex based STO by Tsunegi et al. [80] but a magnetic field is still required. In this study, FeB free layers were used instead of NiFe ones in the previous studies on single vortex based STOs. This material has a much lower damping (α=0.005 for FeB compared to 0.01 for NiFe) leading to lower critical current. Thus, at a same dc-current the energy involved in the gyrotropic mode is higher, and so is the effective damping rate which stabilizes the dynamics of the STO and explains the higher quality factors [48].

The record quality factors reported in permalloy based double vortex spin-valves cannot be explained by the material parameters. These observations could rely on either the specific ST torques associated to a vortex polarizer or on the effects of mode coupling on the oscillator's dynamics. In this section, we theoretically focus on both these two aspects and how each of them could impact the characteristics of a double vortex based STOs. We consider the case of an asymmetric system where the thicknesses of the two vortex layers differ V(thick)/NM/V(thin). To illustrate our analytical statements, we take the example of a Py(20nm)/Cu(9nm)/Py(6nm) double vortex system on which we will present experimental results in Chap. 3.

2.3.1 Spin-transfer behavior in the self-sustained regime

To quantify the precise contribution of both core and body ST forces on the oscillator's dynamics, we follow the approach performed by Sluka et al. [123], and N. Locatelli [43] and we numerically calculate the expression of each ST force for a vortex core described by the TVA model and a gaussian model for the vortex core.

2.3.1.1 Spin-transfer force associated to the vortex body

In a double vortex spin-valve, each vortex can be excited by the ST torque associated to the second vortex body if the condition $JC_{thin}C_{thick} < 0$ (with $J > 0$ positive for electrons flowing from thin to thick layer) is fulfilled. However for a given current sign, only one vortex layer is excited by ST torque while the other one is damped. The conditions of excitation are summarized in the following table:

	I>0	I<0
$C_{\text{thin}}C_{\text{thick}} = +1$	thin	thick
$C_{\text{thin}}C_{\text{thick}} = -1$	thick	thin

TABLE 2.1: Excited vortex layer depending on the chiralities of the two vortices. (Positive current corresponding from electrons flowing from thin to thick vortex layer

The integral expression of the spin transfer force associated to the vortex body can be written as:

$$\overrightarrow{F}_{STT-body,thin} = -P_{thin}\frac{a_J J M_S L}{\gamma} C_{thin} C_{thick} f_{body}(\rho_c)\overrightarrow{e_\chi}$$
$$\text{with } f_{body}(\rho_c) = \int_{\rho=0}^{\rho=R}\int_{\chi=0}^{\chi=2\pi} |p_\parallel(\rho,\chi)|\frac{d\Theta}{d\chi}\cos^2(\chi')\rho\, d\chi\, d\rho \quad (2.16)$$

In Fig. 2.6.a, we note that contrary to expectations (Eq. 2.15), the ST force does not saturate at large amplitude radii but still increases with a slower slope. Indeed, the polarization component along $\overrightarrow{e_\chi}$ in the vortex polarizer body, below the vortex core of the excited vortex, is slightly higher when the gyration radius increases. This nonlinear behavior of the spin transfer force will have an influence on the oscillator relaxation damping rate Γ_p presented in Sec. 1.2.4 of Chap 1.

2.3.1.2 Spin-transfer force associated with the vortex core

The force associated with the vortex core is similar to a perpendicular polarizer located at the center of the dot. This situation is well known in nanocontact based STOs in which Kim et al. [124] demonstrated that this force is inversely proportional to the gyration radius ρ. Following this study, we establish a similar analytical expression of such ST force for a vortex core located at the dot center. The profile of this force is precisely described by the following expression and plotted in Fig. 2.6.b :

$$\overrightarrow{F}_{STT-core,thin} = +\frac{a_J J M_S L}{\gamma} P_{thin} f_{core}(\rho_c)\overrightarrow{e_\chi}$$
$$\text{with } f_{core}(\rho_c) = \frac{1}{\rho_c}\int_{\rho=0}^{\rho=R}\int_{\chi=0}^{\chi=2\pi} |p_{z,thick}(\rho)|\sin^2\Theta(\rho,\chi)\frac{d\Phi}{d\chi}\rho\, d\chi\, d\rho \quad (2.17)$$

Given the $\frac{1}{\rho}$ dependency, we see in Fig. 2.6.b that this ST force has a negligible impact for large gyration radius. However it is not the case at small gyration orbits which could induce a non negligible effect on the critical current.

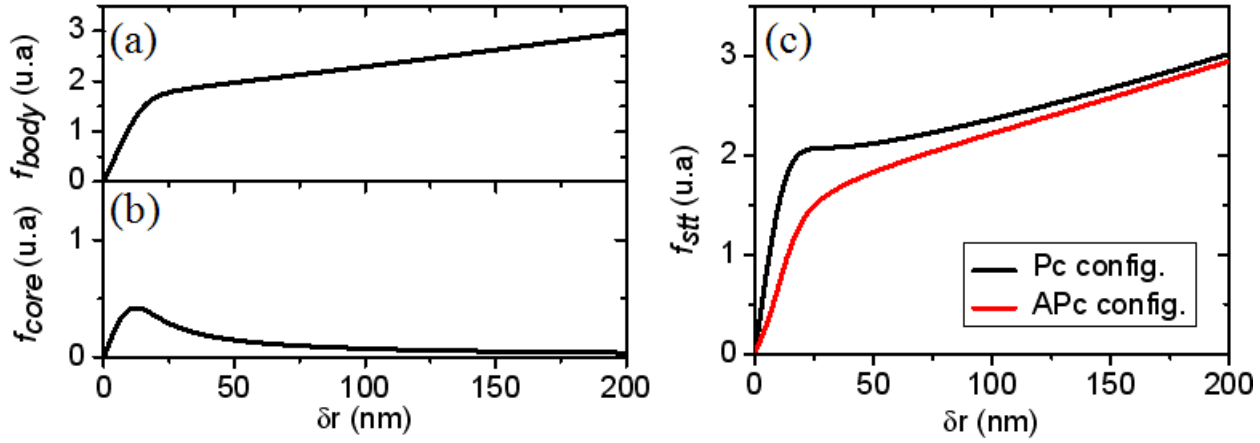

FIGURE 2.6: (a) Profile of the spin transfer force associated to the core of the polarizer vortex (b) Profile of the spin transfer force associated to the body of the polarizer vortex (c) Total profile of the spin transfer forces for parallel (Pc) or antiparallel (APc) cores between the free vortex and the polarizer vortex (δr represents the distance from the dot center).

2.3.1.3 Total spin-transfer for a static vortex polarizer

In a double vortex based STO, the ST torques have thus two components, each of them is either associated to the body or the core of the vortex polarizer. The total ST force depends on both the relative core polarities and chiralities of the system:

$$\overrightarrow{F}_{STT} = -P\frac{a_J J M_S L}{\gamma}\left[CC_{pol} f_{body}(\rho_c) - PP_{pol} f_{core}(\rho_c)\right]\overrightarrow{e_\chi} \tag{2.18}$$

As expected and shown in Fig. 2.6.c, at a large orbit of gyration, the main ST contribution arises from the body of the vortex polarizer. At small intercore distances, the contribution of the vortex core is non-negligible so that the profile of the total ST force strongly depends on the vortex core relative configuration as seen in Fig. 2.6.c. Furthermore the analytical expression of the critical current also depends on the vortex core relative configuration:

$$J_{cr} = \frac{\alpha\eta\kappa_{ms}}{C_{thin}C_{thick}\sigma_{\parallel} + P_{thick}P_{thin}\sigma_z - \alpha\eta b\kappa_{oe}} \tag{2.19}$$

with $\sigma_{\parallel}$ and σ_z the respective efficiency of the forces associated to the body and the core of the vortex polarizer. From the profile of the total ST force (see Fig. 2.6.c) and Eq. 2.19, we expect a lower critical current for parallel core configuration (Pc) than for antiparallel core configuration (APc). However, the first experimental study by N. Locatelli et al. [43] have shown that sustained oscillations of coupled vortices in spin-valves were observed only in the APc configuration. To understand this contradiction, one should notice that we do not consider in this section the magnetic coupling between the two vortices. In the next section, we will

demonstrate how the magnetic coupling between each vortex could impact the double vortex dynamics.

2.3.2 Mode coupling in double vortex systems

To explain the physics present in double vortex systems, a deep focus on the origin of the coupling between each vortex is needed. Indeed, the source and the intensity of the coupling can largely impact the characteristics of the gyrotropic modes.

In a double vortex system, the coupling interaction between each vortex can be of two types: either dipolar or exchange coupling. The total energy of the system can thus be expressed as the following:

$$W_{tot} = \frac{1}{2}k_1\overrightarrow{X_1}^2 + \frac{1}{2}k_1\overrightarrow{X_2}^2 + W_{int} \tag{2.20}$$

where $\overrightarrow{X_{1,2}}$ the respective position of each vortex and W_{int} the interaction energy that can take different form depending on the coupling properties. Due to the interaction energy, the two gyrotropic modes hybridize and are replaced by two coupled modes with different properties that depend on the coupling interaction. In a spin-valve with two vortices as we study in this thesis, only the dipolar interaction between the two vortices has to be taken into account.

2.3.2.1 Body-body coupling

Guslienko et al. [115] first presented a theoretical model for interacting vortices in a FM1/NM/FM2 system with two ferromagnetic vortex layers of different thicknesses. By considering that the net in-plane magnetization is proportional to the vortex core displacement, the Thiele equation for each vortex layer is then expressed as:

$$\overrightarrow{G_i} \times \overrightarrow{X_i} - k_{1,2}\overrightarrow{X_i} - \alpha\eta_i G_i \overrightarrow{X_i} - \mu\overrightarrow{X_j} = 0 \tag{2.21}$$

with $\overrightarrow{G_i}$, $\overrightarrow{X_i}$ and $\overrightarrow{X_j}$ the respective gyrovectors, confinement terms and vortex core positions of each of the two vortices (i,j). The term μ corresponds to the dipolar body-body coupling term between the two coupled vortices.

From the eigenvalues and the eigenvectors of the coupled system, we get access to the hybridized gyrotropic frequencies and to the localization of the two modes in each magnetic vortex layer:

$$\begin{cases} \omega_{1,2} = \frac{k_1}{p_1 G_1}\left(1 + \frac{\mu}{k_1}\beta_{1,2}\right) \\ \left(\frac{X_1}{X_2}\right)_{1,2} = \frac{p_2 G_2}{p_1 G_1}\beta_{1,2} \end{cases} \quad \text{with } \beta_{1,2} = \left[-\left(1 - \frac{p_2 p_1 G_1 k_2}{G_2 k_1}\right) \pm \sqrt{\left(1 - \frac{p_2 p_1 G_1 k_2}{G_2 k_1}\right)^2 + \frac{4 p_2 p_1 G_1 \mu^2}{G_2 k_1^2}} \right] \tag{2.22}$$

with $\omega_{1,2}$ the frequencies of the coupled modes. For each coupled modes, $\left(\frac{X_1}{X_2}\right)_{1,2} = \left(\frac{\rho_1}{\rho_2}\right)_{1,2}$ represents the ratios of the mode gyration radii in each vortex layer.

In Fig. 2.7, we represent the theoretical expectations concerning the frequency and the delocalization of the coupled vortex modes in a double vortex Py(6nm)/Cu(9nm)/Py(20nm) spin-valve. Note that we will present experimental results on similar system in Chap 3.

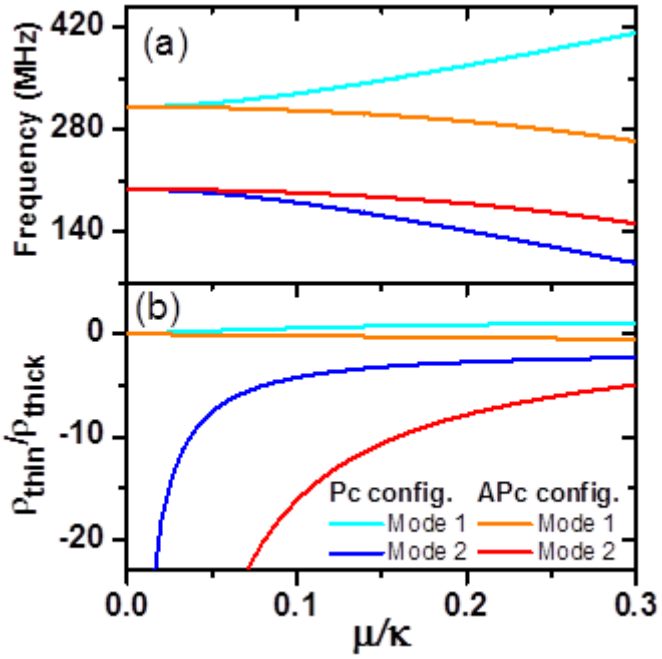

FIGURE 2.7: (a) Frequency and (b) ratio of gyration radii for the two coupled modes vs coupling strengh μ for parallel (blue and blue sky) and antiparallel core (red and orange) configuration.

We can first notice in Fig. 2.7 that the frequencies of the two coupled modes correspond to the non-interacting gyrotropic frequencies at zero coupling. In this case, each mode is thus present only in one vortex layer. As expected the more the coupling is increased, the more the mode frequencies differ from the non-interacting gyrotropic frequencies. In addition, we notice that the ratio of the gyration radii in each layer ρ_1/ρ_2 is largely affected by the coupling strength and by the vortex core configuration, either parallel (Pc) or antiparallel (APc). Thus we can quantify the localization of each coupled mode in the two vortex layers. As seen in Fig. 2.7.b, the two vortex cores are expected to rotate in phase ($\left(\frac{\rho_1}{\rho_2}\right)_{1,2} > 0$) for one coupled mode (see in light blue the high frequency mode in Pc configuration) while the cores should rotate in antiphase ($\left(\frac{\rho_1}{\rho_2}\right)_{1,2} < 0$) for the other coupled modes.

In a spin-torque oscillator, the ST torque should excite only one vortex layer and thus only the coupled mode mainly associated with this magnetic layer. However we will see in Chap. 3 and 5 that for some conditions, the two degenerated modes are simultaneously excited. In such a case, the trajectory of the two vortices is not circular anymore but each vortex core rotates around their common barycenter that is rotating itself around the center of the dot. In this case, the hypothesis of a static vortex polarizer is no longer valid and can lead to exotic dynamics when the two modes are equally excited as we will develop in Chap. 5. Similarly, the trajectory of the vortex cores can become much more complex in the case of strongly coupled vortices as discussed in Chap. 7.

2.3.2.2 Core-core coupling

2.3.2.2.1 Weak coupling case

For a system of two weakly coupled vortices in a single dot, we make the hypothesis that the two vortex cores can be modelled by two monodipoles (equivalent to a gaussian core distribution) in the center of each layer. In that case, we can establish the energy of the dipolar interaction between the two vortices:

$$W_{int,core-core} = \frac{\mu_0 \pi P_1 P_2 M_{s,1} M_{s,2} L_1 L_2 b_1^2 b_2^2}{64 ln(2)^2} \frac{-\rho_c^2 + 2\left(d_{spacer} + \frac{L_1+L_2}{2}\right)^2}{\left(\rho_c^2 + \left(d_{spacer} + \frac{L_1+L_2}{2}\right)^2\right)^{\frac{5}{2}}} \tag{2.23}$$

with b_1 and b_2 the respective diameters of the vortex core for each vortex. In Fig 2.8, we plot the interaction energy as a function of the intercore distance. We can notice that the core-core interaction is negligible when the intercore distance is higher than 25 nm. Thus the vortex core interaction is generally negligible, compared to the vortex body interaction, in the auto-oscillating regime. However, below the critical current, when the two vortex core are located close to the dot center, the strong intercore interaction can play a predominant role.

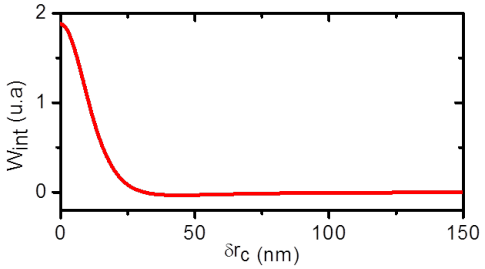

FIGURE 2.8: Amplitude of the core-core dipolar energy interaction depending on the intercore distance. (Here we consider a spacer of 9 nm between the two magnetic layers as studied in Chap. 3)

Depending on the relative vortex core configuration, the core-core interaction (for parallel chiralities) is either repulsive (for antiparallel vortex cores) and so acts against the dot confinement or attractive (for parallel vortex cores) and reinforces the dot confinement. Thus, it is easier to move the vortex core from the dot center in APc configuration. One should expect that the critical current needed to observe sustained oscillations is potentially either strongly decreased in APc configuration or increased in Pc configuration. It has to be noticed that this conclusion is opposite to what we expect from the different ST contributions but in agreement with the experimental observation of N. Locatelli et al.[43].

Micromagnetic simulations performed by A. Khvalkovskiy have even predicted a zero critical current in APc configuration as presented in Fig. 2.9. One should notice that zero critical current are obtained only for a dot diameter larger than 200 nm. This is related with a lower confinement when the dot diameter increases.

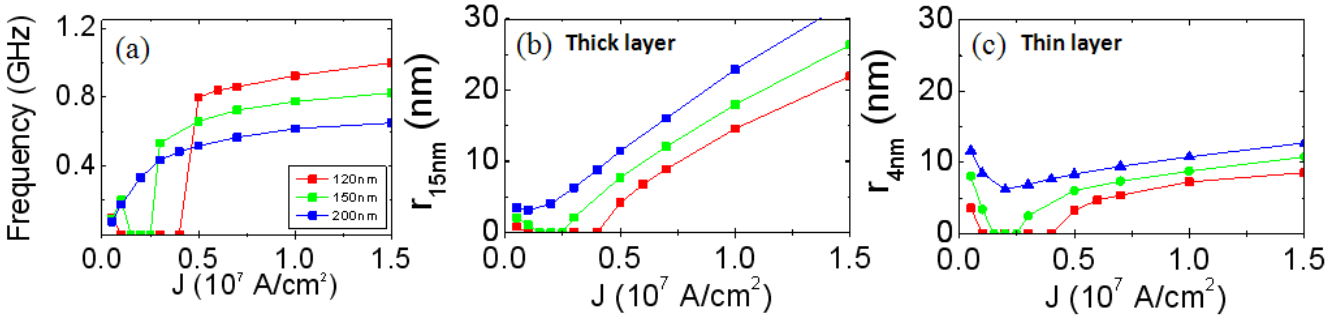

FIGURE 2.9: (a) Frequency of the excited coupled mode. Associated gyration radii in the excited thick (b) and damped thin (c) vortex layers. (Adapted from [125])

2.3.2.2.2 Strong coupling case:

Recently, different studies [126, 127] have reported, on Py/Cu/Py based spin-valves with a Cu spacer lower than 5 nm, that the dynamics of coupled vortices is modified in the strong coupling regime. In this strong coupling regime, the inter-layer exchange interaction becomes non-negligible compared to the dipolar interaction and the mode dynamics change.

In this regime, Cherepov et al. [126] have thus demonstrated that high frequency azimutal and vibrational modes appear for parallel vortex core configurations and anti-parallel chiralities (see Fig. 2.10.a-b). Introducing a mass term for the vortex and a third order gyrovector is necessary to model these new modes that present eigenfrequencies in the GHz range. These new modes, the rotational mode around 2 Ghz and the vibrational mode above 5 GHz as seen in 2.10.c, could offer an interesting perspective to enhance the frequency of vortex based STOs.

As for the weak coupling regime, the strong vortex core repulsion acts against the confinement in the APc configuration. In the high coupling regime, F. Boust et al. [128] highlighted through

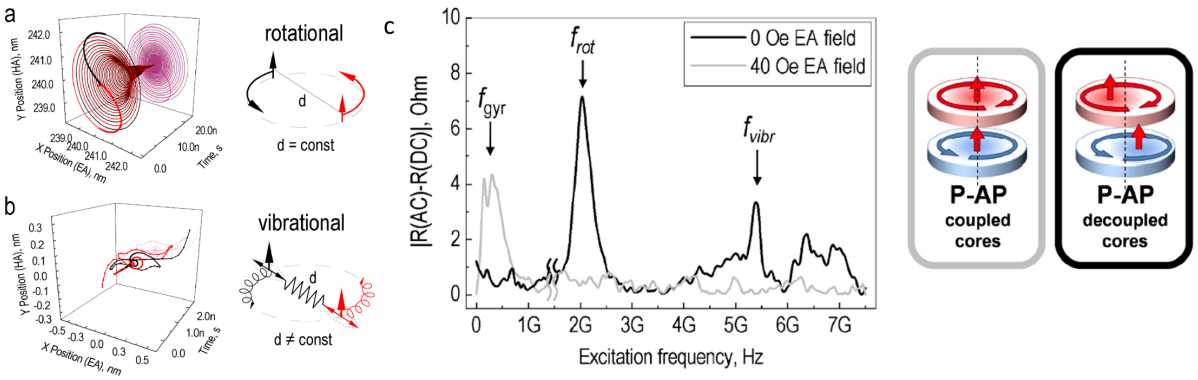

FIGURE 2.10: Micromagnetic illustration of the vortex core trajectories for the rotational mode at 2 GHz (a) and the vibrational mode at 6 GHz (b). (c) Microwave spectroscopy data for Pc-AP vortex core with coupled or uncoupled vortex core. (The vortex cores are decoupled with a 40 Oe in-plane field). Adapted from [126]

micromagnetic simulations that the decrease of the confinement can induce a reduction of the mode frequency down to a few MHz or even suppress it completely (see Fig. 2.11). This indicates that the dot confinement tends to zero, which should strongly reduce the critical current needed to observe sustained oscillations of the magnetization. As such, thus could be of great interest in the perspectives of spintronics based low power consumption electronics [129].

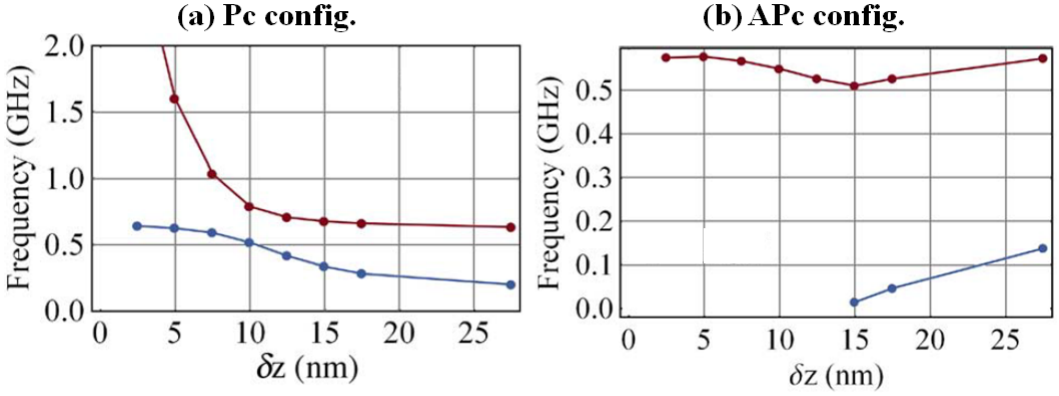

FIGURE 2.11: Resonance frequencies of the two vortex core modes (red and blue lines) as a function of the interdisk distance δz for paralell Pc (a) and antiparallel APc (b) vortex core configurations with parallel chiralities. Extracted from [128]

In this chapter, we presented the main characteristics of vortex based spin-torque oscillators which have the advantage of presenting a high spectral coherence. Since the first vortex based STO developed in 2007 [36], different kinds of polarizers, from a perpendicular polarizer to a vortex polarizer, have been proposed to excite a magnetic vortex by spin-transfer torque at zero applied field [43, 89, 119, 130]. Here, we particularly discussed how mode coupling in a double vortex based STO leads to the hybridization of the vortex gyrotropic modes and how it could improve the rf-properties (critical current, mode localization, frequency and spectral coherence) of vortex based STOs.

Part II

Dynamics of vortex based spin-torque oscillators in the autonomous and non-autonomous regimes

Chapter 3

Double vortex dynamics in the self-sustained regime

In this chapter, we investigate how coupled vortex modes can impact vortex based spin transfer nano-oscillators. In such a system, spin transfer will give rise to self-sustained oscillations of hybridized gyrotropic modes that depend on the relative configuration of each vortex (core polarity and chirality) as seen in Chap. 2. Thus, it can be considered as being a model system [43] for the study and the improvement of the properties of spin transfer nano-oscillators through collective modes dynamics.

The studied samples are nanopillars made from a multilayer stack containing an in-plane magnetized CoFe/Ru/CoFeB synthetic antiferromagnet (SAF), an MgO barrier and on top of it a NiFe/Cu/NiFe spin-valve (see App. A for more details), where each NiFe layer has a vortex magnetic configuration. The coupled modes (and thus the emitted power) are essentially detected through the vortex dynamics in the NiFe layer adjacent to the MgO barrier layer. Thus we cannot directly access the dynamics of the two vortex layers. To avoid this issue, we investigate two different systems that give us the opportunity to independently probe the dynamics of the excited and the damped vortex layers, and to report record output emitted powers (0.8 μW) for permalloy based STOs.

In this study, we demonstrate the strong influence of the relative core polarity configurations on the non-linear mode behavior as well as on the main features of the associated microwave signal e.g. frequency, spectral coherence, critical current, mode localization etc... By investigating the oscillator's dynamics in frequency and time domain measurements, we discuss the evolution of the STO's nonlinear parameters with I_{dc}. Finally, we succeed in demonstrating how the mode coupling offers new perspectives to handle the rf-features of vortex based STOs.

3.1 Dynamics of coupled vortices in "Sample A" STOs

The samples A, studied here, consist of a NiFe (20 nm) / Cu (9 nm) / NiFe (8 nm) spin-valve on top of a MgO barrier and a SAF (see Fig. A.1 in the Appendix A).

3.1.1 Intrinsic properties of coupled modes

In double vortex based STOs, the different configurations of vortex polarities and chiralities considerably increase the number of accessible magnetic configurations ($2^3 = 8$). Thus we can excite by ST torque one of the 16 coupled modes, each of these coupled modes have different intrinsic properties. The mode coupling between vortices will thus offer us an original way to enhance the limited range of accessible frequencies [36], or to develop STO based memories [43] or logic gates [131].

3.1.1.1 Coupled modes for chiralities parallel to the induced Oersted field

3.1.1.1.1 Mode selection driven by spintransfer

First, to prepare the two vortices with chiralities parallel to the Oersted field, we apply a large dc-current I_{dc} that generates a sufficient Oersted field to impose the vortex chiralities in both layers. In this configuration, it is anticipated that for a negative current (i.e electrons flowing from thin to thick layer) the ST torque excites the thin top vortex layer and thus the coupled mode dominated by this layer. On the contrary, for parallel polarities and positive I_{dc}, the coupled mode dominated by the bottom thick layer is excited by ST torque. However in our system, the threshold current of the coupled mode mainly located in the thick layer is too high to observe sustained oscillations without damaging the junction barrier. This originates from the width of the thick vortex (20 nm) which enhances the mode energy. Thus, we focus our study on negative dc-currents that will generate spin transfer oscillations of the coupled vortex system along the coupled mode dominated by the thin layer. This mode is expected to have a lower frequency than the one dominated by the thick layer given that eigenfrequencies are proportional to the ratio L/R with L the thickness and R the radius of the vortex layer as seen in Sec. 2.1.2.4 in Chap. 2.

In such a configuration, we observe sustained oscillations for parallel (Pc) or anti-parallel (APc) vortex core polarities. The preparation of the vortex polarities is performed by field cycling, similar to N. Locatelli et al. [43] who showed that the polarity switching field of the vortex core depends on thickness of the vortex layer.

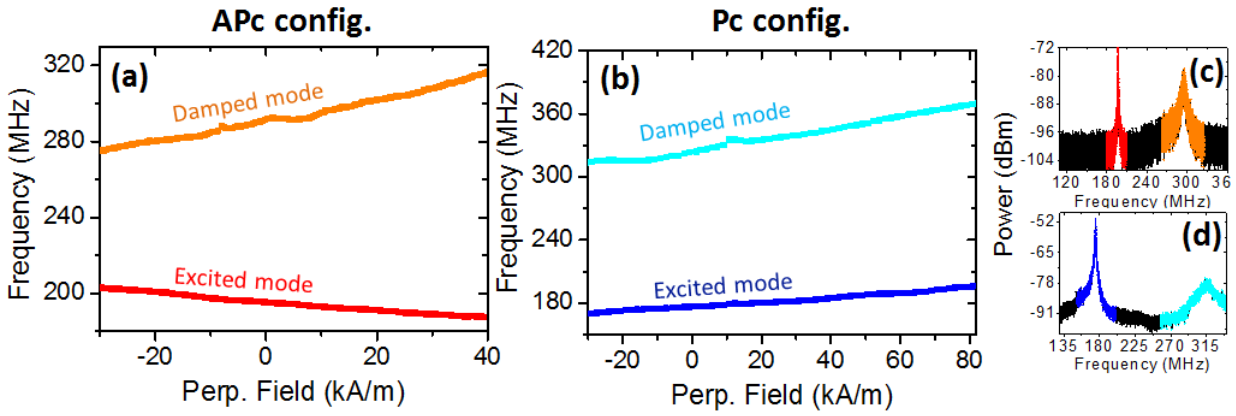

FIGURE 3.1: Field dependence of the low frequency "excited" mode and the high frequency "damped" mode for (a) APc and (b) Pc configuration at $I_{\mathrm{dc}} = -16$ mA. Frequency spectrum of the output emitted signal at $H_z = 0$ kA/m for (c) APc and (d) Pc configuration.

For both cases, as shown in Fig. 3.1.c-d, we detect a peak with a large amplitude and a narrow linewidth at a frequency of 190 MHz, close to the predicted gyrotropic frequency for the isolated thin layer's vortex (197 MHz). We also record a much broader peak (linewidth above 4 MHz) at a higher frequency which is attributed to the thermal excitation of the second coupled mode. In Fig. 3.1.a (resp. Fig. 3.1.b) we show for anti-parallel (resp. parallel) core polarities, the linear frequency evolution of these two modes as a function of the perpendicular applied field H_{perp}. As expected, the slopes of these modes have the same (resp. opposite) sign for parallel (resp. anti-parallel) core polarities [118]. We also note that the best spectral coherence for the excited modes has been measured in the APc configuration, with a minimum linewidth of 80 kHz (at $H_{\mathrm{perp}} = 30$ kA/m and $I_{\mathrm{dc}} = -16$ mA) leading to a Q factor of 2400 compare to a $Q_{\mathrm{max}} = 300$ in the Pc configuration.

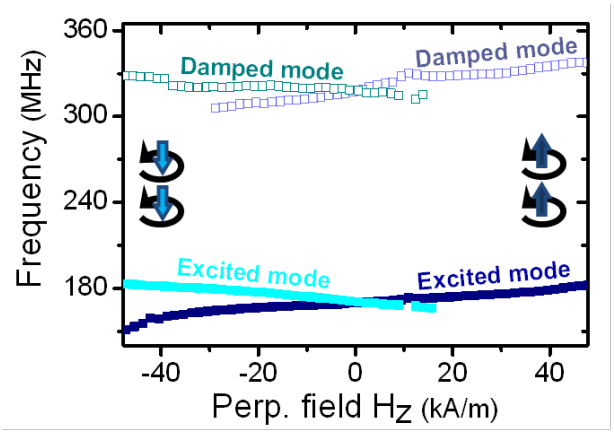

FIGURE 3.2: Field dependence of the low frequency "excited" mode and the high frequency "damped" mode for both Pc configurations (both vortex cores up or down) at $I_{\mathrm{dc}} = -16$ mA and room temperature

In Fig 3.2 we present the excited and damped modes for the two Pc configurations (for a negative I_{dc}). Their eigenfrequencies present as expected the same frequency dependencies with field revealing the symmetry of the two configurations. However the range of field where we can observe the different modes is not the same for the two configurations. This may

indicate the presence of pinning defects that do not have the same influence depending on the system configuration.

3.1.1.1.2 Spectral coherence and power of the coupled modes

To further investigate the properties of the excited coupled modes, we display in Fig.3.3.a-b the evolution of the frequency and the integrated power of the excited low frequency mode with I_{dc} for both Pc and APc core configurations at zero applied magnetic field and room temperature. Several important features can be noticed. Firstly, we find an almost linear dependence of the frequency with I_{dc}. This feature is interesting for frequency modulation using STOs [59] as it permits an easy control of the STO frequency with a modulating current. Moreover the two df/dI_{dc} slopes are identical and are separated by a constant frequency difference of 20 MHz. Secondly, the output emitted power of the excited mode is about 10 times smaller in the APc core configuration (around 10 nW) compared to Pc case (around 100 nW). Third, the threshold current I_c is found to be much lower in the APc configuration ($I_{C\text{-}AP} = -12$ mA and $I_{C\text{-}P} = -15.6$ mA). To understand the different features associated with each coupled mode, we have developed an analytical model combined with micromagnetic simulations of our double vortex system.

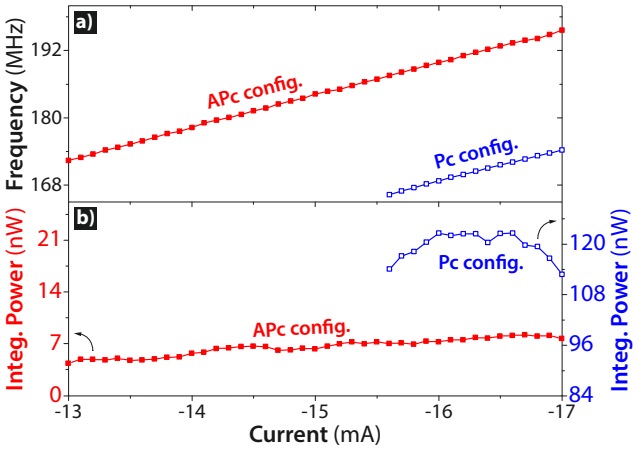

FIGURE 3.3: Evolution of the frequency (a) and the integrated output emitted power (b) with the dc-current for APc (red dot) and Pc (blue dot) configurations at zero applied field and room temperature.

3.1.1.1.3 Analysis of the coupled mode behavior

The large differences of microwave features of the excited modes in the two core configurations can be analyzed using the analytical model developed in Sec. 2.3.2.1 of Chap. 2. By analytically solving the system of coupled Thiele equations, we can extract for both the Pc and APc configurations, the hybridized resonant mode frequencies $\omega_{1,2}$ as well as the ratio of gyration

radii in each layer $\rho_1/\rho_2 = \frac{X_1}{X_2}$. We recall at this stage that neither the ST torque nor the nonlinear contribution of the confining force and the damping force are taken into account to describe the coupled modes.

In Fig. 3.4, we display the evolution of the frequency (Fig. 3.4a) and the ratio of the gyration radii (Fig. 3.4.b) of the low frequency mode as a function of the coupling strength normalized to the confinement μ/κ_1 for the Pc core configuration (blue line) and for the APc one (red line).

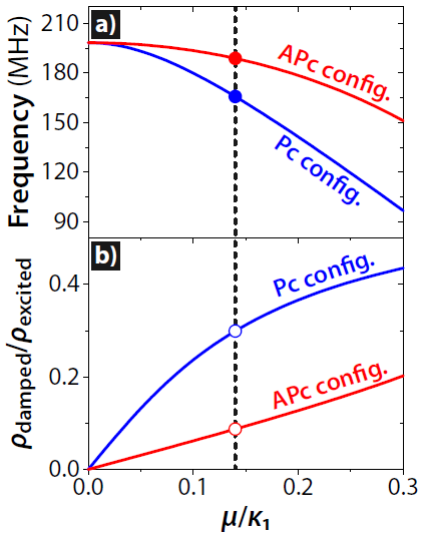

FIGURE 3.4: Frequency coupling dependency for the lowest excited mode in parallel core (blue) and antiparallel core (red) for $I_{dc} = -16$ mA at zero field (b) Ratio of gyration radii between thin and thick layer for the lowest frequency mode in parallel (blue) and anti-parallel (red) configurations [Filled (unfilled) circles represents the (expected) experimental points]

From the 20 MHz frequency difference between the two cores configurations found experimentally (Fig. 3.3 in Sec. 3.1.1.1.2) we can estimate the matching value of the coupling coefficient (see dotted line in Fig 3.4.a-b to be equal $\mu = 0.14\kappa_1$, as well as the corresponding gyration radii ratio from Fig 3.4b: $\rho_1/\rho_2 = 0.3$ for Pc configuration and $\rho_1/\rho_2 = 0.1$ for APc configuration.

These latter predictions for the ratio of the gyrotropic radius for each vortex have been confirmed by micromagnetic simulations (see Fig. 3.5) done by F. A. Abreu Araujo in UCL, Louvain. For $I_{dc} = -16$ mA, we find similar radii for the gyrotropic motion of the thin layer vortex (about 90 nm) for both core configurations whereas the radius of the thick layer vortex motion strongly depends on the core configuration: 9 nm in APc and 32 nm in Pc. Furthermore, the emitted power by the STO comes from the dynamics of the vortex layer close to the MgO barrier, i.e from the bottom thick vortex layer. Thus the difference of gyration amplitude of the thin and thick vortex layer shown in Fig. 3.4.b allows explaining, even quantitatively the strong difference of emitted power found experimentally between Pc and APc core configuration (see Fig. 3.3.b) : 100nW/10nW $\propto (\rho_{1,Pc}/\rho_{1,APc})^2$ [45].

This large difference of gyration radii in the thick layer cannot be attributed to the influence of the spin-transfer as it is not taken into account in the analytical model. Rather, it comes

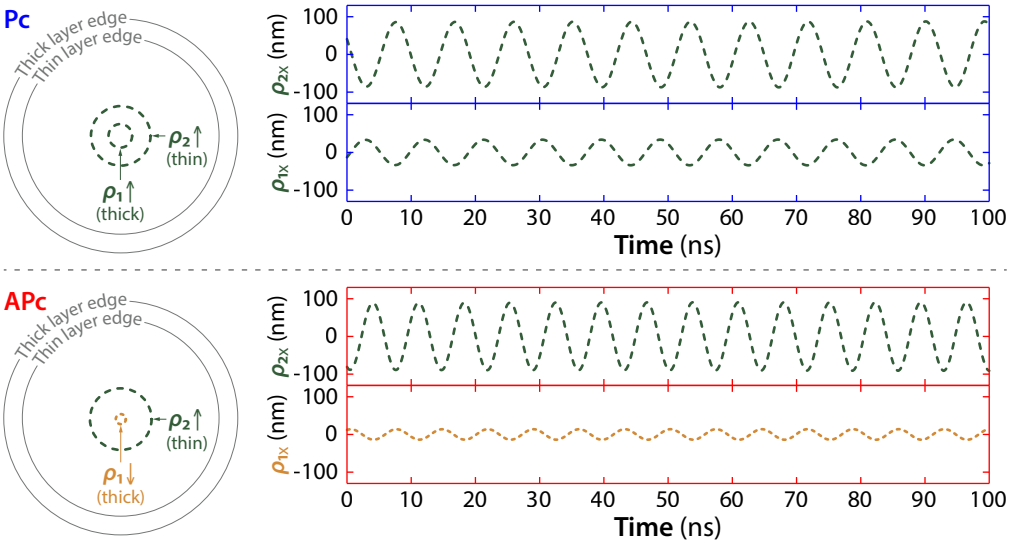

FIGURE 3.5: Micromagnetic simulations of gyration radii in both layers for Pc and APc configurations at zero field and $I_{\mathrm{dc}} = -16$ mA. (The dot radii of each vortex layer differ due to ion etching as shown in the Appendix A)

directly from the sense of gyration of the vortex thick layer. Indeed we want to emphasize that, even when vortices have opposite core polarities, the two vortex cores are in phase and gyrate in the same direction, thus confirming that the spin transfer torque excites a single coupled mode and not two independent gyrotropic motions. In this configuration, the vortex core of the thick layer follows the dynamics of the vortex in the thin layer and rotates in a direction opposite to its "normal" (defined by its own polarity [115, 118]). The frustration of the system can thus explain the low gyration radius in the bottom thick vortex layer in APc configuration.

3.1.1.2 Coupled modes for chiralities antiparallel to the induced Oersted field

In this section, we present the dynamics of the coupled modes excited by ST torque for chiralities antiparallel to the induced Oersted field. To do so, we first applied a positive I_{dc} to impose similar chiralities in both layers and a high field to impose parallel polarities. We then sweep the current back to a negative current that do not switch the vortex chiralities. We now expect to excite the coupled mode mainly associated to the vortex thin layer but with a lower critical current than for chiralities parallel to the current. Indeed, in this configuration the Oersted field generated by the dc-current acts against the dot confinement and thus reduces the mode energy.

In Fig 3.6, we report a threshold current of 9.1 mA. This value must be compared to the 16 mA threshold current observed for parallel polarities and chiralities parallel to the dc current (see Fig. 3.4). The mode frequency is also lower in this configuration, around 130 MHz, and slightly decreases with the current as the Oersted field compensates the confinement. The

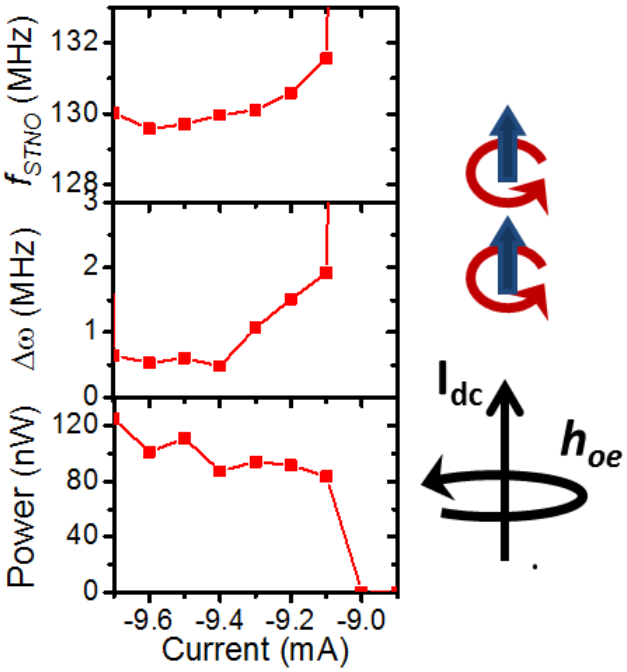

FIGURE 3.6: Current dependence of the low frequency "excited" mode for Pc configuration with chiralities antiparallel to the current at zero applied field

linewidth and the power are similar to the case of chiralities parallel to the current. However the emitted signal disappears for $I_{dc} > |9.8mA|$ which corresponds to a chirality switching in the thin vortex layer. The ST force then favors the thick layer vortex but the critical current is still too high to observe sustained oscillations of its associated coupled mode.
We also notice that the experimental dc-current that triggers the chirality switching has a dispersion of ± 0.2 mA. This indicates that the mode excited before the switching is not fully stable. Indeed the vortex configurations with chiralities parallel to the induced Oersted field is energetically more stable. Thus the vortex configurations with chiralities antiparallel are not appropriate for the synchronization experiments where the STO interacts with an external signal.

3.1.2 Nonlinear behavior of mode coupling

3.1.2.1 Frequency and time domain measurements

To understand the different spectral coherences associated with each coupled mode, it is anticipated that the non linear behavior inherent in spin-transfer oscillators, which has not been taken into account up to now, should play a crucial role. Indeed several approaches have been proposed to evaluate the influence of the non-linearities on the STO linewidth [46, 101, 132, 133]. Notably, it has been demonstrated that the normalized dimensionless nonlinear frequency shift ν (see Sec. 1.2.4 in Chap. 1) results in a conversion of amplitude fluctuations into phase fluctuations that are detrimental for the phase coherence of the STO. It has been proposed

recently that this important parameter can be extracted through the analysis of the linewidths of the signal's harmonics [134].

In Fig. 3.7, we present the evolution of the linewidth of the low frequency coupled mode and its first harmonics (measured but out of the frequency range of Fig. 3.1.b-c) as a function of I_{dc}. In the APc core configuration (for parallel chiralities and parallel to the induced Oersted field), we find that the ratio between the linewidth of the fundamental mode Δf_0 and the first harmonic Δf_1 is close to 4 for all values of injected current (see Fig. 3.7.a). Such behavior is consistent with an oscillator that is quasi-isochronous ($\nu \ll 1$) for which it has been predicted the linewidth of the n-th harmonic is $\Delta f_n/\Delta f_0 = (n+1)^2$. This behavior strongly differs for the Pc configuration (Fig. 3.7b) for which we find a ratio close to 2 between Δf_0 and Δf_1 for all I_{dc}. This corresponds to a non-isochronous oscillator (large ν), a case for which $\Delta f_n/\Delta f_0 = (n+1)$ as reported for a uniformly magnetized STO by M. Quinsat et al. [134].

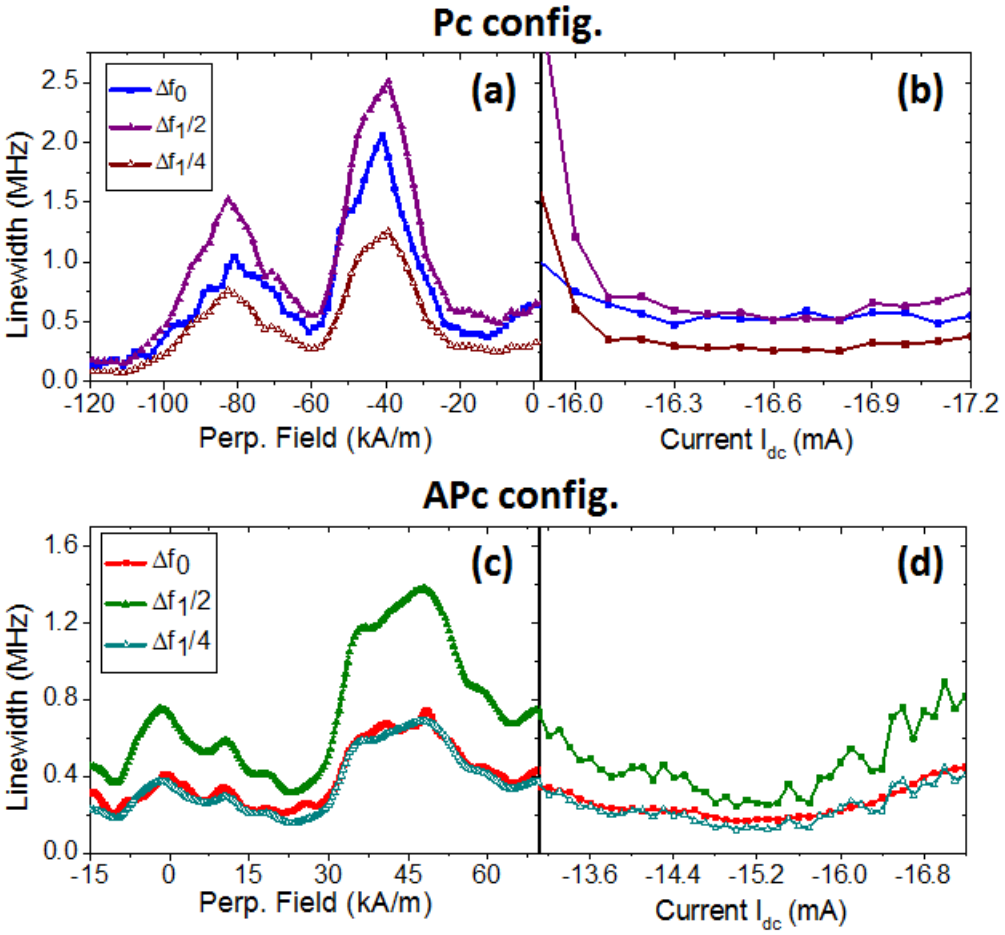

FIGURE 3.7: Spectral linewidth of the fundamental and the first harmonics divided by two (filled symbols) and four (open symbols) for APc (a-b) and Pc (c-d) configuration measured. (a)(c) Evolution with field for $I_{dc} = -16$ mA. (b)(d) Evolution with the dc-current at zero applied magnetic field.

Note that this latter case obtained for Pc core configuration also appears to be similar to the single vortex case in which large values of the normalized dimensionless non-linear frequency

shift ν have been found (between 6 and 20 in Ref. [48][1], around 13 in Ref. [135]). Moreover, the strong reduction of non linearity in APc configuration is consistent with the much smaller linewidth (about 100 kHz) we found in APc configuration. Indeed, linewidth broadening is directly correlated to the nonlinear behavior of the oscillator [46]. We emphasize that these features have been reproduced for several other samples and are also consistent with our previous studies in spin-valve nanopillars for APc configuration [69].

To understand the differences between Pc and APc configuration, we identify the origins of the different non linear behaviors. As described in Chap. 1, the normalized dimensionless nonlinear frequency shift ν is expressed as $\nu = Np/\Gamma_p$ where N is the nonlinear frequency shift, p is the normalized oscillation power and Γ_p is the effective damping rate that describes how fast an oscillator returns to its stable trajectory after a deviation of its amplitude. It is important to note that the normalized power is related to the motion of both thick and thin layer vortices while the detected emitted power corresponds only to the thick layer vortex gyration in our system.

Experimentally, we can estimate the parameter N from the evolution of the frequency with I_{DC} : $f = f_0(I) + 2\pi Np$. For both configurations, we find similar linear df/dI_{DC} (see Fig. 3.4 (a)) which indicates that the nonlinear frequency shift N is small and of comparable amplitude. The normalized power p can be easily estimated from micromagnetic simulations. We estimate from Fig. 3.5 that the normalized oscillation power is only slightly higher in the Pc configuration (about 12% higher) than in the APc case. This slight difference of the normalized radii compared to the measured output emitted powers is due to the fact that we detect it through the dynamics of the thick vortex layer, in which the radii differ for both configurations, but the gyration radii in the excited thin layer are much larger and around 90 nm for the two configurations. Thus, the main contribution to the normalized radius p comes from gyration radius of the thin layer.

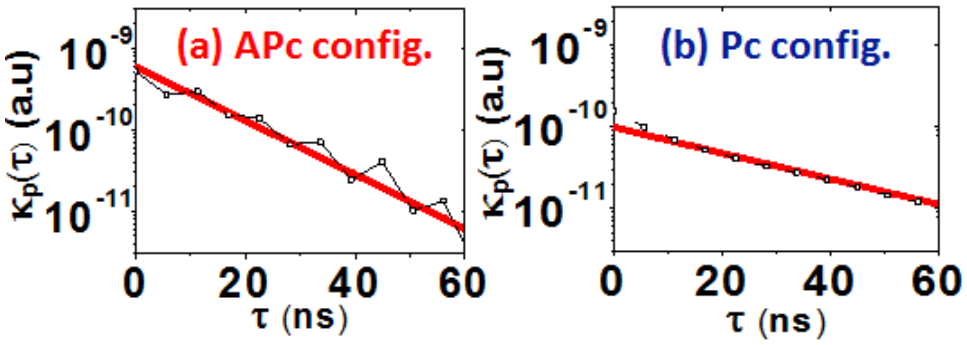

FIGURE 3.8: Autocorrelation function of power fluctuations for both configurations APc (a) and Pc (b) at zero field for $I_{dc} = -17$ mA.

[1]In Ref. [48], an error in the analytic expression of ν makes it two times smaller than its actual value

The last term entering in the expression of the non linear frequency shift ν is the effective damping rate Γ_p. This parameter can be extracted from the experiments through the study of the temporal evolution of the signal. To do so, we have performed Hilbert transforms on 5 ms time traces and fitted the autocorrelation function of the power fluctuations (as shown in Fig 3.8 c and d) with the following expression [136]:

$$\kappa_p = \langle \delta p(\tau) \mid \delta p(0) \rangle = A(p_0, \Gamma_p e^{-2\Gamma_p|\tau|}) \tag{3.1}$$

Through such analysis, we find that, at a given I_{dc}, Γ_p is twice as large in the APc configuration ($\sim$ 30 MHz) than in the Pc case ($<$ 13 MHz) as seen in Fig. 3.8. Finally, taking into account all the contributions, we deduce that the nonlinear frequency shift ν is about 3 times larger in the Pc core configuration than in the APc. It is however to be emphasized that this "small" difference leads to drastically different microwave features, thus demonstrating the importance in tuning precisely the nonlinear parameters of STOs. An interesting feature of our coupled vortex oscillators is the factor 2 difference in the effective damping rate Γ_p that could be of a great interest for rf-applications. Indeed, M. Quinsat et al. [68] demonstrated that the effective damping is directly linked to the modulation bandwidth as we will see in Chap. 4 and 6.

3.2 Dynamics of coupled vortices in "Sample B" STOs

In this section, we study NiFe(6nm)/Cu(9nm)/NiFe(20nm) double vortex based STNOs similarly to the previous section. However here the thin vortex layer, that we can easily excite by ST torque, is close to the MgO barrier beneath the spin-valve (see Fig A.2). Thus the dynamics of the coupled mode mainly associated with the thin vortex can be directly detected. We thus measure a much larger output emitted power, up to 0.6 μW. Such a large power is not only useful for rf-applications but also to have a more precise insight into the dynamics of the coupled modes. Furthermore, we choose here to focus our study on the coupled modes with chiralities parallel to the Oersted field. The mode stability is much lower, with a detrimental impact for applications, when one or two chiralities are antiparallel to the Oersted field due to switching of chirality (see section 3.1.1.2).

3.2.1 Coupled modes with parallel chiralities (and parallel to the Oersted field)

3.2.1.1 Mode selection driven by ST torque

3.2.1.1.1 Negative current

For a negative I_{dc}, we can excite, via ST torque, the coupled mode dominated by the top vortex thick layer in the APc configuration. Given that the thick layer is located at the top of the spin-valve, we detect the excited coupled mode through the dynamics of the bottom thin layer. In that case, we again observe (see Fig. 3.9 in the App. A) a narrow peak close to the frequency of the gyrotropic frequency of the isolated thick layer's vortex, and a low frequency thermally activated peak associated to the second mode. As expected, the slopes of these modes have opposite sign given that the core polarities are anti-parallel.

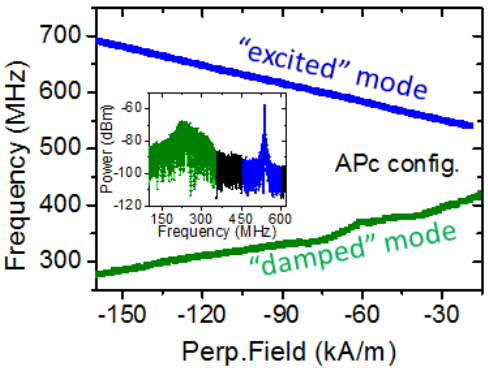

FIGURE 3.9: Field dependence of the low frequency "damped" mode and the high frequency "excited" mode for APc configuration at $I_{\mathrm{dc}} = -13$ mA. Inset: Frequency spectrum of the output emitted signal at $H_{\mathrm{z}} = 0$ kA/m

For these conditions, the detected power of the excited mode is only of about 30-50 nW which is even lower than the power of the thermally activated peak. This is related to the weak delocalization of the excited mode in the bottom thin layer in APc configuration.

3.2.1.1.2 Positive current

For positive I_{dc}, we excite, via ST torque, the coupled mode dominated by the bottom vortex thin layer and thus we detect for Pc and APc configurations a low and narrow linewidth (below 1 MHz, down to 100 kHz) peak close to the eigenfrequency of the thin vortex layer and broader peaks (linewidth above 10 MHz) at a higher frequency which is attributed to thermal excitation of the second coupled mode (see Fig. 3.10). In the inset of the Pc configuration in Fig. 3.10, we notice the presence of not only the fundamental frequencies of the excited and the damped modes but also the first harmonic of the excited mode. Furthermore, we do not detect sustained

oscillations in the Pc configuration at a low applied field due to the current, without breaking the junction, being below the threshold current (the field range of Fig. 3.10.a is limited from 90 to 190 kA/m). This again highlights the strong impact of vortex core repulsion on the threshold current in Pc configuration (see Sec. 3.1.1.1.2).

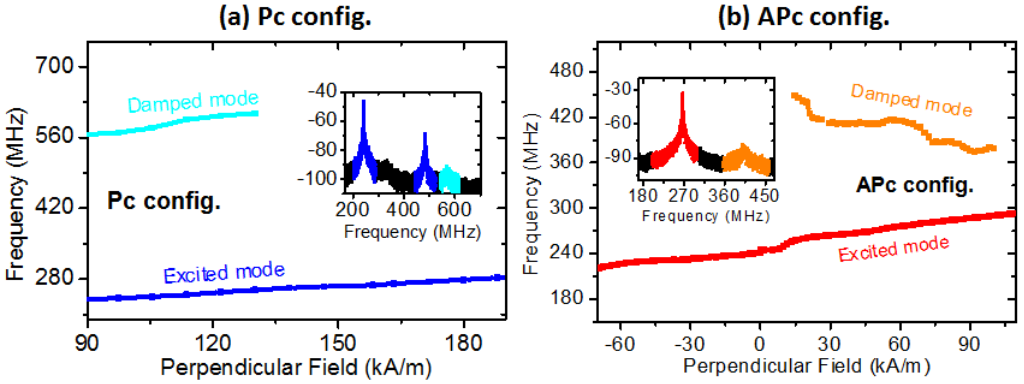

FIGURE 3.10: (a) & (b) Field dependence of the low frequency "excited" mode and the high frequency "damped" mode for APc (a) and Pc (b) configuration at $I_{dc} = +11$ mA. Inset: Frequency spectrum of the output emitted signal at $H_z = 50$ kA/m for APc (a) and $H_z = 100$ kA/m for Pc (b) configuration.

The frequency of the excited mode is lower in Pc than APc configuration (50 MHz lower at $I_{dc} = +11$ mA and $H_{perp} = 50$ kA/m) and its output emitted power is large for both configurations as shown in Fig. 3.10. The two main issues of having the excited vortex layer close to the MgO barrier are thus : the detected emitted signal of the excited mode is of a few hundreds of nanowatts for both configurations (compared to a maximum of 130 nW for the previous sample generation) and the detected signal of the thermally activated peaks is much smaller. Indeed, the thermally activated mode is mainly localized in the damped thick layer and is difficult to observe in the excited bottom thin layer.

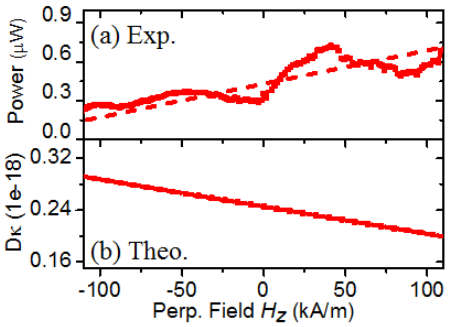

FIGURE 3.11: (a) Field dependence of the emitted power associated to the low frequency "excited" mode for APc configuration at at $I_{dc} = +11$ mA (b) Field dependence of the damping term Dκ

We focus our study on the APc configuration for which we can excite by ST torque a coupled mode at zero or small applied perpendicular fields. We note in Fig. 3.11 (a) that the detected power of the excited mode increases when the applied field is parallel to the vortex core of the excited layer. This behavior is explained by a decrease of the damping force with the field

(see the expected analytical evolution of the damping term Dκ in Fig. 3.11.b). As soon as the vortex core is deformed by a perpendicular field, the energy dissipates by the dynamics of the vortex core decreases. Hence the total damping term is reduced as the core represents its main contribution. One could imagine decreasing the damping of a vortex based STO by expelling the vortex core from the dot and exciting C-state's modes as evoked in [137].

All these experimental results for positive and negative I_{dc} confirms our initial observations made on samples A and our theoretical predictions about the intrinsic properties (frequency and localization of the coupled modes) of coupled vortex modes.

3.2.2 Nonlinear behavior of mode coupling

3.2.2.1 Frequency domain vs time domains analysis

In section 3.1.2, we highlighted the weak nonlinear behavior in the APc configuration but without systematic time domain measurements given the low emitted power and the large thermally activated peaks. The large output emitted power in this second generation of samples gives the opportunity for a deeper insight into coupled mode dynamics. In this section, we choose to focus our study on APc configuration for positive current, a configuration for which the emitted power is large and for which we observe sustained oscillations at zero field as expected for potential applications.

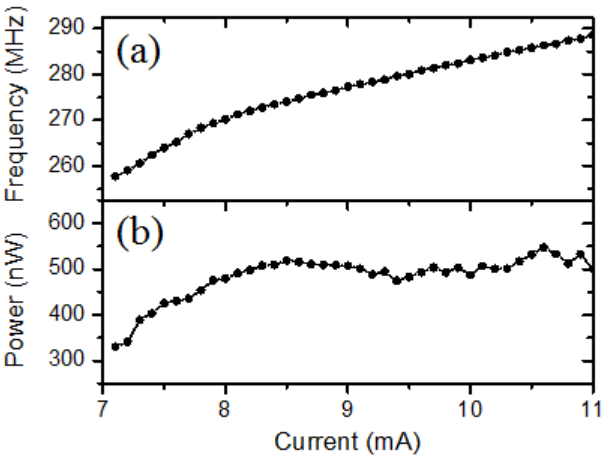

FIGURE 3.12: STO frequency (a) and power (b) dependency with current in APc configuration (The STO has a dot diameter of 300 nm)

In Fig. 3.12, we show that the frequency of the excited mode has a strictly linear dependency with I_{dc} in the self-sustained regime. Again a sharp increase of power, from zero to 350 nW, is observed when I_{dc} reaches the threshold current. This behavior is completely different from the single vortex case [48, 119, 138] for which the power increases linearly from 0 nW above the critical current. In the double-vortex case, the threshold current in APc configuration is expected to be much lower than the experimental value due to the core-core repulsion as

presented in Chap. 2. This discrepancy with theoretical expectation may be associated to the presence of pinning defects in our nanodot. In that case, the vortex core radius present a drastic enhancement when I_{dc} exceeds the critical pinning current.

By harmonics analysis, we deduce that the STO has an apparent linear behavior just above the threshold current I_{th} given that $\Delta f_1/\Delta f$ is close to 4 above +8 mA as shown in Fig. 3.13. To go beyond this qualitative analysis as presented in section 3.1.2, we performed time domain measurements. As we mentioned, this is possible in "samples B" as the amplitude of the thermally activated peaks is low and the emitted power of the excited mode is high.

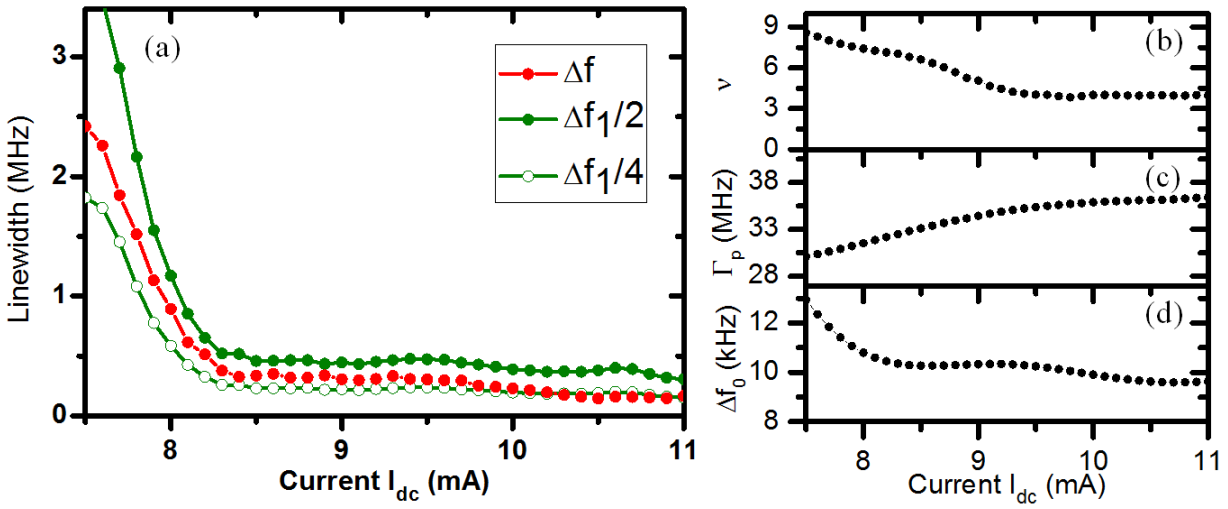

FIGURE 3.13: (a) Spectral linewidth as a function of I_{dc} for the fundamental mode (Δf) and for its first harmonic (Δf_1) divided by two (filled symbols) and four (open symbols) for APc configuration. Associated current dependency of the oscillator nonlinear parameters (Δf_0 (b), Γ_p (c), ν (d)).

We plot in Fig. 3.13 the evolution of the STO nonlinear parameters (the nonlinear dimensionless parameter ν, the effective damping Γ_p and the linear linewidth Δf_0). Above I_{th}, i.e 7 mA, all the nonlinear parameters present a quasi-linear evolution with I_{dc} (increase in Γ_p and decrease in ν and Δ_0). For a higher current, their evolution is still linear but with a lower slope. The profile of the spin-transfer force associated with the vortex body, which nearly saturates at large gyration amplitude, can explain this behavior.

One should notice that the effective damping, Γ_p is never zero, and about 27 MHz just above I_{th}. This is contrary to the theoretical expectations (Sec. 1.2.4 in Chap. 1) which predict a linear increase of Γ_p from zero above I_c. This reinforces the hypothesis of pinning defects that may impact the threshold current. In that case, the gyration radius and the effective damping can be large just above I_{th}. Above the threshold current, the effective damping Γ_p increases linearly and reaches up to 35 MHz (15 % of the oscillating frequency) at about 40 % above the experimental threshold current.

Furthermore, the nonlinear dimensionless parameter ν is non zero for all current values. It decreases just above I_c and its values are between 4 and 5 for I>8 mA, i.e in the range of current where we observe $\Delta f_1 = 4\Delta f$. For this sample, the lowest measured ν is about 3, which is by far the minimum value measured for a STO. However it is not the apparent fully linear behavior expected through linewidth analysis. We thus want to emphasize that it is necessary to perform time domain measurements in order to have a quantitative analysis of the nonlinear behavior of a STO. This is a crucial issue as even small ν (below 5) can have a large impact on the oscillator dynamics, especially on its non-autonomous regime as we will develop in chapter 4.

In conclusion, we highlighted, through frequency and time domain measurements, the specific role of mode coupling in the dynamics of a double vortex based STO. We demonstrated the strong correlation between the vortex core configuration and the nonlinear parameters of the oscillator. In particular, the core-core repulsion in the APc configuration is shown to drastically reduce the threshold current to observe self-sustained oscillations and to enhance the spectral coherence of the excited mode by enhancing the effective damping. Furthermore, if the nonlinear dimensionless parameter ν is low (between 4 and 6) in APc configuration, it remains non-negligible which is an important issue to synchronize STOs as we will see in Chap. 4 and 8. All these different features reinforce the potential of mode-coupling for STO based rf-applications. In parallel, we showed that the coupling between the two vortices leads to a hybridization of the gyrotropic modes, and to the delocalization of the different coupled modes in the two vortex layers. Due to the mode selectivity of the spin-transfer torque, we showed that the contribution of the damped mode in the dynamics of the excited layer is generally negligible. However, in some experimental conditions, where the mode interaction is maximal, the hypothesis of a single excited mode is not always valid and can lead to exotic dynamics as we will show in Chap. 5.

Chapter 4

Locking mechanisms in the non-autonomous regime

The small dimensions of STOs (less than 1 μm^3) in the nanometer scale, make them very sensitive to external perturbations and notably to thermal noise despite all research efforts in the last decade. This represents the main limitation of STOs for the development of spintronic based rf-applications. In Chap. 3, we have shown that mode coupling between internal modes offers a perspective to improve significantly the spectral coherence of STOs. Other approaches rely on the external control and on the stabilization of the dynamics of an oscillator with an external reference signal. One is the injection locking of an auto-oscillator with a reference rf-source at the oscillator's eigenfrequency or at its harmonics [45, 53–56, 58, 139]. Alternatively one can self-synchronize an oscillator with its own emitted signal [140]. One other approach relies on the mutual synchronization of auto-oscillators [60, 71, 82, 141]. A fourth one is the resonant excitation of an oscillator in the damped regime [61, 62, 142]. Last but not least, the dynamics of an oscillator can be controlled with a reference modulating signal [59, 68, 143, 144] as it is the case in phase locked loop [145–147].

In this chapter, we study these different possibilities to tune the phase of a STO with an external oscillating signal and adapt it to the vortex case. We experimentally and theoretically highlight the locking mechanisms that drive the injection of a vortex based STO with an rf-current at fraction of its gyrotropic frequency. With time domain measurements, we identify the presence of phase slips as a source of the linewidth enhancement in the phase locked state. Lastly, we demonstrate that a rf-current can also excite a vortex based STOs in the damped regime and discuss the mechanisms of excitation, either "normal" and/or parametric resonances.

4.1 The non-autonomous regimes of an oscillator

In this section, we introduce the different non-autonomous regimes of an oscillator. We especially focus on the phenomena of synchronization and resonance.

4.1.1 Synchronization

The notion of synchronization was first established by the Dutch researcher Christiaan Huygens. He discovered that two oscillating clocks suspended to a common stand ended up oscillating at one similar frequency, in antiphase in his case. He correctly analyzed that an imperceptible motion of the support was responsible for the locking mechanism. Furthermore, he noted that the coupled system went back to its equilibrium when it was slightly perturbed by an external interference. This phenomenon, called *mutual synchronization*, has now been widely observed in science, such as in voltage control oscillators [148] or Josephson junctions [149], in the brain learning rules of neurons [150], but also in wider society [81].

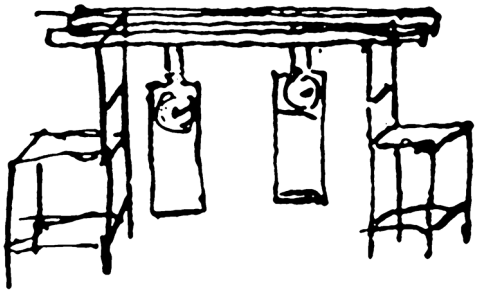

FIGURE 4.1: Original picture of C. Huygens illustrating its experience with two clocks placed on a single support.

In the comprehensive review written by Pikovsky et al.[81] synchronization is defined as the "coadjustment of rhythms of oscillating objects due to their weak interaction". Thus we should call synchronization, a phenomena that fulfills the following conditions:

- The two (or more) oscillators are self-oscillating, i.e, they oscillate even when they are not coupled. The case where at least one oscillator stops oscillating belongs to what is called resonant phenomenom which will be presented in the next section;
- The oscillators can adjust their rhythms thanks to a weak interaction. For example in Huygens' experiment, for a fixed rod that joins the two oscillators, we would not observe a synchronization phenomenon because the two oscillators would be forced to oscillate at the same frequency;

- The oscillators adjust their rhythms within a certain range of frequency mismatch. If the frequency of one of the oscillators is sligthly varied, the synchronization frequency follow this variation. If the frequency mismatch is larger than the bandwidth of synchronization, the two oscillators will oscillate independently (at frequencies corresponding to the weakly coupled modes).

4.1.2 Resonant excitation

It is important to clearly differentiate the phenomena of synchronization from the resonant excitation of a coupled system. In this second case, at least one of the oscillators is not in the self-oscillating regime. To determine if we either face with resonant or synchronization phenomena, it is crucial to know if all the oscillators have their own source of energy so that they can auto-oscillate independently.

A resonant excitation is, for example, the relaxation process of two stable and non-oscillating pendula when one of them is moved away from its stable position. To bring back the total system to its stable position, both pendula oscillate with different amplitudes at a common frequency. However it is not a synchronization phenomena given that the oscillators do not oscillate in absence of the external perturbation.

Similarly, we consider a single pendulum whose weight is replaced by a magnet. If the system is placed close to a coil supplied with an oscillating current at a frequency f, the pendulum is forced to oscillate at the frequency f of the generated alternating field. The pendulum increases its amplitude of oscillation when the frequency of the field approaches its eigenfrequency. However the system stops oscillating when we separate the two parts of the circuit so that it is a resonant phenomenon.

4.1.3 Modulation of the oscillator's dynamics

The auto-oscillator frequency can be tuned through the interaction with an external signal oscillating at a frequency close to its own frequency or close to a fraction of it. Another option to control the frequency of a nonlinear oscillator consists in modulating the amount of energy injected in the system, and thus the amplitude of oscillation. The nonlinear coupling between phase and amplitude permits the transformation of an amplitude modulation into a modulation of the oscillator frequency. To observe an effect of modulation, the input of energy has to vary slowly so that the oscillator has enough time to continously adapt its frequency.

4.2 Sources of locking in vortex based STNOs

In this part, we present an overview of the different locking processes for a vortex based STO with an external reference signal. Here, we focus on the case for which the coupling is unidirectionnel which means that a single oscillator (the STO) adapts its frequency to an external reference signal (a reference source). This case will give use crucial information about the locking conditions of a vortex based STO such as the locking mechanism, the locking efficiency and the locking stability. Moreover it will allow us to go further towards the mutual synchronization of STOs, that is one of the main objective of this thesis.

4.2.1 Injection locking with a resonant locking force

4.2.1.1 Injection locking to an rf-field

A uniform in-plane rf-field can phase lock the gyrotropic motion of a vortex based STO. Experimentally an isolated antenna, placed on top of the STO nanopillar and supplied by an rf-current source, can generate an in-plane rf-field used to synchronize the STO dynamics (see Fig. 4.2).

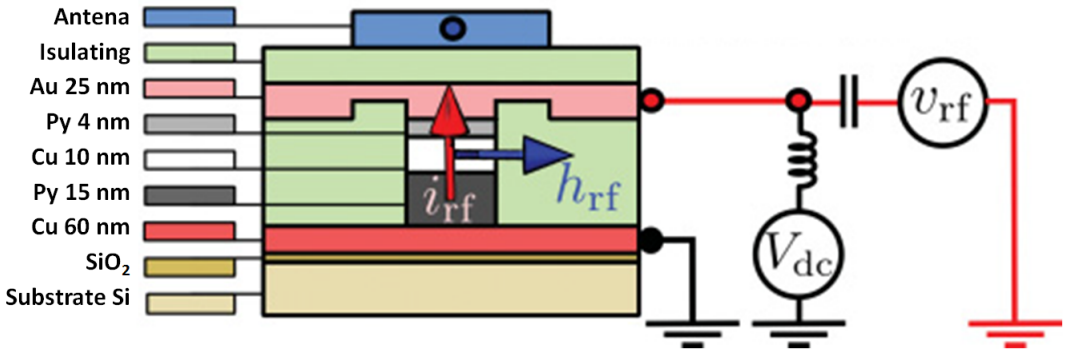

FIGURE 4.2: Experimental setup with a STO pillar and a top isolated rf antenna. The rf-antena generates an in-plane field that can phase lock the dynamics of the STO. Extracted from [67]

The locking force induced by such an in-plane rf-field can be expressed as:

$$\overrightarrow{F_{h_{rf}}} = \mu_0 M_s \xi (\overrightarrow{e_z} \times \overrightarrow{h_{rf}}) = \frac{1}{2}\mu_0 M_s \xi (cos((\omega_s - \omega)t + \phi_s)\overrightarrow{e_\chi} - sin((\omega_s - \omega)t + \phi_s)\overrightarrow{e_\rho}) \quad (4.1)$$

with ξ the factor relating the average magnetization and the position of the vortex core, ω the frequency of the STO, ω_s the source frequency and ϕ_s the dephasing between the source and the STO. The vortex core coordinates are expressed in the cylindrical coordinates of the dot ($\vec{e_\chi}$,$\vec{e_\rho}$) as represented in Fig. 2.3 in Chap. 2.

In collaboration with CEA SPEC, we demonstrated in Ref. [67] that the locking behavior of a double vortex based STO with an rf-field is highly efficient at its eigenfrequency. We observed a phenomenon of synchronization for a minimum rf-field of 0.5 Oe, and a maximum bandwidth of synchronization of 80 MHz for a rf-field of 7 Oe as shown in Fig. 4.3. These results opened the way to the efficient dipolar synchronization of vortex based STOs which we will discuss in Chap. 8.

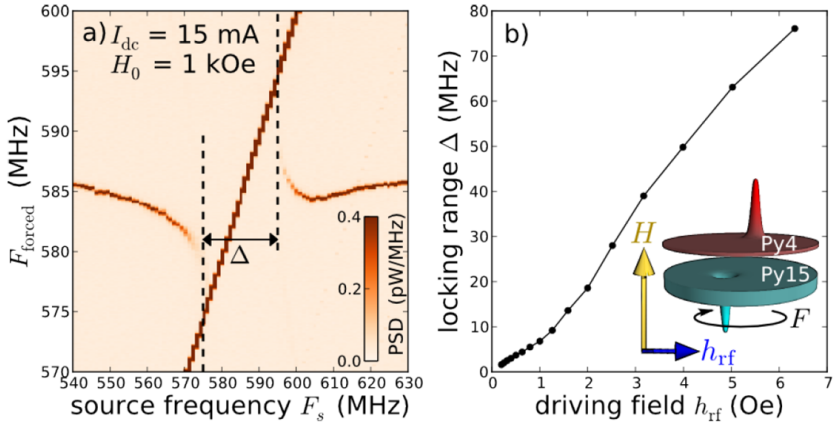

FIGURE 4.3: (a) Evolution of the gyrotropic frequency with the rf-source frequency for a 2.5 Oe amplitude of rf-field. $\Delta\omega$ represents the locking bandwidth (b) Locking bandwidth depending on the amplitude of rf-field. Extracted from [67]

4.2.1.2 Injection locking with an in-plane spin-polarized rf-current

For rf-applications, it is more appropriate to use an rf-current as a locking source than an rf-field that is more easily attenuated. For the case of electrical synchronization, we can also inject both the dc-current and the rf locking current directly in the STO which reduces the size of the total system. The mechanism that locks the vortex STO with an rf-current $J_{rf}\cos(\omega_s t)$ is driven by the ST forces that act directly on its phase $\theta(t)$. As noted in Chap. 2, the two active ST torques in our junctions are the Slonczewski and Field-like torques associated with the in-plane spin polarization arising from the magnetization of the top SAF layer. These two active torques have similar forms but they are respectively along $\vec{u_x}$ and $\vec{u_y}$ (see Eq. 2.14 in Chap. 2). Thus their combined contribution can be expressed as:

$$\overrightarrow{F_{i_{rf}}} = \overrightarrow{F_{SL}} + \overrightarrow{F_{FL}} = \sqrt{\Lambda_{SL}^2 + \Lambda_{FL}^2} J_{rf}(sin((\omega_s - \omega)t + \Phi_{st})\overrightarrow{e_\chi} - cos((\omega_s - \omega)t + \Phi_{st})\overrightarrow{e_\rho}) \quad (4.2)$$

From Eq. 4.2, one should notice that the driving force phase shift $\Phi_{st} = \arctan(\frac{\Lambda_{FL}}{\Lambda_{SL}})$ (for $\frac{\Lambda_{FL}}{\Lambda_{SL}} > 0$) depends on the ratio of the strengths of the two locking forces. From the expressions of the two locking torques (see Eq. 2.14 in Chap. 2), we establish that this ratio is equal to $b/(2R\xi_{FL})$ with ξ_{FL} the Field-like torque efficiency [151]. Thus the total phase shift, between

the rf-current and the STO phase, will significantly depend on the relative contribution of the two ST locking torques.

4.2.2 Parametric locking force

The locking forces considered until now have a common characteristic: they do not compensate the damping term but act as "classical" resonant forces when their frequency is close to the eigenfrequency of the STO. Here we consider an other source of locking, called parametric synchronization or parametric resonance, where the oscillator's motion is driven by the variation of (at least one of) its intrinsic parameters. Thus the effective damping will be reduced, eventually fully compensated or even more. The classical example of this phenomenon is a child swinging on a swing (see Fig. 4.4) who moves his legs backwards and forwards at twice the oscillating frequency. The child's movements modify the center of inertia of the total system making it oscillate. Such a parametric locking process is efficient only for excitation frequency at $\frac{2f}{n}$ (decreases as n increases). Thus, for an excitation frequency at f it can be difficult to distinguish it from a "classical" resonance as we will see later on.

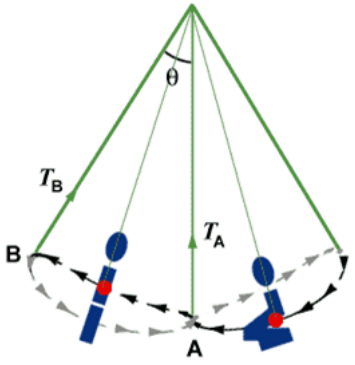

FIGURE 4.4: The change in the position of the centre of mass when swinging with an increasing amplitude. Adapted from [152]

For a parametric excitation, the amplitude of the parametric locking force $V_{parametric}(\rho)$ depends on the amplitude of oscillation ρ. Thus the excitation has to reach a threshold to result in a forced regime of excitation. Above the threshold, the system is in a regime of parametric instability. In this regime, the amplitude of oscillation grows exponentially and is only limited by the nonlinear relaxation process of the STO [61, 62].

Parametric phenomena have been discussed either in uniformly magnetized [61, 153, 154] or vortex [62] based STOs. Urazhdin et al.[61] have shown that the parametric excitation bandwidth of uniform based STOs with an rf-field should evolve as:

$$\Delta_{parametric} = \frac{1}{\pi}\sqrt{(VI_{rf})^2 - (\Gamma_+ - \Gamma_-)^2} \tag{4.3}$$

with V the coupling coefficient between the rf-current, that generates a rf-field through an antena, and the magnetization, and Γ_- and Γ_+ the respective damping and anti-damping torque terms.

In this equation, it can be noted that the parametric bandwidth is not defined below a threshold in field. This threshold depends on the difference between the damping and anti-damping terms. A similar equation can be obtained for a parametric excitation with an rf-current. As the anti-damping term increases with I_{dc}, the threshold rf-current $I_{e,th}$ to observe a parametric excitation decreases with an increase of I_{dc} as seen in Fig. 4.5.

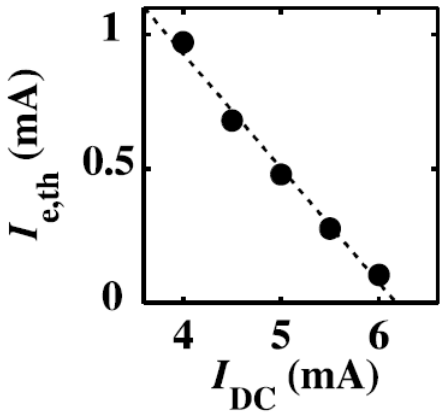

FIGURE 4.5: Excitation threshold $I_{e,th}$ as a function of the dc-current I_{dc}. Adapted from [143]

More recently, P. Bortolotti et al. [62] at CNRS/Thales lab have shown that similar parametric behavior can be observed in confined vortex based STOs with an alternative Oersted field as a source of excitation. As we mentioned, the ST forces act as resonant forces and not as parametric forces. To induce parametric oscillations through the oscillating Oersted field, the vortex core has to be non-centered, i.e. slightly shifted from the dot center at the equilibrium, which is experimentally the case. Indeed, the vortex core is generally moved from the dot center either because of a remaining stray field from a SAF, of an externally applied in-plane field or of the in-plane components of the Slonczewski and Field-like ST forces associated with a dc current [151].

To fit the experimental observations with this model, a relatively large displacement of the vortex core from 20 % of the dot center ($x_0 = 0.2R$) has been assumed [62]. For low rf-current, below the regime of parametric excitation, a regime of parametric amplification is observed in which a thermally activated peak is amplified and detected (see Fig. 4.6.a-b). Indeed at small amplitude of excitation (below the threshold current), the mechanism of parametric excitation permits the amplification of an existing oscillating signal such as a thermally activated STO. This phenonemon may lead to the development of low noise amplifiers [87] as we could imagine to combine a regime of resonant excitation and parametric excitation in a single STO. We will

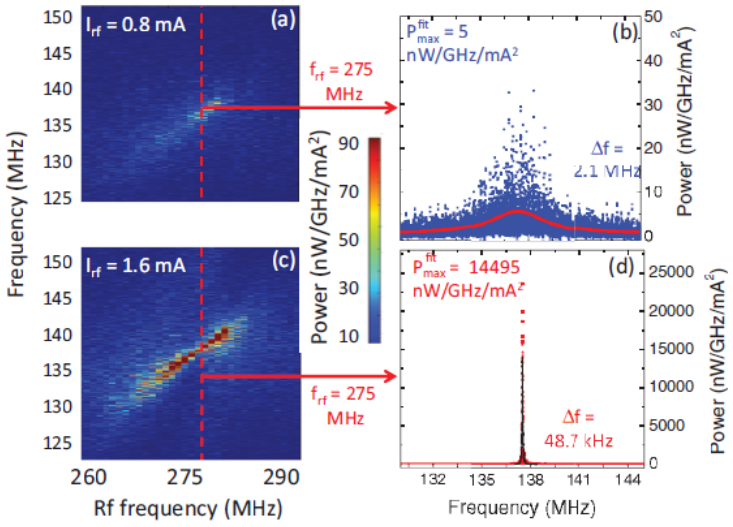

FIGURE 4.6: (a)–(c) Colored maps of emitted power for the frequency of the gyrotropic core motion vs the external rf frequency measured (a) for a small $I_{rf} = 0.8$ mA and (c) a large $I_{rf} = 1.6$ mA current. $I_{dc} = 3$ mA and $H_{perp} = 360$ kA/m. (b)–(d) Power spectral density vs frequency measured with an external rf current at $f_{rf} = 275$ MHz. Extracted from [62]

discuss such a perspective in Sec. 4.4 by studying the forced excitation of a vortex based STO in the sub-critical regime. For larger rf-current, we observe a regime of parametric instability with a much higher spectral coherence and for which the amplitude of oscillations is only limited by the nonlinearities of the system (see Fig. 4.6.c-d).

4.2.3 Modulation force

As we mentioned previously, an rf-current can not only resonantly or parametrically phase lock a STO in the autonomous regime but a low frequency current I_{mod} can also modulate the dynamics of a STO by modulating the anti-damping term Γ_- [59, 68, 77, 144, 155]. The frequency of the modulating current has to be lower than the effective damping that defines the rate at which the STO reacts to an external signal. Generally, the modulation frequency has thus to be at least, one order of magnitude lower than the auto-oscillation frequency. Therefore the modulation current can be considered as an "extra" dc-current I_{dc} and contributes to the anti-damping term of the LLG equation:

$$\Gamma_-(I_{dc+mod}(t), |c|^2) \text{ with } I_{dc+mod}(t) = I_{dc}(1 + \mu_m \cos \omega_m t) \tag{4.4}$$

with Γ_- the anti-damping term and $\mu_m = I_{rf}/I_{dc}$ the modulation strength.

In my work, I do not investigate experimentally the regime of modulation. Detailed studies of this regime for the vortex case have been performed by S. Y. Martin et al. [63] in nanopillar STOs and by M. Manfrini et al. in nanocontact STOs [77, 156]. However, we will focus our study on a similar regime in Chap. 6 in which we consider the case of a STO locked by a phase locked loop. In a phase locked loop, the signal emitted by the STO is compared with a reference signal to generate an error signal that modulates the injected dc-current. In such

electrical device, we find that the effective damping is again a key issue that strongly impacts the phase-locked state.

4.3 Fractional phase locking of a self-oscillating vortex based STO

Here, we study the injection locking of vortex based STOs with an rf-current that has already been studied for different types of STOs [54, 55, 61, 66]. However, in all the reported studies, the phase noise remains large even in the locking state and the presence of detrimental phase slips is reported in micromagnetic simulations [157].

We propose here theoretical and experimental insights on the phase locking regime of a vortex based STO. Similarly to the previous chapter, we study a double vortex spin-valve on top of an MgO based magnetic tunnel junction with a synthetic antiferromagnet (see "sample B" in the App. A). With frequency and time domain measurements, we can determine with precision the locking conditions of a vortex based STO. These results will be particularly useful to achieve for the first time the mutual synchronization of two STOs with electrical coupling presented in Chap. 8.

4.3.1 Theoretical predictions for vortex based STO with inplane polarizer

In the self-sustained regime, it is known that a STO can be well described in the general auto-oscillator framework developed by A. Slavin et al. [45] (see also Sec. 1.2.4 in Chap. 1). Here we extend this approach to the non-autonomous regime in our case of interest, i.e. the vortex oscillator under an external rf current with a frequency, $2\pi F_s = \omega_s$, close to the oscillator fundamental frequency f_0. In Sec. 4.2.1.2, we found that only the Slonczewski and Field-like torques associated with the in-plane spin polarization drive the locking mechanism. At the first order (in the regime of small perturbation), we can then establish (from the Thiele equation) the equations describing the dynamics of the power fluctuations δp and the phase difference $\Phi(t) = \theta(t) - \omega_s t$ between the oscillator and the rf-source [45, 70]:

$$\begin{cases} \frac{d\delta p}{dt} = -2\Gamma_p \delta p + 2F p_0 \cos(\Phi + \Phi_{st}) \\ \frac{d\Phi}{dt} = +N\delta p - F\sin(\Phi + \Phi_{st}) - \Delta\omega_0 \end{cases} \tag{4.5}$$

where Γ_p is the effective relaxation damping rate, N the nonlinear frequency shift, $F = \frac{\sqrt{\Lambda_{SL}^2+\Lambda_{FL}^2}}{2GR\sqrt{p_0}}$ the normalized external driving force, $\Phi_{st} = arctan(\frac{\Lambda_{FL}}{\Lambda_{SL}})$ the additional locking force phase shift for positive dc-voltage (our experimental case), $\Delta\omega = \omega_s - 2\pi f_0$ the frequency detuning, p_0 the normalized power in the self-oscillating regime.

Contrary to the autonomous regime, in which the phase drifts over time, in the phase locking regime the locking force plays the role of a retroaction process that acts on the phase of the oscillator. The oscillator phase is locked to the external signal, because of the unidirectionnal coupling, and is supposed to follow the phase dynamics of the reference. Thus the spectral coherence of the locked oscillator is expected to increase up to the spectral coherence of the reference signal. From Eq. 4.5 we can also notice that the phase locking process is directly determined by the characteristics of the two ST locking forces. An intriguing feature of STOs is that the retroaction process can in turn be controlled through the adjustment of the different ST forces.

4.3.1.1 Locking equilibrium and locking bandwidth

A stable phase locked state ($\frac{d\delta p}{dt} = 0, \frac{d\Phi}{dt} = 0$) can exist only within the locking range defined as:

$$\Delta\omega_s = \sqrt{(1+\nu^2)}F \tag{4.6}$$

The locking range corresponds to the main locking range, i.e when the external current frequency F_s is around f_0. Similar expressions can be obtained for locking ranges at multiple of the oscillator's eigenfrequency (f_0:qF_s) where q is an integer. In that case, the (1:q) locking range can similarly be defined as $\Delta\omega_s = \sqrt{(1+\nu^2)}g_{1,q}F$ with a parameter $g_{1,q}$ that describes the efficiency of the driving force F at higher harmonic frequencies [61].

Within the locking range, the oscillator adapts both its amplitude and its phase relative to the source. A new equilibrium is defined and can be expressed, in the first order, as:

$$\begin{cases} \delta p_0 = p_0 \frac{\nu + \sqrt{(1+\nu^2)F^2 - \Delta\omega^2}}{(1+\nu^2)\Gamma_p^2} \\ \Phi_0 = \arctan(\nu) - \arcsin\left(\frac{\Delta\omega}{\sqrt{(1+\nu^2)}F}\right) - \Phi_{st} \end{cases} \tag{4.7}$$

where $\nu = Np/\Gamma_p$ is the nonlinear dimensionless parameter [45, 46]. The phase shift Φ_0 corresponds to the phase difference between the reference source and the STO. This parameter is crucial for rf-applications and should ideally be zero if synchronizing multiple STOs connected in series or in parallel with an increase in emitted power is targeted (see Chap. 8).

In the case of uniform STOs, the driving force phase shift Φ_{st} is zero as only a Slonczewski ST force is involved in the locking process (in all the reported studies). In such a case, the dephasing parameter Φ_0 is equal to $+\pi/2$ at zero detuning ($\Delta\omega = 0$) given that STOs are

also highly nonlinear oscillators (and thus have large ν parameters) [70, 85, 86, 158]. For vortex based STOs, the locking process involves two different ST forces which offer a unique opportunity to tune the phase shift Φ_0 through the additional term Φ_{st}. This will make the electrical synchronization of two STOs possible as we will show in Chap. 8.

4.3.1.2 Transient regime and phase noise level

Zhou et al.[70] have shown that the transient regime can be investigated by linearizing Eq. 4.5 near the stable solutions (see Eq. 4.7). We then obtain the decay rates of phase and power fluctuations:

$$\lambda = \Gamma_p + \frac{1}{2}F\cos(\Phi_0 + \Phi_{st}) \pm \sqrt{\left(\Gamma_p - \frac{1}{2}F\cos(\Phi_0 + \Phi_s t)\right)^2 - 2\nu F\sin(\Phi_0 + \Phi_s t) + F^2} \quad (4.8)$$

The decay rates correspond to the retroaction times of the oscillator's phase and amplitude. In injection locking experiments with an external rf-current, it is thus expected to reduce, down to the phase noise level of the reference signal, all the noise contributions with a characteristic time lower than the retroaction times. It can be notice that the square root term can be negative and leads to oscillating transient regime (instead of asymptotic).

To go beyond this analysis, we determine (by calculation in complex form) the power spectral density (PSD) of both the phase and amplitude noises:

$$\begin{cases} S_{\delta\phi} = \dfrac{\Delta f_0}{\pi} \dfrac{\left[f^2\left(-\nu+F/f_p\sin(\Phi_0+\Phi_{st})\right)^2+\left(f_p+2F\cos(\Phi_0+\Phi_{st})\right)^2\right]+f_p^2F^2\cos(\Phi_0+\Phi_{st})^2}{\left[f^2+F^2\cos(\Phi_0+\Phi_{st})^2\right]\left[\left(F^2-Ff_p\sqrt{1+\nu^2}\sin(\Phi_0+\Phi_{st}+\arctan(1/\nu))-f^2\right)^2+f^2\left(f_p+2F\cos(\Phi_0+\Phi_{st})\right)^2\right]} \\ S_{\delta p} = \dfrac{\Delta f_0}{\pi} \dfrac{F^2+f^2}{\left[\left(F^2-Ff_p\sqrt{1+\nu^2}\sin(\Phi_0+\Phi_{st}+\arctan(1/\nu))-f^2\right)^2+f^2\left(f_p+2F\cos(\Phi_0+\Phi_{st})\right)^2\right]} \end{cases} \quad (4.9)$$

These expressions are quite complex and difficult to discuss. Nevertheless, we can at least notice from Eq. 4.9, that both amplitude and phase noises are reduced in the locked state and that their levels are strongly correlated with the locking strength F, i.e on the amplitudes of the two locking torques (the Slonczewski and Field-like torques), and with the phase shift Φ_0. Given that Φ_0 depends on the frequency detuning $\Delta\omega$, the shape of noise PSDs also varies within the locking range. To analyze more in detail these expressions, we will compare them to our experimental results in Sec. 4.3.4.2.

4.3.2 Fractional phase locking

In our experiments, we observe a locking state when the frequency of the current source F_s approaches the fundamental gyrotropic frequency f_0 (see Fig. 4.7.a-b). Beyond this expected behavior, we observe that a frequency locking can be also achieved when F_s is around qf_0, with q an integer ($q = 1$ in Fig. 4.7.b, $q = 2$ in Fig. 4.7.c; and $q = 3$ in Fig. 4.7.d). The mechanism of synchronization at higher harmonics (q integer) is usually associated with the presence of harmonics in the autonomous regime [159, 160] (which drive the synchronization process). The rf-current signal can thus lock with the q-harmonics around qf_0. The locking efficiency at harmonics, proportional to the locking bandwidths, decreases as q increases (as the amplitude of harmonics decreases with q as seen in Fig. 4.7). Thus we report a locking bandwidth of 12%, 4% and 2% at F_s around f_0, $2f_0$ and $3f_0$ respectively for a locking amplitude $\mu = I_{rf}/I_{dc} = 20\%$.

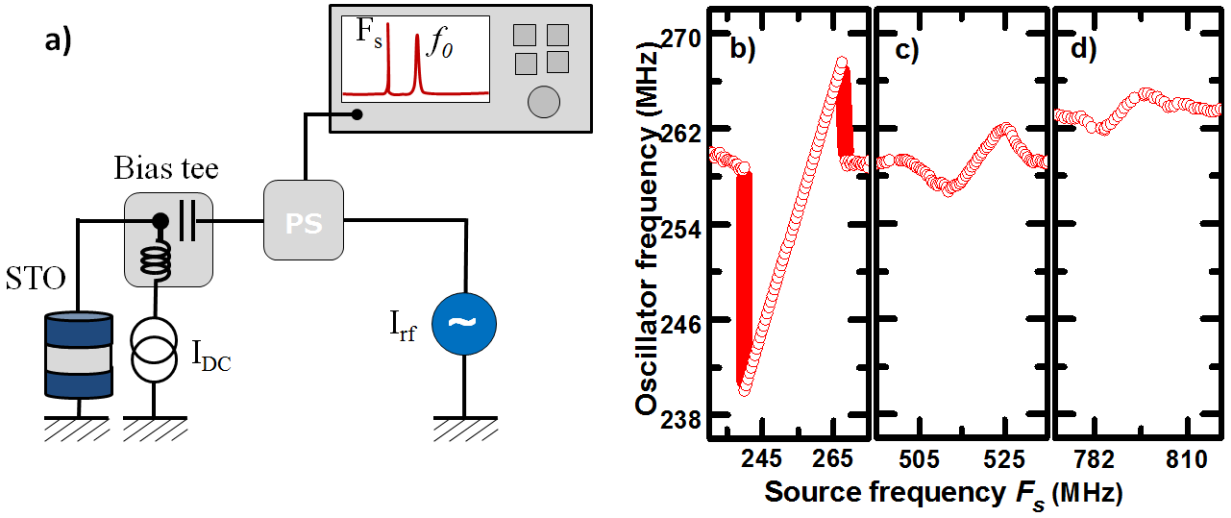

FIGURE 4.7: (a) Schema of the electrical circuit to phase lock a STO, alimented by a dc source I_{dc}, with a rf-source I_{rf}. The detected signal is measured by a spectrum analyzer, connected to the circuit with a -6 dBm power splitter (PS). (Right) Frequency of STO vs external source frequency F_s around f_0 (a), $2f_0$ (b), $3f_0$ (c) for $I_{rf} = 2$ mA (at zero applied field and $I_{dc} = +11$ mA and $\varnothing = 300$ nm)

We note that the phase locked state is ultra-stable with a minimum linewidth of 1 Hz (as shown in Fig. 4.8.b for $F_s = 2f_0$), only limited by the resolution bandwidth of the spectrum analyzer (note the change of x-scale for the two graphs). One should notice that this value is about 10^2 lower than the autonomous regime (700 kHz, Fig. 4.8.a). This strong linewidth reduction is combined with an output emitted power (integral of the intensity) increased from 0.8 μW in the autonomous regime to 1.1 μW in the synchronized regime. This enhanced power is associated with an increase of the radius of core gyration in the synchronized state. Indeed, as expected from Eq. 4.7, the phase of a nonlinear STO adapts its dynamics through a modification of the amplitude.

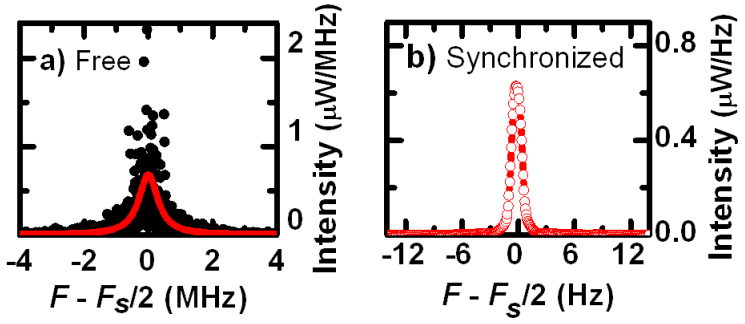

FIGURE 4.8: Emitted spectrum in (a) the autonomous regime without any external signal and in (b) the synchronized state with a rf source at $F_s = 2f_0$

Importantly, such a significant improvement of the spectral coherence is observed not only at high harmonics of synchronization but also at sub-harmonics. Indeed as displayed in Fig. 4.9.a-b, we report, for the first time in the case of an STO, a synchronization with the external rf current even for a fraction of the oscillator frequency (f_0/q), at F_s around $f_0/2$ and $f_0/3$.

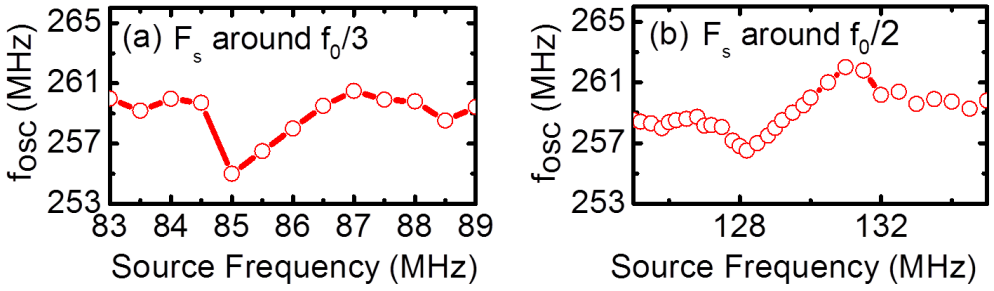

FIGURE 4.9: Oscillator frequency f_{osc} vs external source frequency F_s around $f_0/3$ (a), $f_0/2$ (b) for $I_{rf} = 2$ mA (at H=0 and $I_{dc} = +11$ mA and Ø = 300 nm)

It should be noted that sub-harmonic phase locking in STOs has been predicted in micromagnetic calculations [161] but never observed experimentally. Indeed, sub-harmonic synchronization $(1/q)$ usually relies only on the nonlinear behavior of the oscillator. Thus when an rf-signal is applied at a given frequency f, it is assumed that a nonlinear system will generate a small response at nf [159, 160] (with n integer). The small amplitude of this response explains why here the locking ranges at $f_0/2$ and $f_0/3$ are small (respectively around 2% and 1% of f_0) compared to f_0. The origins of this mechanism of excitation will be further investigated in the section concerning the forced oscillations of a STO in the sub-critical regime (see Sec. 4.4).

4.3.3 Evolution of the locking characteristics with I_{dc} and I_{rf}

4.3.3.1 At F_s around f_0

In this part, we study the characteristics of the synchronized state depending on the locking conditions and compare it with our analytical model. First, we present in Fig. 4.10 the evolution of the locking bandwidth with I_{dc} for a fixed amplitude of rf-current (I_{rf} = -14 dBm) at $F_s \approx f_0$. We note a decrease of the locking bandwidth from 17 MHz at I_{dc}= + 10.7 mA (i.e close to 10.5 mA the threshold current) to 9 MHz at I_{dc}=+11.6 mA, and then a small increase up to 11 MHz at I_{dc} = +12.0 mA. This trend is linked to the STO characteristics in the autonomous regime. As seen in Fig. 4.10, we observe in the autonomous regime a similar trend for the nonlinear dimensionless parameter ν (obtained with time domain measurements) which evolves from 7 at I_{dc} = +10.7 mA to 4.5 at I_{dc} = 12 mA. A more precise fit of the locking bandwidth dependency can be obtained by taking into account the evolution of the gyration radius with I_{dc}. In that case, we observe an excellent agreement (see Fig. 4.10) between the trends of the locking bandwidth and the ratio $\sqrt{1+\nu^2}/\sqrt{p_0}$ (with $\sqrt{p_0} = \rho/R$) as expected from Eq. 4.6.

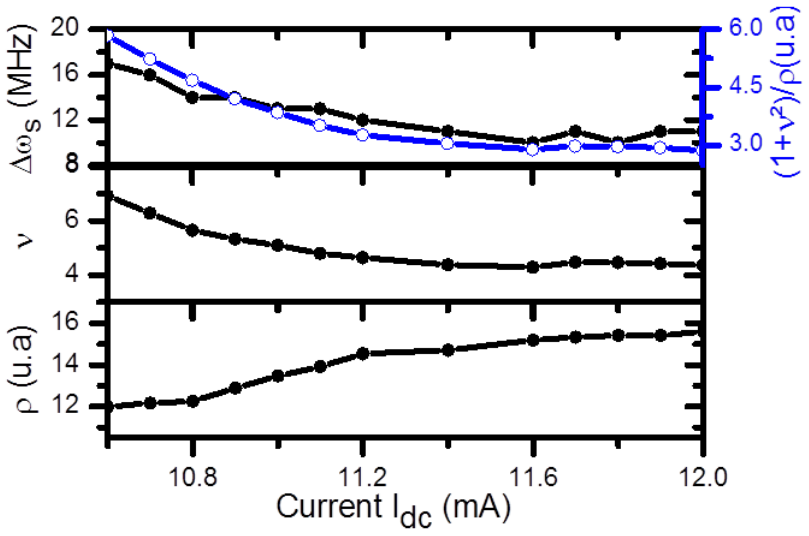

FIGURE 4.10: Evolution of the locking bandwidth with I_{dc} for I_{rf}= -14 dBm (at H=0). Evolution of the nonlinear dimensionless parameter ν and of the gyration radius with I_{dc}. (The nonlinear parameter ν is extracted from the phase noise curves)

We have also studied the locking bandwidth as a function of the locking strength $\mu = I_{rf}/I_{dc}$ for I_{dc} = +11 mA. We observe, as shown in Fig. 4.11, a quasi-linear dependency of the locking bandwidth at small locking strength μ. For larger driving forces, a small change of slope appears. This is most probably related to a significant change of the normalized power δp, i.e of the gyration radius of the vortex core, that increases with the locking strength μ (see the evolution of the normalized power with the amplitude of the synchronization force F in

Eq. 4.7), which may also impact the nonlinear behavior ν. By comparing our experimental observations to our analytical model, we can extract an estimation of the efficiency of the Field-like torque. Indeed, we notice in Fig. 4.11 that the expected locking range in absence of the Field-like torque (see Eq. 8.3) does not fit with the experimental locking. On the contrary, we get a quantitative agreement with a large Field-like torque efficiency $\xi_{FL} = 0.4$. A large Field like torque is expected for assymetric magnetic tunnel junctions [22, 23] but the value reported here is quite high. However, it is not surprising as a large Field like efficiency of a factor $\xi_{FL} = 0.4$ has already been reported through spin-diode measurements performed by Matsumoto et al.[162] and Chanthbouala et al. [18] on similar magnetic tunnel junctions. This Field-like torque efficiency leads to a torque ratio $\Lambda_{FL}/\Lambda_{SL}$ equal to 6 ($0.4 \times 150/10$) for this vortex based STO. Thus the locking process is mainly driven by the Field-like torque. It must be emphasized that the Field like torque is amplified compared to the Slonczewski torque in vortex based STOs given that they are respectively dependent on the size of the body and the core of the vortex (and $b << R$)[151].

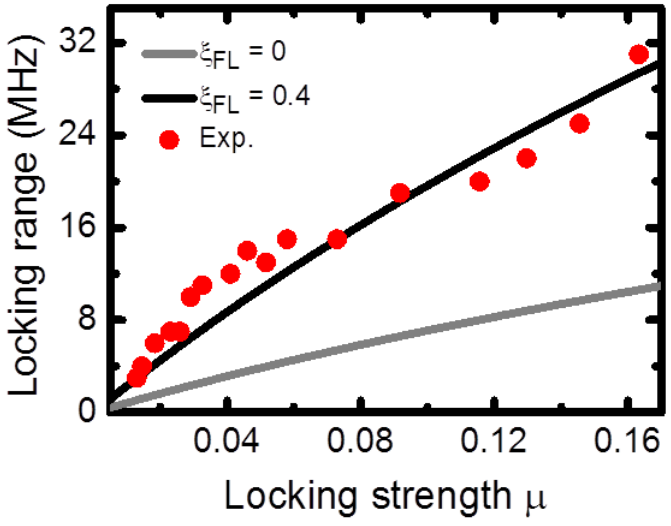

FIGURE 4.11: Evolution of the locking bandwidth with I_{rf} for $I_{dc} = +11$ mA (at zero applied field). Expected locking bandwidth for $\xi_{FL} = 0$ (grey line) and $\xi_{FL} = 0.4$ (black line)

4.3.3.2 At F_s around $2f_0$

Here we study the STO when it is phase locked with an external current at $F_s \approx 2f_0$. Contrary to the previous case, the properties of the locked oscillator are not masked by the large power of the rf source. In Fig. 4.12, we display how the experimental locking range $\Delta\omega_{sync}$ (defined by the difference between the maximum and minimum frequencies of the locked STO) and the normalized power evolve with the locking strength μ. For $\mu < 0.05$, we observe a linear dependence of the locking range and then a change of slope for a large driving force. Again

this deviation from an linear dependency may be associated with an increase of the normalized power in the locked regime (see Fig. 4.12.b). Note that this dependence of the locking range with p_0 is expected only in the case of normal resonance and not for parametric resonance as developed in Sec. 4.2.

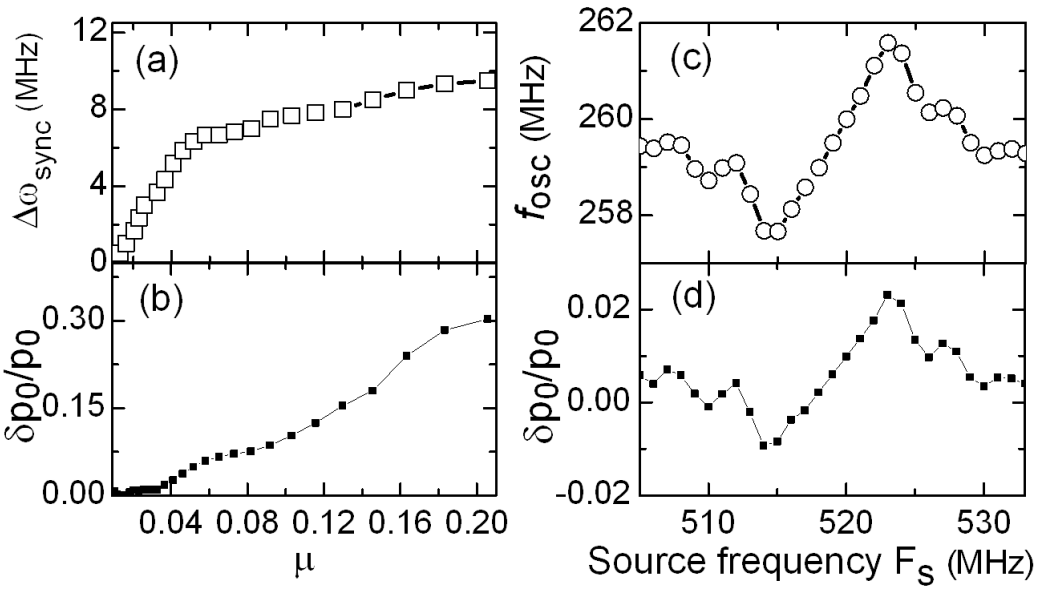

FIGURE 4.12: Evolution of (a) the locking range (for $F_s \approx 2f_0$) and of (b) the normalized power p_0 (for $F_s = 2f_0$) as a function of the amplitude of injected rf-current. STO frequency (c) and normalized power p_0 (d) dependency with the rf-source frequency F_s. (The measurements are done with an oscilloscope at zero field, for $I_{dc} = +11$ mA and $\emptyset = 300$ nm. The normalized power is extracted from the amplitude of voltage oscillation [138]).

Furthermore, as predicted from Eq. 4.7 and shown in Fig. 4.12.c-d, the vortex oscillator adapts its frequency to the external frequency through a substantial modification δp of its normalized power p_0 and hence its gyration radius. These two features illustrate the amplitude/phase coupling of our nonlinear oscillator that adapts its phase dynamics through a modification of its amplitude (even in APc configuration for which ν is small).

4.3.4 Dynamics of a STO in the locked state

4.3.4.1 Stability of the locking regime

To gain a deeper understanding of the 1 Hz linewidth when the oscillator is locked, we perform time domain measurements by recording 5 ms long output voltage time traces with a single-shot oscilloscope (for details see [48]). By Hilbert transform, we are able to extract the power spectral densisty of the phase and amplitude noises. Given that the phase noise is much larger than the amplitude noise, we focus our study on the properties of the phase noise.

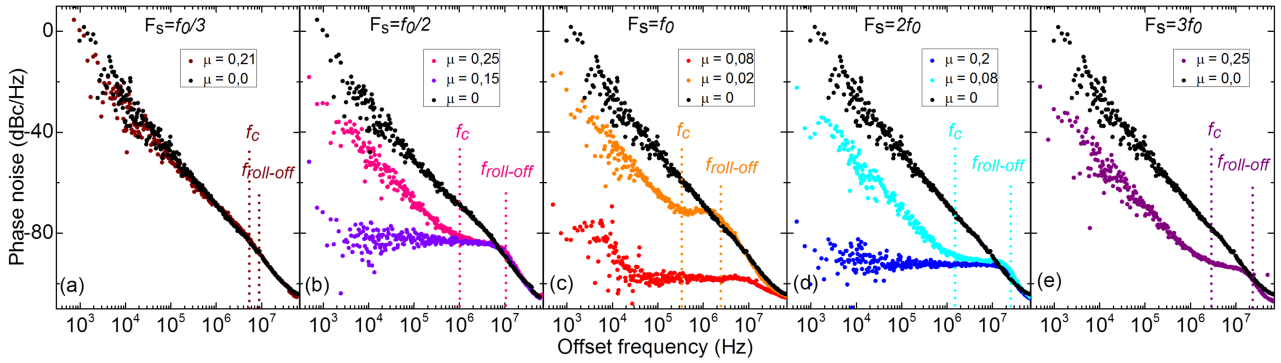

FIGURE 4.13: Phase noise of the locked oscillator for different driving force (at zero field, I_{dc} = +11mA and Ø = 300 nm) at $f_0/3$ (a), $f_0/2$ (b), f_0 (c), $2f_0$ (d), and $3f_0$ (e).

As already reported for other STOs [48, 134, 138], we find that the power spectral density (PSD) of the phase noise in the autonomous regime displays a $1/f^2$ dependence from the carrier frequency that is associated to a white frequency noise (see black curves in Fig. 4.13). This level of phase noise is seemingly modified when the frequency of the external current I_{rf} approaches f_0, $f_0/2$, $2f_0$, $f_0/3$ or $3f_0$. When $F_s = f_0$, a significant reduction of phase noise is observed even for a low driving force $\mu = I_{rf}/I_{dc} = 0.02$ (see orange curve in Fig. 4.13.c). For such a low injection power, we observe a plateau in the phase noise from a high frequency roll-off, $f_{roll-off}$, down to a low offset frequency corner f_c (for example, for $\mu = 0.02$ at $F_s = f_0$ in Fig. 4.13.c, f_c = 200 kHz and $f_{roll-off}$ = 3 MHz). Similar behaviors with larger external rf current are obtained for an external frequency at $2f_0$ (cyan curve in Fig. 4.13.d with μ = 0.08), $3f_0$ (violet in Fig. 4.13.e with μ = 0.25), $f_0/2$ (magenta curve in Fig. 4.13.b with μ = 0.15) or even $f_0/3$ (wine curve in Fig. 4.13.a with μ = 0.21).

For an offset frequency lower than f_c, the phase noise has a $1/f^2$ dependency because of the phase slips in the phase dynamics [81, 157, 163, 164]. Similar features were reported in micromagnetic simulations [157] but not observed in time domain measurements. The phase slips are associated to desynchronization-resynchronization events occurring because of the thermal fluctuations.

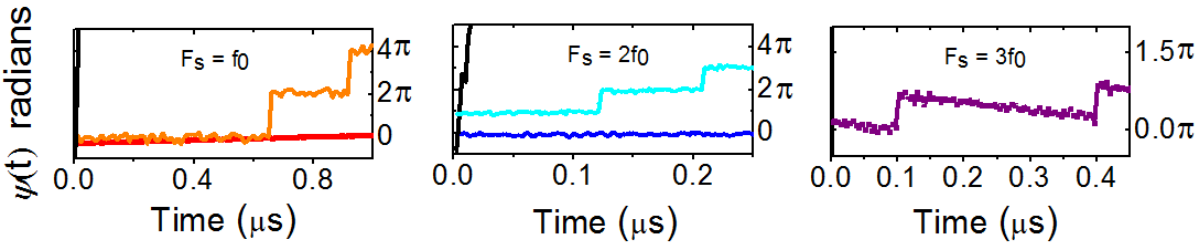

FIGURE 4.14: Phase deviation ($\Phi(t) = \Theta(t) - 2\pi f_0 t$) associated to phase noise curve of Fig. 4.13 at f_0, $2f_0$, and $3f_0$

The amplitude of these phase slips is related to the number of stable positions available over one period, which directly depends on the frequency of the current source. As a consequence,

for a driving force frequency around qf_0, the phase deviation ($\Phi(t) = \theta(t) - 2\pi f_0 t$ with $\theta(t)$ being the phase of the STO) of the locked oscillator presents some phase slip events with an amplitude of $2\pi/q$. In Fig. 4.14, the amplitude of the measured phase slips is thus, as expected, respectively 2π, π, $2\pi/3$ for the f_0, $2f_0$, and $3f_0$ cases.

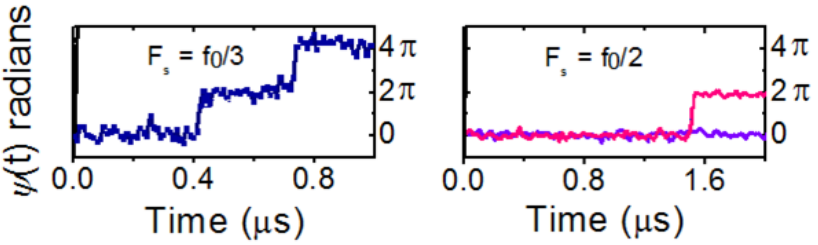

FIGURE 4.15: Phase deviation ($\Phi(t) = \Theta(t) - 2\pi f_0 t$) associated to phase noise curve of Fig. 4.13 at $f_0/3$, $f_0/2$

However when the source frequency is smaller than that of the STO, and F_s is close to f_0/q, we only observe phase slips of 2π as shown in Fig. 4.15 for F_s around $f_0/2$ and $f_0/3$. These 2π phase slips confirm that the STO can phase lock with an injected rf-current around f_0/q because of its nonlinear behavior. The STO generates at f_0 a harmonic replication of the injected rf-current which allows the locking process. It can also be seen that for each locking range, all the observed phase slips present the same amplitude, which demonstrates the absence of chaotic behavior or other dynamical regimes related to multi-stability [81] in our STOs.

For large enough driving forces (in Fig. 4.13.b-d, resp. $\mu = 0.25$ purple curve at $f_0/2$, $\mu = 0.08$ red curve at f_0 and $\mu = 0.2$ dark blue curve at $2f_0$), a constant phase noise level from $f_{roll-off}$ to 300 Hz offset frequency (lowest value associated with our oscilloscope memory) is observed. In this ultra-stable locked regime, we note the absence of phase slips (see Fig.4.14. The phase deviation remains below 2π with an associated resulting noise level of -90 dBc/Hz at 1 kHz from the carrier when the external frequency is at $2f_0$ (see Fig. 4.13.d). Note that a similarly low phase noise is reached at f_0 (Fig. 4.13.c) but the data at very low offset frequencies are hindered by the phase noise of our Agilent rf-current source. Furthermore, we observe that this pure phase locking state is indeed not achieved for F_s equal to $3f_0$ or $f_0/3$ as the efficiency of the locking process is too weak in these two conditions.

The presence or the absence of phase slips highlights here the fundamental difference between the largely reported "frequency locked state" [52–55, 58, 61, 89] and a "pure" (or "real") phase locked state, which only exists in the absence of any phase slip events.

4.3.4.2 Transient regime of synchronization and phase noise level

The constant phase noise level, reported in the previous section, is characteristic of the retroaction process acting on the phase of the oscillator. Indeed, all thermal noise events with a

characteristic frequency lower than the retroaction frequency (here indicated as the frequency roll-off $f_{roll-off}$ in Fig. 4.13) are strongly reduced or suppressed. This retroaction frequency corresponds to a direct observation of the phase noise retroaction time λ as defined in Eq. 4.8.

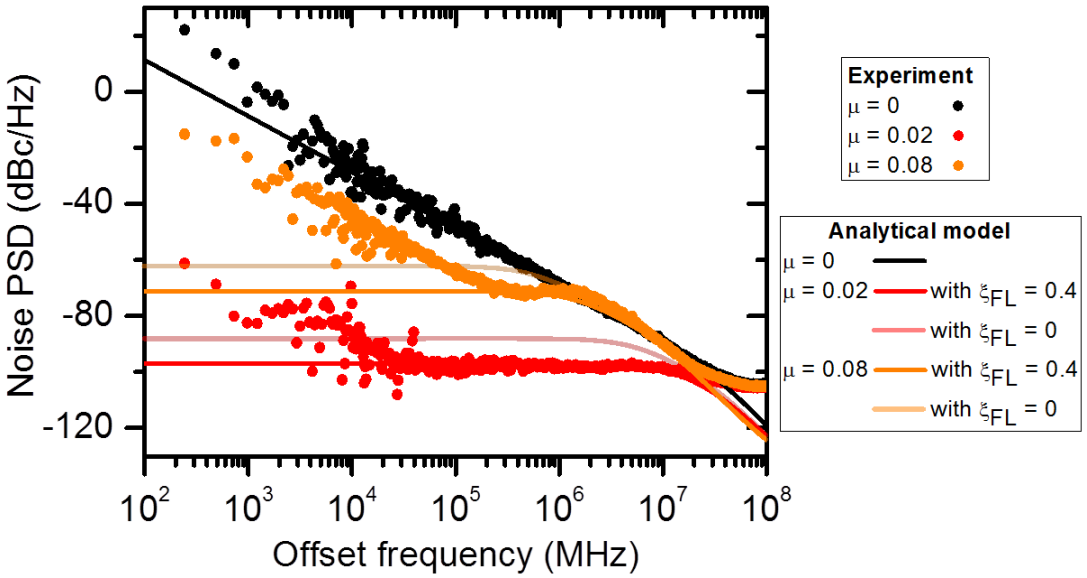

FIGURE 4.16: Experimental phase noise spectra at $F_s = f_0$ for $\mu = 0.08$ (orange dots) and $\mu = 0.2$ (red dots) at zero field and $I_{dc} = +11$ mA (Ø = 300 nm). Modelled phase noise spectra for $\xi_{FL} = 0$ (light red and orange lines) and $\xi_{FL} = 0.4$ (red and orange lines)

As we presented in section 4.3.1.2, we can extract some crucial information on the transient regime of the locking process by analyzing the phase noise in the locked state. As expected, the retroaction constant increases with the locking strength and thus induces a decrease of the phase noise level. In Fig. 4.16, we plot with Eq. 4.9 the expected phase noise levels for $\mu = 0.08$ and $\mu = 0.2$ with $\xi_{FL} = 0$ and $\xi_{FL} = 0.4$. It can be noticed that the experimental curves fit with our model for $\xi_{FL} = 0.4$ which confirms the crucial role of the FL torque in the locking process.

We can thus deduce from Eq. 4.7 that the phase shift introduced by the locking ST forces $\Phi_{st} = \arctan(\Lambda_{FL}/\Lambda_{SL})$ is close to $\pi/2$ and compensates the phase shift due to the STO nonlinear behavior ($\arctan \nu$ with ν around 10 for the functioning point in Fig. 4.16). Thus we can deduce that the phase shift Φ_0 between the injected rf-current and the STO phase is close to zero at zero detuning (see Eq. 4.7). This will be an important and crucial issue for our mutual synchronization measurements (see Chap. 8).

Finally, we succeed to demonstrate "pure" injection locking of a vortex based spin transfer oscillator by an external current with multiple integers, i.e., f_0, $2f_0$ and $3f_0$, as well as half and third integer frequencies $f_0/2$ and $f_0/3$. A "pure" phase locking state with no phase slips and a large output power ($> 1\mu W$) is observed at room temperature and zero magnetic field. It is associated with a record low phase noise down to -90dBc/Hz at 1 kHz offset. We demonstrate

that the physical mechanisms at play for the oscillator to be locked, notably in the transient regime of synchronization, are correlated to the symmetry of the ST locking forces.

4.4 Forced oscillations in the sub-critical regime

For rf-applications, an important concern is to reduce the energy consumption and thus to reduce I_{dc} and so the Joule heating. Until now, we have studied the case of a vortex based STO in the self-sustained regime where a large dc-current is applied to compensate the losses. In this section, we consider a vortex oscillator in the sub-critical regime where no sustained oscillations are observed. One open question here is to determine the conditions for which we can observe a regime of forced excitations when we supply the STO with an rf-current. Answering this question could eventually give rise to the perspective of zero dc-current frequency multiplier or divider. To do so, it is necessary to identify the locking mechanisms that could be involved in this regime of forced excitation.

In the literature, it was reported that a vortex based STO in the damped regime could be excited with an external current at $2f_0$ and f_0 [62], and also at $3f_0$ [89]. The authors attributed their observations to a phenomenon of parametric excitation. However this is partially in contradiction, at least because $3f_0$ works, with the fact that a parametric phenomenon is efficient only when the source frequency fulfilled the condition $F_s = \frac{2f_0}{n}$.

Here we first show that we can observe forced oscillations not only when the source frequency is around $2f_0$, or f_0 but more generally when the condition $F_s{=}\frac{f_s}{q}$ is fullfiled (with q an integer). Then we discuss the different mechanisms of excitation at $2f_0$ and f_0. We compare our analytical results with analytical predictions taking into account both parametric resonance and normal resonance and find that both these processes are involved in the mechanism of excitation. We support our conclusion by simulations performed in collaboration with the group of M. Stiles in NIST.

4.4.1 STO response depending on the frequency of the rf-source

In our study, we apply a dc-current so that the anti-damping term Γ_- partially compensates the damping term Γ_+. The damping constant in our permalloy based STO is too high to observe a forced regime of excitation without applying any dc-current. Thus we performed our experiments for I_{dc}= +7 mA, i.e 80% of the threshold current in our junction with a 300 nm diameter, at zero applied field. By applying an additional rf-current, we could then observe a forced regime for a source frequency F_s around qf_0 or f_0/q with q an integer as seen in Fig. 4.17 for I_{rf} =2 mA (i.e a locking amplitude of 30%).

The efficiency of the excitation is then determined by the ability of the oscillator to modify its intrinsic frequency. Thus to compare the different locking efficiencies, we measure the forcing interval defined as $\omega_s = \frac{\omega_{s,max} - \omega_{s,min}}{q}$ where $\omega_{s,max}$ and $\omega_{s,max}$ are respectively the maximal and mininal external frequencies that lock the oscillator for each locking bandwidth[1]. We note that the locking interval is larger for F_s around f_0 (14% of the vortex eigenfrequency). At F_s around $\frac{f_0}{2}$, $2f_0$ and $3f_0$, the different locking intervals are of similar order of magnitude, respectively 9%, 6% and 5% of the vortex gyrotropic frequency. At F_s around $\frac{f_0}{3}$, the locking bandwidth is much smaller, about 3% of the vortex gyrotropic frequency.

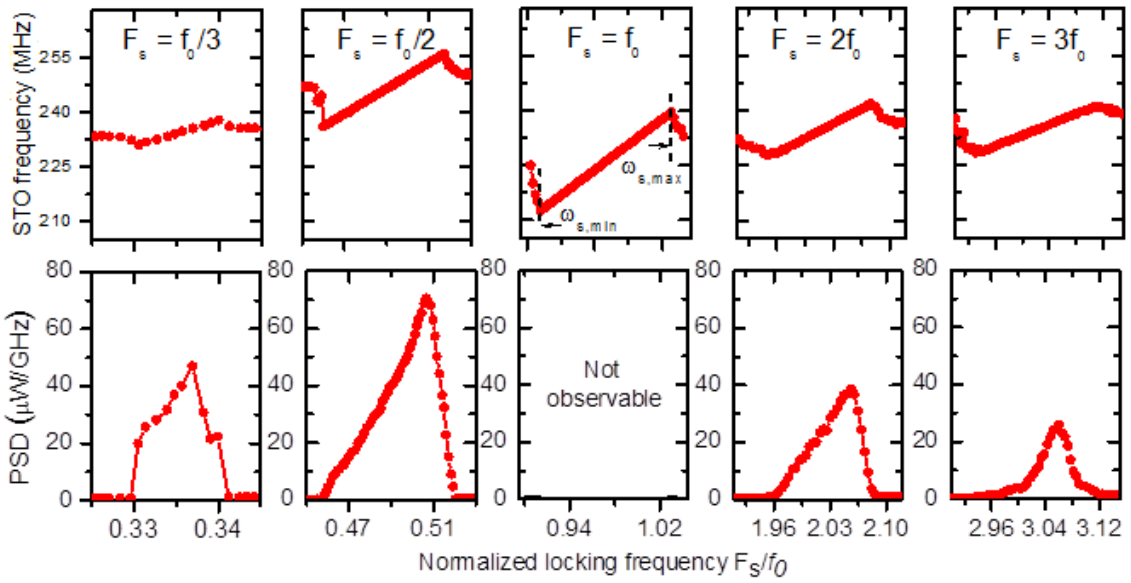

FIGURE 4.17: Frequency and amplitude of forced oscillations as a function of the normalized frequency of the external rf current (with I_{rf} = 2 mA, H=0, I_{dc} = + 7 mA and Ø = 300 nm)

In fact, these regions of excitation and the magnitudes of the locking ranges do not well agree with a complete regime of parametric excitation. Indeed this phenomenon should only be observed for an excitation frequency around $F_s = 2f_0/n$ with n an integer and its efficiency should decrease as n increases. Here, we observe a response at $F_s = 3f_0$ and no signal at $F_s = \frac{2f_0}{3}$. Thus we conclude that parametric excitation alone cannot account for the results that we observed.

4.4.2 Excitation mechanism at *f* and *2f*

To envisage the possible mechanism of excitations, we first analyze the locking characteristics for a source frequency around f_0 or $2f_0$. In Fig. 4.18, we note that for each case the bandwidth of excitation evolves linearly with μ. However, for $F_s \approx 2f_0$ a threshold of excitation is observed

[1]This is equivalent to measuring the minimal and maximal frequencies of the locked oscillator for each locking bandwidth.

(at $\mu \approx 0$) whereas there is no threshold at f_0 (see Fig. 4.18). We will discuss more in details this observation with simulations later on.

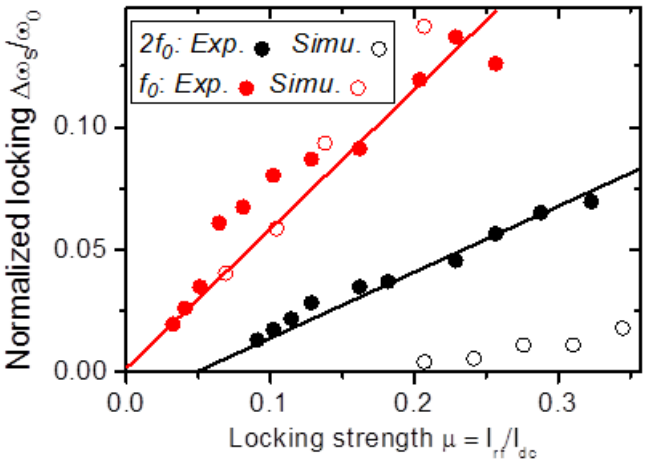

FIGURE 4.18: Evolution of the locking bandwidth with the locking strength μ at F_s around f_0 and $2f_0$ at zero external field (Filled dots: experimental values / Unfilled dots: Matlab simulations for $H_{\parallel} = 4kA/m$)

For $F_s \approx 2f_0$ we can also plot the evolution of the gyration radius with μ as seen in Fig. 4.19. To do so, we extract the power of the STO from the power spectral density (PSD) and take its square root [48]. Thus we first observe that the radius increases rapidly and linearly with the amplitude of rf-current I_{rf} and then more slowly due to the nonlinearities of the system.

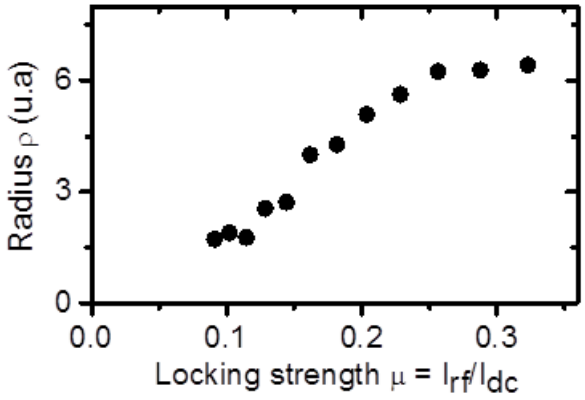

FIGURE 4.19: Evolution of the gyration radius as a function of the locking strength in the center of the locking range at $F_s = 2f_0$

The observed thresholds at $F_s \approx 2f_0$ have been associated in the literature to parametric effects. In particular, P. Bortolotti and al. [62] highlighted on vortex based STOs that the oscillating Oersted field associated with the rf-current could induce a parametric excitation only for non-symmetric systems (see Sec. 4.2.2).

On the contrary, at F_s around f_0, the absence of a threshold tends to prove that we have a normal resonant process. Thus contrary to Martin et al. [89], we cannot attribute our results to a parametric phenomenon. Contrary to parametric forces, the Slonczewski and Field-like in plane torques of the SAF polarizer, as we have seen previously, do not depend on the gyration radius of the vortex. Thus their action can lead to forced oscillations of a vortex based STO in the subcritical regime, without any threshold of excitation. For an excitation frequency at

$2\pi F_s = \omega$, we can establish (from the Thiele equation) the expression of the resulting gyration radius:

$$\rho = \frac{\frac{J_{rf}}{2GR}\sqrt{\Lambda_{FL}^2 + \Lambda_{SL}^2}}{\sqrt{(\omega - \omega_0)^2 + (\Gamma_- - \Gamma_+)^2}} \tag{4.10}$$

with G the gyrovector, R the dot radius, Λ_{FL} and Λ_{SL} the respective efficiency of the Slonczewski and Field-like in plane torques, Γ_- the anti-damping term, Γ_+ the damping term.

From Eq. 4.10, we predict a linear increase of the excitation bandwidth with the amplitude of rf-current as it is the case in our experiment. This efficiency of the excitation process is sufficiently high in our MTJ so that it can lead to the expulsion the vortex core from the junction as we will see in Chap. 7. From these experiments in the sub-critical regime, it seems that the process of excitation relies on phenomena of normal resonance at f_0 and of parametric resonance at $2f_0$ (due to the presence of an excitation threshold).

To further understand the mechanisms behind these excitations in the sub-critical regime, we simulate our vortex based STO for $I_{dc} = 0.8I_{th}$ with a Matlab program that solves the Thiele's equation. Using this program developed in collaboration between J. Grollier and the NIST group of M. Stiles, we study the response of the system when we excite it with an rf-current at different amplitudes. To evaluate the contribution of the parametric excitation in our experiments, we observe the temporal dynamics with or without an in-plane field that shifts the vortex core from the dot center as required for parametric excitation. To evaluate the effect of the normal resonance, we simulate the system with or without the Slonczewski and Field-like in plane force (as previously, ξ_{FL} is fixed to 0.4).

In the simulation results represented in Fig. 4.18, we notice that a regime of forced dynamics at $2f_0$ is observed only in presence of an in-plane field that shifts the vortex core by 0.3 of the radius. At f_0, a resonant excitation is observed only when the ST in-plane torques are considered. This shows that the process of excitation mainly relies on phenomena of normal resonance at f_0 and of parametric resonance at $2f_0$.

Furthermore, one may notice in Fig. 4.18 that the locking bandwidth obtained by our Matlab code at $2f_0$ is much smaller than the experimental locking. This discrepancy can be reduced by increasing the in-plane field considered in our Matlab code but the locking bandwidth remains lower than the experimental one for realistic values of field (lower than the field that will expulse the vortex core from the STO). This could be explained by the fact that we consider perfectly circular dots in our Matlab code. In our experiments the nanopillars are not perfectly circular (see Appendix A) which can lead to a non-perfectly circular gyrotropic motion. Thus, the

presence of high harmonics, as reported in the experiments, can enhance the locking process at $2f_0$ through a process of normal resonance at the frequency of the harmonics.

4.4.3 Superharmonic resonance at $\frac{f_s}{q}$

In mechanical systems [165], it has been reported that superharmonic resonances could be observed for large amplitudes of excitation. This phenomenon is only observed in highly nonlinear oscillators when F_s is around $\frac{f_s}{q}$. Indeed, as seen in Chap. 4, the rf-excitation of a nonlinear oscillator at a fraction of its eigenfrequency generates a response at harmonics of the input frequency. This response can be close to f_0 so that a resonant excitation at f_0 can be observed. In our vortex based STOs, the nonlinearities arises from the damping term Γ_+ and the confinement term ω_0 (see Sec. 2.1.1 in Chap. 2) which depends on the gyration radius ρ at the second order.

In our experiments, we can observe, as shown in Fig. 4.20.a, a resonant response at f_0 for an excitation frequency at $\frac{f_s}{q}$. This behavior corresponds to the regime of superharmonic resonance. Given that the efficiency of this process is low, the locking bandwidth increases slowly with the locking strength μ. Thus it is difficult to observe it for low driving forces. For example, we do not detect any response at $\frac{f_s}{3}$ for $\mu < 0.2$.

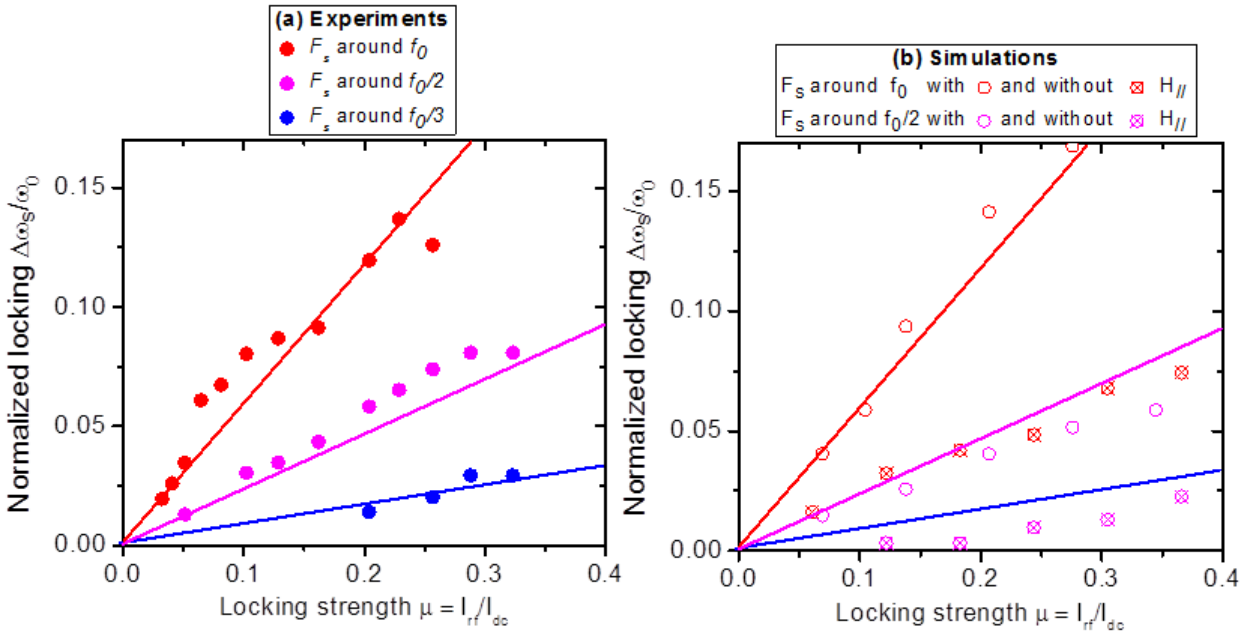

FIGURE 4.20: Excitation bandwidth at $\frac{f_0}{3}$, $\frac{f_0}{2}$, and f_0 as a function of the locking strength μ: (a) Experiments and (b) Matlab simulations $H_{||} = 4kA/m$ and $H_{||} = 0$) ($\varnothing$ = 300 nm)

The same behaviors are observed in our Matlab simulations at zero applied field as shown in Fig. 4.20.b. For a vortex based STO similar to the experimental case, we note that there is no threshold in the response at $\frac{f_0}{2}$. Furthermore, we do not get any response if we switch off the ST

forces. These different observations confirm that the excitation process is mainly driven by an effect of superharmonic resonance and not by a parametric excitation driven by the oscillating Oersted field. However, we get a quantitative agreement with our experiments for F_s around $\frac{f_0}{2}$ or around $2f_0$ only in presence of a small in-plane field (similar to the experimental SAF stray field). This means that the process of excitation combines two mechanisms, i.e a classical resonant effect amplified by a parametric effect.

We also want to point out that with our Matlab code, we get a response at $\frac{f_0}{3}$ only for an unrealistic locking strength of 0.6 (not represented in Fig. 4.20) and only in presence of a small in-plane field. This behavior must be related with the fact that our model only takes into account the second order of nonlinearities. Taking into account the higher order of nonlinearities should be necessary to fit more precisely with our experiments. Nevertheless, the good agreement in the response at $\frac{f_0}{2}$ and at f_0 already represents a clear evidence of superharmonic resonance assisted by parametric amplification. Such phenomenon had never been reported in magnetic systems and it will open new perspectives for spin-torque oscillators.

In summary, we achieved phase locking of a vortex based STO with an rf-current at multiple integers, as well as half and third integer frequency. In the locked state, we reported a record minimum phase noise of -90 dBc/Hz at 1 kHz offset with a large output power ($> 1\mu W$). With time domain measurements, we improved our understanding of the locking behavior and of its stability. We developed an analytical model that indicates that the locking process of a vortex based STO is controlled through different sources of spin-transfer locking torques, i.e the Slonczewski and Field-like in-plane torques. By fitting our experiments, we highlighted the crucial role of the Field-like in-plane torque in the locking process.
We then showed that an rf-current can excite a forced excitation of a vortex based STO in the damped regime either at multiples or at fractions of the gyrotropic frequency. With frequential measurements and analysis based on Thiele equation, we demonstrated that the mechanism of excitation relies on both parametric amplification and normal resonance. Finally, we observed, for the first time, the presence of superharmonic resonance in a STO.
Finally, vortex based STOs in magnetic tunnel junction can easily synchronize with an external rf-current thanks to large Field-like torques. In Chap. 6, this high efficiency of the locking process will help us to probe the coupled motion of two vortices and to observe exotic dynamics associated to the locking of both damped and excited coupled modes.

Chapter 5

Limitations of the "single mode" hypothesis

Spin-torque oscillators generally present one single mode excited by spin-transfer. Indeed, the spin-transfer process first excites the lowest mode in energy that can become unstable. As we previously discussed, the dynamics of the excited mode is well described by the auto-oscillator model [45]. Nevertheless, different studies reported the presence of multi-mode generation in uniform STOs, with either mode hopping or mode coexistence [101, 166]. The coupling between those modes can be driven by different parameters (current and field [65, 167], noise [168]). Theoretical extention of the auto-oscillator model with more than one mode have permitted to fit well the experimental observations but the physical origin of the coupling often remains unclear [101]. For example, the inter- or intra-layer mode coupling have been reported to lead to really different features such as linewidth enhancement or reduction [69, 101, 109, 169]. Only recently Iacocca et al. [170] explained, in the limit of equally excited mode by ST torque, these different behaviors through different coupling regimes, either mode hopping or mode co-existence. However the direct observation of different coupled modes is often difficult to perform so that strong hypotheses are needed to model the mode-coupling mechanisms.

In this specific chapter, we highlight the limitations of the single mode approach in double vortex based STOs. We first focus our study on the coupling mechanism at harmonic mode crossings that we reported to strongly impact the spectral coherence of the STO [69]. By time domains measurements, we identify with precision the parameters that drive the coupling between modes and show the strong impact of mode coupling on the effective damping of the different modes. Then, we present, for the first time, a direct and simultaneous observation of two inter-layer coupled modes, one damped and one excited by ST torque. We highlight that mode coupling can lead to self-resonant excitation in a single isolated STO. Then we use

an external rf-source to demonstrate that we can control with precision the coupling between modes and that it can lead to exotic phenomena such as the annihilation of the excited mode, the overlapping of two locking bandwidths and potentially chaotic behavior.

5.1 Energy transfer between coupled modes

5.1.1 Mode crossing at multiple harmonics

In double vortex based STOs in spin-valve, we recently highlighted in a study performed in collaboration with CEA SPEC [69] that the dynamics of the excited mode could be strongly affected by the interaction with the damped mode. At harmonic crossings between the damped and the excited mode ($nF_{damp} = mf_{exc}$ with m and n integers), a strong increase of the linewidth of the excited mode is observed (see Fig. 5.1.a). In parallel, we notice a softening of the frequency dependency with field as shown in Fig. 5.1.b. This behavior has been attributed to the transfer of energy from one mode to another.

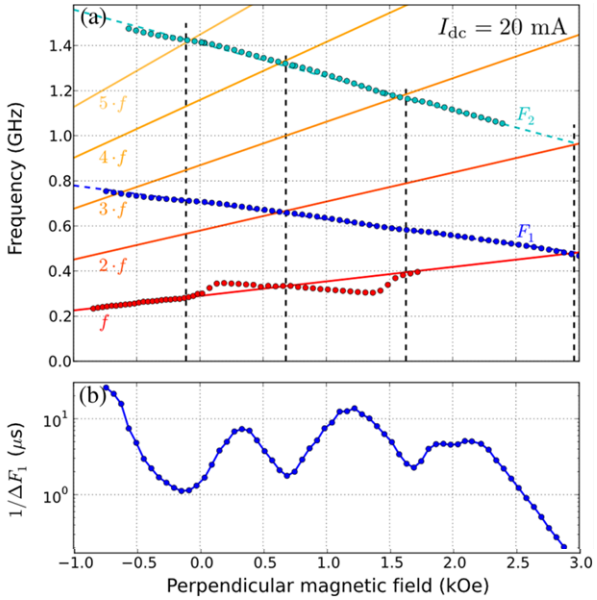

FIGURE 5.1: Blue dots: fundamental frequency F_1 and harmonics F_2 of the auto oscillating mode dominated by the thick layer (vortex core polarity p_B = -1) as a function of the perpendicular field. Red dots: frequency f of the overdamped mode dominated by the thin layer (polarity p_A = +1). Red tone straight lines are guides to the eye and show successive harmonics of f. (b) Evolution of the inverse generation linewidth. Adapted from [69]

Such exchanges of energy have been reported in other magnetic or non-magnetic systems [171, 172] having several eigenmodes. When the mode frequencies cross each other, some energy is transferred from one mode to another [173–176]. In the case of STOs, if one of these modes is excited by spin-transfer, the transfer of energy is generally from the excited mode to the damped

mode which facilitates the dissipation of energy. The mode interaction can be mediated either by spin-waves [60], dipolar [69, 72, 175–177] or electrical coupling [83]. In the dynamics of double vortex based STOs, the interaction between the two coupled modes is mediated either through a dipolar coupling between the vortex bodies and/or an electrical coupling due to reciprocal ST forces.

The coupling strength depends on the frequency (i.e energy) difference between modes. To reduce the mode interaction, STOs should thus operate at the largest gaps in energy, i.e far from harmonic crossings (as we did in the previous chapters), between excited and damped mode. Far from mode crossings, the hypothesis of a single excited mode is valid and we can use the auto-oscillator model. On the contrary, the hypothesis of a single excited mode is probably less or even not valid at the crossings when there is a large transfer of energy from one excited mode to other damped modes. Furthermore, the physics associated to the interaction between coupled modes still remains an open question that can lead to new phenomena such as chaotic behavior [81, 178–180].

5.1.2 Correlation between mode parameters and energy exchange

In the literature, several groups [65, 69, 101, 101, 109, 166–169] have tried to understand the dynamics of coupled modes in STOs but numerous questions still remain open as it is often difficult either to identify the different coupled modes or to access separetely their properties. Among these studies, Iacocca et al. [101, 170] theoretically demonstrated that the auto-oscillator model could be well adapted to mode interaction. However such theoretical predictions are often difficult to perform given the large number of unknown and adjustable nonlinear parameters for the different modes. Experimentally, the excited mode can either present an increase [169] or a decrease [69, 181] of the linewidth at the crossings of harmonics. From all these studies, it appears that the mode interaction is mediated by a modification of damping and thus of the effective damping ratio of the coupled modes. Here, we try to understand in more details, with time domain measurements, the coupling mechanisms at harmonic crossings in a double vortex based STO.

We focus our study on samples B (see Appendix A) where the excited thin vortex layer is close to the MgO barrier so that the emitted power associated with the excited mode is large. In APc configuration, we observe oscillations of the linewidth (from 200 kHz to 7 MHz) due to harmonic crossings ($f_{exc} = f_{damp}/2$ and $f_{exc} = f_{damp}/3$ in Fig. 5.2). In parallel, we note that f is globally linear with the applied field H_{perp} but that some frequency softenings appear at harmonic crossings (see Fig. 5.2.b). These softenings of df/dH_{perp} correspond to the new frequency dispersion curve due to the interaction between modes [173]. In Fig. 5.2.c, we notice

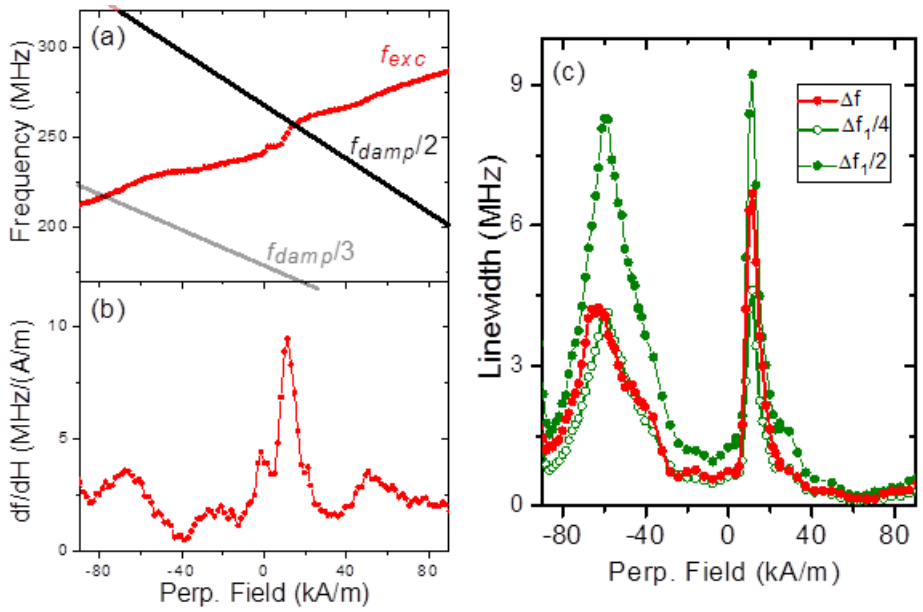

FIGURE 5.2: (a) Evolution of the frequency of the excited mode with field (b) Derivation of the frequency with field (c) Corresponding linewidths for the fundamental (Δf) and the first harmonic (Δf_1 divided by 2 and 4)

from the analysis of harmonics (used to evaluate the nonlinear parameters as seen in Chap. 3) that the STO seems to have a quasi-linear behavior in the all field range as the linewidth of the first harmonic Δf_1 is close to four times the linewidth of the fundamental $4\Delta f$.

In Fig 5.3, we display the evolution of the nonlinear parameters with I_{dc} for four different perpendicular fields: either close (-55 kA/m, black dots), far (-15 kA/m, green dots) or between (-48 kA/m and - 30 kA/m, red and orange dots) two crossings. The parameters ν, Δf_0 and Γ_p are extracted from the diagrams of phase and amplitude noise. The nonlinear frequency shift $N = d\omega/dp$ is extracted from $d\omega/dH_{perp}$ and dp/dH_{perp} (as $d\omega/dp = d\omega/dH_{perp} \times dH_{perp}/dp$). First, we can notice that the different nonlinear parameters globally present a quasi-linear dependence with I_{dc} for the different field conditions as expected in the auto-oscillator model. Only the linear linewidth Δf_0 first decreases with I_{dc} and then slightly increases far from the crossing (-15 kA/m) and at high surcriticalities ($I_{dc} > +10$ mA). Similar behavior was observed in a single vortex STO by E. Grimaldi [48] and it may correspond to a change in the vortex structure.

Nevertheless, if we focus our analysis for $I_{dc} = +11$ mA (the case represented in Fig. 5.2), we notice that the nonlinear dimensionless parameter ν is non-zero for all the range of fields as we would have not expected from the analysis of the harmonic linewidths. This confirms, as we noticed in Chap. 3, that we have small but non-zero ν for double vortex based STOs in the APc configuration.

We note that the linear linewidths Δf_0 and the nonlinear frequency shifts N do not depend on the fields at I_{dc}=+11 mA . On the contrary, the nonlinear dimensionless parameter ν and the

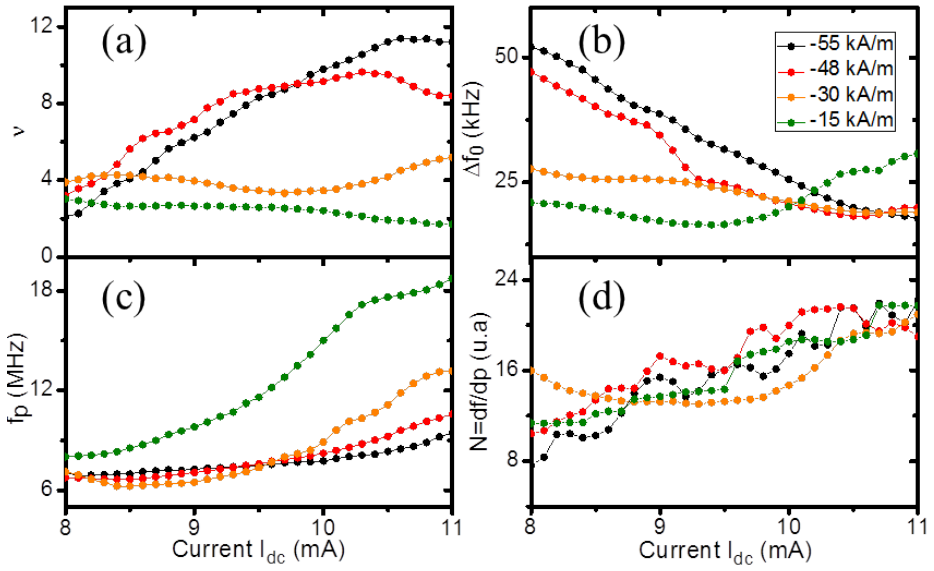

FIGURE 5.3: Nonlinear parameters dependency with current for four different fields: nonlinear dimensionless parameter ν (a), the linear linewidth Δf_0 (b), the effective damping Γ_p (c) and the nonlinear frequency shift N (d). The different fields are either close (-55 kA/m) or far (-15 kA/m) from an harmonic crossing.

effective damping Γ_p take completely different values for the four values of fields. They present higher ν and Γ_p close to the crossing of the harmonics (at -55 kA/m).

Moreover, we experimentally found that the critical currents are larger close to the harmonic crossings (+8 mA at -55 kA/m against +7 mA at -15 kA/m). Combined with the lower effective damping at harmonic crossings, it indicates that the exchange of energy between modes can be modelled by an extra-damping term α that affects the dynamics of the excited mode [182]. This extra-damping term $\alpha_{coupling}$ leads to a decrease of the effective damping ratio Γ_p close to the harmonic crossings.

This non-intuitive deduction comes from the fact that the effective damping ratio is defined as $\Gamma_p = (d\Gamma_-/dp - d\Gamma_+/dp)p_0$ (see Chap. 1 and Ref. [48, 183]). Thus it can be expressed as $\Gamma_p = (\xi - 1)\Gamma_G$ with ξ the surcriticality and Γ_G the damping force. Given that ξ is inversely proportionnal to α and Γ_G is proportional to α, the effective damping ratio is thus proportionnal to $A - B\alpha$ and not directly to α. As a consequence, the effective damping ratio Γ_p thus decreases when the damping increases.

In our experiments, the enhanced damping α at the harmonic crossings leads to larger threshold currents and thus to lower surcriticalities ξ, which in turn induces a lower effective damping. This lower effective damping ratio at harmonic crossings explains why the lowest linewidths are observed far from the crossings given that the linewidth is defined as $\Delta f = (1 + \nu^2)\Delta f_0 = (1 + (Np_0/\Gamma_p)^2)\Delta f_0)$. The fact that M. Romera [182] observed lower linewidths at harmonics

crossings may be correlated to a strong softening of the nonlinear frequency shift $N = df/dp$ that leads to larger ν parameters.

In summary, we identify the effects of mode coupling on the dynamics of a mode excited by ST torque that interacts with a damped mode. In particular, we highlight that the transfer of energy from one mode to another modifies the damping of the excited mode.

5.2 "Resonance" of damped modes

To analyze in more detail the mechanisms of energy exchange, a direct observation of both the damped and excited modes is required. In this section, we study sample A (see Appendix A) for which both the excited and the damped modes can be detected simultaneously as seen in Fig. 5.4 (see also Chap. 3). We perform our study for vortices with parallel chiralities and anti-parallel core polarities (APc) in the autonomous and non-autonomous regimes.

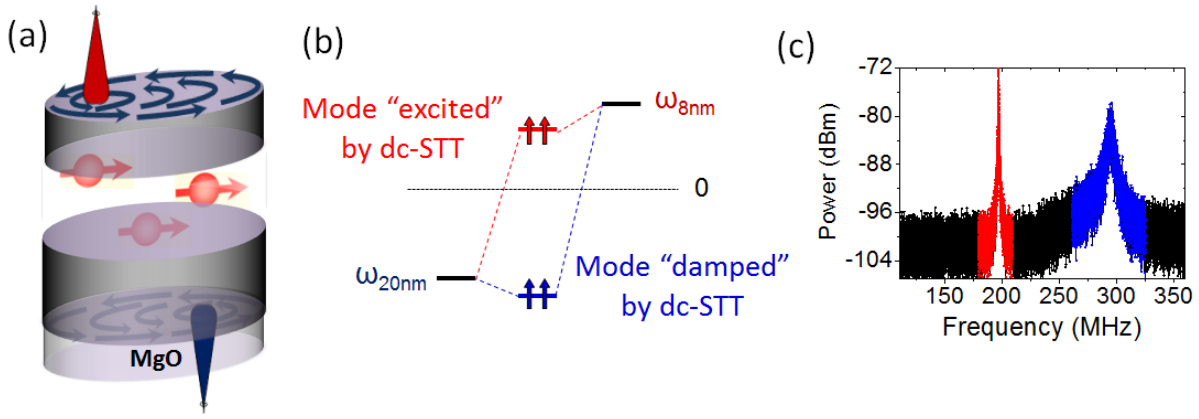

FIGURE 5.4: (a) Schema of the vortex configuration and (b) of the mode degeneracy in APc configuration with parallel chiralities. (c) Example of a detected spectrum for a double vortex based STO (Ø = 600 nm) for which we probe the dynamics of the thick vortex layer with a MgO barrier above a SAF layer (see "Sample A" in the Appendix A)

5.2.1 Self-resonance in the autonomous regime

In Fig. 5.5, we plot the evolution of the frequency of the excited and the damped modes as a function of H_{perp} for $I_{dc} = -14.5$ mA. One striking feature is the" synchronization of the damped mode" with the excited and self-sustained mode for F_{damp} around $3/2f_0$. At this harmonic crossing, both mode frequencies soften as seen in Fig. 5.5.a. In particular, the frequency of the damped mode adapts its frequency to follow the frequency of the excited mode[1]. This observation highlights that we force the dynamics of the damped mode through

[1]Similar features have been observed in double vortex based spinvalves for $F_{damp} = 1/2f_0$ with a MRFM setup to probe the dynamics of the damped mode

an internal process of self-resonance with an excited mode in an STO without any external rf-signal. This process can be mediated through spin-transfer [69, 72] and/or dipolar [173] interaction. It must also be emphasized from the time domain measurements in Fig. 5.5.d-f that the two modes coexist without any mode hopping between them in the all range of field.

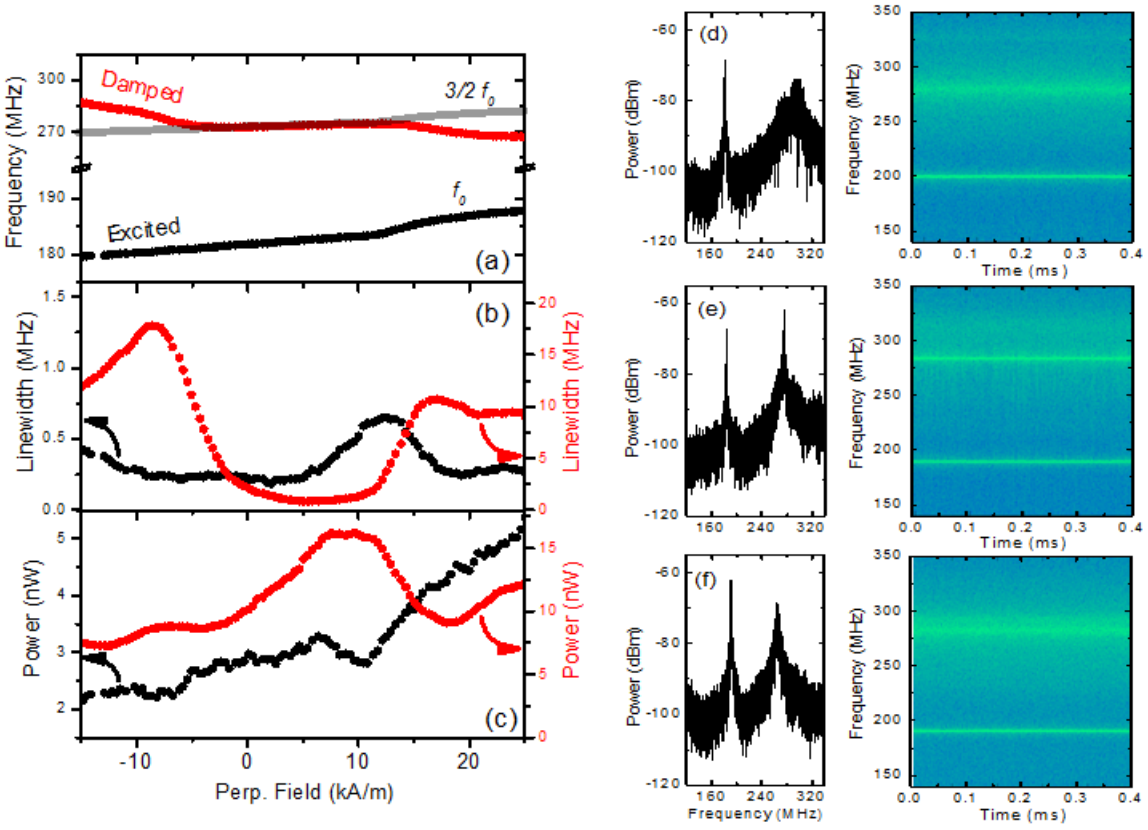

FIGURE 5.5: Evolution with field of the frequencies (a), linewidths (b), powers (c) of both the excited (black dot) and damped (red dots) modes. Power spectrum and instantaneous frequency time traces for three value of fields: -10 kA/m (d), 3 kA/m (e), 20 kA/m (f) (I_{dc} is fixed to -15 mA)

In this forced regime, the spectral coherence of the damped mode is strongly enhanced. The minimum linewidth is of 800 kHz at 5 kA/m, close to the 350 kHz of the excited mode as seen in Fig. 5.5.b. This feature indicates that the "damped" mode enters in a steady state in this region of field. Consequently, the emitted power of the "damped" mode is also enhanced. However it cannot be quantitatively correlated to the power decrease of the excited mode given that this mode is mainly located in the top thin layer (for "Sample A", we probe the dynamics of the bottom thick layer through the MgO barrier as presented in Chap. 3).

Contrary to the case of uniform STOs in nanocontacts [101, 170], the linewidths of the two coupled modes do not evolve as a function of the coupling strength (maximum at harmonic crossings) in our regime of mode co-existence. In Ref. [170], the two modes are assumed to be equally excited by ST torque while in our case, one mode is damped by ST torque while the other one is excited by ST torque. Here we even notice that the variations of linewidths of

the two coupled modes are not directly correlated between them. The linewidth of the excited mode decreases as the power of the damped mode increases as seen in Fig. 5.5. This is coherent with the fact that the transfer of energy from the auto-oscillating mode to the "damped" mode leads to an enhancement of the linewidth of the excited mode. The linewidth of the "damped" mode is minimum at the center of the "self-resonance" bandwidth and maximum at the edges as it is the case in injection locking experiments due to the effect of frequency pulling [51]. The rf-features of the two coupled modes are thus sensitive to the transfer of energy between them but also to the fact the dynamics of one mode is enslaved by the second one.

5.2.2 Forced resonance in the non-autonomous regime

In this section, we demonstrate that the mode coupling between the damped mode and the excited mode can be controlled with an external rf-current. Such a precise control can lead to more exotic effects such as the presence of multiple lockings ranges, the annihilation of the excited mode, or the overlapping of two locking bandwidths and even chaotic behaviors.

As in Chap. 4, the Slonczewski and Field-like ST torques from the SAF can synchronize the dynamics of our STO. In sample A, the layer close to the MgO barrier is the thick permalloy layer. Thus the locking process will drive the STO through the dynamics of the bottom thick vortex layer. The rf-current directly affects the thick layer and can thus simultaneously synchronize the excited mode that is delocalized in the bottom thick layer and resonantly excite the damped mode mainly localized in thick laye. In this mode competition, two parameters are crucial: the amplitude of rf-current and the frequency detuning.

5.2.2.1 Overlapping of locking bandwidths

We first consider a double vortex system under the conditions for which we can clearly observe the excited mode (f_0 = 215 MHz in Fig. 5.7.e) but barely the damped mode (F_{damped} = 390 MHz in Fig. 5.7.e) on our spectrum analyzer. There we perform injection locking experiments at an rf-frequency F_s around twice the eigenfrequency of the excited mode $2f_0$ for different levels of rf-current.

In Fig 5.6.a-e, we note that a single locking range for F_s around $2f_0$ (around 430 MHz) is observed at -18 dBm. At -12 dBm, we surprisingly notice the appearance of a second locking range at lower driving frequency F_s (around 400 MHz). The bandwidth of this second locking increases with I_{rf}. In this locking range, the STO still adapts its frequency at half the driving frequency. The position of this second locking range corresponds to the region for which we expect to have a resonant excitation of the damped mode (F_s around F_{damped}). From this

observation, we deduce that the rf-current resonantly excites the damped mode and that the excited mode adapts its frequency to synchronize with the forced oscillations of the damped mode.

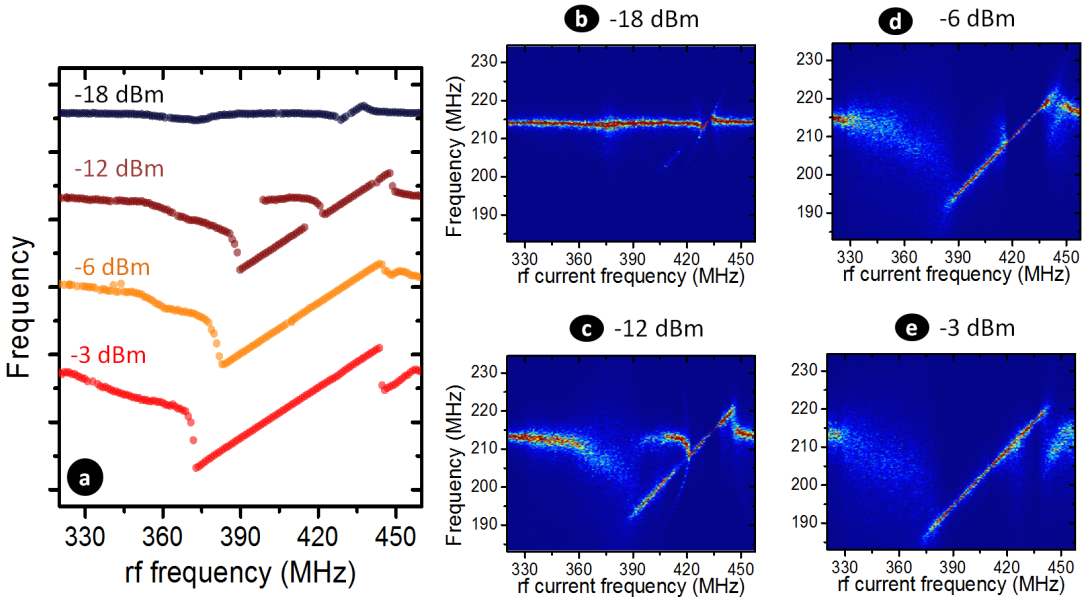

FIGURE 5.6: (a) Evolution of the locking bandwidth for F_s around $2f_0$ at different amplitude of rf-current (b-d)

In the second locking range ($F_s \approx F_{damped}$), the system is highly frustrated between one mode (f_0) that is favored by the dc ST torque and another mode (F_{damped}) favored by the rf ST torques. Indeed, the senses of gyration for each mode are opposite given that the two vortices have opposite polarities (and each mode is mainly driven by one of the two vortices). Thus this second locking state is less stable and its corresponding linewidths are higher than for $F_s \approx 2f_0$ as seen in Fig. 5.7.a. The linewidths are thus larger in this second locking state, and the time traces also present more phase slips than in the first locking state (see Fig. 5.6.b compared to Fig. 5.6.d).

One should also notice that the locking range associated to the fundamental resonance of the damped mode (around F_{damped}) increases more quickly with the amplitude of the rf-current (see Fig. 5.6 and Fig. 5.7.a). This highlights that the fundamental resonance of the damped mode F_{damped} is a more efficient process than the one associated with the excited mode for $F_{damped} \approx 2f_0$. This thick layer mediated locking of the excited mode offers news possibilities to enhance the locking range of a STO far from its fundamental locking.

Interestingly, the two locking regions ($F_s \approx F_{damped}$ and $F_s \approx 2f_0$) are close and can even merge for large rf-current (-6 dBm and -3 dBm in Fig. 5.6.d-e). At the intersection of the two locking ranges, we measure an increase of the linewidth (see inset of Fig. 5.7.a) and many more phase slips as seen in Fig. 5.7.c. In this region, the phase slips are π and 2π (see Fig. 5.7.c)

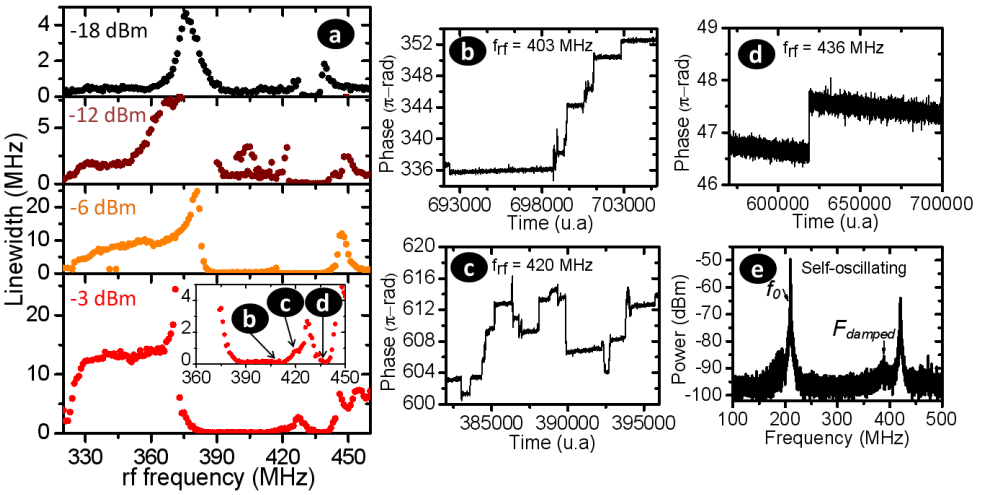

FIGURE 5.7: (a) Linewidth of STO as a function of the rf-frequency for different rf-amplitudes (b-d) Example of time traces for different frequency of rf-current (in the two different locking ranges and in the region of overlap) at -3 dBm. (e) Power spectrum in the self-sustained state. The experimental conditions are : $H_{perp} = 205$ kA/m, $I_{dc} = -15$ mA, and the dot diameter is of 600 nm.

while they are 2π in the first locking region (see Fig. 5.7.b) and π in the second one (see Fig. 5.7.d). Such a "frustrated" response shows the strong instability of the STO in the overlapping region and probably indicates the presence of a chaotic behavior [180]. Theoretically, it was demonstrated that the response of an oscillator in the overlapping region corresponds to erratic jumps between the different locking states [81, 178].

In this specific chapter, we demonstrated that the dynamics of a double vortex based STO cannot be fully described in the single mode approach. In a double vortex based STO, we showed that the mode interaction at harmonic crossings leads to a large energy transfer from the excited mode to the damped mode of the coupled vortex system. This energy transfer increases the damping associated with the excited mode, reducing its power and its spectral coherence. For some certain experimental conditions, we even reported the possibility of resonantly exciting the damped mode because of the action of the excited mode. The STO can thus be self-resonantly excited. Finally, we demonstrated that the two coupled modes of the system can be excited with an rf-current. At large rf-excitation, the locking bandwidths of the two coupled modes overlap so that we simultaneously excite the two coupled modes. This leads to an complex and incoherent motion that may correspond to a chaotic behavior.

Part III

Spin-torque oscillators for rf-nanodevices

Chapter 6

Towards spintronic rf-nanosources by the integration of STO in phase locked loop

A phase locked loop (PLL) consists of an electronic circuit with a controllable oscillator (generally a VCO, voltage controllable oscillator) whose phase is constantly adjusted to match with the frequency of a reference input clock. A phase locked loop permits the reduction of the phase difference between a reference signal and a local oscillator by using a feedback loop. This type of device, first developed in 1932 by de. Bellescize [184], is currently widely use for various rf-applications such as frequency demodulators, stable frequency generators at multiples of the input frequency or as a frequency distributors in microprocessors.

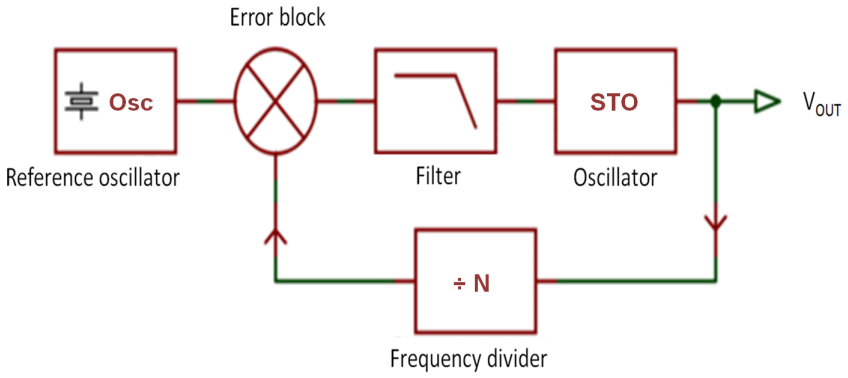

FIGURE 6.1: Schema of a phase locked loop. The PLL consists in a error detector block, a frequency divider, a filter, a slave oscillator (here a STO) and a reference oscillator (see Appendix C for details about each block).

In this chapter, we present the concept of an STO based phase locked loop (see Fig. 6.1, more details about classical phase locked loops can be found in Appendix C). Recently, different

studies have demonstrated the potential of this type of device for reducing the phase noise of an STO [146, 147]. Here, we show preliminary results for an on-chip phase locked loop with our vortex based STO. This on-chip phase locked loop has been developed by M.Kreissig from TUD (Dresden) within the EU project MOSAIC coordinated by U. Ebels.

6.1 Expectations for spintronic based phase locked loops

The specific advantages of STOs compared to classical VCOs, such as their small size and radiation hardness, have created significant interest in STO based phase locked loop. One could argue that the size of the loop is often much more limiting than the size of the STO in our case. However, as we mentioned, one potential application could be a phase locked loop that drives at long distance multiple STOs and acts as a frequency distributor in which the size of the local oscillators is crucial. Furthermore, for space system applications, the main advantage of STOs is not their size but their resistance to electromagnetic radiations.

The theoretical background of a phase locked loop is well-known for many years (see Appendix C). In this section, we briefly report the characteristic of an STO based phase locked loop depending on the characteristics of the loop and of the STO. The oscillator dynamics can be well described in the auto-oscillator framework by adding a modulating feedback current ΔI [185]:

$$\frac{dc}{dt} + i\omega(|p|)c + [\Gamma_+(|p|) - \Gamma_-(I + \Delta I)]c = 0 \tag{6.1}$$

with $\Delta I = \epsilon K(p)F(\Delta\Phi)$, $\epsilon = \Delta I/I_0$, $\omega(|p|)$ the STO eigenfrequency, $K(p)$ the filter transmission coefficient, $F(\Delta\Phi)$ the normalized feedback signal of the phase detector and $\Delta\Phi$ the phase difference between the STO and the reference oscillator. One should also notice that the retroaction force corresponds to a modulation of the dc spin-transfer force that drives the self-sustained oscillations. Thus the feedback force acts only on the amplitude of the STO.

By considering no spurious peaks and no loop instability, A. Mitrofanov et al. [185] recently studied the loop characteristics of an ideal filterless ($K(p) = 1$) PLL with a phase detector $F(\Delta\Phi) = \sin(\Delta\Phi)$. The phase detector provides a signal that corresponds to the low frequency component of a frequency mixer. Such an ideal case permits the identification of the STO parameters that may limit the functioning of the phase locked loop (if the filter itself is not the limiting aspect).

Here we do such a study for a vortex based STO. Contrary to uniformly magnetized STOs [185], the vortex based STO has a linear anti-damping torque Γ_-. For such a case, we derive

the expressions of the normalized power p and of the phase shift Φ_0 between the phases of the driving current and of the STO in the locked state:

$$\begin{cases} p = p_0 \left(1 + \frac{p_0 f_{pll}}{\Gamma_p} \sin(\Phi_0)\right) \\ \Phi_0 = \arcsin\left(\frac{2\Delta\omega}{\nu f_{pll}}\right) \end{cases} \tag{6.2}$$

$\Delta\omega = \omega_0 - \omega_{ref}$ (or $N_{div}\omega_{ref}$ if a frequency divider is considered, with N_{div} the number of division) is the frequency detuning, p_0 is the normalized power, ν is the nonlinear dimensionless parameter, and $f_{pll} = \Gamma_-(I)\epsilon$ is the normalized locking force.

From Eq. 6.2, we can obtain the expression of the PLL bandwidth that strongly depends on the nonlinear behavior of the STO:

$$\Delta\omega_{band} = 2\nu f_{pll} \tag{6.3}$$

Then we derive the expressions of the noise power spectral density for the PLL locked vortex based STO in presence of thermal fluctuations:

$$\begin{cases} S_{\delta p} = \frac{\Delta f_0}{\pi} \frac{\left(\frac{f_{pll}}{2\pi}\sin(\Phi_0)\right)^2 + f^2}{\left[f^2 + \nu f_p \frac{f_{pll}}{2\pi}\sin(\Phi_0)\right]^2 + f^2\left(f_p + \frac{f_{pll}}{2\pi}\cos(\Phi_0)\right)^2} \\ S_{\delta\phi} = \frac{\Delta f_0}{\pi f^2} \frac{f^2\left[\nu^2 f_p^2 + \left(f_p + \frac{f_{pll}}{2\pi}\cos(\Phi_0)\right)^2\right] + f^4}{\left[f^2 + \nu f_p \frac{f_{pll}}{2\pi}\sin(\Phi_0)\right]^2 + f^2\left(f_p + \frac{f_{pll}}{2\pi}\cos(\Phi_0)\right)^2} \end{cases} \tag{6.4}$$

Due to the amplitude/phase coupling, both amplitude and phase noise are strongly reduced by the effect of the PLL although the feedback force acts only on the oscillator amplitude. The noise levels are reduced down to the level of noise that corresponds to the retroaction times of the PLL. For large driving amplitudes, one should notice that the phase and amplitude noises are reduced for offset frequencies higher than the effective damping ($\Gamma_p = \pi f_p$) as represented in Fig. 6.2. We can thus conclude that the effective damping is not a direct limitation for the development of an STO based phase locked loop.

6.2 Experimental development

In this section, we present a short state of the art of PLL experiments with a STO and then some preliminary results obtained for a vortex based STO with the on chip phase locked loop developed in TUD.

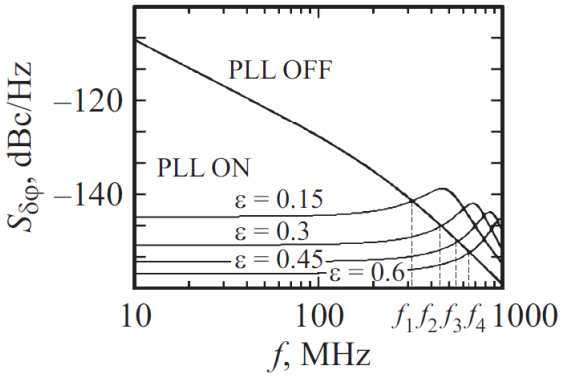

FIGURE 6.2: Phase noise spectral density of a PLL locked STO for different amplitudes of current feedback. (Adapted from [185])

6.2.1 State of the art on STO based PLLs

In 2009, Keller et al.[147] from the NIST in Boulder performed the first experiments with a STO based PLL. With a commercial PLL of a 1 MHz bandwidth and a single vortex based STO, they could observe a drastic reduction of the linewidth (by a factor 80, from 780 kHz down to 10 kHz) in the PLL locked state as shown in Fig. 6.3. However they couldn't observe any reduction of phase noise with time domain measurements (probably due to a limited oscilloscope memory as mentioned).

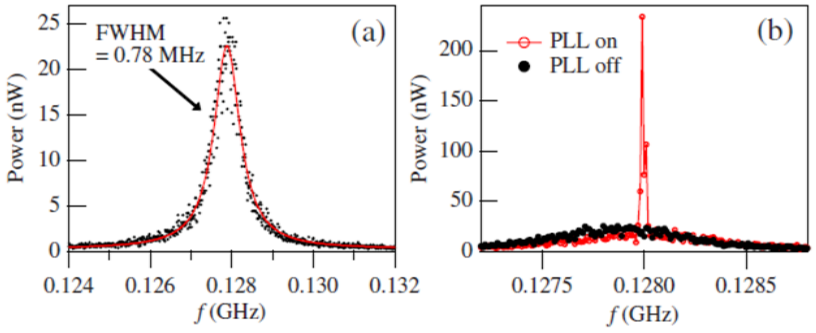

FIGURE 6.3: Spectrum analyser measurements of amplified STO signal (a) PLL OFF with a lorentzian fit (b) PLL ON, with same data as in (a) for comparison. (Adapted from [146])

Recently, similar studies have been done with uniform based STOs in AIST in Tsukuba, Japan. S. Tamaru recently demonstrated [146] for short time traces that the linewidth of a 5 GHz uniform STO could be reduced down to 1 Hz in the PLL locked state, with an associated record quality factor of 5e9 (see Fig. 6.4). For longer time traces, they still observe the presence of phase desynchronizations.

Similarly to Keller et al.[147], they use a PLL with a bandwidth of a few MHz. Such features are quite unconventional compared to the usual rf-applications based on phase locked loops. Generally, the PLL bandwidth is between a few kHz and a few hundreds of kHz. Indeed large

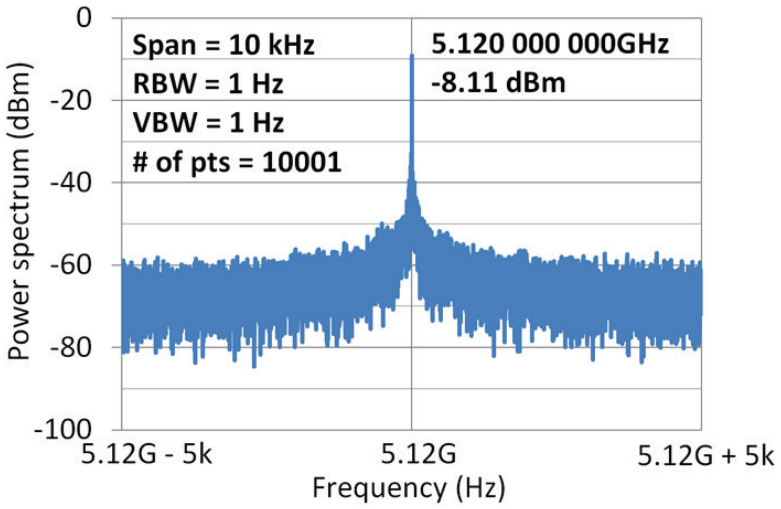

FIGURE 6.4: Spectrum analyser measurement of an amplified STO locked in a PLL with a 80 MHz reference clock (Extracted from [146])

PLL bandwidths often lead to the presence of detrimental spurious noises. However the poor spectral coherence of STOs, compared to the classicaly used VCOs, requires the use of a large bandwidth PLL in order to observe a real increase of the spectral coherence in the locked state. To go beyond these preliminary and promising results, there is thus a real challenge to develop a phase locked loop that precisely fits with the specific features of STOs.

6.2.2 CMOS integrated PLL for vortex based STOs

The development of a CMOS integrated STO based PLL requires a collaboration between research groups from both spintronic and conventional electronic domains. Due to technical problems, the final development of CMOS integrated PLL for a vortex based STO is still under development in Dresden. However preliminary and promising results could already be obtained with the first generation of PLL. As shown in Fig. 6.5.a, the idea is to combine the local oscillator, the phase locked loop with the amplifiers and the reference oscillator on a single micro-chip.

With this first generation of CMOS PLL, we could lock the STO with the reference signal and obtain a maximum phase noise reduction of -40 dBc/Hz on a 100 kHz bandwidth from the carrier frequency as shown in Fig. 6.6. In this experiment, the STO carrier frequency is equal to 406 MHz, the reference clock has a 25.4MHz frequency and the dividing ratio of the PLL N_{div} is equal to16. However, we couldn't observe locking bandwidths larger than 100 kHz although the PLL bandwidth had been designed to be tuned up to 1 MHz. Similar tests on VCOs are undergoing to identify the origin of this discrepancy between our experiments and the theoretical expectations.

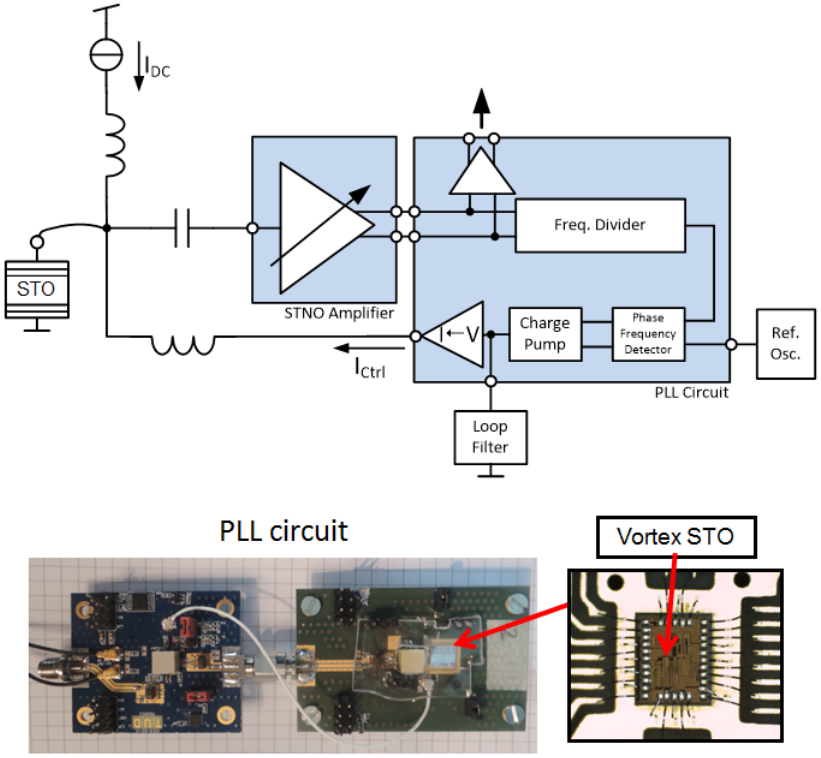

FIGURE 6.5: (a) On Chip STO based phase locked loop. The STO is directly connected on the chip. The STO signal is first amplified by a 40 dBm amplifier and its frequency divided by flip-flop logic. Then the signal is compared with a reference oscillator (either a quartz or a pulse generator), the error signal integrated with a charge pump and filtered with a low pass filter.

One can also notice that the expected presence of periodic kicks on the STO phase in the inset of Fig. 6.6.b. These kicks correspond to the action of the PLL that periodically corrects the phase dynamics and reduces the STO phase deviation. The frequency of these kicks corresponds to the PLL bandwidth.

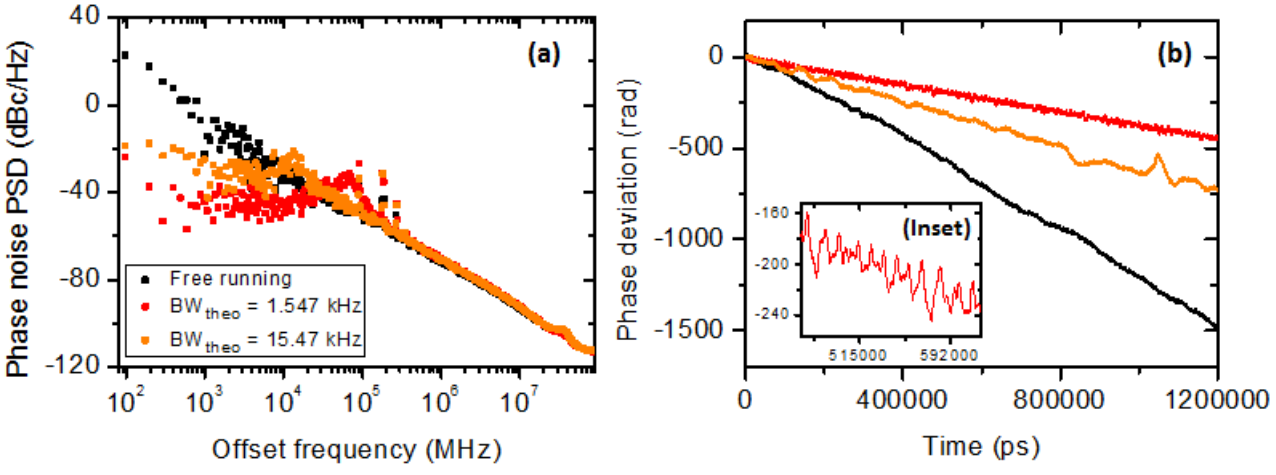

FIGURE 6.6: (a) The noise of the free and the PLL locked STO (b) Corresponding phase deviations during time. Inset: phase deviation of the best locking conditions for which we see the periodic kicks due to the feedback of the PLL (The frequency of the free running STO is 406 MHz and its linewidth 2.5 MHz)

In this short chapter, we have shown how the development of STO based phase lock loops could permit the drastic reduction of the phase noise for this type of nanoscale oscillator. We aimed at demonstrating that it is possible to develop STO based CMOS integrated phase locked loops. We believe that these first results give an interesting outlook for potential rf-applications based on spintronic phase locked loops (such as a frequency distributor or a STO based associative memory driven by a PLL [186]).

Chapter 7

Efficient rf-detection by a resonantly excited vortex based STO

7.1 Spin-diode based rf-detection in spin-transfer nano-oscillator

In 2005, Tulapurkar et al. [90] observed the generation of a spin-torque rectification voltage in a STO excited at its eigenfrequency by an rf-current. This rectified voltage is the result of the mixing between resistance and current oscillations. Since this pioneering work, several studies [91, 95] have confirmed that STOs could be considered for the field of high frequency detection as their sensitivity already exceeds the conventional Schottky diode [91].

In this chapter, we first introduce the concept of spin diode and develop an analytical model for the case of vortex based STOs. Then, we experimentally, in particular in the postdoc of A. Jenkins, study the spin-diode response of a single vortex based STO ("sample C" in Appendix A) excited by a rf-current. At large amplitudes of rf-currents, we find that the rf excitation can result in an expulsion of the vortex core from the junction and thus a change of the magnetic configuration inducing a change of the resistance state due to the effect of the magnetoresistance. We thus propose a new rf-detection scheme based on the reversible change of resistance. In a second part, we demonstrate that vortex based STOs can cover a wide range frequency as expected for rf-detectors. We show that we can control the magnetic configuration (polarity and chirality) of vortex based STO with an rf-current. Finally, we report a high rectification voltage for a rf-excitation above 2 GHz in a magnetic tunnel junction with two strongly coupled vortices. Thus, we take advantage of mode coupling to develop a high frequency detection scheme based on vortex based STOs.

7.1.1 Concept of spin-diode

When a spin-polarized rf-current is applied at the free layer eigenfrequency of a spin-torque oscillator, it can induce forced oscillations of the magnetization and thus the emission of an rf-signal driven by the reference signal as we have seen in Chap. 4. Nevertheless, another phenomenon called the spin-diode effect can simultaneously be observed. When an STO is resonantly excited by an rf-current, it is possible to measure a rectification voltage at its terminals [90]. Indeed, the forced oscillations of resistance can be either in-phase or out-of-phase with the injected rf-current. Thus the mean voltage can be non-zero depending on the dephazing between the oscillations of the STO's resistance and the rf-current (see Fig. 7.1). The name of spin-diode was then choosen in reference to the rectification effect in standard electrical diodes.

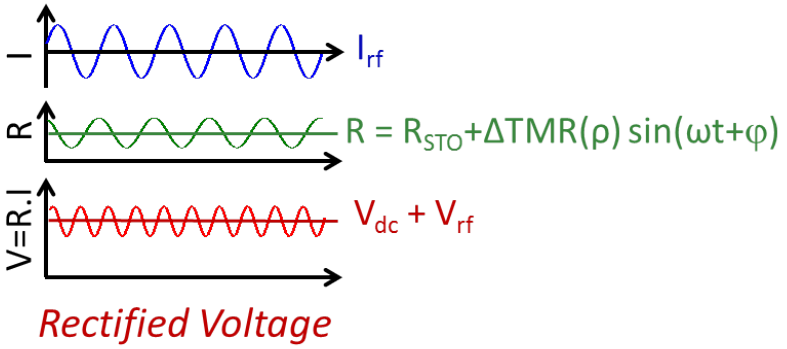

FIGURE 7.1: Principle of the spin-diode rectification voltage

7.1.2 Excitation of the gyrotropic mode in vortex based STOs

In the last decade, this spin-diode effect have been mainly studied for uniform modes in magnetic tunnel junctions [90, 91, 95, 187]. Here, we consider a magnetic vortex confined in a magnetic tunnel junction with a synthetic antiferromagnet as a polarizer. As seen in Chap. 4, the efficient ST torques are the in-plane Slonczweski and Field-like torques. By taking into account these two torques in the Thiele equation, we obtain the evolution the core radius ρ as a function of the rf-current frequency ω and amplitude J_{rf} as developed in Chap. 4. We can also obtain of the dephazing angle θ_0 between the rf-current and the oscillations of resistance:

$$\begin{cases} \rho = \frac{J_{rf}\sqrt{\Lambda_{FL}^2+\Lambda_{SL}^2}}{2GR\sqrt{(\omega-\omega_0)^2+(\Gamma_--\Gamma_+)^2}} \\ \theta_0 = \arcsin\left(\frac{C(\omega-\omega_0)}{\sqrt{(\omega-\omega_0)^2+(\Gamma_--\Gamma_+)^2}}\right) - \arctan\left(\frac{\Lambda_{FL}}{\Lambda_{SL}}\right) \end{cases} \tag{7.1}$$

with G the gyrovector, R the dot radius, Γ_- the anti-damping term, Γ_+ the damping term, C the vortex chirality. One may notice that these expressions are more difficult to solve for large amplitudes of rf-excitation when the nonlinear dependency of the oscillator frequency $\omega_0(\rho)$ and damping $\Gamma_+(\rho)$ have to be taken into account.

At the first order, we can obtain the analytical expression of spin-diode rectification voltage V_{sp} which has, similarly to the uniform case, two distinguished contributions: one lorentzian part associated with the Slonczweski torque efficiency (Λ_{SL}) and one anti-lorenztian part associated with the Field-like torque efficiency (Λ_{FL}):

$$\begin{aligned} V_{sp} =< \Delta R_{osc}(t) J_{rf}(t) >= \lambda \frac{\rho J_{rf} \cos(\theta_0)}{2} \\ = \lambda \frac{J_{rf}}{2GR} \left[\frac{Csign(\frac{\Lambda_{FL}}{\Lambda_{SL}})\Lambda_{FL}(\omega - \omega_0)}{\sqrt{(\omega-\omega_0)^2 + (\Gamma_- - \Gamma_+)^2}} - \frac{\Lambda_{SL}(\Gamma_- - \Gamma_+)}{\sqrt{(\omega-\omega_0)^2 + (\Gamma_- - \Gamma_+)^2}} \right] \end{aligned} \quad (7.2)$$

with λ the conversion factor between the oscillations of magnetization and the oscillations of resistance (see Ref. [48]). By analyzing the shape of the rectified voltage, spin-diode measurements have been studied as a mean to extract a quantitative estimation of the Field-like torque efficiency which remains unknown in many spin-valve systems [19, 162].

7.2 Optimization of the detection process: spin-diode vs reversible magnetization switching

7.2.1 Amplitude of excitation as a function of the applied rf-current

7.2.1.1 For small rf-excitation

In Fig. 7.2, we present the evolution of the rectified voltage with the frequency of the applied rf-current at zero field and zero dc-current. In this pure spin-diode measurement, we observe a rectified voltage of 0.8 mV when the rf-frequency matches with the gyrotropic frequency, here around 110 MHz. As discussed in the previous section (see Eq. 7.2), the lineshape of the generated peak is a combination of two peaks: one lorentzian and one antilorentzian. Here the shape is close to an anti-lorentzian indicating that the Field-like torque is the most efficient torque.

The resonant orbital trajectory of the vortex core can also be modelled micromagnetically, and the transient trajectory of the vortex core is shown in Fig. 7.2.b. From Eq. 7.2, we estimate the radius of excitation as a function of the frequency of excitation. We obtain an excellent agreement between our experiments and the micromagnetic and analytical developments with

the following input parameters: M_S = 580x10^3 A/m, Gilbert damping α = 0.009, a vortex layer of 5 nm, a dot diameter of 500 nm, a polarisation P = 0.2 [119] and a Field-like torque efficiency ξ_{FL} = 0.4 (the micromagnetic simulations were carried out with the OOMF code [188] with a mesh size of 5x5 nm). All these parameters, excepting the efficiency of the Field-like torque, are known experimentally or from previous studies [151]. Thus, one can notice that a Field-like torque efficiency ξ_{FL} equal to 0.4, i.e. $\Lambda_{FL}/\Lambda_{SL} = R\xi_{FL}/b \approx 10$ permits us to fit all our experimental results.

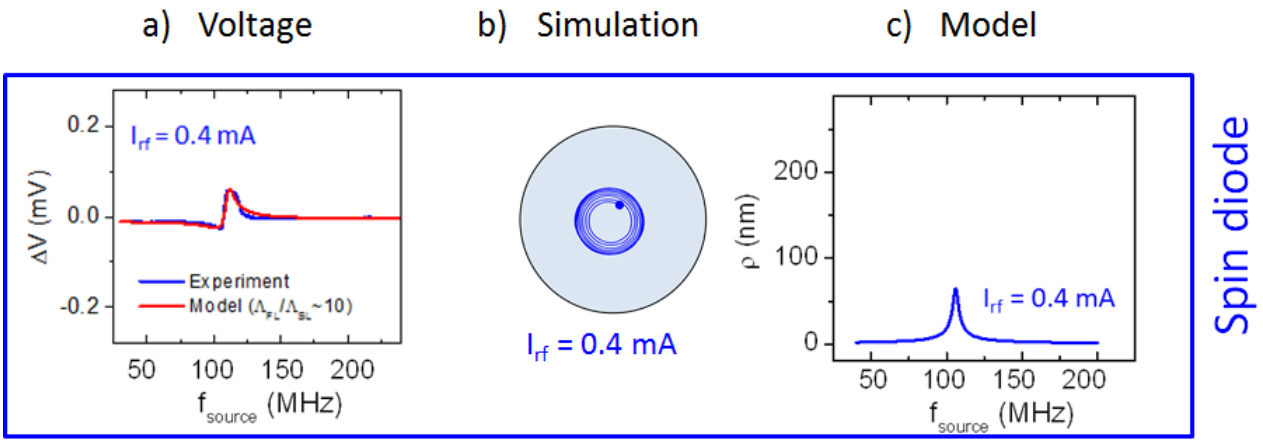

FIGURE 7.2: (a) Measured voltage as a function of the source frequency for I_{rf} = 0.4 mA, with I_{dc} = 0 mA, and H_{perp} = 160 kA/m. (b) Micromagnetic simulation of the transient trajectory of the vortex core when excited at f_{source} = 100 MHz for I_{rf} = 0.4 mA. (c) Estimation of the radius of excitation, ρ, for I_{rf} = 0.4 mA extracted using Eq. 7.1.

7.2.1.2 For large rf-excitation

For higher amplitude of injected rf-current, the shape of the dc-voltage drastically (at $I_{dc} = 0$) changes and an abrupt zero voltage plateau appears close to the vortex eigenfrequency as shown in Fig. 7.3.a. Indeed above an rf-current threshold, the vortex core reaches the edges of the dot and is expelled. The system then enters a stable and static C-state. The free layer returns to a vortex configuration only when the frequency of the rf-current is out of the resonant conditions.

The change of magnetic configuration (dynamical vortex to static C-state) in the "expulsion regime" is associated with a large drop in resistance. Thus the dc-voltage response no longer depends on the amplitude of rf-current:

$$V_{rect.} = \Delta R_{exp} I_{dc} + < \Delta R_{osc}(t) J_{rf}(t) > \tag{7.3}$$

with $\Delta R_{exp} = (R_p + R_{ap})/2$, R_p and R_{ap} the respective resistance in the parallel and antiparallel state (we assume that the static C-state is close to a uniformly magnetization state as shown in micromagnetic simulations).

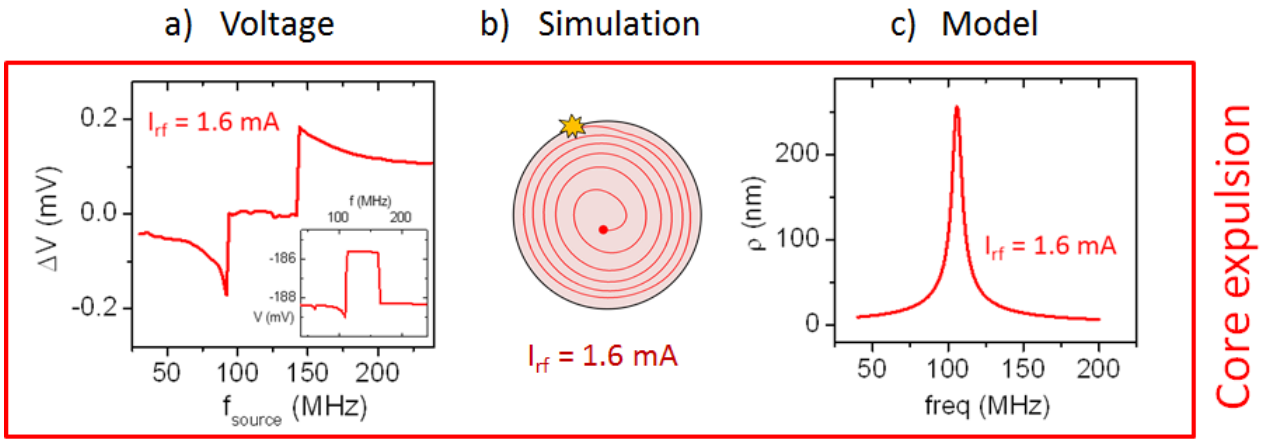

FIGURE 7.3: (a) Measured voltage as a function of the source frequency for I_{rf} = 1.6 mA, with I_{dc} = 0 mA, and H_{perp} = 160 kA/m (inset shows voltage response at I_{dc} = 5 mA). (b) Micromagnetic simulation of the transient trajectory of the vortex core when excited at F_s = 100 MHz for I_{rf} = 1.6 mA. (c) Estimation of the radius of excitation, ρ, for I_{rf} = 1.6 mA extracted using Eq. 7.1. (The vortex core was initially located in the centre of the 500 nm diameter disk and was excited with a current polarised in the (0 0.8 0.2) direction. The radius was modelled by calculating $\rho = \rho_{osc} + \rho_{disp} + \rho_H$, and expulsion is assumed when $\rho > 0.75$, as observed in micromagnetic simulations.)

For the vortex core expulsion, only the first term of Eq. 7.3 contributes to the rectified voltage. The generated signal is thus linear with the injected dc-current. On one hand, the voltage response is thus zero at zero injected current. On the other hand, the voltage response is directly scalable with the dc-current. In the inset of Fig. 7.3, we show that a large rectified voltage can be obtained for a 5 mA dc-current. The direct scalability of the response voltage with both the dc-current and the TMR ratio opens a new perspective to drastically enhance the voltage response of STOs [94].

7.2.2 Evolution with the dc-current

In the rectified response of vortex based STOs, it should be considered that the spin-transfer torque associated with the dc-current also acts as an anti-damping term. In single vortex based STOs with a synthetic antiferromagnet, the anti-damping torque is efficient only in presence of a perpendicular spin-polarization that is obtained by applying a perpendicular field [36]. Thus at zero field, the dc-current only amplifies the voltage response. On the contrary, when a perpendicular field is applied it contributes not only to amplify the voltage response but also to act on the magnetization dynamics (a positive current acts against the damping).

In Fig. 7.4, we show that $I_{rf,min}$, as expected from Eq. 7.1, the minimum rf-current needed to expel the vortex core from the dot is constant at zero field while it decreases as the dc-current increases at high perpendicular field. Our experimental results can be well fitted with our analytical model and the system parameters used in the previous section. It has only to be

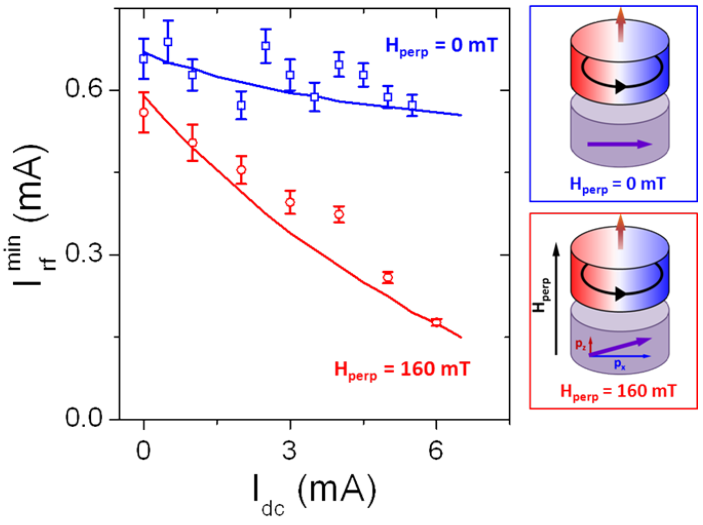

FIGURE 7.4: Evolution of I_{rf}^{min} as a function of I_{dc} for two magnetic fields, $H_{perp} = 0$ and 125 kA/m, where the data points are the experimental data and the line is the fit with Eq. 7.1

noticed that we assume here that the vortex core is expelled when $\rho > 0.75R$ to take into account the experimental roughness at the edges of the nanopillar (see Appendix A).

Thus the applied dc-current determines both the minimum rf-current needed to expel the vortex core and the amplitude of the rectified voltage. In Fig. 7.5, we note that the voltage response is almost linear with the injected rf-current in the spin-diode regime (without expulsion) and then constant in the expulsion regime where the rectified voltage is only determined by the dc-current. At +6 mA, the vortex core is expelled as soon as we applied an rf-current at the gyrotropic frequency (as low as 0.15 mA in our experiments).

Interestingly, the voltage response is independent of the injected rf-current. From an application point of view, it represents a great opportunity to detect a low rf-current without an amplifier and a breakthrough compared to the previous published studies (see Table 7.1) in which the detected power always depends on the injected rf-current. It is also important to note that this study was performed with MTJs which had a relatively low TMR ratio (8.5%), an order of magnitude lower than the junctions presented in [91]. A subsequent improvement of the maximum generated voltage associated to the vortex core expulsion may be anticipated for larger TMR ratio (as we will see later on our double vortex system with a 70 % TMR ratio).

Furthermore, this system could also be considered for the development of a powermeter. Indeed, by a sweep in dc-current the minimal value of dc-current needed to expulse the vortex core can be obtained. This value is directly related with the amplitude of the injected rf-current. The time of measurement is determined by the number of dc-steps with a minimal time scale per step corresponding to the retroaction constant of the system Γ_p. The precision of the

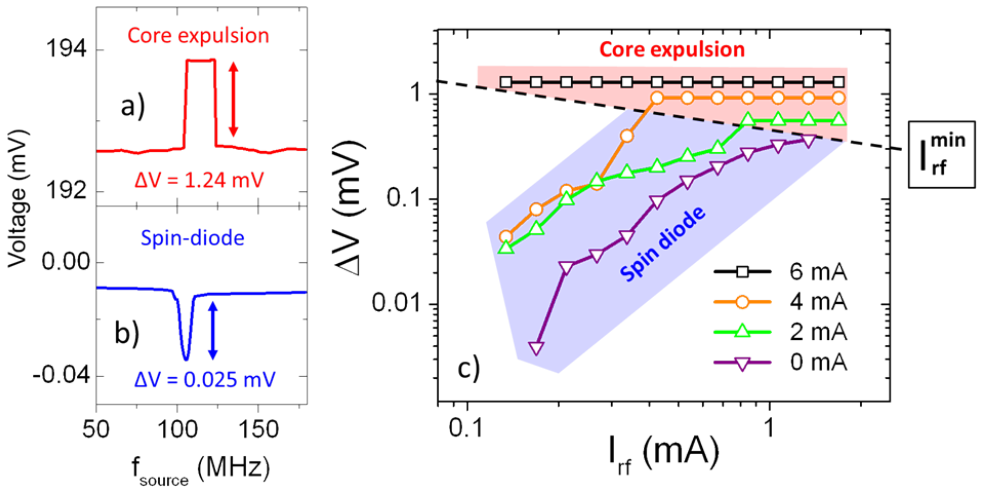

FIGURE 7.5: (a) Rectified observed voltage for the a) core expulsion and b) the spin-diode measurements taken at 6 mA and 0 mA, respectively, for a I_{rf} = 0.2 mA. (c) Evolution of the generated voltage, ΔV, as a function of the excitation current, I_{rf}, for a range of d.c. currents, at H_{perp} = 120 kA/m.

	$\mathbf{V_{max}}$ (μ V)	$\mathbf{V_{min}}$ (μ V)	$\mathbf{P_{max}}$ (dBm)	$\mathbf{P_{min}}$ (dBm)
Tulapurkar (IPP, MTJ) [90]	32	3.9	-11	-19
Miwa (OPP, MTJ) [91]	1,300	2.4	-26	-67
Resonance* (@ 0mA)	100	0.63	-10	-32
Expulsion* (@ 6mA)	2,000	2,000	-5	-43

TABLE 7.1: Table of current state of the art in voltage rectification measurements available (* = this study)

measurement will be limited by the stochastic switching, due to thermal fluctuations, close to the expulsion threshold. This aspect remains under investigation during A. Jenkins postdoc.

7.2.3 Voltage response as a function of the in-plane field

In the regime of vortex core expulsion, we experimentally notice that the measured resistance associated with a static C-state in the free layer is either close to the parallel or anti-parallel resistance state (see Fig. 7.6.b-c) depending on the direction of the applied in-plane field (mainly due to either the SAF stray field, or to an external field). In Fig. 7.6, we present experimental results and micromagnetic simulations for a slightly tilted perpendicular field of 120 kA/m (90.35° and 89.65°). The vortex core is always expelled so that the C-state net in-plane magnetization is parallel to the in-plane field as seen in Fig. 7.6. Thus the direction of the in-plane component of the field selects the C-state configuration.

However one should remark that the frequency bandwidth of vortex core expulsion differs for symetric angles around 90° degrees. Indeed, the dc-components of the in-plane Slonczewski and

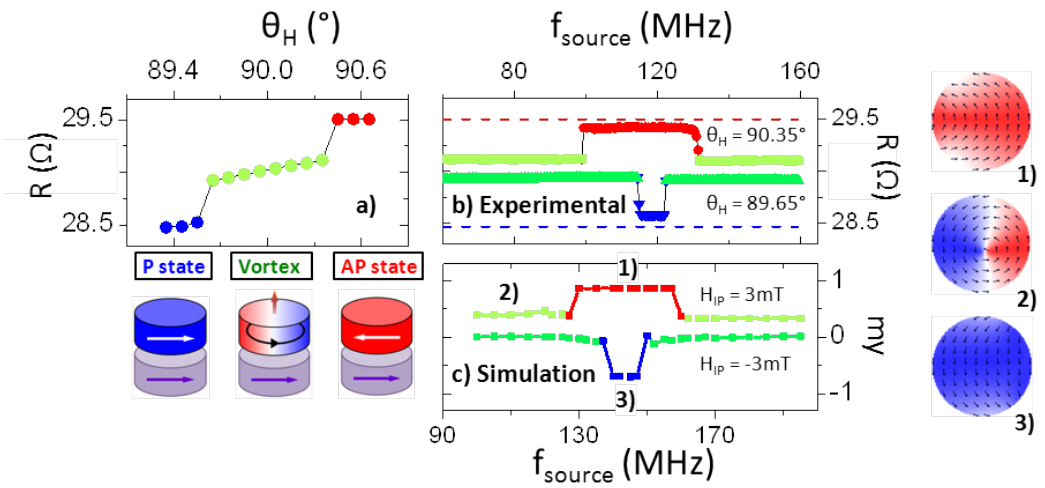

FIGURE 7.6: (a) Resistance state as a function of the angle of the applied at I_{dc} = 5 mA and H_{perp} = 120 kA/m. (b) Measured resistance as a function of the rf source frequency for two different angles of field. The blue (red) corresponds to the parallel (antiparallel) state, and the green to the vortex state, and the vortex state is suppressed when the source is equal to the gyrotropic frequency, F_s = 120 MHz. (c) Micromagnetic simulation of the m_y component as a function of source frequency for an in-plane magnetic field of ±3 mT, where the final m_y component is shown for the points labelled 1), 2) and 3).

Field-like torques act like an in-plane field whose sign depends on the sign of the dc-current. Thus it favors the vortex core expulsion in only one direction. To evaluate accurately the vortex dynamics under a resonant excitation, it is necessary to take into account a small initial displacement from the dot center ρ_{disp}, of a few nm, (which has been done in all our fittings) associated with the dc-inplane torques: $\rho_{disp} = \sqrt{\left(\frac{J_{dc}}{2G\omega_0}\right)^2 \left(\Lambda_{SL}^2 + \Lambda_{FLT}^2\right)}$.

Finally, the current needed to observe core expulsion can be tuned either by reducing the effective damping with a dc-current and a perpendicular field, or by displacing the vortex core within the dot with an in-plane field or polarized current.

7.3 Spin-diode in double vortex based STOs; Beyond a single low frequency detection channel

Few limits of vortex based STOs for applications are their frequency, which is limited between 100-2000 MHz, and their frequency tunability with I_{dc} which is of about 15% of the gyrotropic frequency. One other drawback of vortex based STO is that we have to apply a field and/or a dc-current cycling to initialize the vortex configuration.

In this section, we focus our study on double vortex based STOs. We first demonstrate that a regime of vortex core expulsion can be observed in double vortex systems at zero applied field.

Then we highlight that we can excite with an rf-current not only the vortex gyrotropic mode but also high frequency modes (of a few GHz) that are associated with core-core interactions [126].

7.3.1 Record voltage rectification in double vortex based STOs

First, we study a spin-valve with two weakly coupled vortices above a synthetic antiferromagnet as in Chapter 3 (see "sample A" in the Appendix A). In this sytem, the effect of the rf-current is as expected similar to the single vortex case. The large TMR (about 70%) of our double vortex systems gives rise to a record rectified voltage in the regime of vortex core expulsion. In Fig 7.7, we present the rectification voltage associated to vortex core expulsion for different level of dc-current. For a positive bias (as in Fig. 7.7), the dc-current acts as an additional damping term. In that case, the width of the rectification voltage, region of vortex core expulsion, decreases as we increase I_{dc} but its amplitude still increases. A maximum rectification voltage of +12 mV is thus obtained for $I_{dc} = +6$ mA. This is one order of magnitude larger than in our single vortex based STOs with a 8.5 % TMR ratio, and could even be enhanced with the recent development of FeB based STO with a 130 % TMR ratio [80].

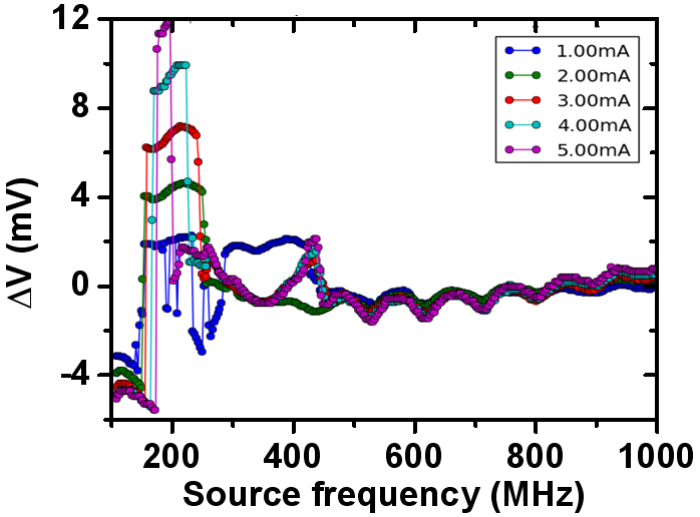

FIGURE 7.7: Response of the vortex at different power of dc-current for a 400 diameter junction. The rf-current is fixed at -10 dBm and no field is applied.

We see again here that the voltage response is directly scalable with the amplitude of the dc-current. Furthermore we notice that we can control the bandpass of detection with the sign of I_{dc}. The rectification voltage associated with vortex core expulsion is thus highly scalable in amplitude and frequency bandpass.

7.3.2 Mode splitting due to core-core interaction: towards high frequency detectors

In this section, we consider a magnetic tunnel junction with two strongly coupled vortices, without an in-plane SAF polarizer, and with a 10 % TMR ratio (see "sample D" in the Appendix A). By controlling the vortex chiralities, we expect to switch the system from a low resistance state of 12 Ohms (parallel chiralities) to a high resistance state of 13.5 Ohms (anti-parallel chiralities). This rectification voltage could thus be twice as high as for a single vortex based magnetic tunnel junction with a SAF (for a same TMR ratio).

Without a SAF polarizer, the Slonczewski and Field-like spin-transfer torques do not have the right symmetry to excite the gyrotropic mode of the two vortices for weakly coupled vortices. However, in the strong coupling case we can control the vortex configuration with an rf-current in our experiments. In Fig. 7.8.a, we display the stability diagram of the vortex chiralities with the dc-current and the perpendicular field. One should notice in Fig. 7.8.b that we can switch with an rf-current the vortices configuration from parallel chiralities to anti-parallel chiralities for fixed initial conditions ($I_{dc} = +2$ mA for the all range of perpendicular field). The chirality switching of the thin vortex layer occurs when the rf-source frequency is around the resonant frequency of the gyrotropic mode mainly associated to the thin layer. Micromagnetic simulations are still in progress to explain these observations. The profile of the spin-transfer forces is probably strongly impacted by the the strong core-core interaction.

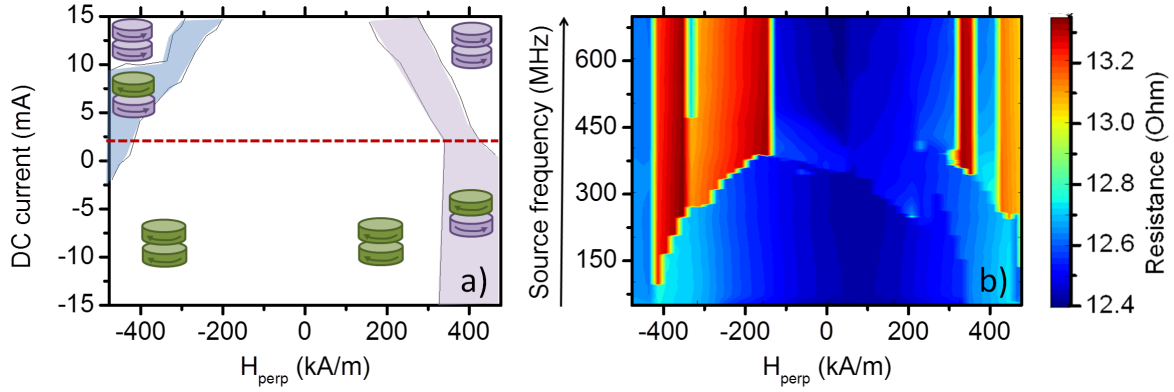

FIGURE 7.8: (a) Stability diagram as a function of the dc-current and of the perpendicular field. (b) Stability diagram as a function of the rf-source frequency and of the perpendicular for I_{dc}= +2 mA and I_{rf}= -10 dBm (the source frequency is swept from low to high frequency). The system consists of a 200 nm diameter double vortex system (Py(7 nm) / MgO(1 nm) / Py(11 nm))

The strong core-core interaction can also lead to new mode dynamics that strongly differ from the usual gyrotropic mode. In such a system, Cherepov et al. [126] have observed the presence of high frequency azimutal and translationnal modes that are associated with a strong core-core interaction [126]. Imaging experiments by J. F. Pulecio et al. [127] have also revealed

the presence of incoherent dynamics in this strong coupling regime. In our system we observe the presence of one of these high frequency modes in Fig. 7.9. Interestingly, a large voltage response is obtained under resonant excitation by an rf-current so that it can be detected without any locking setup. In Fig. 7.9, one should notice that this mode disappears at large field when the top thin vortex is not anymore stable. At lower field, its frequency decreases with the perpendicular field while the rectified voltage increases with field.

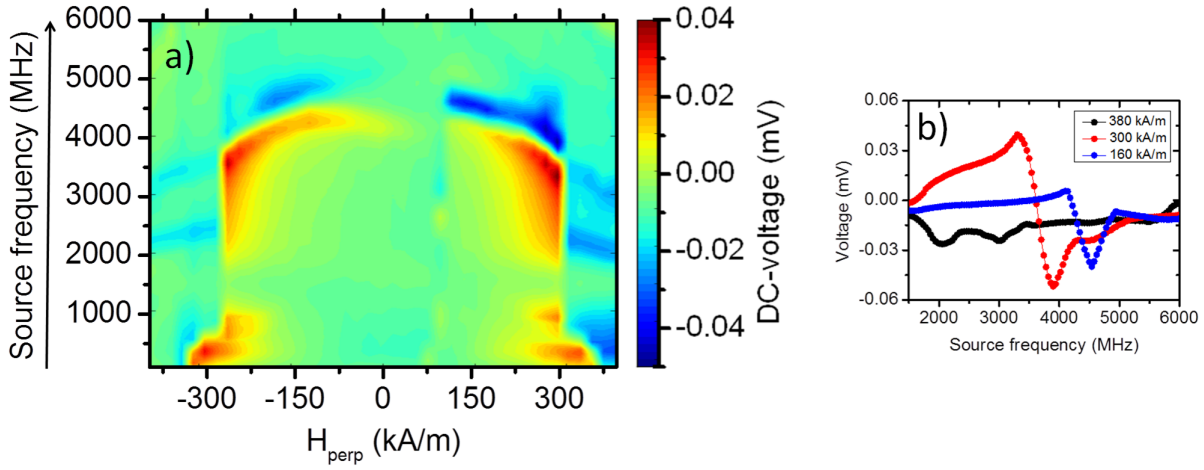

FIGURE 7.9: (a) Color map of dc-voltage response as a function of the excitation and of the perpendicular field for $I_{rf} = -10$ dBm (the source frequency is swept from low to high frequency) at $I_{dc} = 0$. (b) Spectrum for different perpendicular field. The system consists of a 200 nm diameter double vortex system (Py(7 nm) / MgO(1 nm) / Py (11 nm)).

One can notice that with this system we do not observe any switching of magnetization at high frequency. Recentely, we studied similar samples with FeB vortex layers. In this case, thanks to the lower damping of FeB compared to Permalloy, we could induce, similarly to the single vortex case, a reversible switching of the magnetization at the frequency of the gyrotropic mode or at the high frequency mode as seen in Fig. 7.10. This switching is associated with a large change of resistance from the parallel state (120 Ω) to the anti-parallel state (200 Ω). We can thus conclude that the change of magnetization corresponds to a chirality switching of one of the two vortices.

The mechanism that leads to this chirality switching is still under experimental and micromagnetic investigation. Nevertheless, we can mention that Guslienko et al. [189] have demonstrated that the state of antiparallel chiralities is more stable than the parallel state at zero dc-current. Here, I_{dc} favors the state of parallel chiralities through the generated Oersted field. On the contrary, the rf-current destabilizes this state of parallel chiralities by exciting the two vortex cores.

To conclude, the high frequency switching in these double vortex systems opens new promising perspectives for vortex based STOs. It highlights the interest of studying the vortex core

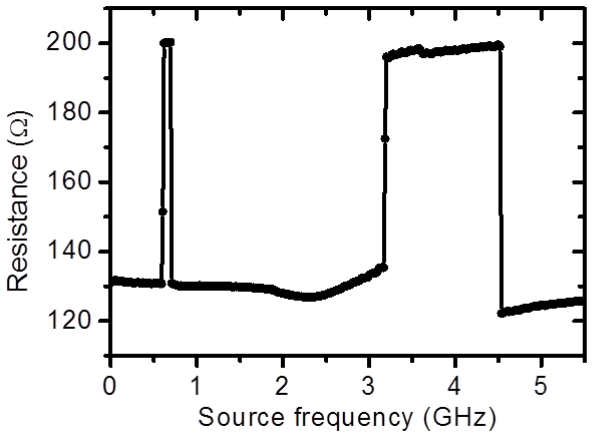

FIGURE 7.10: Evolution of the STO resistance state as a function of the rf-source frequency. ($H_{perp} = 240kA/m$, $I_{dc} = 0.3$ mA and $I_{rf} = -8$ dBm). The system consists of a 200 nm diameter double vortex system (FeB(4 nm) / MgO(1 nm) / FeB (8 nm)).

modes in magnetic systems with strongly coupled vortices and it enhances the classical range of frequency of vortex based STOs towards the perspective of high frequency rf-applications.

In this chapter, we demonstrated that the spin-diode response of a single vortex based STO ("sample C") can be large in magnetic tunnel junctions with a large Field-like torque. This allowed us to develop a new rf-detection scheme based on reversible switchings of resistance controlled by rf-current. With the rf-excitation, we controlled the magnetization of the STO and thus the resistance of the junction through the effect of magnetoresistance. Instead of the rectified voltage of classical spin-diode effect, we measured a voltage response due to a change of resistance. In that case, the detection voltage is scalable with I_{dc} and not with I_{rf} as for conventional diode effects. In a magnetic tunnel junction with only 8.5 % of TMR, we could report a record voltage peak of 2.000 μV.

In a second part, we highlighted that we can use vortex based STOs with strongly coupled vortices ("Sample D") for rf-detection at frequencies above to 2 GHz contrary. In a system of two strongly coupled vortices, we showed that rectified voltages can be obtained for rf-excitation between 2 and 5 GHz. We associated this response to the modes corresponding to the strong core-core interaction. Finally, we also demonstrated that we can reversibly switch the vortex magnetization by exciting these high frequency modes. We believe that these high frequency modes will open a path to develop a high frequency detection scheme based on vortex based STOs.

Chapter 8

Mutual synchronization of spin-torque oscillators through electrical coupling

The first demonstration of the mutual synchronization of spin-torque oscillators have been realized more than ten years ago in 2005 by two differents groups [60, 82]. Since there, all the published studies have mainly focused on spin wave coupling [59, 71], excepting in Ref. [73]. Only recently, we demonstrated in spin-valve based STOs that the dipolarly coupling could be used for synchronizing oscillators. All these coupling relies directly on the magnetization dynamics of each oscillator. In parallel, electrical coupling have been largely studied theoretically [66, 83, 85, 93] and through micromagnetic simulations [190–192] as a promising approach to develop tunable and controllable arrays of synchronized STOs. However no experimental demonstration have been reported yet. Indeed, this type of coupling relies not only on the magnetization dynamics but also on both the two fundamental mechanisms at the root of spintronic: (i) the conversion of the magnetization dynamics in oscillation of resistance through the magnetoresistance effect (ii) the effect of a spin-polarized current on the magnetization dynamics through the ST torques. These two mechanisms have thus to be highly efficient to observe an electrical synchronization of two STOs. In our double vortex based STOs, the high output emitted power (associated to the 70 % TMR ratio) and the strong efficiency of the Field-like torque permit to face these issues and to achieve mutual synchronization of two STOs driven by self-emitted current.

In this chapter, we first present the state of the art about mutual synchronization of spin torque oscillators and focus on the theoretical expectations for two electrically synchronized STOs. Then, we show the first experimental observation of the mutual synchronization of two double vortex based STOs driven by self-emitted current[193]. We investigate the properties of the synchronized state and highlight that the electrical coupling can be tuned either by an

extrinsic delay (by adding an electrical delay line between the two STOs) or by the spin-transfer locking forces. In the synchronized state, we observe a drastic improvement of the rf-features, i.e. a enhancement of the spectral coherence by a factor 2 and of the output power by a factor 4.

8.1 State of the art on mutual synchronization

8.1.1 Coupling via the spin-wave interaction

The first observations showing the mutual synchronization of STOs were observed by two differents groups in similar systems, i.e. in uniformely magnetized point contact STOs. Two point contact STOs, separated by a few hundred nanometers share a common free layer and are supplied by independent [82] or comon [60] dc-sources (see Fig. 8.1.a.). Under an applied field, they observed two independent peaks corresponding to the self-sustained regime of each point contact STO. By sweeping the dc-current of one (or two) STO, the peak frequencies change, getting closer and eventually merging into one as shown in Fig. 8.1.b. In the region where a single peak is observed, the output emitted power is enhanced by more than a factor 2 (up to 4!). This indicates that the phase difference between the two STOS is bounded and thus that the two STOs are synchronized.

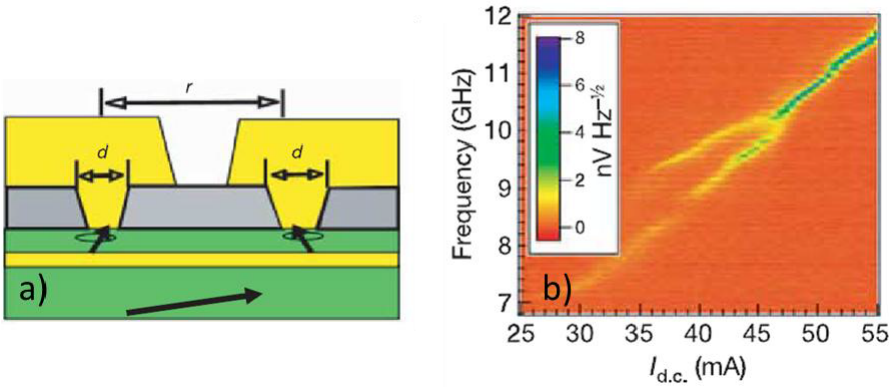

FIGURE 8.1: (a) Schema of the experimental setup used to synchronize two point contact STOs through spin-wave coupling. (Extracted from [82]) (b) Spectrum of the emitted signal depending on the applied dc-current. (Extracted from [60])

In these systems, the STOs are coupled both by spin-wave and dipolar coupling. However it was demonstrated theoretically [194] and experimentally [74] that the spin-wave coupling is the main mechanism involved in the synchronization process. Thus the synchronization phenomenon is limited by the attenuation length of the spin-waves (around 1.5 μm in permalloy). After these two pioneering works, it took eight years to reproduced similar results with four STOs [71].

Indeed, spin-wave coupling have two main disadvantages that make difficult the synchronization of multiple STOs with this kind of coupling: (i) the spin-wave coupling is a local coupling so that the synchronization of the STO arrays can only occur through the synchronization of closely neighbouring STOs which may lead to the unexpected formation of synchronized clusters within a single oscillator network (ii) the emission of the spin-wave is non-isotropic so that two STOs can synchronize only if they have an appropriate relative orientation.

The first observation of mutual synchronization with more than two oscillators have been performed in four vortex based point contact STOs through exchange coupling by A. Ruotolo et al. [73] at the CNRS/Thales lab. In such structure, they showed that the four small peaks observed at low current merge into one at high current as seen in Fig. 8.2.

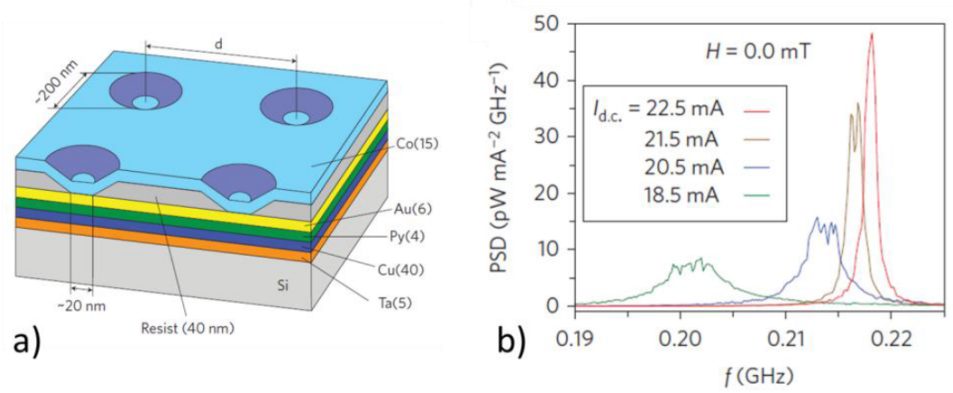

FIGURE 8.2: (a) Schema of the experimental setup used to synchronize four point contact vortex based STOs through exchange coupling. (b) Spectrum of the emitted signal depending on the applied dc-current. (Extracted from [73])

8.1.2 Coupling via the dipolar interaction

The dipolar coupling is generally too weak compared to the spin-wave coupling to synchronize uniformely magnetized STOs. However, Belanovsky et al. [195] demonstrated, in collaboration with CNRS/Thales, through micromagnetic simulations that the situation can be completely different in confined vortex based STOs. Indeed, the self-sustained regime of these STOs presents large oscillation of the net in-plane magnetization. The rf-field emitted by the dynamics of the vortex body can thus be large enough to synchronize closely neighbouring STOs.

Recently, we reported in collaboration with CEA-SPEC the mutual synchronization of a pair of vortex-based STOs through dipolar coupling [72]. With two 200 nm diameter spin valve nanopillars separated by 100 nm, we achieved mutual synchronization despite a significant frequency mismatch between the STOs (see Fig. 8.3.a). Interestingly, we highlighted that the coupling efficiency strongly depends on the magnetic configuration (core polarity and vortex chirality) of the two STOs. In particular, we demonstrated that the locking bandwidth is

three time larger for anti-parallel core configuration compared to parallel core configuration as shown in Fig. 8.3.b-c. However we couldn't observe an increase of the power or a decrease of the linewidth in the synchronized state.

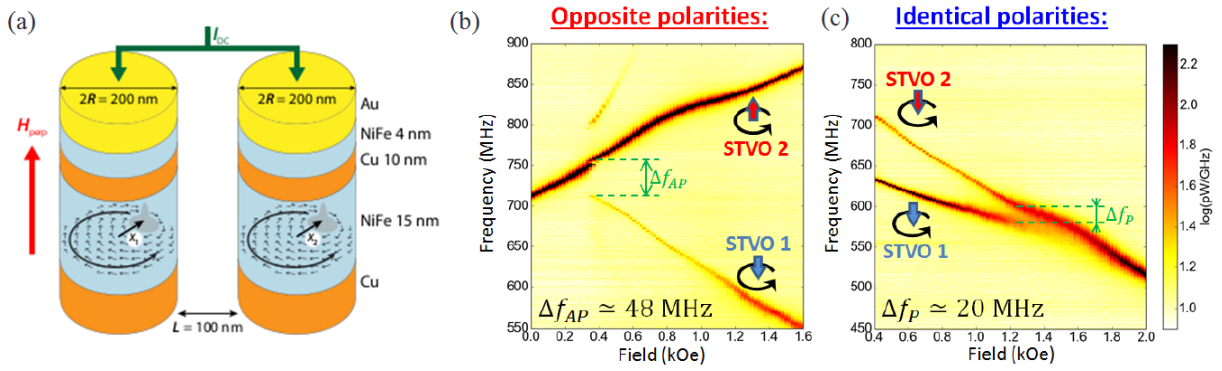

FIGURE 8.3: (a) Schema of the experimental setup used to synchronize a pair of vortex based STOs through dipolar coupling. (b)(c) Power spectrum maps versus perpendicular field measured for opposite (b) and parallel (c) polarities. (Extracted from [72])

Furthermore, this coupling mechanism is once more limited by the attenuation of the emitted rf-field. F. A. Araujo et. al. [196], also in collaboration with our group, recently showed through micromagnetic simulations that a pair of vortex based STOs could not synchronize for larger interdot distance than 600 nm in the optimal magnetic configuration. In our study, we choose to focus on the electrical coupling case that do not have such limitations.

8.2 Electrical synchronization of two vortex based STOs: Theoretical study

8.2.1 For two identical oscillators

For two mutually synchronized STOs, the phase dynamics of each STO can be well described through the analytical model developed in Chap. 4 for a STO locked with a reference rf-current source but here we don't have a master reference and a slave STO. The two synchronized STOs mutually influence their phase dynamics. The effective phase dynamics of a vortex based STO can then be expressed as [194]:

$$\frac{d\Phi_i}{dt} + \omega_i = -\sqrt{1+\nu_i^2}F_{e(j,i)}\cos(\Phi_j - \Phi_i - \Psi_{e,i} + \Psi_{\Delta\tau}) \tag{8.1}$$

with Φ_i the phase of one oscillator, ω_i its frequency, ν_i its nonlinear normalized parameter, $F_{e(j,i)} = \frac{I_{rf}\sqrt{\Lambda_{SL}^2+\Lambda_{FL}^2}}{2GR\sqrt{p_{0,i}}}$ the amplitude of the total locking force (Slonczewski and Field-like) that inversely depends on the oscillator normalized power $p_{0,i}$ and on the emitted current of

the second oscillator $I_{rf,j}$. The intrinsic phase shift $\Psi_{e,i} = \arctan\nu - \arctan\left(\frac{\Lambda_{FL}}{\Lambda_{SL}}\right)$ quantifies the dephasing between the locking rf-current and the output oscillations of resistance. The parameter $\Psi_{\Delta\tau}$ represents the delay of the coupling signal. For electrically coupled STOs, it corresponds to the delay introduced by the electrical circuit and it can be tuned with a tunable delay line [85]. For dipolarly or spin-wave coupled STOs, $\Psi_{\Delta\tau}$ is constant and defined by the spatial distance between oscillators [59, 72].

Here we consider in our analytical development the case of two "almost identical" oscillators that differ only in frequency. A more general approach has been developed by A. Slavin et al. [194]. In the case of two "almost identical" oscillators, the synchronized state can be described by the phase sum $\Phi = \Phi_1 + \Phi_2$ and the phase difference $\Psi = \Phi_1 - \Phi_2$:

$$\begin{cases} \frac{d\Phi}{dt} = -2\omega + 2\sqrt{1+\nu^2}F_e \sin\left(\Psi_{\Delta\tau} - \Psi_e\right)\cos\left(\Psi\right) \\ \frac{d\Psi}{dt} = -\Delta\omega - 2\sqrt{1+\nu^2}F_e \cos\left(\Psi_{\Delta\tau} - \Psi_e\right)\sin\left(\Psi\right) \end{cases} \tag{8.2}$$

with $\Delta\omega = \omega_1 - \omega_2$ the detuning frequency, $\omega = (\omega_1 + \omega_2)/2$ the average frequency.

8.2.1.1 Locking bandwidth

The dynamics of the phase difference Ψ is slow compared to the phase sum so that we focus on this term to establish the equilibrium conditions of the synchronized state. Then we obtain the bandwidth of synchronization [45]:

$$\Delta_{band} = 2F_e\sqrt{1+\nu^2}\cos\left(\Psi_{\Delta\tau} - \Psi_e\right) \tag{8.3}$$

From Eq. 8.3, we see that the locking bandwidth oscillates π-periodically as a function of the electrical delay $\Psi_{\Delta\tau}$. For a nonlinear oscillator (large ν) without a ST locking phase shift (i.e, $\Psi_{st,i} = 0$), as for uniformed STOs, the locking bandwidth is thus expected to be zero for zero electrical delay ($\Psi_{\Delta\tau} - \Psi_e = \Psi_e = \arctan\nu$). We conclude here that controlling the intrinsic phase shift $\Psi_{e,i}$ and the nonlinear behavior ν of a STO are crucial issues for mutual synchronization.

8.2.1.2 Locking frequency in the synchronized state

Within the locked state, the two STOs oscillate at the same frequency ω_s. Nevertheless this frequency is not necessarily the average frequency $\overline{\omega}$:

$$\omega_s = \overline{\omega} - \sqrt{\Delta_{band}^2 - \Delta\omega^2}\tan\left(\Psi_{\Delta\tau} - \Psi_e\right) \tag{8.4}$$

The frequency of the synchronized state is constrained between the eigenfrequencies of the two STOs and depends on the conditions of synchronization through the $\tan(\Psi_{\Delta\tau} - \Psi_e)$ term. By tuning the delay, we can thus modify the frequency of the synchronized state.

8.2.1.3 Output emitted power in the synchronized state

Similarly to the previous section, we can obtain the total output power of the synchronized STOs [45] which depends on the intrinsic phase difference Ψ_0:

$$p_{tot} = \left(\frac{2\rho\cos(\Psi_0)}{R}\right)^2 = 4p_0\cos^2\left(\frac{\Psi_0}{2}\right) = 4p_0\left(1 - \frac{1}{2}\left(\frac{\Delta\omega}{\Delta_{band}}\right)^2\right)^2 \tag{8.5}$$

When the oscillators are phase locked with a constant phase shift Ψ_0, the amplitude of the synchronized signal is twice the amplitude of a single STO so that the power can be enhanced up to $4p_0$ in the synchronized state. It can be noticed that these best conditions, i.e. $4p_0$, are expected at zero dephazing. For non-synchronized STOs at a same frequency, the total signal will be average to $2p_0$.

For electrically synchronized STOs, the situation can be a little more complicated depending on the experimental setup. The detected power depends on the electrical length between the STOs, as we will see later on, and on the total impedance of the circuit. Thus, for parallel or serial connections, B. Georges et al. [51] demonstrated (without taking into account the dephasing between each oscillator) that the total outpower of N synchronized STOs should be:

$$P_{series,parallel} = \frac{Z_0 N^2}{Z^2_{series,parallel}}(\Delta R_{osc})^2 I_{dc}^2 \text{with} \begin{cases} Z_{series} = Z_0 + NR \\ Z_{parallel} = NZ_0 + R \end{cases} \tag{8.6}$$

with R the oscillator resistance, Z_0 the load resistance, ΔR_{osc} the amplitude of the magnetoresistance oscillations, and N the number of synchronized oscillators. In our system, the load impedance is fixed to 50Ω. Nevertheless, for on chip applications, the impedance could be optimized depending on the type of connections in the synchronized arrays. For parallel and serial connections, it should respectively be fixed so that $R = 10Z_0N$ or $Z_0 = 10RN$. For hybrid systems, i.e for the case of N groups of M STOs connected in parallel, the expected emitted power is $P_{hybrid} = \frac{Z_0N^2M^2}{(NR+MZ_0)^2}(\Delta R_{osc})^2 I_{dc}^2$ if the optimal load is fixed so that $NR = MZ_0$. Such synchronization of arrays could strongly enhance the emitted power of STOs.

8.2.1.4 Limiting conditions for mutual synchronization

Since the first works of J. Grollier et al. [83], a lot of theoretical studies [66, 85, 93, 190–192] on the electrical synchronization of STOs have been published but no experimental observation have been reported until now. This absence of experimental realization is most probably due to too small emitted power of a STO to control a second one under thermal fluctuations. Another reason is the frequency dispersion of the STOs due to the lithography process. For a network of STOs directly connected in parallel or in series (i.e. negligible electrical delay), the electrical coupling K should thus overcome a critical value K_c in order to observe the mutual synchronization of N-oscillators [197]:

$$K = F_e\sqrt{1+\nu^2}\cos(\Psi_e) i_{hf,N-STOs} > K_c = 2(\Delta\omega_{disp} + \Delta\omega_{LW}) \tag{8.7}$$

with $i_{hf,N-STOs}$ the rf-current emitted by the N-oscillators, $\Delta\omega_{LW}$ the linewidth of a single STO and $\Delta\omega_{disp}$ the range of the STOs frequency distribution.

Hence we emphasize that this condition to get mutual synchronization requires STOs with a narrow linewidth, a large output power together with an efficient injection locking process on to an external rf current and a global low frequency scattering. These drastic requirements motivated our choice to work with the vortex based STOs developped in AIST that show excellent figures as far as rf characteristics are concerned.

For the 300 nm diameter double vortex STOs ("sample B" in Appendix A), the coupling constant K is of a few MHz (for an output power of a few hundreds nano-watts and relatively small nonlinear parameter ν between 3-8) and the linewidth of a single STO is generally below 1 MHz for an oscillating frequency around 300 MHz. Thus these samples have the required features to achieve mutual synchronization.

8.2.2 Linewidth reduction in the synchronized state

In the presence of thermal fluctuations, the phase sum Φ and difference Ψ are defined by the following system of equations:

$$\begin{cases} \frac{d\Phi}{dt} = -2\omega + 2\sqrt{1+\nu^2}F_e \sin(\Psi_{\Delta\tau} - \Psi_e)\cos(\Psi) + \xi_1(t) + \xi_2(t) \\ \frac{d\Psi}{dt} = -\Delta\omega - 2\sqrt{1+\nu^2}F_e \cos(\Psi_{\Delta\tau} - \Psi_e)\sin(\Psi) + \xi_1(t) - \xi_2(t) \end{cases} \tag{8.8}$$

with $\xi_1(t)$ and $\xi_2(t)$ the white noise sources in each oscillator. In the hypothesis of "almost identical" oscillators (same linewidth), the two white noise sources are uncorrelated but have a similar diffusion constant D_0: $\langle \xi_1 | \xi_2 \rangle = 2D_0^2\delta_{1,2}\delta(t-t')$.

In the best locking conditions for which the locking bandwidth is the largest, i.e $\Psi_{\Delta\tau} - \Psi_e = n\pi\,[\pi]$, there is no retroaction process on the dynamics of the phase sum Φ. Thus the diffusion of the phase sum is much larger than the diffusion of the phase difference ($D_\Phi = 2\sigma_0^2 >> D_\Psi$). We can then deduce the diffusion constants of the phase of each synchronized STO (given that $\Phi_1 = (\Phi + \Psi)/2$ and $\Phi_2 = (\Phi - \Psi)/2$). We obtain $D_{s,1} \approx D_{s,2} \approx D_\Phi/2 = \sigma_0^2$, i.e. half the diffusion constants of the non-interacting oscillators ($D_1 = D_2 = 2\sigma_0^2$). For these conditions, the phase noise of each synchronized oscillator is reduced by a factor 2. Out of the best locking conditions, the decrease will be lowered as demonstrated by [81]. This approach can be generalized in the case of N oscillators where a decrease of linewidth by a factor N is expected at the best.

8.3 Electrical synchronization of two vortex based STOs: Experimental demonstration

8.3.1 Experimental setup

For these measurements, we electrically connect in parallel two double vortex based STOs (see Fig. 8.4). Each STO is independently supplied by a dc current source, allowing them to enter in a regime of sustained oscillations through the action of spin torque. In practical, the rf ports of the two bias tees are electrically connected through rf cables and a tunable delay line. Electrical mutual synchronization can thus be achieved through the electrical signals generated by each STO. Finally, we insert a power splitter (PS) in the circuit in order to record the output rf signal originating from the two STOs using a spectrum analyzer.

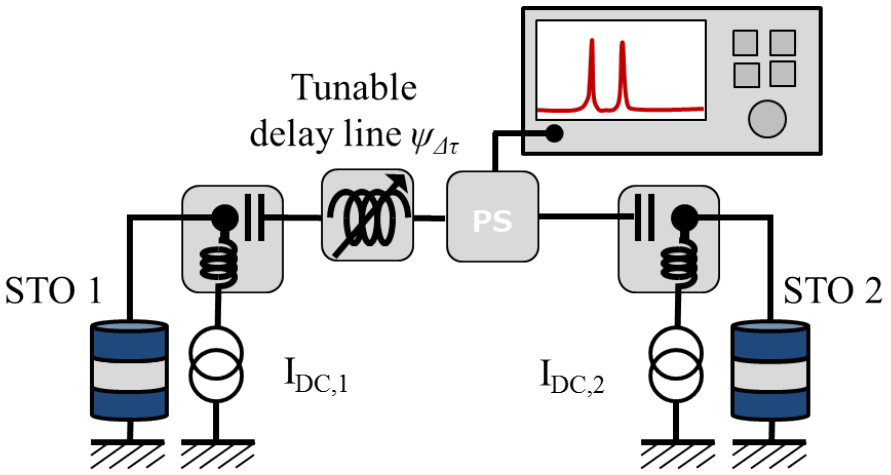

FIGURE 8.4: Schema of the electrical circuit for the mutual synchronization of two oscillators independently alimented by two currents and connected through the rf-port of two bias tee with a tunable delay line $\Psi_{\Delta\tau}$. The detected signal is measured by a spectrum analyzer, connected to the delay with a -6 dBm power splitter (PS)

One should notice that this setup is appropriate to study the locking conditions depending on the delay length. However the determination of the total power is not an easy task. Indeed the total emitted power is not directly detected close to the terminals of both oscillators but it depends on the location of the power splitter that is connected to the spectrum analyzer. A direct consequence is that the dephazing parameter between the emitted signals by each STO is not necessarily Ψ_0 at the detection point so that Eq. 8.5 is not directly valid in this case. A careful choice of the detection point, or a power renormalization, is thus necessary to get access to the dephazing parameter Ψ_0 and to the real output power.

8.3.2 Pre-characterization of the non-interacting STOs

The double vortex based STOs used here are the "samples B" (see Appendix A). We know precisely from Chap. 3 what are the vortex configurations and the spin torque components (the ones associated to the vortex-like spin polarization), that results in a sustained dynamical state at room temperature showing a strongly coherent (few hundreds kHz) and powerful (few hundreds nW) emitted radio frequency (rf) signal. Moreover, we have seen in Chap. 4 that these STOs synchronize with an alternative rf-current through the Slonczewski and Field-like torques originating from the SAF polarizing layer. Thus we have all the conditions needed for mutual synchronization.

In this work, we study 300nm diameter STOs with $R = 32\Omega$. We choose experimental conditions (field and angle) so that the two STOs possess similar properties as shown in Fig. 8.5. In most of our measurements, the dc-current is fixed for the STO 1 ($I_{DC,1} = +10.6$ mA) and is swept for the STO 2 ($I_{DC,1}$ varies from +10.5 to +11.8 mA). In these conditions, their properties differ by less than 15%, ie, linewidth (STO 1 $\sim$ 1.15 MHz, STO 2 $\sim$ 1-1.25 MHz in Fig. 8.5.b), power (STO 1 $\sim$ 0.44 μW, STO 2 $\sim$ 0.35-0.52 μW in Fig. 8.5.c) and nonlinear parameter ν (STO 1 $\sim$ 3.4, STO 2 $\sim$ 3-4.8 in Fig. 8.5.d). For these conditions, the two STOs are "almost identical" oscillators that only differ in frequency. This is particularly the case when the two STOs have the same frequency for $I_{DC,1} = +10.6$ mA and $I_{DC,1} = +11.2$ mA. Thus we can compare our experiments of mutual synchronization with our theoretical model.

8.3.3 Evolution of the locking bandwidth with the electrical delay length

The purpose here is to study the evolution of the locking conditions when the delay time $\Psi_{\Delta\tau}$ varies with the a tunable delay line. For some particular delays, we report a maximum bandwidth of 2 MHz as shown in Fig. 8.6.(3) while for some others, we note the complete absence of synchronization as shown in Fig. 8.6.(1). For the best synchronization bandwidth, the power spectral density (PSD) is strongly enhanced in the synchronized state which indicates

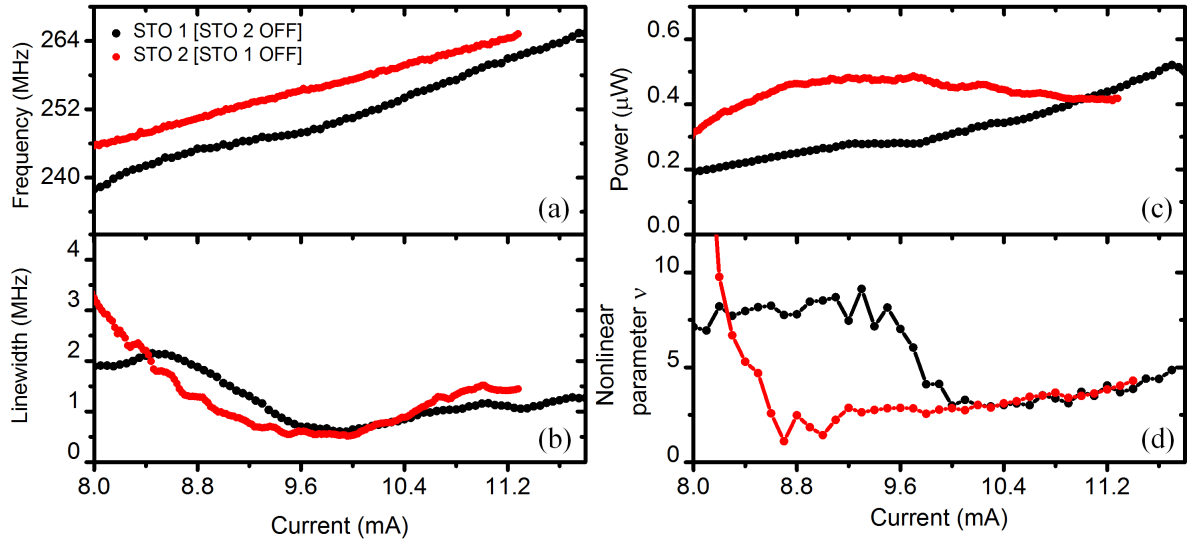

FIGURE 8.5: Frequency (a), linewidth (b), power (c) and nonlinear parameter ν (d) for each non interacting oscillator (STO 1 and STO 2) depending on the dc-current applied in their respective current source

that the two STOs oscillates in phase (see Fig. 8.6.(3)). On the contrary, the PSD stays constant when the frequencies of the two STOs cross without leading to a synchronized state(see Fig. 8.6.(1)). These features are coherent with our theoretical expectations (see Eq. 8.3) as we also report a π periodic dependency of the synchronization bandwidth with the delay.

The use of the delay line provides the ability to determine the optimal delay for synchronizing a large number of STOs in parallel or in series. Experimentally, this optimal delay can be determined by pointing in Fig. 8.6 at which values of delay are located the maxima (resp. minima) of the locking bandwidth. We find that the minima and the maxima of the locking bandwidth are respectively obtained for delay constants $\Psi_{\Delta\tau}$ around $2\pi/5[\pi]$ and $9\pi/10[\pi]$. It means that non-zero locking bandwidth $\Delta\omega_{band}$ can be obtained (see Eq. 8.3) for zero delay, i.e $\Psi_{\Delta\tau}$=0. These observations are in agreement with the prediction that can be done through the determination of the intrinsic phase shift Ψ_e.

As developed previously, the intrinsic phase shift of vortex based STO has the specificity, compared to other STOs [45], to be the sum of two terms $\Psi_e = \arctan(\nu) + \arctan\left(\Lambda_{FL}/\Lambda_{SL}\right)$. It is thus sensitive not only to the nonlinear oscillator behavior but also to the ratio of the two ST locking forces. The nonlinear dimensionless parameters ν have been determined experimentally in the previous section giving $\arctan(\nu) \sim 2\pi/5$. Moreover, we have, as previously discussed, a large $\Lambda_{FL}/\Lambda_{SL}$ ratio leading to $\arctan\left(\Lambda_{FL}/\Lambda_{SL}\right) \sim \pi/2[\pi]$. Thus the locking maxima are expected for $\Psi_{\Delta\tau} = \Psi_e \sim 9\pi/10[\pi]$ in excellent agreement with our experimental values (see Fig. 8.6). This robust observation permits us to consider the synchronization of multiple vortex based STOs without the necessity to add a large length of rf cables between each oscillator and so to avoid detrimental constraints for real applications.

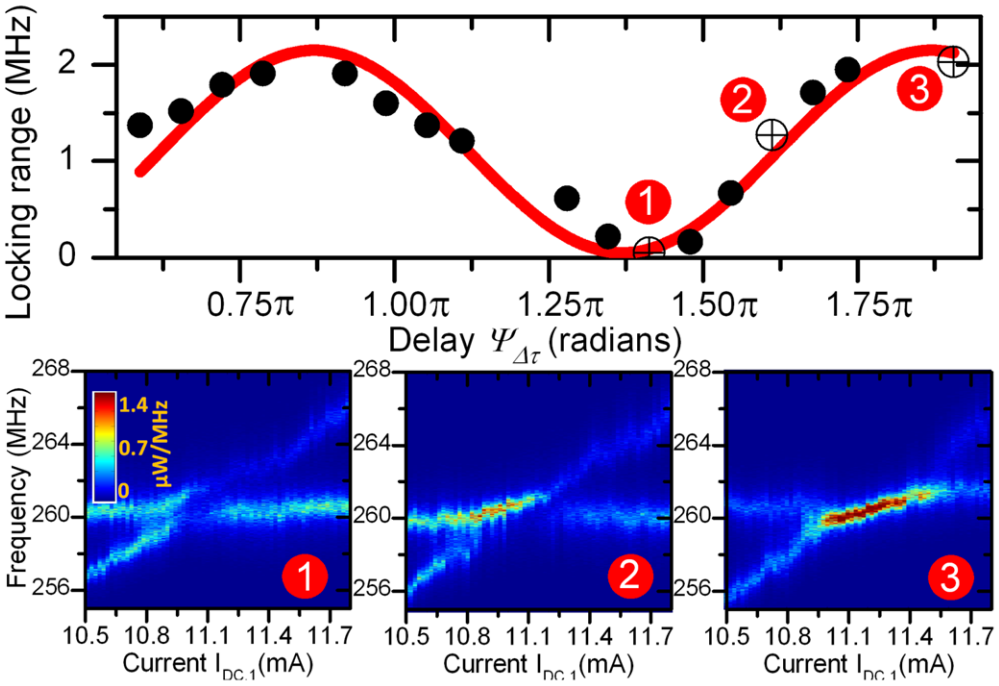

FIGURE 8.6: Evolution of the locking bandwidth of the two mutually synchronized oscillators (STO 1 with $I_{dc,2} = +10.6$mA and STO 2 with $I_{dc,1}$ swept) depending on the delay constant (associated to the length of the delay line) (a) Map of the locking characteristics for different bandwidth of synchronization at different delays: minimum locking (1) for $\Psi_{\Delta\tau} = 1.4\pi$ (b) intermediate (2) for $\Psi_{\Delta\tau} = 1.6\pi$ (c) maximum (3) for $\Psi_{\Delta\tau} = 1.9\pi$ (d)

8.3.4 Characteristics of the synchronized state

8.3.4.1 Bandwidth of synchronization

Experimentally, we report a maximum bandwidth of synchronization of 2 MHz, i.e. 1% of the synchronized frequency. This value is indeed small compared to the frequency of the STO. This is simply due to the fact that the electrical coupling strength, related to the output power of the STO, is small. Here, we demonstrate that the experimental bandwidth of synchronization fits with our theoretical expectations. As mentioned earlier, we suppose that the two STOs are almost identical. In this case, we can estimate the rf-current emitted by one STO that will drive the second oscillator:

$$J_{rf,STO} = \frac{I_{rf,STO}}{\pi R^2} = \frac{\sqrt{P_{int}/R_{STO}}}{\pi R^2} \tag{8.9}$$

with P_{int} the emitted power and R_{STO} the resistance of one STO. In our experimental setup, the presence of a power divider used to detect the emitted power on a spectrum analyzer results in a decrease by 6 dBm of the effective locking signal that is applied on each oscillator. The impedance mismatch between the circuit resistance (50Ω) and the oscillator resistance (32Ω) is also contributing to the decrease of the effective locking rf current. We note this effective

locking current $I_{rf,eff} = (1 - R_{re})I_{rf}/2$ with $R_{re} = (50 - 32)/(50 + 32)$. The locking range is then expressed by the following expression:

$$\Delta\omega_s = \frac{I_{rf}\sqrt{\Lambda_{SL}^2 + \Lambda_{FL}^2}}{2GRp_0} \tag{8.10}$$

with the normalized power $p_0 = \frac{18P_{int}}{R_{load}}(\frac{R_{load}+R_{STO}}{I_{dc}\Delta R_{TMR}})^2$ [48]. For the presented measurements, ($I_{rf,STO} = 0.5$ mA, $\nu = 3.4 - 3.7$, $p_0 = 0.21$, $\Delta R_{TMR} = 14\Omega$, R =150 nm and $I_{dc} = +11$ mA), Λ_{FL} and Λ_{SL} from Chap. 7, and $H_{perp} = 70$ kA/m. Injecting these parameters, we deduce $\Delta\omega_s = 1.6 - 2.1$ MHz, a value being in excellent agreement with our experimental observations (2 MHz).

Different solutions can be considered to enhance the locking range. Enhancing the output power of STNOs can be an option. Thus, we could use FeB based STOs that present larger TMR ratio than permalloy based STOs. Furthermore, a careful choice of the oscillator nonlinear behavior is also an option to increase the locking range.

8.3.5 Effect of the STO nonlinear behavior on the synchronization bandwidth

By changing the functioning point of the STO 2 from $I_{DC,STO2} = +10.6$ to $+11$ mA, we change its nonlinear dimensionless parameter ν from to 3.4 to 4. The frequency of STO 1 crosses that of STO 2 for larger currents (aroung +11.5 mA) where the corresponding nonlinear parameter ν is also increased up to 4. In these new locking conditions, we note that the maximal locking range is increased by 40%, up to 3 MHz, compared to the previous results (as shown in Fig. 8.7). These observations validate the influence of the nonlinear behavior of two STOs on the locking process. Larger ν could be obtained at lower currents but we were not able to observe synchronization as we couldn't find a frequency crossing point where both oscillators were in a self-sustained state.

8.3.5.1 Frequency evolution in the synchronized regime

Our experimental approach allows us to describe the dynamical properties of each oscillator when they are interacting or when they are independent. This provides a unique opportunity to properly characterize the rf properties in the synchronized state. The way to proceed is to compare the measured signal on the spectrum analyzer in two series of measurements. The first ones have been recorded when the two STOs are self-oscillating due to spin transfer torque (the two dc sources supplying the STOs are switched ON, see Fig. 8.4). For that, we keep constant the dc current applied on STO 2 and vary the one applied on STO 1. Thus we can obtain the rf properties of the two interacting STNOs within the synchronized regime (red dots

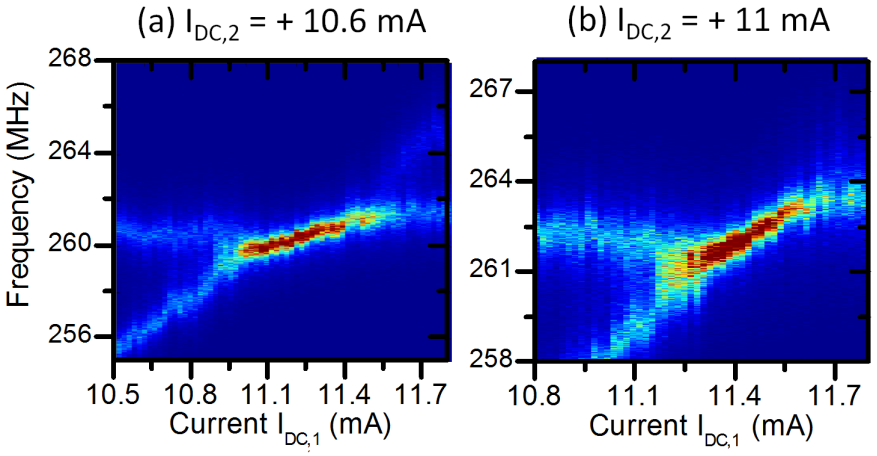

FIGURE 8.7: Maximal locking bandwidth of the two mutually synchronized STOs for two different $I_{DC,1}$, either (a) $I_{dc,2} = +10.6$ mA or (b) $I_{DC,2} = +11$ mA (with $I_{DC,1}$ swept). The two current values are respectively associated with two different nonlinear parameters ν (3.4 and 4) for the STO 1.

in region 2 in Fig. 8.8) as well as outside it (green and brown dots in region 3 in Fig. 8.8). For the second series of measurements, presented in Sec. 8.3.2, we record independently the rf signal from each STO while the other one is not supplied in dc current. For STO 1 alone ($I_{DC,1}$ in ON, $I_{DC,2}$ is OFF), the data are shown in light brown open dots in Fig. 8.8 and for STO 2 alone ($I_{DC,2}$ in ON, $I_{DC,1}$ is OFF) in light green open circles. Note that for all these measurements, the delay time is kept fixed to $\Psi_{\Delta\tau} = 1.9\pi$ which corresponds to a maxima of the locking range (see Fig. 8.6).

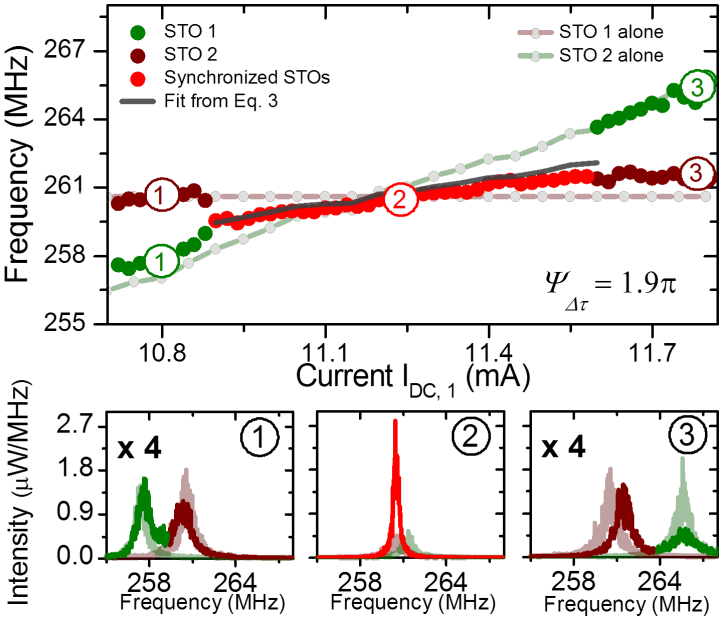

FIGURE 8.8: Evolution of the frequency of the interacting STOs as a function of $I_{DC,1}$, while $I_{DC,2}$ is fixed to + 10.6 mA. Bottom: Corresponding spectra for $I_{DC,1}$= +10.8 mA (1), +11.25 mA (2), +11.8 mA (3) (Non-interacting oscillator properties when one is switched off are in green and brown softened curves)

In these best locking conditions, we have $(\Psi_{\Delta\tau} + \Psi_e) \sim 0[\pi]$ so that, as expected from Eq. 8.4, the locked frequency is close to the average frequency of the non-interacting STOs as shown in Fig. 8.8. To verify this behavior, we change the delay and note that the frequency of the synchronized state becomes different from the average frequency. At zero frequency detuning, the synchronized frequency is larger for $\Psi_{\Delta\tau} = 1.6\pi$ rad than for $\Psi_{\Delta\tau} = 1.25\pi$ rad as predicted from Eq. 8.4.

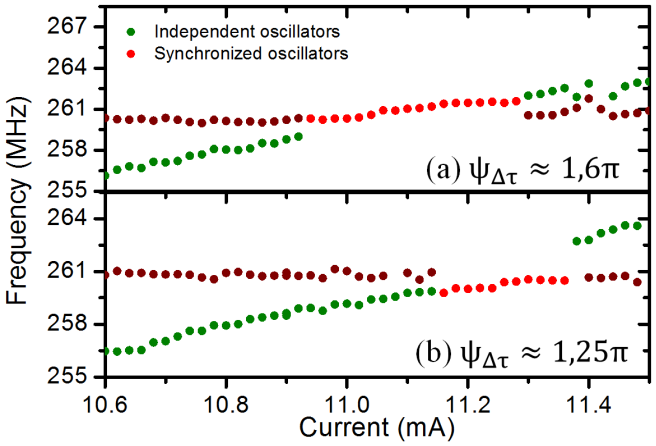

FIGURE 8.9: Synchronization frequencies depending on the dc-current injected in the oscillator 1 ($I_{DC,2}$ is fixed to + 10.6 mA) for two delay legnths $\Psi_{\Delta\tau} = 1.6\pi$ rad (a) and $\Psi_{\Delta\tau} = 1.25\pi$ rad (b)

Furthermore, one should notice that for the optimal delay, i.e $\Psi_{\Delta\tau} = 1.9\pi$ rad, we report an increase of both the output emitted power and the spectral coherence in the synchronized state as seen in region (3) in Fig. 8.8. To precise our analysis, we will perform a quantitative analysis of these two key parameters in the all bandwidth of synchronization.

8.3.5.2 Output emitted power

In the best locking conditions ($\Psi_{\Delta\tau} = 1.9\pi$ rad), we note that the power evolves like a bell-shape curve with a maximum of power near the center of the synchronization bandwidth and minima at the edges as seen in Fig. 8.10. Furthermore, we notice that the two non-synchronized "almost identical" oscillators have similar powers ($p_{STO1} \sim p_{STO2}$) so that we can assimilate them to their average value p_0. Then we conclude that the experimental maximum power nearly reaches $4p_0$ and that the minima are close to $2p_0$. This strong power enhancement in the synchronized state at zero frequency detuning is a key parameter in order to face with the low emitted power of STOs. The fact that the maximum power is not exactly $4p_0$ can be associated with the not fully identical properties of the two non-synchronized STOs, or with the fact that the delay length is not zero.

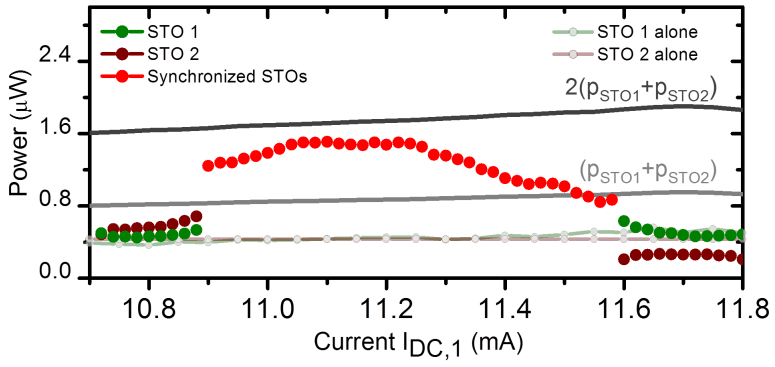

FIGURE 8.10: Power dependency with the dc-current injected in the oscillator STO 1 ($I_{DC,2}$ is fixed to + 10.6 mA for STO 2, $\Psi_{\Delta\tau} = 1.9\pi$ rad) (Oscillator properties when one is switched off are in green and brown softened curves)

8.3.5.3 Spectral coherence

In parallel to this increase of power we report a quantitative enhancement of the spectral coherence in the synchronized state as represented in Fig. 8.11. At the center of the locking, the linewidth is reduced down to 550 kHz, i.e by a factor two compared with the non-interacting states. Such a reduction confirms that the phase noise in the synchronized state is driven by the dynamics of the phase sum Φ as developed in Sec. 8.2.2. At the left edge of the locking range, we observe a large linewidth which can be associated with phase slips and frequency pulling, i.e STO 1 try to adapts its frequency to get synchronized (see Fig. 8.9),.

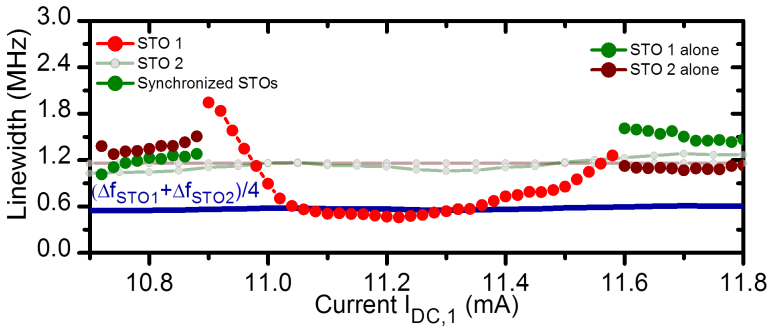

FIGURE 8.11: Power dependency with the dc-current injected in the oscillator STO 1 ($I_{dc,2}$ is fixed to + 10.6 mA for STO 2, $\Psi_{\Delta\tau} = 1.9\pi$ rad) (Oscillator properties when one is switched off are in green and brown softened curves)

8.3.5.4 Amplitude and phase noise

As we have seen previously, both phase and amplitude dynamics have to be taken into account to analyze the spectral coherence of a STO in the autonomous regime [46, 48, 54] due to the nonlinear behavior of STOs. Such an issue is not necessary to understand the general features of two mutually synchronized STOs. However we demonstrate here that we should study in more detail the amplitude dynamics of two synchronized STOs. Indeed, in our experiments

we always observe an increase of amplitude noise simultaneously to the decrease of phase noise as seen in Fig. 8.12. For the case of two phase locked STOs, the amplitude noise remains lower than the phase noise but in large arrays of phase locked oscillators, the situation could eventually be reversed. Moreover, one should notice that the amplitude noise is more enhanced (by 10 dBm) than the phase noise is decreased (by 3 dBm). We cannot understand this behavior at this stage with our analytical model but it may be possible in the theoretical framework of Aronson et al. [198] that describes more in details the synchronization of weakly nonlinear oscillators.

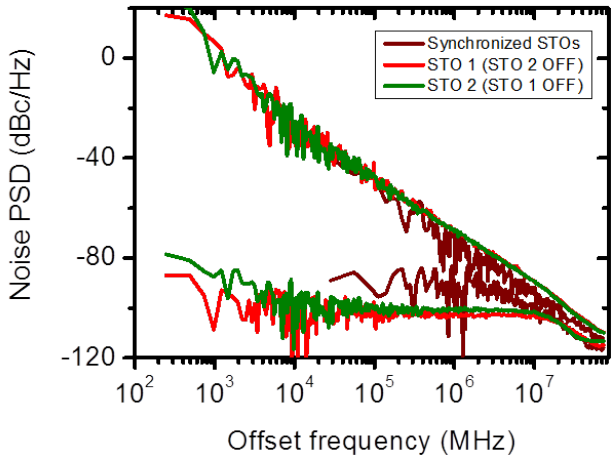

FIGURE 8.12: Phase and amplitude noises in the synchronized state ($I_{dc,1}$=+11mA, $I_{dc,2}$=+10.6mA), and for the non-interacting STNOs in similar conditions

8.4 Electrical synchronization of two vortex based STOs in series

In this section, we connect two STOs, of 300 nm diameter, directly in series with one single current source as represented in Fig. 8.13. By a proper choice of the field conditions, we can observe electrical mutual synchronization.

For I_{DC} between 9 and 9.8 mA, the two STOs are not synchronized. The STO with the highest frequency adapts its frequency to the second one so that we see the presence of frequency pulling. Then, the two oscillators synchronize for I_{DC} between +9.8 and +11 mA, and desynchronize for higher current values. The frequency of the synchronized state is always close to the frequency of one of the two STOs. This behavior is related to the fact that we don't have two "almost identical" STOs in this experiment [194].

In this experiment, the bandwidth of synchronization reaches about 8 MHz. These results validate our previous study as we succeed to synchronize two STOs without any electrical delay between them. The synchronization bandwidth is here about four time larger than in

our previous study. This indicates that the synchronization bandwidth is close to be optimized at zero delay. We have here all the key elements to succeed the electrical synchronization of STO arrays in a near future.

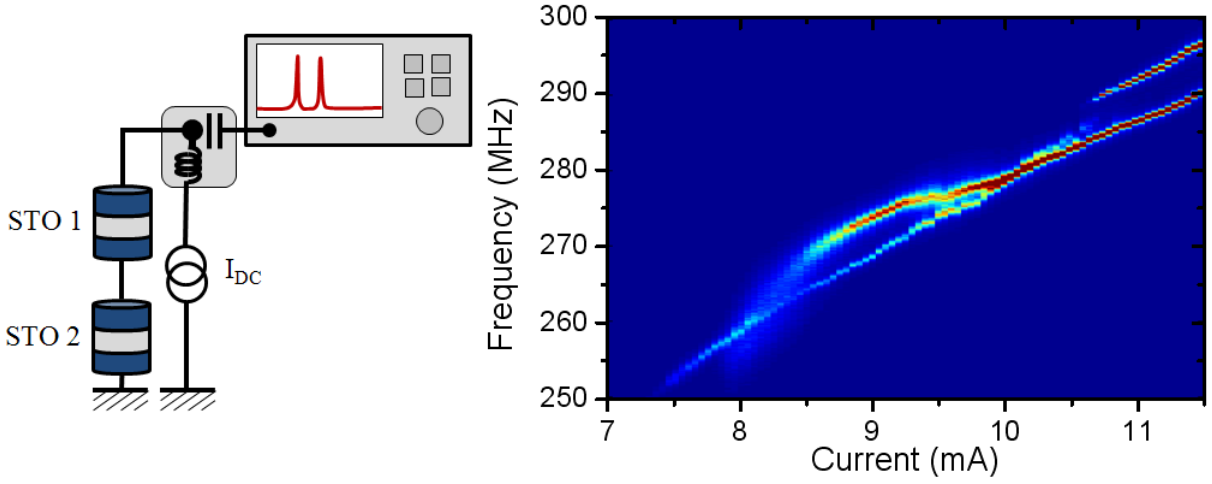

FIGURE 8.13: (Left) Electrical circuit for the synchronization of two nano-oscillators connected in series with a single dc-current source. The two oscillators are connected by a gold wire bonding and the length of cable between the two oscillators is of a few mm. (Right) Power spectral density of the two nano-oscillators depending on the applied dc-current at H_{perp}= 200 kA/m. (The sample diameter is 300 nm).

In this chapter, we demonstrated for the first time electrical mutual phase-locking of two STOs. We showed that the power and the spectral coherence in the synchronized state are strongly improved (up to 1.6 μW and 550 kHz) and in coherence with the properties of the non-interacting oscillators. The observed spectral coherence and emitted power in the synchronized state confirmed that the power and the spectral coherence of N-synchronized oscillators should respectively be enhanced by a factor N^2 and N [45, 81]. The locking bandwidth is tuned from zero to a few MHz with an electrical delay line. Similar results has been obtained by sweeping I_{dc} and thus by changing the nonlinear behavior of the different oscillators. We thus highlighted that we can change the electrical coupling between two STOs by acting either on their intrinsic properties or on the electrical coupling vector. Last but not least, we obtained the maximum locking range at zero delay which makes possible the perspective of easily electrically synchronizing STO-arrays.

Conclusion

Within the last two decades, the commercialization of GMR reads head has represented the first large scale industrial implementation of spintronic based technologies. Recently, a new step have been reached with the development of a new generation of magnetic memories, called Magnetic Random Access Memories (MRAM), and which are already commercialized by major electronic companies. MRAMs take advantage of magnetoresistive effects and of the more recently discovered spin-transfer effects. More generally, spin transfer torque has revealed the potential of spintronics devices for a new generation of electronic component showing multiple functionalities, notably in the field of radio-frequency applications [93, 129]. Since their discovery in 2003, large expectations have risen around a new type of nano-scale oscillator called spin-torque oscillator (STO). Indeed, the spin transfer effect in a magnetic nanostructure offers the possibility to nonlinearly convert a dc current into a rf voltage, or a rf current in a dc voltage. Through intensive research studies, it has been shown that STOs could be considered in various classical integrated telecommunications devices such as rf-sources, rf detectors, self-homodyne detectors or for non-conventional applications such as bio-inspired or spin-logic devices. In this perspective, understanding and controlling the nonlinear magnetization dynamics and its effects on the microwave properties of an STO is a crucial issue. Another key issue concerns the interaction of a STO with its environment, especially with an oscillating external signal (rf field or rf-current sources, or a second STO in the case of mutual synchronization).

The main purpose of my thesis was to identify the mechanisms that control the properties of a spin-torque oscillator. I focused my work on vortex based STOs, given their high spectral coherence [119], and demonstrated that the magnetization dynamics of this type of STO can be governed by an external reference signal or through collective mode dynamics. We performed experimental studies, supported by analytical developments, to analyze the role of the dipolar coupling and of the spin-transfer torque in the autonomous and non-autonomous regimes of an STO, and we presented and discussed different perspectives for the development of STOs based spintronic devices.

Several key results can be highlighted from this thesis. We measured an STO with a large output signal (0.8 μW) and high spectral coherence (100 kHz at zero field and room temperature) in a hybrid magnetic tunnel junction with two coupled vortices. We demonstrated by frequential and time domain analysis that the coupled mode dynamics strongly differs with the magnetic configuration of the two vortices (chiralities and polarities) [114, 181]. In particular, the vortex core configuration was shown to influence not only the oscillator frequency but also the output emitted signal and the mode spectral coherence. In a dedicated chapter, we highlighted that mode coupling can also induced energy transfer between coupled modes which lead to drastic modifications in the STO dynamics and potentially to chaotic behaviors. These results highlight

that the excitation of collective modes allows the harnessing the rf-properties of a single and isolated oscillator.

Another approach to improve the performance of an STO is to lock its dynamics with an external signal [45, 53–56, 58, 139]. In our work, we showed that the high spectral coherence of a double vortex based STO permits the "perfect" phase-locking of a STO with an external rf-current [88]. To go beyond this analysis, we noticed that a 1 Hz minimum linewidth could be associated with the absence of phase slips, i.e desynchronization events, in the locked state. In this phase locked state, we reported a record phase noise of -90 dBc/Hz at 1 kHz offset.

We demonstrated that two spin-transfer torques can drive the locking process of a vortex based STO with an rf-current: the in-plane Slonczewski and Field-like torques. This gives the possibility to control with precision the oscillator locking process. In our double vortex based STO, we could even obtain a regime of multi-mode synchronization, i.e a simultaneous synchronization of the two coupled modes. More generally, the different spin-transfer torques, with the development of spin-orbitronics, which may allow locking of an STO, opens multiple possibilities to tune the STO rf-features. Such a degree of control, unexpected for a nano-scale oscillator, is particularly promising for the development of STO based nanodevices.

In the second part of my thesis, we presented a series of three different studies on how we can control the properties of a vortex based STO with the ST locking torques. These studies give key indications on the dynamics of an STO and show the potential of STOs for the development of nanoscale rf-sources, rf-detectors or bio-inspired devices.

First, we studied the implementation of a spin-torque oscillator in an on-chip phase locked loop. We presented preliminary results in which the STO phase noise is reduced by more than 30 dBc/Hz close to the frequency carrier. If the spectral coherence of a STO is expected to remain lower than the classically used VCO, their radiation hard properties are anticipated to make them excellent candidates as local oscillators for space telecommunications.

Then, we studied the resonant excitation of a vortex based STO with an rf-current in the sub-critical regime. This source of excitation induces a reversible change of the magnetic configuration, from vortex to uniform magnetization, at the resonant conditions. The associate reversible change of resistance R leads to a voltage response scalable with the TMR ratio. Record features, compared to classical Schottky diode, are reported with only 15% TMR junction [94, 199]. In the strong coupling regime of two magnetic vortices, we showed the possibility of exciting high frequency modes, associated with the core-core interaction, of a few GHz which is expected to enhance the frequency range of vortex based STO.

Finally, we experimentally demonstrated the mutual electrical synchronization of two vortex based STOs connected in parallel or in series. This is one of my most important results,

that had been predicted a decade ago [83] but never observed experimentally. It represents a breakthrough for both the improvement of STO properties and the development of STO bio-inspired devices. In the synchronized state, we showed a strong improvement of both the spectral coherence and the output power (500 kHz and 1.6 μW compared to 1 MHz and 0.4 μW in the non-interacting state). With an electrical delay line, we studied the impact of the phase shift between the two STOs on the synchronized regime and demonstrated that the best conditions for synchronization, i.e a minimum linewidth and a maximum power, can be obtained for zero delay. We demonstrated that this feature is related to the existence of a large Field-like torque in our junction. Thus we highlighted that the synchronized state is controlled by the amplitude and the symmetry of the locking torques. These promising results open the way for the synchronization of STO arrays at zero field and without electrical delays.

Beyond the improvement of the rf-features of STOs, the mutual synchronization of STOs is expected to be intriguing for spintronic associative memories [186]. For supervised associative memories, we can externally control the dynamics of STO based networks through the electrical coupling constant of each STO which can be achieved either with a tunable electrical delay or the ST locking torques. For non-supervised associative memories, a promising approach would be to introduce spintronic memristors between the STO based neurons. The memristor resistance state will drive the electrical coupling between the interconnected STO neurons. The learning rule of the memristor will be driven by the rectified voltage, i.e the spin-diode response, of the synchronized STOs. Finally, many other approaches could be considered given the tunable nature of the electrical coupling.

We demonstrated in this thesis that the physics of spin-transfer torques can still reveal promising perspectives for controlling the rf-properties of STOs. Fundamental issues still remain to be tackled in order to understand the underlying physics, such as the origins of the Field-like torque and of mode coupling. An alternative approach to spin-transfer torques is to develop STO driven by spin-orbit torques generated by pure spin-currents as seen in recent studies [200, 201]. Spin Hall or Rashba spin-orbit torques multiply the means to control STOs and offer new possibilities to synchronize STO networks [52]. Another promising approach to control the dynamics of STOs is the optical spin-transfer torque controlled by circularly polarized laser pulses [202, 203]. These two last approaches are particularly suitable to integrate STOs in magnonic devices for the development of spin-logic circuits in which the STOs will play the role of a spin-wave source [204].

I focused my work on vortex based STOs as they present higher thermal stabilities than other types of STOs (but also lower frequencies other STOs, far from the expected THz STOs based on antiferromagnets [76]). In recent years, it has been shown that new magnetic solitons like skyrmions [38, 205] could be stabilized with the DMI interaction in perpendicularly magnetized

multilayers. Sampaio et al. [206] demonstrated that these skyrmions are extremely small and easily movable [206]. They are also difficult to annihilate due to their topologically protected structure. Thus we can wonder if a topologically protected skyrmion could be easily manipulated and weakly sensitive to thermal fluctuations as expected for the potential skyrmion based STOs [207].

Ten years after their first study [32], spin-torque oscillators have not yet revealed all their potential. Promising applications have been targeted, in order to realize a spin logic circuit, bio-inspired spintronic devices and more classical rf-applications. Although there have been many promising results showing the feasibility and advantages associated with potential spin-torque oscillator applications, much remains to be done in order to understand aspects of the rich physics inherent in nanoscale and highly nonlinear systems.

Appendix A

Studied samples

In this thesis, we study the dynamics of vortex based spin-transfer nano-oscillators confined in nanodots. We mainly focus our research on double vortex based STOs but also demonstrate in some sections that our results can be extended to the single vortex case. All these different generations of samples have been grown by sputter deposition and patterned in the group of S. Yuasa in AIST (Tsukuba, Japan). These different types of junctions have been developed to optimize the rf-properties of the vortex based STOs.

A.1 Double vortex based STOs: Samples A-C

A.1.1 Hybrid magnetic tunnel junctions

An hybrid magnetic tunnel junction consists of a double vortex spin-valve on top of a magnetic tunnel junction with a synthetic antiferromagnet (SAF), i.e, // SAF / MgO (1.075 nm) / NiFe (X1 nm) / Cu (9.5 nm) / NiFe (X2 nm) with (X1,X2)=[(20,8) or (6,20)]. Each NiFe layers contain a magnetic vortex as the ground state. The dipolar coupling between the two vortices implies that the two gyrotropic modes associated to each vortex hybridize. Each of these two coupled modes being predominantly associated to one of the vortices, the one that will be effectively excited by spin torque depends on the sign of injected current and on the relative configuration of the system (as presented in Chap. 2).

The GMR ratio of the Cu based spin-valve is only about 2% and the Cu thickness is chosen so that the two vortex layers are only weakly coupled through dipolar interaction. The TMR ratio of the crystalline MgO is about 70%. The pinned SAF structure is made up of a PtMn (15 nm) / CoFe (2.5 nm) / Ru (0.85 nm) / CoFeB (3 nm) structure with a high coercive field

and a weak dipolar stray field. The PtMn antiferromagnetic layer imposes the magnetization of the CoFe layer to be parallel to its magnetization. The CoFeB layer is antiferromagnetically coupled with the CoFe layer by a RKKY coupling through the Ru layer.

Due to the large TMR ratio compared to the GMR ratio, we detect the output power associated with the dynamics of the NiFe vortex layer close to the MgO barrier. In our study, we study two kinds of samples that differ only by the position of the thick and thin vortex layers. The layer close to the MgO barrier is either the thin (6 nm) or the thick (20 nm) one. Thus for each vortex system we have a direct and deep insight into the dynamics of either the thin or the thick vortex layer. The generation of sample for which the thick vortex layer is close to the MgO barrier is called "Sample A", and the one for which the thin vortex layer is close to the MgO barrier is called "Sample B" (see Fig. A.1).

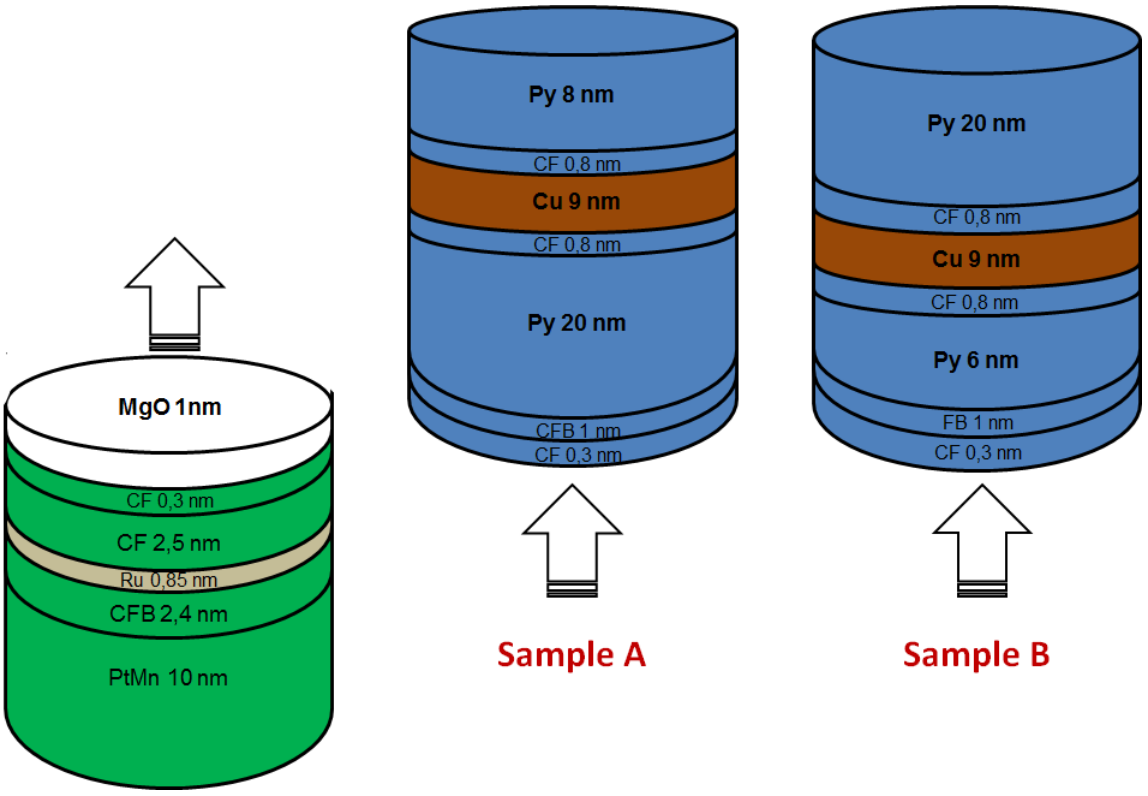

FIGURE A.1: Double vortex based hybrid magnetic tunnel junction: SAF / MgO (1.075 nm) / NiFe (X1 nm) / Cu (9.5 nm) / NiFe (X2 nm) with (X1,X2)=[Sample A (20,8) or Sample B (6,20)]

One should notice that the total dot thickness is much larger than standard MTJ. Thus, the etching process during the nanofabrication results in a conic shape pillar. Given that the etching has a 45° angle, a "Sample A" with a nominal 300 nm radius results in a 290 nm radius for the top thin NiFe layer and 340 nm radius for the bottom thick layer as shown in Fig. A.2.

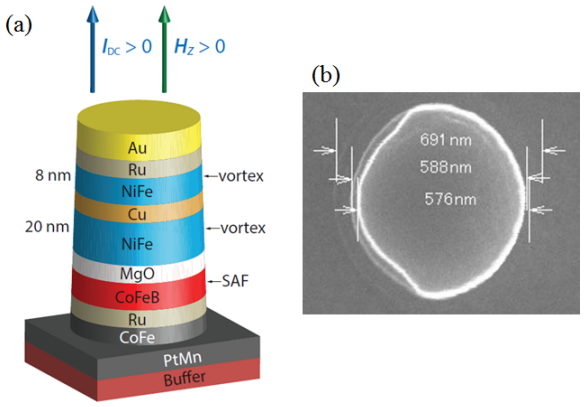

FIGURE A.2: (a) Schematic of an hybrid magnetic tunnel junction: a Cu based spin-valve system with the two vortex Py layer (8 nm at the top, 20 nm at the bottom) above a 1 nm MgO barrier and a CoFeB based synthetic antiferromagnet. (b) Image of a dot taken by electron beam microscopy. The dot radius was expected to be 300 nm. The three different measurements for the dot diameter indicate its conic shape.

A.1.2 Simple magnetic tunnel junctions: Sample C

In this thesis, we also study the dynamics of strongly coupled vortices. In this case, the stack is more simple. The system consists of a simple magnetic tunnel junction with one vortex in each ferromagnetic layer, i.e a NiFe (7 nm) / MgO (0.85 nm) / NiFe (11 nm) multilayer stack. The two vortices are strongly coupled due to the thin MgO spacer.

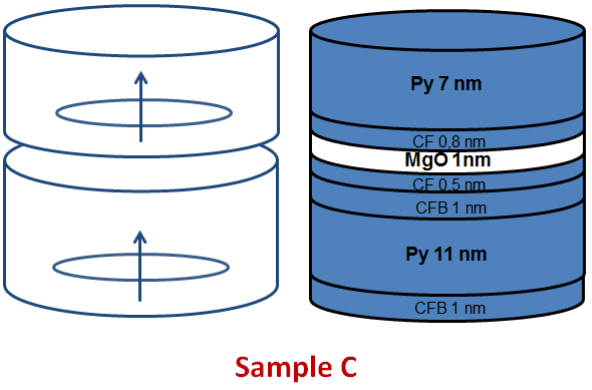

FIGURE A.3: Sample C: Double vortex based magnetic tunnel junction NiFe (7 nm) / MgO (0.85 nm) / NiFe (11 nm)

This system is expected to have a perfectly circular symmety. Thus for a circular motion, as for a gyrotropic motion, we do not expect to detect any emitted signal through the TMR effect. However, N. Locatelli et al. [43] experimentally observed coupled mode dynamics with transport measurements in similar spin-valves. This probably relies to the presence of edge defects. In our study, we will focus our works on high frequency modes associated with the regime of strong coupling. This generation of sample is called "Sample C" in the manuscript.

A.2 Single vortex based STOs: Sample D

In the spin-diode chapter (see Chap. 7), we study single vortex based STOs. This system consists of a magnetic tunnel junction with a synthetic antiferromagnet as a bottom polarizer and a vortex in the top free layer (see Fig. A.4). The TMR ratio of this sample generation, 8.5 %, is much lower than the other generations of sample due to the absence of the CoFe and CoFeB buffers that help the MgO crystallization and thus enhance the TMR ratio. Our study confirms that the locked regime is driven, both in single and double vortex systems, by the spin-transfer torques associated with the SAF (see Sec. 4.2.1.2 in Chap. 4).

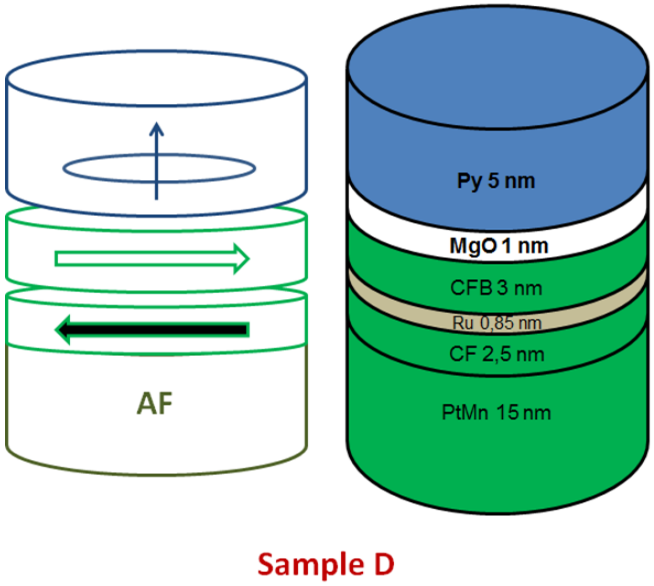

FIGURE A.4: Sample D: Single vortex based STO with a 5 nm permalloy free layer above a MgO barrier and a synthetic antiferromagnet polarizer

A.3 Experimental setup

The sample is placed on a gold plated holder that is connected to the ground of the circuit (see Fig. A.5.c). We use a wire bonding machine to connect with gold wires one sample electrode to a 50 Ω electrical line and the other to the holder. The holder is then put in a cavity located in an electromagnet and connected to the electrical circuit with a SMA cable as shown in Fig. A.5. b. In our electrical circuit, we use a bias tee that permits to decouple the rf and the dc signals (see Fig. A.5. a). The dc port is linked to a dc source that supplies the STO. In parallel, a nanovoltmeter detects the voltage at the STO terminals. A resistance bridge is placed between the STO and the dc source to protect the STO from high voltage fluctuations. The rf-port of the bias tee is either connected to a spectrum analyzer or to an oscilloscope. To

study the non-autonomous regime, we add a power splitter after the rf port. This permits to keep the detection scheme and to supply the STO with an rf current emitted by a rf source or a second STO.

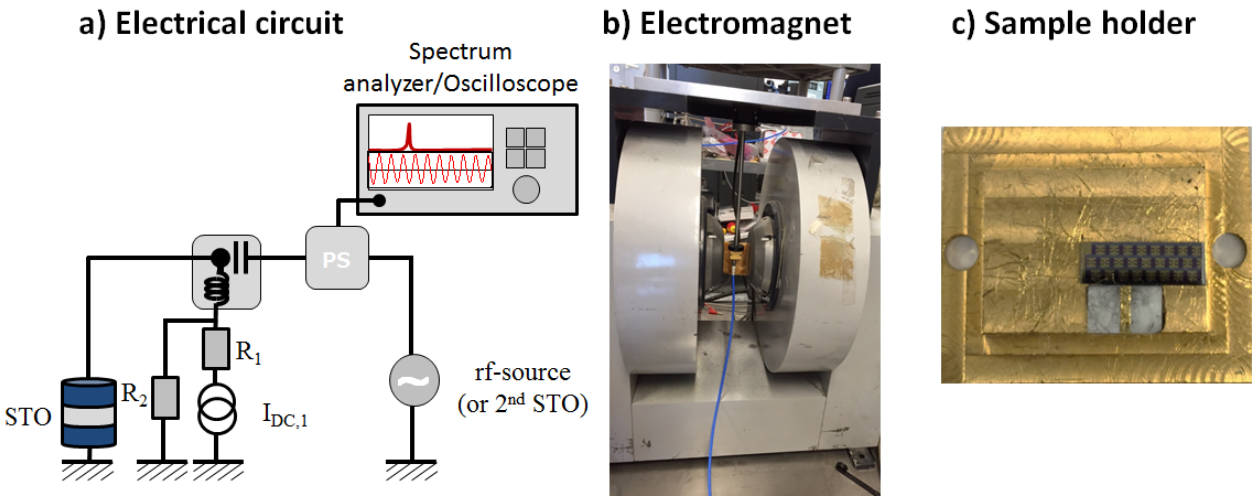

FIGURE A.5: (a) Electrical setup: the rf-source is a Agilent E8257D, the dc-source a Keythley 6221 and the nanovolmeter is a Keythley 2182. The spectrum analyzer is a Agilent E4446A and the oscilloscope is also a Agilent. The resistance bridge used to protect the STO consists of two resistances R1 and R2 respectively equal to 1 and 100 $k\Omega$. (b) Electromagnet, supplied by two Keypco sources, in which we put the sample holder (c) Sample holder: one STO terminal is connected to a 50 Ω electrical line and the other one to the gold holder

Appendix B

Appendix B: Locking ratio in the self-resonant state

In Chap. 5, we have seen in a double vortex based STO that an excited mode could synchronize with an rf-current source through the fundamental resonance of a damped mode. This is a general behavior that offers multiple possibilities to synchronize an STO as we will see now. Here we consider a sample A (see Appendix A) with 400 nm diameter for which the frequency ratio between the two coupled modes is not an integer.

In Fig. B.1, we plot the locking ratio $\Omega = F_s/f_{sto}$ of STOs as a function of the frequency of the rf-source. The locked states of an oscillator are associated to plateau and generally to fractional winding numbers. Here, we focus our study for locking ratios between 2 and 3. For our vortex STO, we observe the expected locking ranges associated with the second ($\Omega = 2$) and the third (Ω) harmonics but also for an extra range of locking. Surprisingly, it is difficult to determine in this locking state if the associated locking ratio has a rational value or not. We measure a locking ratio around 2.55 and its closest fraction is 51/20. This give one more clue that we may face with chaotic synchronization that often present irrational winding number [81, 178]. Furthermore, we also want to point out that by controlling the frequency ratio of the two modes (with the dc-current, the field or by designing the aspect ratio of the two layers) we obtain efficient and tunable fractional locking that cannot be obtain with classical nonlinear behavior [53, 88].

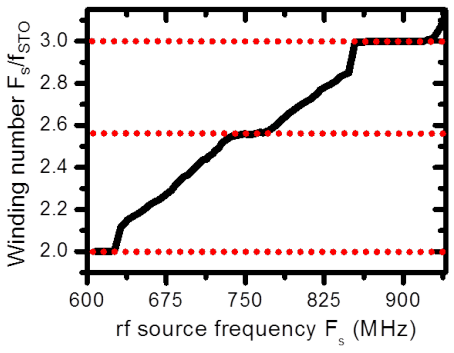

FIGURE B.1: Locking ratio of depending on the rf-current source frequency (We focus our study for F_s between $[2f_0 : 3f_0]$. The experimental conditions are : $H_{perp} = 320kA/m$, $I_{dc} = -30mA$, and the dot diameter is of 800 nm.)

Appendix C

Appendix C: Principle of the phase locked loop

A phase locked loop contains a controllable oscillator, a error detector block that generates a signal proportional to the phase difference between the oscillator signal and the reference signal, a low pass filter that determines the loop dynamics and eliminates high frequency spurious and a feedback path (see Fig. C.1). In this annexe, we present the function of these different elements.

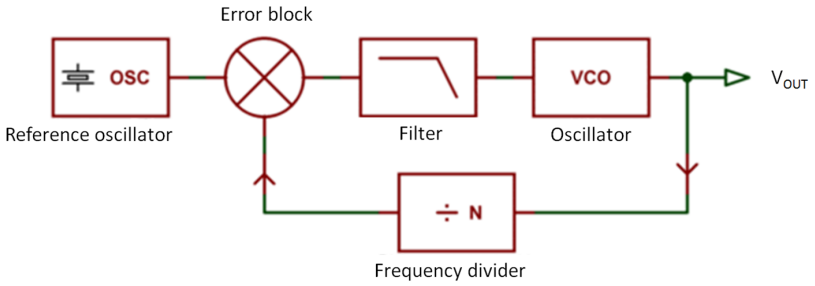

FIGURE C.1: Schema of a phase locked loop. The PLL consists in a error detector block, a frequency divider, a filter, a slave oscillator and a reference oscillator.

C.1 Error detector block

A frequency mixer represent the most simple error detector block that can be used in PLL. For a reference signal at f_0 and an oscillator at f frequency, it generates two responses signals: one low frequency signal at $(f - f_0)$ and one high frequency signal at $(f + f_0)$. Higher order spurs are also generated in nonlinear system. The low pass filter, discussed later on, eliminates the spurious peaks and generates a feedback signal proportional to the low frequency signal.

When the PLL is locked in frequency, the modulation amplitude of the low frequency signal is expressed as $A_{f-f_0}(t) = A_f A_{f_0}/2cos(\Phi_f - \Phi_{f,0})$ and is proportional to the phase difference between the oscillator and the reference signals. Thus the oscillator dynamics can be controlled through the amplitude of the feedback voltage.

Other simple error detectors like XOR phase detectors can be used. However in commercial devices, the error detector generally combines more complex structures with a frequency phase detector and a charge pump. A frequency phase detector has two particularities: (i) it can lock when the reference and the input signals have different frequencies (ii) it gives a voltage response proportional to a 180° phase difference and not only to a 90° phase difference as simple phase detectors. Frequency phase detectors use flip-flop that consists in a circuit made of logic NAND and NOR gates and which has two stables states that are controlled by the two inputs of the circuit. A widely used frequency phase detector consists of JK flip-flop. As represented in Fig. C.2, this type of phase detector is edge-triggered.

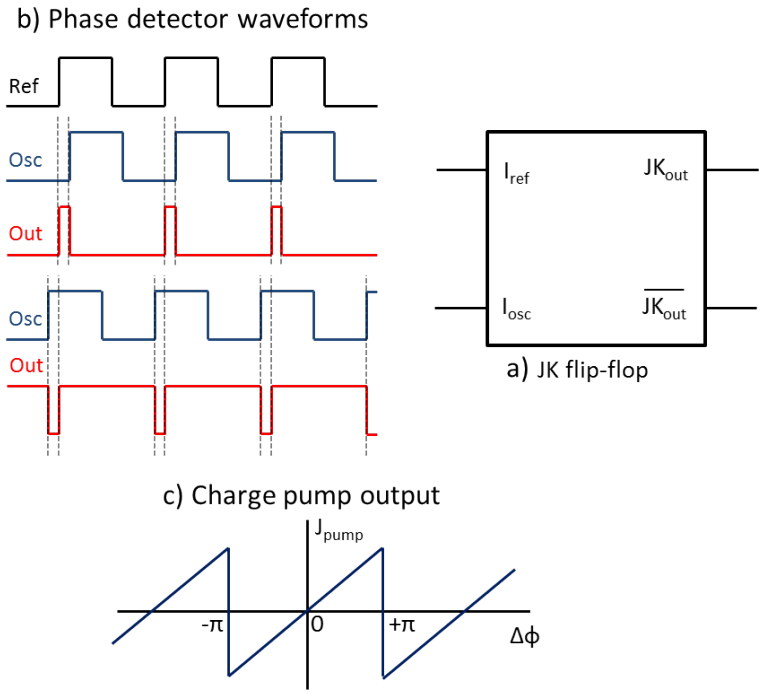

FIGURE C.2: (a) Schema of a JK flip-flop (b) Phase detector wave form for positive and negative phase difference between the oscillator and the reference (c) Charge pump output

The characteristic equation of the JK flip-flop is $JK_{out,next} = I_{ref} JK_{out} + I_{osc} J\bar{K}_{out}$. Thus the output signal of the flip-flop is not the same for positive or negative phase difference. It must be noted that frequency phase detector can be limited by the toggling frequency of the flip-flop.

Frequency phase detectors are often used with charge pump to deliver not a pulsed but continuous voltage response proportional to the phase shift. This type of electrical device used capacitors to store entrance energy and deliver softened voltages. This permits to avoid the

use of dead-band or the presence of small pulses even when the phase are locked. However the charge pump frequency is generally low. Thus a charge pump can drastically reduce the PLL bandwidth down to ω_p the charge pump frequency.

C.2 Loop filter

The function of the loop filter is to eliminate the high frequency signal, i.e the spurious peaks, and to control the bandwidth of the loop. The cut-off frequency determines the speed of change in voltage. High-frequency cut-off filters enable faster changes but can let unwanted frequencies pass. Similarly the loop gain determines the sensitivity of the loop to the phase difference.

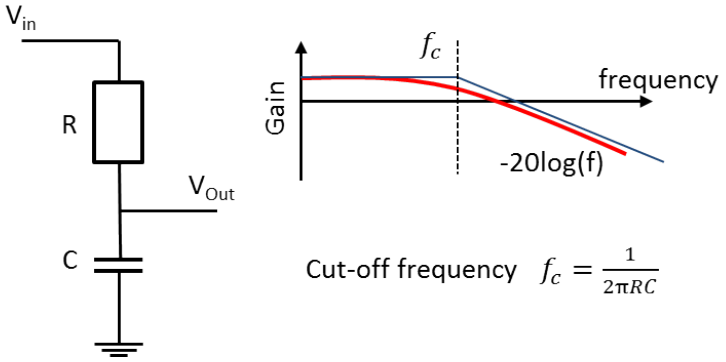

FIGURE C.3: Main characteristics of a first order RC filter

However the stability of the phase locked loop is also governed by the gain and the cut-off frequency of the loop filter (see for example first order filter in Fig. C.3). For too large gain and cut-off frequencies, resonance effects associated to the high frequency peaks can appear and destabilize the PLL. A careful design of the loop is thus necessary to face all these different issues.

C.3 Frequency divider with a "divide-by-n" binary counter

In rf-applications such as a frequency generator at a multiple of the reference frequency, it is necessary to add a frequency divider in the feedback path. The oscillator signal is then compared to a reference signal generated by a much more stable low frequency oscillator like quartz. A half-frequency divider can be obtained with D flip-flop, i.e a pair of cross coupled NOR gates (see Fig. C.4). The Q bar output is connected to the D-input and the data to the CLK input. If both input are low or high, the output is low. If one of them is high, it is high. Large division ratio are obtained with cascades of D flip-flops.

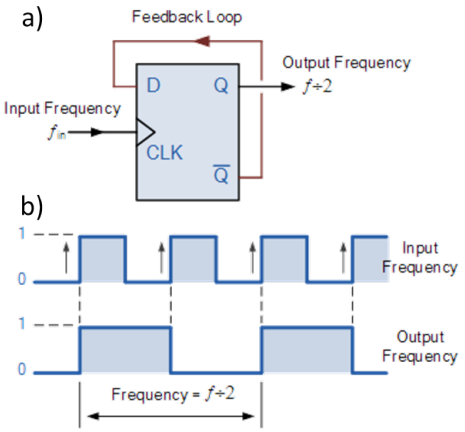

FIGURE C.4: (a) Schema of a D flip-flop frequency divider (b) Phase detector wave form [Adapted from www.electronics-tutorials.ws]

Appendix D

Résumé en français

Mes travaux de thèse concernent l'un des développements prometteurs de l'électronique de spin à travers l'étude de nano-oscillateurs à transfert de spin (STO). Ces nano-oscillateurs prennent appui sur deux mécanismes de base régissant le transport de spin: la magnéto-résistance géante et le transfert de spin. En 1988, A. Fert[2] et P. Grunberg [3] démontrèrent que la résistance aux bornes d'une vanne de spin, i.e un empilement de couches minces ferromagnétiques séparées par une couche non-magnétique, varie fortement selon l'orientation des couches minces. En 1996, J. Slonczewski [9] prédit qu'il est possible d'agir sur l'aimantation d'une nano-couche ferromagnétique en la faisant traverser par un courant polarisé en spin. Dans un dispositif de type vanne de spin, les electrons d'un courant traversant cet empilement se polarise selon la direction d'aimantation de la première couche, fixe et dite polarisatrice, puis traverse la couche mince non-magnétique, en conservant sa direction de spin, exerçant ensuite un torque sur l'aimantation de la seconde couche magnétique. En 1998, Tsoi et al.[120] introduisit les bases du concept de nano-oscillateurs à transfert de spin en montrant dans une vanne de spin que le courant pouvait entrainer l'aimantation dans un régime de précessions auto-entretenues. Un nano-oscillateur à transfert de spin convertit ainsi un courant continu en oscillations de résistance et de tension par l'effet de magnétorésistance de la vanne de spin. La fréquence des oscillations est alors déterminée par le mode magnétique excité dans le système et peut aller de 100 MHz à 70 GHz selon le type d'oscillateurs[30]. Dans la dernière décennie, de nombreuses études ont mis en évidence les atouts de ces nano-oscillateurs pour le développement d'une nouvelle génération de dispositifs radio-fréquences, allant d'applications classiques de type détecteurs/émetteurs à des dispositifs bio-inspirés de type mémoires associatives[114].

Au début de ma thèse la puissance (de l'ordre du nW) et la cohérence spectrale (largeurs de raie supérieures au MHz) de ces oscillateurs restaient trop faibles pour les applications envisagées. L'objectif principal de ma thèse fut d'identifier, de comprendre les mécanismes régissant la

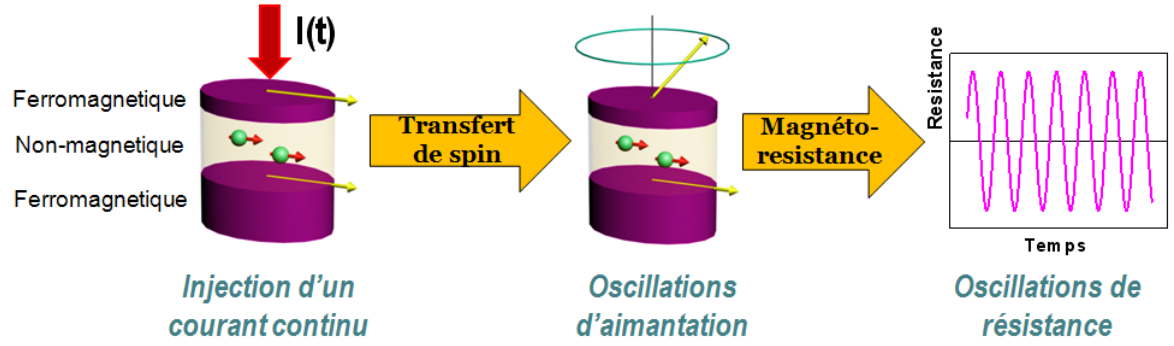

FIGURE D.1: Schéma de principe de l'oscillateur à transfert de spin : lorsqu'un courant traverse un empilement composé de deux couches ferromagnétiques séparées par une couche non-magnétique, le phénomène de transfert de spin induit une précession de l'aimantation. La variation relative des aimantations de chacune des couches magnétiques entraîne alors une oscillation de résistance par le phénomène de magnétorésistance géante, et a fortiori une oscillation de la tension aux bornes du dispositif.

dynamique d'aimantation d'un oscillateur à transfert de spin, et de proposer différentes pistes pour controler et améliorer leurs propriétés radiofréquences. Mes travaux de thèse se sont en particulier focalisés sur le cas d'oscillateurs à base de vortex magnétiques et ont été effectués sur des échantillons réalisés dans le groupe de S. Yuasa à partir de jonctions tunnel magnétiques, i.e une vanne de spin avec une couche non-magnétique isolante, afin d'augmenter la puissance émise par les oscillateurs. Au cours de ma thèse, je me suis intéressé aux différents regimes d'excitationd'un STNO en commencant par l"étude de la dynamique d'aimantation de modes couplés dans le cas d'un seul STNO dans le régime auto-oscillant. J'ai par la suite cherché à mettre en évidence différentes approches permettant de controler les propriétés d'un oscillateur avec un signal extérieur de référence (excitation résonante, paramétrique ou synchronisation unidirectionnelle). Suite à cette étude, j'ai développé une approche novatrice pour améliorer la cohérence spectrale et la puissance des STNOs en réussissant à synchroniser mutuellement deux oscillateurs en utilisant les courants rf émis par chacun d'entre eux comme vecteur de couplage.

D.1 Etude des modes couplés dans des spin-valves hybrides à deux vortex magnétiques

Les nanopiliers étudiés comportent une vanne de spin avec un vortex dans chacune des deux couches magnétiques. L'électrode magnétique inférieure est commune avec une jonction tunnel magnétique permettant de détecter la dynamique d'aimantation du vortex de la couche commune (couplé dipolairement avec le vortex de la couche supérieure) et d'émettre de forte puissance (qui est proportionnelle au carré de la TMR). On détecte ainsi dans la dynamique du vortex de la couche inférieure deux modes couplés (voir Fig. D.2), respectivement excité et

amorti par transfert de spin (ST) selon le signe du courant. Le mode excité par ST correspond à celui dont la fréquence est proche du mode gyrotropique du vortex présent dans la couche excité par ST.

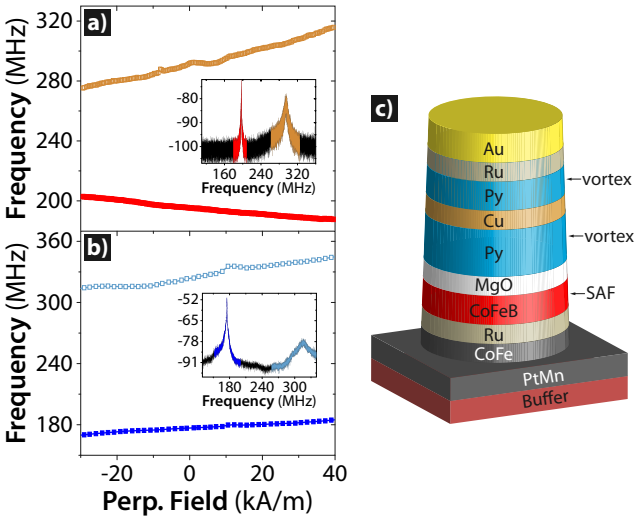

FIGURE D.2: (a) (b) Dépendance de la fréquence du mode "excité" basse fréquence et du mode "dampé" haute fréquence avec le champ magnétique appliqué pour les configurations AP (a) et P (b) pour un courant $I_{dc} = -16$ mA. Inset: Spectres fréquentiels du signal émis à $H_{ext} = 0$ kA/m pour les configurations AP (a) et P (b)/(c) Schéma des dispositifs étudiés Selon les configurations relatives des deux vortex (chiralités des corps de vortex et polarités des cœurs de vortex opposées ou parallèles), différents modes couplés peuvent être excités. On observe expérimentalement que les propriétés hyperfréquences des modes excités pour des chiralités parallèles et des polarités parallèles (Pc) ou antiparallèles (APc) sont très différentes (voir Fig. D.3.a-b). Dans notre étude (pour $I_{dc} > 0$), le mode excité (dampé) par ST est proche en fréquence du mode gyrotropique de la couche fine (épaisse).

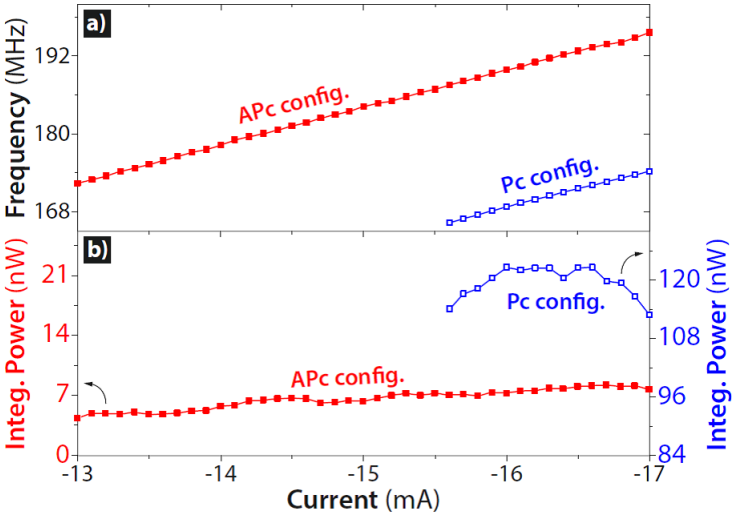

FIGURE D.3: Evolution de la fréquence (a) et de la puissance émise (b) en fonction du courant continu appliqué pour les configurations Pc (points bleus) et APc (points rouges). Les mesures sont effectuées sans champ appliqué et à température ambiante.

Sur la Fig. D.3, on peut noter que la puissance détectée est plus élevée et la fréquence est plus faible dans la configuration APc sur toute la gamme de courant mesurée. Ces observations

expérimentales, confirmées par des simulations micro-magnétiques faites en collaboration avec F. Abreu Araujo à Louvain-la-Neuve, ont pu être expliqué par un modèle analytique que nous avons développé. En introduisant, un terme de couplage dipolaire dans l'équation de Thiele décrivant la dynamique de chacune des couches nous avons pu prédire les fréquences des modes observées (voir Fig. D.4) ainsi que la délocalisation des différents modes couplés dans chacune des couches. En configuration APc, le ratio est beaucoup plus faible qu'en configuration Pc. En effet, le sens de giration d'un vortex magnétique est usuellement défini par sa polarité[118]. Dans le cas de polarités APc, le vortex de la couche épaisse suit la dynamique de celui de la couche fine et a donc un sens de giration opposé à son sens naturel. La frustration dans un tel système explique que le mode excité par ST soit davantage délocalisé en configuration Pc qu'en configuration APc.

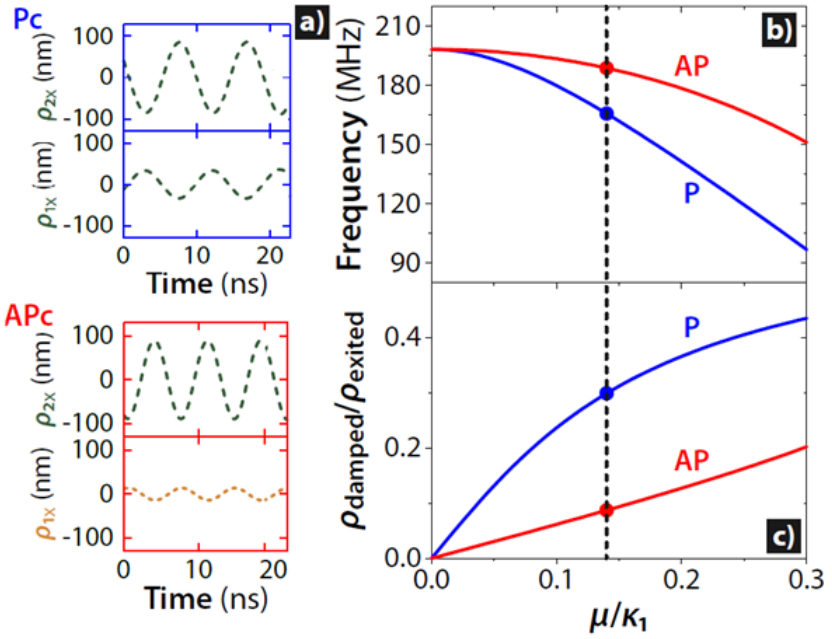

FIGURE D.4: (a) Simulations micro-magnétiques des rayons d'oscillations dans les deux couches vortex pour les configurations Pc et APc. (b) Dépendance de la fréquence des modes couplés excités selon l'intensité μ du couplage dipolaire pour les deux configurations Pc et APc. (c) Evolution du rapport des rayons d'oscillations dans les deux couches pour les deux configurations. (Les points rouge et bleu ainsi que la ligne noire correspondent au cas expérimental). Les trois figures correspondent au cas d'un courant $I_{dc} = 16$ mA sans champ appliqué.

En parallèle de cette étude sur l'effet de la polarité des cœurs sur les propriétés intrinsèques des modes couplés (fréquence et puissance), nous avons observé que la cohérence spectrale du mode excité était beaucoup plus élevée en configuration APc. Par des mesures combinées dans le domaine temporel et en fréquence, nous avons pu démontrer une forte réduction des non linéarités du système dans la configuration APc. Cette réduction des non-linéarités, et donc du couplage phase/amplitude, est liée au courant de seuil plus faible dans cette configuration (15.8 mA en Pc contre 13 mA en APc). La répulsion des cœurs en configuration APc aide à démarrer des auto-oscillations ce qui explique que l'amortissement effectif du STO soit plus élevé dans

cette configuration pour un même courant appliqué[45]. Cette stabilisation plus rapide de la dynamique de l'oscillateur explique la plus faible non-linéarité[45] en configuration APc et donc les plus faibles largeurs de raies [9] observées en polarités antiparallèles. Dans cette première étude, nous avons ainsi pu mettre en évidence la possibilité de modifier drastiquement les caractéristiques radiofréquences d'un STO avec deux vortex couplés en jouant sur le couplage magnétique entre les deux vortex. Le couplage de mode est ainsi aujourd'hui considéré comme une approche originale pour améliorer les propriétés radiofréquences d'un oscillateur à transfert de spin[181].

D.2 Synchronisation d'un oscillateur avec une source radiofréquence de référence

Différentes stratégies sont envisagées dans la perspective d'augmenter la cohérence spectrale d'un STO comme la synchronisation de réseaux de STO[60, 82] ou l'auto-synchronisation[158]. Dans cette optique, la capacité des STO à se synchroniser avec des sources extérieures oscillantes (courant ou champ) sur de larges gammes de fréquences avec une cohérence spectrale maximale est un objectif primordial[52, 53, 58, 66]. Dans cette seconde étude, nous reportons tout d'abord la possibilité de synchroniser le système précédent avec un courant rf dont la fréquence est proche d'un multiple (qf_0) de la fréquence de l'oscillateur ou d'une fraction (f_0/q avec q un entier) de celle-ci comme on peut le voir sur la Fig. D.5. Cette seconde observation permet d'envisager d'utiliser un STO non plus seulement comme un diviseur de fréquence comme c'était le cas jusqu'à présent mais aussi comme un multiplicateur de fréquence.

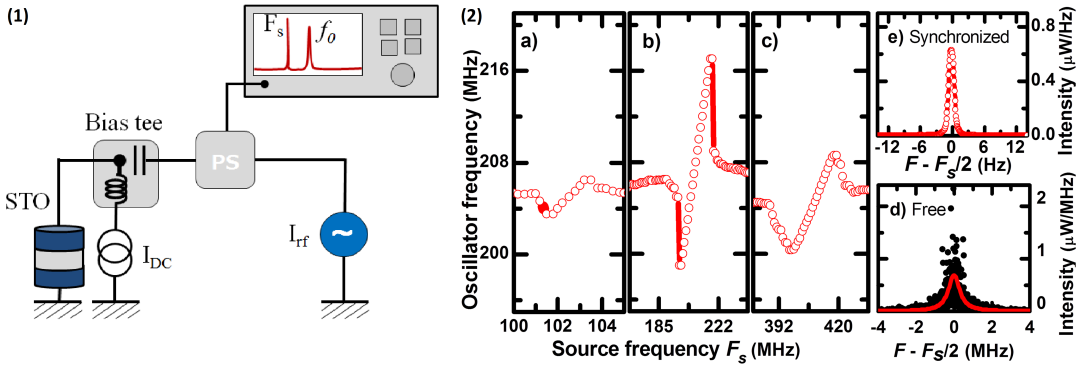

FIGURE D.5: Schéma électrique du banc de mesure : le STO est alimenté par une source de courant continu I_{dc}, auto-oscille à une fréquence f_0, et peut se synchroniser par une source de courant radiofréquence Irf à une fréquence Fs. Les signaux rf et dc sont séparés par un bias tee, et le signal rf-détecté à l'aide d'un analyseur de spectre connecté au dispositif électrique par un diviseur de puissance. (2) Fréquence du STO en fonction de la fréquence F_s de la source externe autour de $f_0/2$ (a), f_0 (b) et $2f_0$ (c). Signal dans l'état auto-oscillant (d) et dans l'état synchronisé pour $F_s = 2f_0$ (e) (conditions expérimentales : $I_{rf} = 2$ mA, $I_{dc} = 11$ mA, et aucun champ magnétique n'est appliqué)

L'état synchronisé que nous mesurons présente par ailleurs une largeur de raie d'1 Hz (voir Fig. D.5.e), similaire à celle de la source, et bien en dessous des quelques kHz observés dans toutes les études précédentes. Par des mesures temporelles, nous avons pu mettre en évidence que cet état de pure synchronisation correspond à un bruit de phase plat autour de la porteuse (cf Fig. D.6.a-c, courbes violette, rouge et bleu foncé). Cette situation est drastiquement différente du régime auto-oscillant où le bruit de phase évolue en $1/f^2$ autour de la porteuse (cf Fig. D.6.a-c, courbes noires). Pour de faibles amplitudes de courant rf, nous observons une situation intermédiaire où le bruit de phase est réduit mais où une dépendance en $1/f^2$ persiste autour de la porteuse (cf Fig. D.6.a-c, courbes rose, orange et bleu clair).

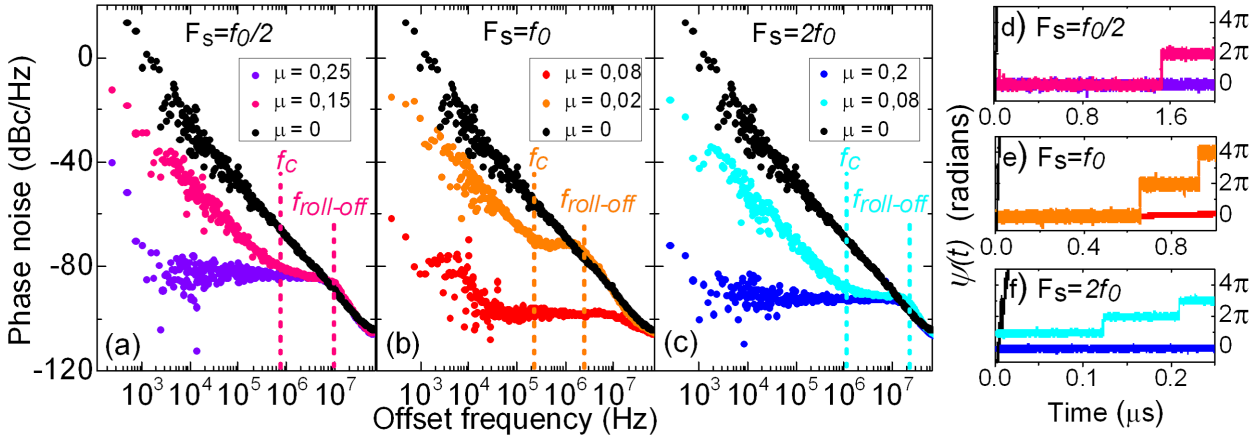

FIGURE D.6: Bruit de phase du STO synchronisé pour différentes amplitudes de courant rf $\mu = I_{rf}/I_{dc}$ pour une fréquence de synchronisation F_s égale à $f_0/2$ (a), f_0 (b) et $2f_0$ (c). (d-f) Déviation de la phase dans l'état synchronisé pour les différentes courbes de bruit de phase. (conditions expérimentales : I_{dc} = 11 mA et aucun champ magnétique n'est appliqué)

Ces trois situations (dépendance en $1/f^2$, bruit de phase plat et situation intermédiaire) peuvent être respectivement corrélées à une diffusion de la phase au cours du temps effet, à une absence de diffusion et à une situation intermédiaire où la phase du STO suit parfaitement celle de la source rf excepté à des évènements quasi-ponctuelles appelées glissement de phase (voir Fig. D.6.d-f). En effet, les fluctuations thermiques peuvent générer des évènements de désynchronisation/resynchronisation, appelés glissements de phase, lors desquels le STO perd ou gagne une fraction de période par rapport à celle de l'oscillateur. Cette fraction de période est déterminée par la fréquence du signal de référence et par le nombre de positions stables pour une période d'oscillations. Dans le cas d'un STO à base de vortex, l'efficacité du processus de synchronisation est telle qu'il est possible de ne pas observer de glissement de phase dans l'état synchronisé pour des temps de mesures de l'ordre de la minute.

Pour mieux comprendre la synchronisation de ce type d'oscillateurs, nous avons développé un modèle analytique qui nous a permis d'identifier les deux couples de transfert de spin impliqués dans le mécanisme de synchronisation : un couple planaire de Slonczewski ($\Lambda_{SL,//}$) et un couple planaire de Field-like ($\Lambda_{FL,//}$) associé au SAF de la jonction tunnel magnétique (MTJ). Ces

deux couples permettent de synchroniser sans effet de seuil un STO à base de vortex avec un courant rf mais l'un agit sur le cœur de vortex et l'autre sur le corps du vortex. De plus, ils possèdent des symétries différentes et sont en quadrature de phase. Le déphasage entre les oscillations du courant rf injecté et celles de du STO dépendra donc, comme nous le verrons par la suite, fortement des efficacités respectives des couples mis en jeu. Expérimentalement, nous avons étudié l'évolution du bruit de phase dans l'état synchronisé selon l'amplitude de la force de synchronisation pour évaluer la contribution de chacun des couples (voir Fig. D.7). Nous avons ainsi pu mettre en évidence l'importance du couple de Field-like dans le processus de synchronisation. En effet, le ratio des deux torques $(\Lambda_{FL,//}/\Lambda_{SL,//})$ est égal à $(2R\xi_{FL}/b)$. Dans nos expériences, les rayons R des nanopiliers sont au minimum de 100 nm, le rayon d'un cœur de vortex b de l'ordre de 10 nm et l'efficacité du Field-like ξ_{FL} est mesurée à 0.4 (voir Fig. D.7), comme dans de précédentes études sur des MTJ, ce qui implique un ratio $\Lambda_{FL,//}/\Lambda_{SL,//}$ supérieur à 10.

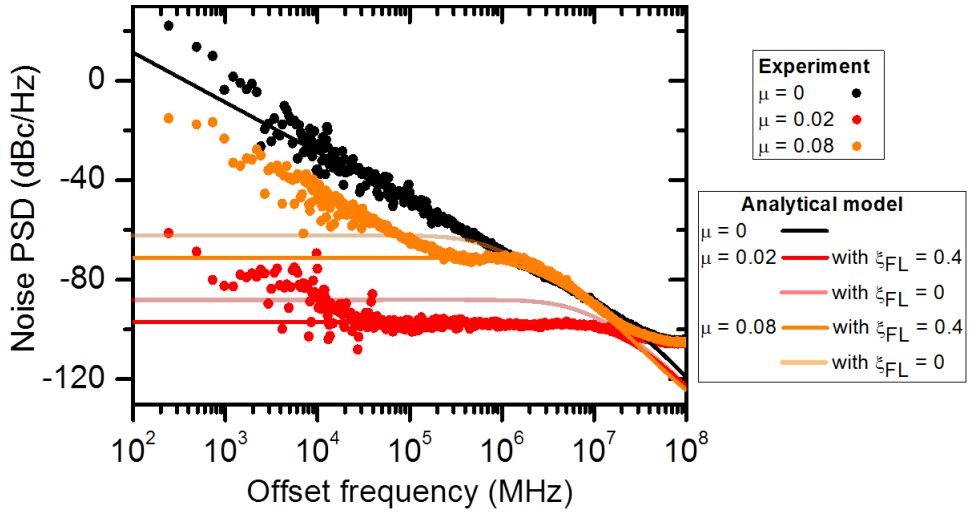

FIGURE D.7: Bruit de phase expérimentale pour $F_s = f_0$ pour $\mu = 0$ (points noirs), $\mu = 0.08$ (points oranges), $\mu = 0.2$ (points rouges) sans champ appliqué et pour $I_{dc} = +11$ mA. Bruit de phase modelisé analytiquement pour$\xi_{FL} = 0$ (lignes orange et rouge atténuées) et $\xi_{FL} = 0.4$ (lignes orange et rouge).

Contrairement aux STOs à aimantation uniforme, le processus de synchronisation de ces STO à base de vortex est dirigé par un couple de transfert de spin de type Field-like[88]. L'efficacité importante de ce couple dans les jonctions tunnels magnétiques utilisées explique la facilité à synchroniser et à stabiliser la dynamique des STOs étudiés avec un courant rf.

D.3 Potentielle application : Renversement réversible de l'aimantation d'un STO pour la détection de signaux radiofréquences

Avant de nous intéresser à la synchronisation mutuelle d'oscillateurs, nous avons cherché à prendre avantage de la forte efficacité du couple de Field-like dans ces STOs à base de vortex pour développer un nouveau dispositif de détection radiofréquence basé sur un renversement réversible de l'aimantation d'un STO.

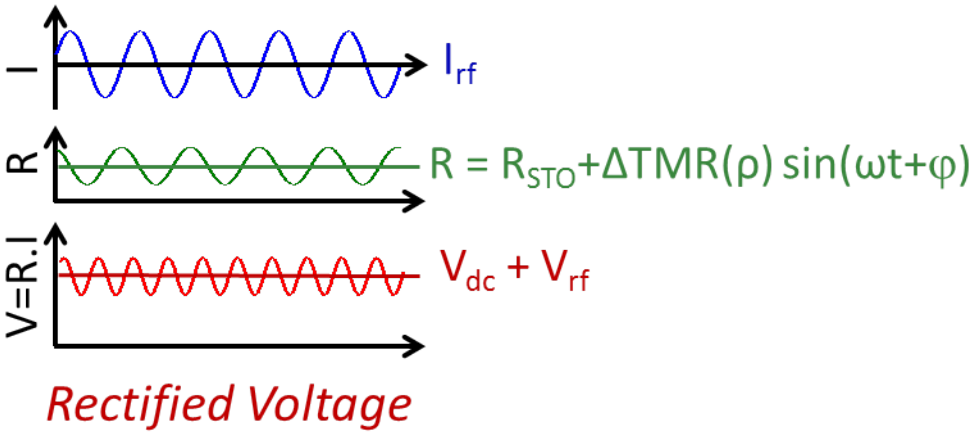

FIGURE D.8: Principe de l'effet spin-diode. Dans les conditions résonantes d'excitation, le produit du courant rf injecté dans le STO et des oscillations de magnétorésistance mènent à une tension en moyenne non-nulle aux bornes du STO.

Au début de cette thèse, les STOs étaient déjà présentés comme de potentiels candidats au remplacement des diodes Schottky utilisées pour la détection radiofréquence. L'excitation d'un STO dans un régime non-entretenu avec un courant rf permet d'observer un effet de rectification de tension lorsque la fréquence du courant rf est proche de la fréquence propre de l'oscillateur. Cet effet appelé « spin-diode », en référence aux diodes Schottky, consiste au fait que le produit des oscillations du courant rf et de la résistance du STO (liées aux oscillations d'aimantation par l'effet de magnéto-résistance) peut générer une tension continu[90]. Le niveau de tension détecté dépend ainsi de l'amplitude du courant rf et des oscillations d'aimantation ainsi que de l'effet de magnétorésistance. En 2013, Miwa et al. [91] démontrèrent que l'effet de spin-diode dans un STO à aimantation perpendiculaire peut être plus efficace que celui d'une diode Schottky. Dans notre étude, nous avons tout d'abord reproduit l'expérience de Miwa (voir Fig. D.9) dans le cas d'un STO à base de vortex et j'ai développé un modèle analytique qui montre que le processus d'excitation dépend là encore de l'efficacité du couple de Field-like.

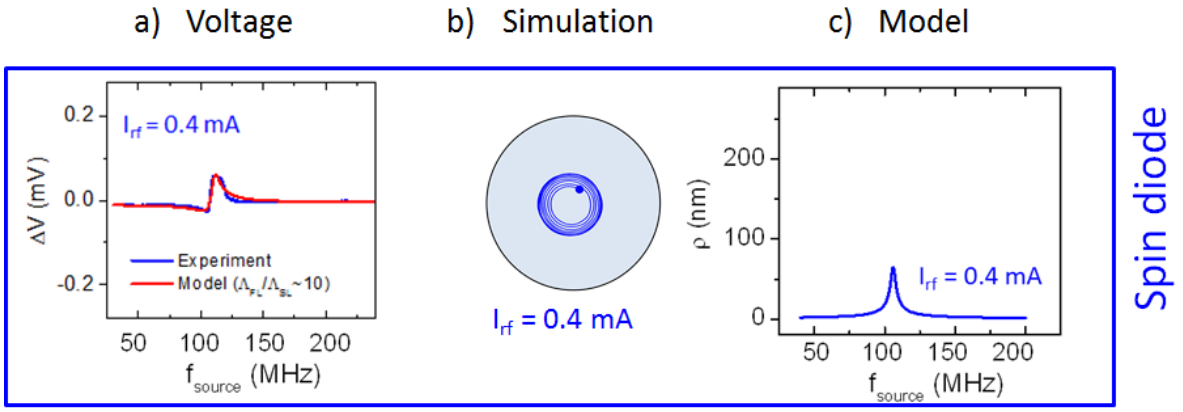

FIGURE D.9: (a) Tension mesurée en fonction de la fréquence de la source radiofréquence pour I_{rf} = 0.4 mA, I_{dc} = 0 mA et H_{perp} = 160 kA/m (en rouge le signal analytique attendue pour ξ_{FL} = 0.4) (b) Simulations micro-magnétiques du régime transitoire d'excitation pour f_{source} = 100 MHz (c) Modélisation analytique du rayon d'excitation dans les conditions expérimentales.

Cependant pour de fortes amplitudes d'excitation, le signal rectificatif disparait en l'absence de courant continu comme nous pouvons le noter sur la Fig. D.10.a. A l'inverse, lorsqu'on augmente le courant continu on observe l'apparition d'une forte tension de rectification (voir inset de la Fig. D.10.a). Par des simulations micromagnétiques, il a été mis en évidence que pour de fortes excitation rf le cœur de vortex est expulsé du dot de manière réversible autour de la fréquence propre du STO. La couche libre du STO passe alors d'une aimantation vortex oscillante à un état magnétique statique proche d'une aimantation planaire uniforme. Ce renversement magnétique est associé à un changement de résistance qui peut être détecté en appliquant un courant continu. Le signal détecté est alors proportionnel non plus au courant radiofréquence mais au courant dc appliqué. Ce schéma de détection permet ainsi d'accroitre considérablement le signal rectificatif, au délà de l'état de l'art des diode Schottky et de l'effet classique de type spin-diode dans les STOs.

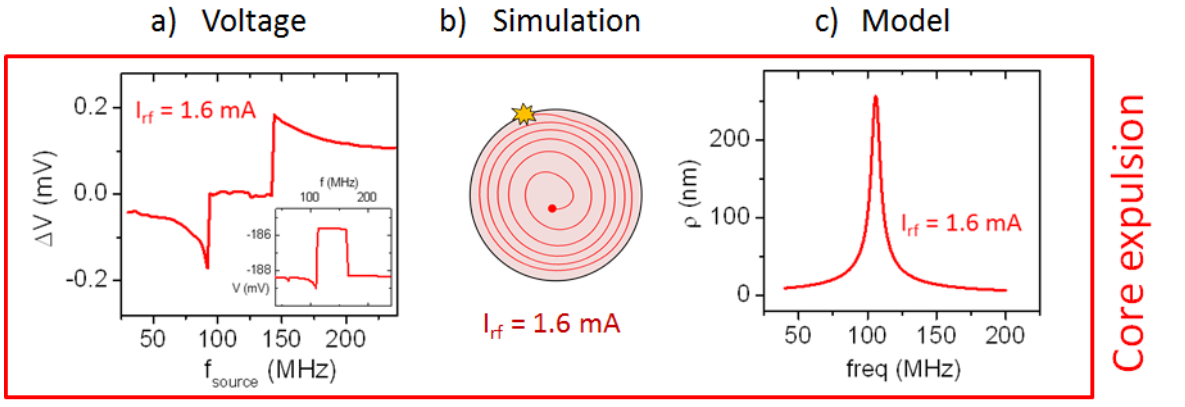

FIGURE D.10: (a) Tension mesurée en fonction de la fréquence de la source radiofréquence pour I_{rf} = 1.6 mA, I_{dc} = 0 mA et H_{perp} = 160 kA/m (Inset montre la réponse en tension pour I_{dc} = 5 mA) (b) Simulations micro-magnétiques du régime transitoire d'excitation pour f_{source} = 100 MHz (c) Modélisation analytique du rayon d'excitation dans les conditions expérimentales.

D.4 Synchronisation mutuelle de STOs par couplage électrique à partir de leurs courants émis

Un enjeu crucial pour les nano-oscillateurs à transfert de spin est de passer de la synchronisation d'un STO et avec un signal extérieur à la synchronisation mutuelle d'oscillateurs. La synchronisation mutuelle d'oscillateurs est un phénomène observé et conceptualisé par Huygens au XVIIème siècle dans le cas de deux pendules synchronisés par leur support et qu'on retrouve largement dans la nature, de la synchronisation de métronomes à celle des neurones du cerveau[81]. La synchronisation mutuelle de STOs permet d'observer des phénomènes collectifs et non-linéaires non-observés à l'échelle nanométrique mais aussi, comme nous le recherchions, d'augmenter la puissance et la cohérence spectrale du signal émis[45].

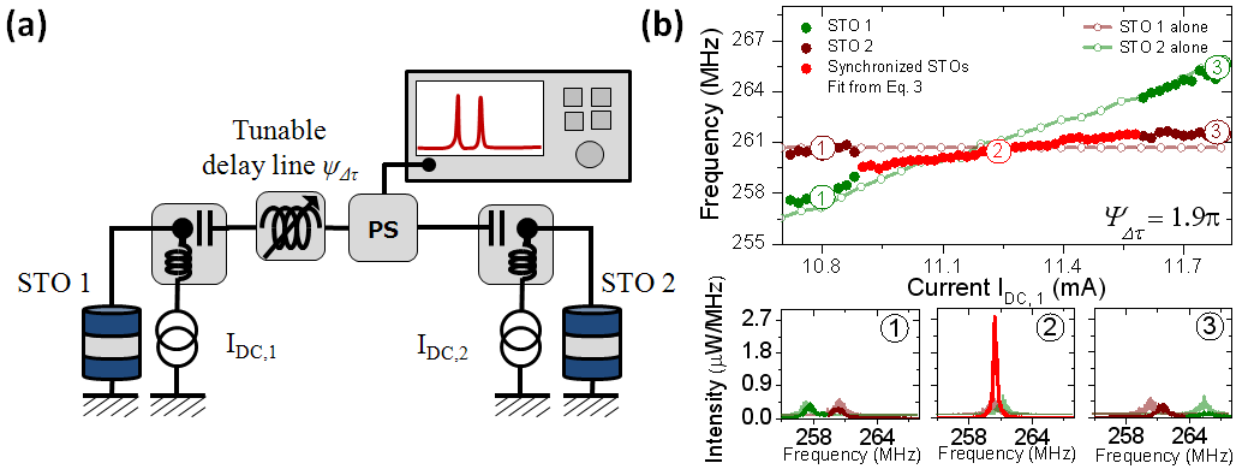

FIGURE D.11: (a) Schéma du circuit électrique pour la synchronisation mutuelle de deux oscillateurs alimentés indépendamment par deux sources de courants continues et connectés par les ports rf de deux bias tee avec une ligne à retard modifiable $\Psi_{\Delta\tau}$. Le signal détecté est mesuré sur un analyseur de spectre connecté au circuit par un diviseur de puissance (PS) (b) Evolution de la fréquence des STOs en interaction en fonction du courant $I_{DC,2}$, le courant $I_{DC,1}$ du STO 1 est fixé à 10.6 mA. En dessous : Spectres mesurés pour $I_{DC,2}$ = 10.8 mA (1), $I_{DC,2}$ = 11.25 mA (2), $I_{DC,2}$ = 11.8 mA (3). (Les propriétés des STOs oscillant indépendamment sont obtenues en éteignant une des deux sources de courants et représentées par les lignes rouge et verte atténuées)

Dans cette thèse, nous avons tout d'abord réussi à réduire la largeur de raie d'un STO à deux vortex en contrôlant le couplage entre les deux cœurs de vortex. Les puissances et les cohérences spectrales élevées de ces STOs et l'efficacité de leur synchronisation avec un courant rf ont permis de réussir à synchroniser deux STOs connectés en parallèles tel qu'il fut prédit par J. Grollier et al.[83] en 2006. Les deux STOs sont alimentés indépendamment par deux sources de courant continu, et connectés électriquement par les ports radio-fréquences de deux bias tee. Ainsi le signal émis par chaque STO est injecté dans le second ce qui permet de les synchroniser mutuellement. Nous avons aussi ajouté une ligne à retard entre les deux oscillateurs pour contrôler le déphasage du signal injecté dans chaque STO. En optimisant nos

conditions expérimentales (champ magnétique, courant appliqué, ligne à retard), nous avons ainsi pu synchroniser deux STOs sur une gamme de fréquence d'environ 2 MHz comme nous pouvons le voir sur la Fig. D.11.b.

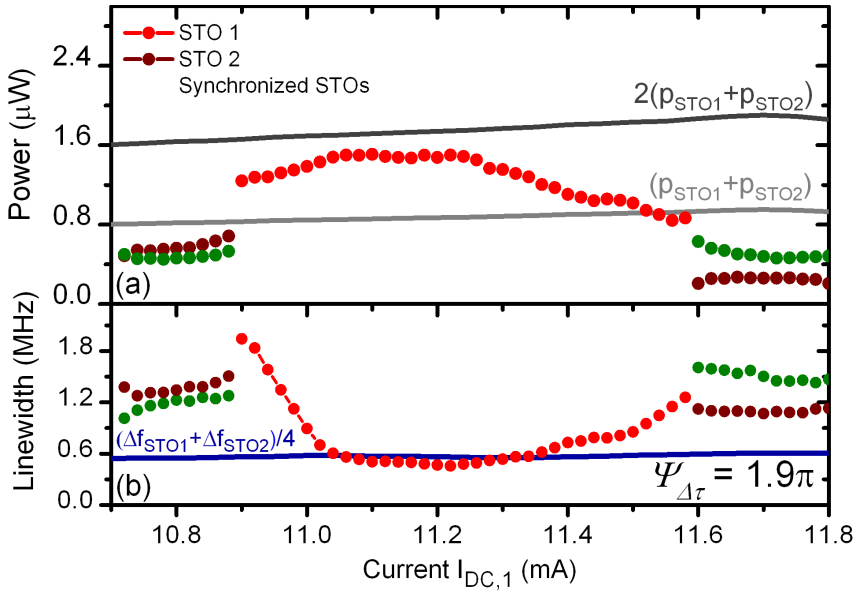

FIGURE D.12: Evolution de la puissance (a) et de la cohérence spectrale (b) en fonction du courant $I_{DC,1}$ injecté dans le STO 1 ($I_{DC,2}$ est fixé à +10.6 mA)

Avec le montage que nous utilisons, nous pouvons comparer quantitativement le signal synchronisé et les signaux non-synchronisés en allumant alternativement les deux sources de courant dc pour obtenir le signal synchronisé ou seulement une des deux pour obtenir le signal non-synchronisé d'un seul des STOs. Dans le cas présent, on peut noter que la fréquence du signal synchronisé est proche de la fréquence moyenne des deux STOs. De plus, on peut noter que la puissance émise et la cohérence spectrale semble fortement améliorer. En effet, on peut voir sur la figure D.12 que la puissance a une forme parabolique inversé dans la gamme de synchronisation avec un maximum proche de 4 fois la puissance d'un seul STO. De plus, la largeur de raie du signal synchronisé est deux fois plus faible que celle d'un seul STO (voir Fig. D.12.b). Ces drastiques améliorations de la cohérence spectrale et de la puissance correspondent quantitativement aux attentes des modèles théoriques développés par A. Slavin[45] et A. Pikovsky[81].

En modifiant la longueur électrique entre les deux STOs à l'aide de la ligne à retard nous avons pu aussi mettre en évidence l'influence du déphasage entre les deux STOs sur l'état synchronisé. Comme nous le montrons sur la Fig. D.13.a, la largeur de la gamme de synchronisation évolue de façon π-périodique avec la longueur électrique (exprimée en période d'oscillations). De cette évolution π-périodique on peut en déduire qu'il est possible de synchroniser deux oscillateurs directement connecté en parallèle ou en série ($\Psi_{\Delta\tau} = 0$). De plus, on peut noter que la fréquence de synchronisation dépend du déphasage, elle peut être soit égale, soit supérieure ou inférieure

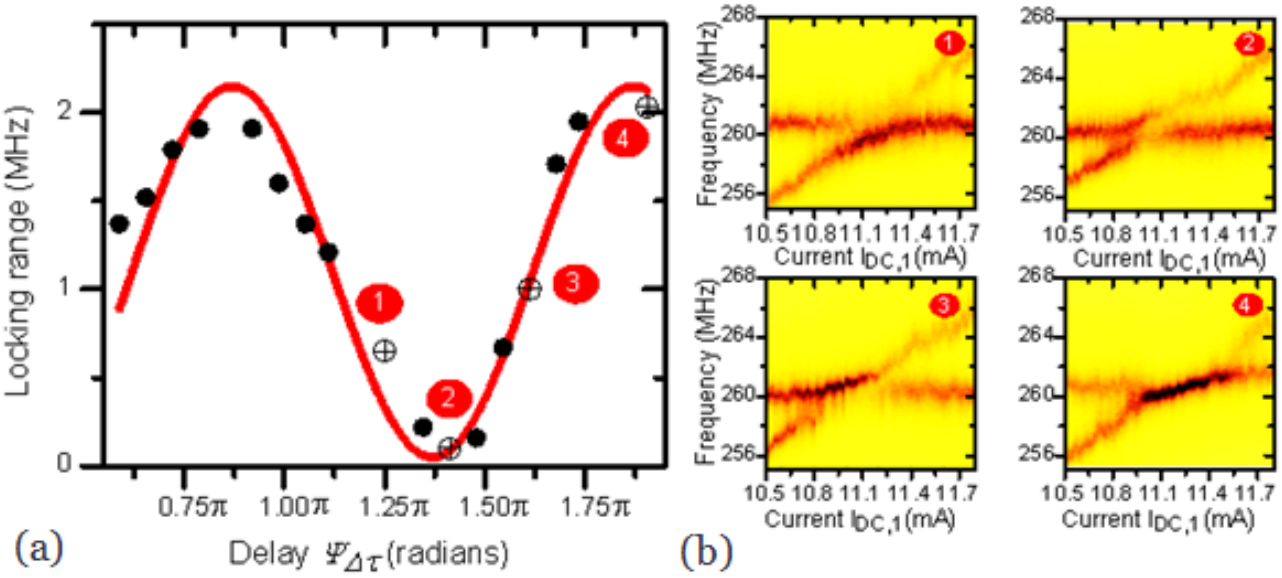

FIGURE D.13: (a) Evolution de la gamme de synchronisation des deux STOs synchronisés en fonction de la longueur électrique entre les deux STOs (exprimées en radians, et associée à la ligne à retard). (b) Puissance spectrale émise par les deux STOs en fonction du courant appliqué pour quatre longueurs électrique : gammes de synchronisation minimale $\Psi_{\Delta\tau} = 1.4\pi(2)$, intermédiaires $\Psi_{\Delta\tau} = 1.25\pi$ (1) et $\Psi_{\Delta\tau} = 1.6\pi$ (3), et maximales $\Psi_{\Delta\tau} = 1.9\pi$ (3).

à la fréquence moyenne des deux STOs comme on peut sur la Fig. D.13.b. Le déphasage entre deux oscillateurs représente ainsi une approche originale pour modifier la synchronisation entre ces oscillateurs. Ces résultats pourraient être mis à profit pour développer des réseaux d'oscillateurs spintroniques bio-inspirés de type mémoires associatives[191]. Cette thèse, qui s'inscrit dans l'objectif d'améliorer les performances rf des nano-oscillateurs à transfert de spin, a permis de dégager différentes approches pour contrôler la dynamique de ces oscillateurs, allant de la dynamique de modes couplés dans un seul oscillateur isolé à la synchronisation mutuelle d'oscillateurs par couplage électrique.

Bibliography

[1] A. Fert and I. A. Campbell. Two-Current Conduction in Nickel. *Physical Review Letters*, 21(16):1190–1192, October 1968. doi: 10.1103/PhysRevLett.21.1190. URL http://link.aps.org/doi/10.1103/PhysRevLett.21.1190.

[2] M. N. Baibich, J. M. Broto, A. Fert, F. Nguyen Van Dau, F. Petroff, P. Etienne, G. Creuzet, A. Friederich, and J. Chazelas. Giant Magnetoresistance of (001)Fe/(001)Cr Magnetic Superlattices. *Physical Review Letters*, 61(21):2472–2475, November 1988. doi: 10.1103/PhysRevLett.61.2472. URL http://link.aps.org/doi/10.1103/PhysRevLett.61.2472.

[3] G. Binasch, P. Grünberg, F. Saurenbach, and W. Zinn. Enhanced magnetoresistance in layered magnetic structures with antiferromagnetic interlayer exchange. *Physical Review B*, 39(7):4828–4830, March 1989. doi: 10.1103/PhysRevB.39.4828. URL http://link.aps.org/doi/10.1103/PhysRevB.39.4828.

[4] Peter M. Levy, Shufeng Zhang, and Albert Fert. Electrical conductivity of magnetic multilayered structures. *Physical Review Letters*, 65(13):1643–1646, September 1990. doi: 10.1103/PhysRevLett.65.1643. URL http://link.aps.org/doi/10.1103/PhysRevLett.65.1643.

[5] Koichiro Inomata, Susumu Okamura, Ryota Goto, and Nobuki Tezuka. Large Tunneling Magnetoresistance at Room Temperature Using a Heusler Alloy with the B2 Structure. *Japanese Journal of Applied Physics*, 42(Part 2, No. 4B):L419–L422, April 2003. ISSN 0021-4922. doi: 10.1143/JJAP.42.L419. URL http://stacks.iop.org/1347-4065/42/L419.

[6] Shinji Yuasa, Taro Nagahama, Akio Fukushima, Yoshishige Suzuki, and Koji Ando. Giant room-temperature magnetoresistance in single-crystal Fe/MgO/Fe magnetic tunnel junctions. *Nature Materials*, 3(12):868–871, December 2004. ISSN 1476-1122, 1476-4660. doi: 10.1038/nmat1257. URL http://www.nature.com/doifinder/10.1038/nmat1257.

[7] T. Valet and A. Fert. Theory of the perpendicular magnetoresistance in magnetic multilayers. *Physical Review B*, 48(10):7099–7113, September 1993. doi: 10.1103/PhysRevB.48.7099. URL http://link.aps.org/doi/10.1103/PhysRevB.48.7099.

[8] M. Julliere. Tunneling between ferromagnetic films. *Physics Letters A*, 54(3):225–226, September 1975. ISSN 03759601. doi: 10.1016/0375-9601(75)90174-7. URL http://linkinghub.elsevier.com/retrieve/pii/0375960175901747.

[9] J. C. SLONCZEWSKI. Current-driven excitation of magnetic multilayers. *J. Magn. Magn. Mater.*, 159:L1–L7, 1996. URL http://ci.nii.ac.jp/naid/80009207894/.

[10] T. Miyazaki and N. Tezuka. Giant magnetic tunneling effect in Fe/Al 2O 3/Fe junction. *Journal of Magnetism and Magnetic Materials*, 139:L231–L234, January 1995. ISSN 0304-8853. doi: 10.1016/0304-8853(95)90001-2. URL http://adsabs.harvard.edu/abs/1995JMMM..139L.231M.

[11] W. J. Gallagher, S. S. P. Parkin, Yu Lu, X. P. Bian, A. Marley, K. P. Roche, R. A. Altman, S. A. Rishton, C. Jahnes, T. M. Shaw, and Gang Xiao. Microstructured magnetic tunnel junctions (invited). *Journal of Applied Physics*, 81(8):3741, 1997. ISSN 00218979. doi: 10.1063/1.364744. URL http://scitation.aip.org/content/aip/journal/jap/81/8/10.1063/1.364744.

[12] J. S. Moodera, Lisa R. Kinder, Terrilyn M. Wong, and R. Meservey. Large Magnetoresistance at Room Temperature in Ferromagnetic Thin Film Tunnel Junctions. *Physical Review Letters*, 74(16):3273–3276, April 1995. doi: 10.1103/PhysRevLett.74.3273. URL http://link.aps.org/doi/10.1103/PhysRevLett.74.3273.

[13] Stuart S. P. Parkin, Christian Kaiser, Alex Panchula, Philip M. Rice, Brian Hughes, Mahesh Samant, and See-Hun Yang. Giant tunnelling magnetoresistance at room temperature with MgO (100) tunnel barriers. *Nature Materials*, 3(12):862–867, December 2004. ISSN 1476-1122, 1476-4660. doi: 10.1038/nmat1256. URL http://www.nature.com/doifinder/10.1038/nmat1256.

[14] X.-G. Zhang and W. H. Butler. Large magnetoresistance in bcc Co/MgO/Co and FeCo/MgO/FeCo tunnel junctions. *Physical Review B*, 70(17), November 2004. ISSN 1098-0121, 1550-235X. doi: 10.1103/PhysRevB.70.172407. URL http://link.aps.org/doi/10.1103/PhysRevB.70.172407.

[15] L. Berger. Emission of spin waves by a magnetic multilayer traversed by a current. *Physical Review B*, 54(13):9353–9358, October 1996. doi: 10.1103/PhysRevB.54.9353. URL http://link.aps.org/doi/10.1103/PhysRevB.54.9353.

[16] Ion Garate, K. Gilmore, M. D. Stiles, and A. H. MacDonald. Nonadiabatic spin-transfer torque in real materials. *Physical Review B*, 79(10), March 2009. ISSN 1098-0121, 1550-235X. doi: 10.1103/PhysRevB.79.104416. URL http://link.aps.org/doi/10.1103/PhysRevB.79.104416.

[17] Yaroslav Tserkovnyak, Hans Joakim Skadsem, Arne Brataas, and Gerrit E. W. Bauer. Current-induced magnetization dynamics in disordered itinerant ferromagnets. *Physical Review B*, 74(14), October 2006. ISSN 1098-0121, 1550-235X. doi: 10.1103/PhysRevB.74.144405. URL http://link.aps.org/doi/10.1103/PhysRevB.74.144405.

[18] A. Chanthbouala, R. Matsumoto, J. Grollier, V. Cros, A. Anane, A. Fert, A. V. Khvalkovskiy, K. A. Zvezdin, K. Nishimura, Y. Nagamine, H. Maehara, K. Tsunekawa, A. Fukushima, and S. Yuasa. Vertical-current-induced domain-wall motion in MgO-based magnetic tunnel junctions with low current densities. *Nature Physics*, 7(8): 626–630, April 2011. ISSN 1745-2473, 1745-2481. doi: 10.1038/nphys1968. URL http://www.nature.com/doifinder/10.1038/nphys1968.

[19] Hitoshi Kubota, Akio Fukushima, Kay Yakushiji, Taro Nagahama, Shinji Yuasa, Koji Ando, Hiroki Maehara, Yoshinori Nagamine, Koji Tsunekawa, David D. Djayaprawira, Naoki Watanabe, and Yoshishige Suzuki. Quantitative measurement of voltage dependence of spin-transfer torque in MgO-based magnetic tunnel junctions. *Nature Physics*, 4(1):37–41, January 2008. ISSN 1745-2473, 1745-2481. doi: 10.1038/nphys784. URL http://www.nature.com/doifinder/10.1038/nphys784.

[20] Jack C. Sankey, Yong-Tao Cui, Jonathan Z. Sun, John C. Slonczewski, Robert A. Buhrman, and Daniel C. Ralph. Measurement of the spin-transfer-torque vector in magnetic tunnel junctions. *Nature Physics*, 4(1):67–71, January 2008. ISSN 1745-2473, 1745-2481. doi: 10.1038/nphys783. URL http://www.nature.com/doifinder/10.1038/nphys783.

[21] Chen Wang, Yong-Tao Cui, Jordan A. Katine, Robert A. Buhrman, and Daniel C. Ralph. Time-resolved measurement of spin-transfer-driven ferromagnetic resonance and spin torque in magnetic tunnel junctions. *Nature Physics*, 7(6):496–501, June 2011. ISSN 1745-2473, 1745-2481. doi: 10.1038/nphys1928. URL http://www.nature.com/doifinder/10.1038/nphys1928.

[22] Ioannis Theodonis, Nicholas Kioussis, Alan Kalitsov, Mairbek Chshiev, and W. H. Butler. Anomalous Bias Dependence of Spin Torque in Magnetic Tunnel Junctions. *Physical Review Letters*, 97(23), December 2006. ISSN 0031-9007, 1079-7114. doi: 10.1103/PhysRevLett.97.237205. URL http://link.aps.org/doi/10.1103/PhysRevLett.97.237205.

[23] Mark D. Stiles and Jacques Miltat. Spin-Transfer Torque and Dynamics. In Burkard Hillebrands and André Thiaville, editors, *Spin Dynamics in Confined Magnetic Structures III*, volume 101, pages 225–308. Springer Berlin Heidelberg, 2006. ISBN 978-3-540-20108-3. URL http://link.springer.com/10.1007/10938171_7.

[24] Shufeng Zhang. Spin Hall Effect in the Presence of Spin Diffusion. *Physical Review Letters*, 85(2):393–396, July 2000. doi: 10.1103/PhysRevLett.85.393. URL http://link.aps.org/doi/10.1103/PhysRevLett.85.393.

[25] V. E. Demidov, S. Urazhdin, E. R. J. Edwards, M. D. Stiles, R. D. McMichael, and S. O. Demokritov. Control of Magnetic Fluctuations by Spin Current. *Physical Review Letters*, 107(10), September 2011. ISSN 0031-9007, 1079-7114. doi: 10.1103/PhysRevLett.107.107204. URL http://link.aps.org/doi/10.1103/PhysRevLett.107.107204.

[26] Ioan Mihai Miron, Kevin Garello, Gilles Gaudin, Pierre-Jean Zermatten, Marius V. Costache, Stéphane Auffret, Sébastien Bandiera, Bernard Rodmacq, Alain Schuhl, and Pietro Gambardella. Perpendicular switching of a single ferromagnetic layer induced by in-plane current injection. *Nature*, 476(7359):189–193, July 2011. ISSN 0028-0836, 1476-4687. doi: 10.1038/nature10309. URL http://www.nature.com/doifinder/10.1038/nature10309.

[27] J. C. Rojas Sánchez, L. Vila, G. Desfonds, S. Gambarelli, J. P. Attané, J. M. De Teresa, C. Magén, and A. Fert. Spin-to-charge conversion using Rashba coupling at the interface between non-magnetic materials. *Nature Communications*, 4, December 2013. ISSN 2041-1723. doi: 10.1038/ncomms3944. URL http://www.nature.com/doifinder/10.1038/ncomms3944.

[28] Kevin Garello, Ioan Mihai Miron, Can Onur Avci, Frank Freimuth, Yuriy Mokrousov, Stefan Blügel, Stéphane Auffret, Olivier Boulle, Gilles Gaudin, and Pietro Gambardella. Symmetry and magnitude of spin–orbit torques in ferromagnetic heterostructures. *Nature Nanotechnology*, 8(8):587–593, July 2013. ISSN 1748-3387, 1748-3395. doi: 10.1038/nnano.2013.145. URL http://www.nature.com/doifinder/10.1038/nnano.2013.145.

[29] T.L. Gilbert. Abstracts of Papers to be Presented at the 1955 Thanksgiving Meeting at the University of Chicago, Chicago, Illinois, November 25 and 26, 1955. *Physical Review*, 100(4):1235–1235, November 1955. doi: 10.1103/PhysRev.100.1235. URL http://link.aps.org/doi/10.1103/PhysRev.100.1235.

[30] Stefano Bonetti, Pranaba Muduli, Fred Mancoff, and Johan Åkerman. Spin torque oscillator frequency versus magnetic field angle: The prospect of operation beyond 65 GHz. *Applied Physics Letters*, 94(10):102507, 2009. ISSN 00036951. doi: 10.1063/1.3097238. URL http://scitation.aip.org/content/aip/journal/apl/94/10/10.1063/1.3097238.

[31] R. Okura, Y. Sakuraba, T. Seki, K. Izumi, M. Mizuguchi, and K. Takanashi. High-power rf oscillation induced in half-metallic Co2MnSi layer by spin-transfer torque. *Applied Physics Letters*, 99(5):052510, 2011. ISSN 00036951. doi: 10.1063/1.3624470. URL http://scitation.aip.org/content/aip/journal/apl/99/5/10.1063/1.3624470.

[32] S. I. Kiselev, J. C. Sankey, I. N. Krivorotov, N. C. Emley, R. J. Schoelkopf, R. A. Buhrman, and D. C. Ralph. Microwave oscillations of a nanomagnet driven by a spin-polarized current. *Nature*, 425(6956):380–383, September 2003. ISSN 0028-0836, 1476-4679. doi: 10.1038/nature01967. URL http://www.nature.com/doifinder/10.1038/nature01967.

[33] W. Rippard, M. Pufall, S. Kaka, S. Russek, and T. Silva. Direct-Current Induced Dynamics in C o 90 F e 10 / N i 80 F e 20 Point Contacts. *Physical Review Letters*, 92(2), January 2004. ISSN 0031-9007, 1079-7114. doi: 10.1103/PhysRevLett.92.027201. URL http://link.aps.org/doi/10.1103/PhysRevLett.92.027201.

[34] Alexey V. Nazarov, Heidi M. Olson, Haeseok Cho, Konstantin Nikolaev, Zheng Gao, Scott Stokes, and Bharat B. Pant. Spin transfer stimulated microwave emission in MgO magnetic tunnel junctions. *Applied Physics Letters*, 88(16):162504, 2006. ISSN 00036951. doi: 10.1063/1.2196232. URL http://scitation.aip.org/content/aip/journal/apl/88/16/10.1063/1.2196232.

[35] Hiroki Maehara, Hitoshi Kubota, Yoshishige Suzuki, Takayuki Seki, Kazumasa Nishimura, Yoshinori Nagamine, Koji Tsunekawa, Akio Fukushima, Alina M. Deac, Koji Ando, and Shinji Yuasa. Large Emission Power over 2 μW with High Q Factor Obtained from Nanocontact Magnetic-Tunnel-Junction-Based Spin Torque Oscillator. *Applied Physics Express*, 6(11):113005, November 2013. ISSN 1882-0778, 1882-0786. doi: 10.7567/APEX.6.113005. URL http://stacks.iop.org/1882-0786/6/i=11/a=113005?key=crossref.100be4707e3af1a5b50f07382eae24cc.

[36] V. S. Pribiag, I. N. Krivorotov, G. D. Fuchs, P. M. Braganca, O. Ozatay, J. C. Sankey, D. C. Ralph, and R. A. Buhrman. Magnetic vortex oscillator driven by dc spin-polarized current. *Nature Physics*, 3(7):498–503, 2007. URL http://www.nature.com/nphys/journal/v3/n7/abs/nphys619.html.

[37] Stefano Bonetti, Vasil Tiberkevich, Giancarlo Consolo, Giovanni Finocchio, Pranaba Muduli, Fred Mancoff, Andrei Slavin, and Johan Åkerman. Experimental Evidence of Self-Localized and Propagating Spin Wave Modes in Obliquely Magnetized Current-Driven Nanocontacts. *Physical Review Letters*, 105(21), November 2010. ISSN 0031-9007, 1079-7114. doi: 10.1103/PhysRevLett.105.217204. URL http://link.aps.org/doi/10.1103/PhysRevLett.105.217204.

[38] W. Jiang, P. Upadhyaya, W. Zhang, G. Yu, M. B. Jungfleisch, F. Y. Fradin, J. E. Pearson, Y. Tserkovnyak, K. L. Wang, O. Heinonen, S. G. E. te Velthuis, and A. Hoffmann. Blowing magnetic skyrmion bubbles. *Science*, 349(6245):283–286, July 2015. ISSN 0036-8075, 1095-9203. doi: 10.1126/science.aaa1442. URL http://www.sciencemag.org/cgi/doi/10.1126/science.aaa1442.

[39] Joo-Von Kim, Felipe Garcia-Sanchez, João Sampaio, Constance Moreau-Luchaire, Vincent Cros, and Albert Fert. Breathing modes of confined skyrmions in ultrathin magnetic dots. *Physical Review B*, 90(6), August 2014. ISSN 1098-0121, 1550-235X. doi: 10.1103/PhysRevB.90.064410. URL http://link.aps.org/doi/10.1103/PhysRevB.90.064410.

[40] D. Houssameddine, U. Ebels, B. Delaet, B. Rodmacq, I. Firastrau, F. Ponthenier, M. Brunet, C. Thirion, J.-P. Michel, L. Prejbeanu-Buda, M.-C. Cyrille, O. Redon, and B. Dieny. Spin-torque oscillator using a perpendicular polarizer and a planar free layer. *Nat Mater*, 6(6):447–453, June 2007. ISSN 1476-1122. doi: 10.1038/nmat1905. URL http://dx.doi.org/10.1038/nmat1905.

[41] T. Devolder, A. Meftah, K. Ito, J. A. Katine, P. Crozat, and C. Chappert. Spin transfer oscillators emitting microwave in zero applied magnetic field. *Journal of Applied Physics*, 101(6):063916, 2007. ISSN 00218979. doi: 10.1063/1.2713373. URL http://scitation.aip.org/content/aip/journal/jap/101/6/10.1063/1.2713373.

[42] A. V. Khvalkovskiy, J. Grollier, N. Locatelli, Ya V. Gorbunov, K. A. Zvezdin, and V. Cros. Nonuniformity of a planar polarizer for spin-transfer-induced vortex oscillations at zero field. *Applied Physics Letters*, 96(21):212507–212507–3, May 2010. ISSN 00036951. doi: doi:10.1063/1.3441405. URL http://apl.aip.org/resource/1/applab/v96/i21/p212507_s1.

[43] N. Locatelli, V. V. Naletov, J. Grollier, G. De Loubens, V. Cros, C. Deranlot, C. Ulysse, G. Faini, O. Klein, and A. Fert. Dynamics of two coupled vortices in a spin valve nanopillar excited by spin transfer torque. *Applied Physics Letters*, 98(6):062501, 2011. URL http://scitation.aip.org/content/aip/journal/apl/98/6/10.1063/1.3553771.

[44] A. Dussaux, E. Grimaldi, B. Rache Salles, A. S. Jenkins, A. V. Khvalkovskiy, P. Bortolotti, J. Grollier, H. Kubota, A. Fukushima, K. Yakushiji, S. Yuasa, V. Cros, and A. Fert. Large amplitude spin torque vortex oscillations at zero external field using a perpendicular spin polarizer. *Applied Physics Letters*, 105(2):022404, July 2014. ISSN 0003-6951, 1077-3118. doi: 10.1063/1.4885537. URL http://scitation.aip.org/content/aip/journal/apl/105/2/10.1063/1.4885537.

[45] A. Slavin and V. Tiberkevich. Nonlinear Auto-Oscillator Theory of Microwave Generation by Spin-Polarized Current. *IEEE Transactions on Magnetics*, 45(4):1875 –1918, April 2009. ISSN 0018-9464. doi: 10.1109/TMAG.2008.2009935.

[46] Joo-Von Kim, Vasil Tiberkevich, and Andrei N. Slavin. Generation Linewidth of an Auto-Oscillator with a Nonlinear Frequency Shift: Spin-Torque Nano-Oscillator. *Physical Review Letters*, 100(1):017207, January 2008. doi: 10.1103/PhysRevLett.100.017207. URL http://link.aps.org/doi/10.1103/PhysRevLett.100.017207.

[47] M. Quinsat, D. Gusakova, J. F. Sierra, J. P. Michel, D. Houssameddine, B. Delaet, M.-C. Cyrille, U. Ebels, B. Dieny, L. D. Buda-Prejbeanu, J. A. Katine, D. Mauri, A. Zeltser, M. Prigent, J.-C. Nallatamby, and R. Sommet. Amplitude and phase noise of magnetic tunnel junction oscillators. *Applied Physics Letters*, 97(18):182507, 2010. ISSN 00036951. doi: 10.1063/1.3506901. URL http://scitation.aip.org/content/aip/journal/apl/97/18/10.1063/1.3506901.

[48] Eva Grimaldi, Antoine Dussaux, Paolo Bortolotti, Julie Grollier, Grégoire Pillet, Akio Fukushima, Hitoshi Kubota, Kay Yakushiji, Shinji Yuasa, and Vincent Cros. Response to noise of a vortex based spin transfer nano-oscillator. *Physical Review B*, 89(10):104404, March 2014. doi: 10.1103/PhysRevB.89.104404. URL http://link.aps.org/doi/10.1103/PhysRevB.89.104404.

[49] D. Houssameddine, J. F. Sierra, D. Gusakova, B. Delaet, U. Ebels, L. D. Buda-Prejbeanu, M.-C. Cyrille, B. Dieny, B. Ocker, J. Langer, and W. Maas. Spin torque driven excitations in a synthetic antiferromagnet. *Applied Physics Letters*, 96(7):072511, 2010. ISSN 00036951. doi: 10.1063/1.3314282. URL http://scitation.aip.org/content/aip/journal/apl/96/7/10.1063/1.3314282.

[50] Makoto Konoto, Hiroshi Imamura, Tomohiro Taniguchi, Kay Yakushiji, Hitoshi Kubota, Akio Fukushima, Koji Ando, and Shinji Yuasa. Effect of MgO Cap Layer on Gilbert Damping of FeB Electrode Layer in MgO-Based Magnetic Tunnel Junctions. *Applied Physics Express*, 6(7):073002, 2013. doi: 10.7567/APEX.6.073002. URL http://apex.jsap.jp/link?APEX/6/073002/.

[51] B. Georges, J. Grollier, V. Cros, and A. Fert. Impact of the electrical connection of spin transfer nano-oscillators on their synchronization: an analytical study. *Applied Physics Letters*, 92(23):232504–232504–3, June 2008. ISSN 00036951. doi: doi:10.1063/1.2945636. URL http://apl.aip.org/resource/1/applab/v92/i23/p232504_s1.

[52] V. E. Demidov, H. Ulrichs, S. V. Gurevich, S. O. Demokritov, V. S. Tiberkevich, A. N. Slavin, A. Zholud, and S. Urazhdin. Synchronization of spin Hall nano-oscillators to

external microwave signals. *Nature Communications*, 5, January 2014. ISSN 2041-1723. doi: 10.1038/ncomms4179. URL http://www.nature.com/doifinder/10.1038/ncomms4179.

[53] Sergei Urazhdin, Phillip Tabor, Vasil Tiberkevich, and Andrei Slavin. Fractional Synchronization of Spin-Torque Nano-Oscillators. *Physical Review Letters*, 105(10), August 2010. ISSN 0031-9007, 1079-7114. doi: 10.1103/PhysRevLett.105.104101. URL http://link.aps.org/doi/10.1103/PhysRevLett.105.104101.

[54] M. Quinsat, J. F. Sierra, I. Firastrau, V. Tiberkevich, A. Slavin, D. Gusakova, L. D. Buda-Prejbeanu, M. Zarudniev, J.-P. Michel, U. Ebels, B. Dieny, M.-C. Cyrille, J. A. Katine, D. Mauri, and A. Zeltser. Injection locking of tunnel junction oscillators to a microwave current. *Applied Physics Letters*, 98(18):182503, 2011. ISSN 00036951. doi: 10.1063/1.3587575. URL http://scitation.aip.org/content/aip/journal/apl/98/18/10.1063/1.3587575.

[55] A. Dussaux, A. V. Khvalkovskiy, J. Grollier, V. Cros, A. Fukushima, M. Konoto, H. Kubota, K. Yakushiji, S. Yuasa, K. Ando, and A. Fert. Phase locking of vortex based spin transfer oscillators to a microwave current. *Applied Physics Letters*, 98(13):132506, 2011. ISSN 00036951. doi: 10.1063/1.3565159. URL http://scitation.aip.org/content/aip/journal/apl/98/13/10.1063/1.3565159.

[56] C. Serpico, R. Bonin, G. Bertotti, M. dAquino, and I.D. Mayergoyz. Theory of Injection Locking for Large Magnetization Motion in Spin-Transfer Nano-Oscillators. *IEEE Transactions on Magnetics*, 45(10):3441–3444, October 2009. ISSN 0018-9464. doi: 10.1109/TMAG.2009.2025515.

[57] Mario Carpentieri, Takahiro Moriyama, Bruno Azzerboni, and Giovanni Finocchio. Injection locking at zero field in two free layer spin-valves. *Applied Physics Letters*, 102 (10):102413–102413, 2013. URL http://ieeexplore.ieee.org/xpls/abs_all.jsp?arnumber=6481264.

[58] W. Rippard, M. Pufall, S. Kaka, T. Silva, S. Russek, and J. Katine. Injection Locking and Phase Control of Spin Transfer Nano-oscillators. *Physical Review Letters*, 95(6), August 2005. ISSN 0031-9007, 1079-7114. doi: 10.1103/PhysRevLett.95.067203. URL http://link.aps.org/doi/10.1103/PhysRevLett.95.067203.

[59] M. R. Pufall, W. H. Rippard, S. Kaka, T. J. Silva, and S. E. Russek. Frequency modulation of spin-transfer oscillators. *Applied Physics Letters*, 86(8):082506, 2005. ISSN 00036951. doi: 10.1063/1.1875762. URL http://link.aip.org/link/APPLAB/v86/i8/p082506/s1&Agg=doi.

[60] F. B. Mancoff, N. D. Rizzo, B. N. Engel, and S. Tehrani. Phase-locking in double-point-contact spin-transfer devices. *Nature*, 437(7057):393–395, September 2005. ISSN 0028-0836, 1476-4679. doi: 10.1038/nature04036. URL http://www.nature.com/doifinder/10.1038/nature04036.

[61] Sergei Urazhdin, Vasil Tiberkevich, and Andrei Slavin. Parametric Excitation of a Magnetic Nanocontact by a Microwave Field. *Physical Review Letters*, 105(23), December 2010. ISSN 0031-9007, 1079-7114. doi: 10.1103/PhysRevLett.105.237204. URL http://link.aps.org/doi/10.1103/PhysRevLett.105.237204.

[62] P. Bortolotti, E. Grimaldi, A. Dussaux, J. Grollier, V. Cros, C. Serpico, K. Yakushiji, A. Fukushima, H. Kubota, R. Matsumoto, and S. Yuasa. Parametric excitation of magnetic vortex gyrations in spin-torque nano-oscillators. *Physical Review B*, 88(17):174417, November 2013. doi: 10.1103/PhysRevB.88.174417. URL http://link.aps.org/doi/10.1103/PhysRevB.88.174417.

[63] S. Y. Martin, C. Thirion, C. Hoarau, C. Baraduc, and B. Diény. Tunability versus deviation sensitivity in a nonlinear vortex oscillator. *Physical Review B*, 88(2), July 2013. ISSN 1098-0121, 1550-235X. doi: 10.1103/PhysRevB.88.024421. URL http://link.aps.org/doi/10.1103/PhysRevB.88.024421.

[64] Ezio Iacocca and Johan \AAkerman. Analytical investigation of modulated spin-torque oscillators in the framework of coupled differential equations with variable coefficients. *Physical Review B*, 85(18):184420, 2012. URL http://prb.aps.org/abstract/PRB/v85/i18/e184420.

[65] P. K. Muduli, O. G. Heinonen, and J. Åkerman. Decoherence and mode-hopping in a magnetic tunnel junction-based spin-torque oscillator. *Physical Review Letters*, 108(20), May 2012. ISSN 0031-9007, 1079-7114. doi: 10.1103/PhysRevLett.108.207203. URL http://arxiv.org/abs/1203.6300.

[66] B. Georges, J. Grollier, M. Darques, V. Cros, C. Deranlot, B. Marcilhac, G. Faini, and A. Fert. Coupling Efficiency for Phase Locking of a Spin Transfer Nano-Oscillator to a Microwave Current. *Physical Review Letters*, 101(1):017201, July 2008. doi: 10.1103/PhysRevLett.101.017201. URL http://link.aps.org/doi/10.1103/PhysRevLett.101.017201.

[67] A. Hamadeh, N. Locatelli, V. V. Naletov, R. Lebrun, G. de Loubens, J. Grollier, O. Klein, and V. Cros. Origin of Spectral Purity and Tuning Sensitivity in a Spin Transfer Vortex Nano-Oscillator. *Physical Review Letters*, 112(25), June 2014. ISSN 0031-9007, 1079-7114. doi: 10.1103/PhysRevLett.112.257201. URL http://link.aps.org/doi/10.1103/PhysRevLett.112.257201.

[68] M. Quinsat, F. Garcia-Sanchez, A. S. Jenkins, V. S. Tiberkevich, A. N. Slavin, L. D. Buda-Prejbeanu, A. Zeltser, J. A. Katine, B. Dieny, M.-C. Cyrille, and U. Ebels. Modulation bandwidth of spin torque oscillators under current modulation. *Applied Physics Letters*, 105(15):152401, October 2014. ISSN 0003-6951, 1077-3118. doi: 10.1063/1.4898093. URL http://scitation.aip.org/content/aip/journal/apl/105/15/10.1063/1.4898093.

[69] A. Hamadeh, Nicolas Locatelli, V. V. Naletov, Romain Lebrun, Grégoire De Loubens, Julie Grollier, Olivier Klein, and V. Cros. Perfect and robust phase-locking of a spin transfer vortex nano-oscillator to an external microwave source. *Applied Physics Letters*, 104(2):022408, 2014. URL http://scitation.aip.org/content/aip/journal/apl/104/2/10.1063/1.4862326.

[70] Yan Zhou, Vasil Tiberkevich, Giancarlo Consolo, Ezio Iacocca, Bruno Azzerboni, Andrei Slavin, and Johan Åkerman. Oscillatory transient regime in the forced dynamics of a nonlinear auto oscillator. *Physical Review B*, 82(1), July 2010. ISSN 1098-0121, 1550-235X. doi: 10.1103/PhysRevB.82.012408. URL http://link.aps.org/doi/10.1103/PhysRevB.82.012408.

[71] S. Sani, J. Persson, S.M. Mohseni, Ye Pogoryelov, P.K. Muduli, A. Eklund, G. Malm, M. Käll, A. Dmitriev, and J. Åkerman. Mutually synchronized bottom-up multi-nanocontact spin–torque oscillators. *Nat Commun*, 4, November 2013. URL http://dx.doi.org/10.1038/ncomms3731.

[72] N. Locatelli, A. Hamadeh, F. Abreu Araujo, A. D. Belanovsky, P. N. Skirdkov, R. Lebrun, V. V. Naletov, K. A. Zvezdin, M. Munoz, J. Grollier, O. Klein, V. Cros, and G. de Loubens. Efficient Synchronization of Dipolarly Coupled Vortex-Based Spin Transfer Nano-Oscillators. *arXiv:1506.03603 [cond-mat]*, June 2015. URL http://arxiv.org/abs/1506.03603.

[73] A. Ruotolo, V. Cros, B. Georges, A. Dussaux, J. Grollier, C. Deranlot, R. Guillemet, K. Bouzehouane, S. Fusil, and A. Fert. Phase-locking of magnetic vortices mediated by antivortices. *Nature Nanotechnology*, 4(8):528–532, August 2009. ISSN 1748-3387, 1748-3395. doi: 10.1038/nnano.2009.143. URL http://www.nature.com/doifinder/10.1038/nnano.2009.143.

[74] M. Pufall, W. Rippard, S. Russek, S. Kaka, and J. Katine. Electrical Measurement of Spin-Wave Interactions of Proximate Spin Transfer Nanooscillators. *Physical Review Letters*, 97(8), August 2006. ISSN 0031-9007, 1079-7114. doi: 10.1103/PhysRevLett.97.087206. URL http://link.aps.org/doi/10.1103/PhysRevLett.97.087206.

[75] H. Hughes, K. Bussmann, P.J. McMarr, Shu-Fan Cheng, R. Shull, A.P. Chen, S. Schafer, T. Mewes, A. Ong, E. Chen, M.H. Mendenhall, and R.A. Reed. Radiation Studies of Spin-Transfer Torque Materials and Devices. *IEEE Transactions on Nuclear Science*, 59 (6):3027–3033, December 2012. ISSN 0018-9499. doi: 10.1109/TNS.2012.2223487.

[76] Ran Cheng, Di Xiao, and Arne Brataas. Terahertz Antiferromagnetic Spin Hall Nano-Oscillator. *arXiv:1509.09229 [cond-mat]*, September 2015. URL http://arxiv.org/abs/1509.09229.

[77] M. Manfrini, T. Devolder, Joo-Von Kim, P. Crozat, N. Zerounian, C. Chappert, W. Van Roy, L. Lagae, G. Hrkac, and T. Schrefl. Agility of vortex-based nanocontact spin torque oscillators. *arXiv:0910.1941 [cond-mat]*, October 2009. URL http://arxiv.org/abs/0910.1941.

[78] Hyun Seok Choi, Sun Yool Kang, Seong Jun Cho, Inn-Yeal Oh, Mincheol Shin, Hyuncheol Park, Chaun Jang, Byoung-Chul Min, Sang-Il Kim, Seung-Young Park, and Chul Soon Park. Spin nano–oscillator–based wireless communication. *Scientific Reports*, 4, June 2014. ISSN 2045-2322. doi: 10.1038/srep05486. URL http://www.nature.com/doifinder/10.1038/srep05486.

[79] I. N. Krivorotov, N. C. Emley, J. C. Sankey, S. I. Kiselev, D. C. Ralph, and R. A. Buhrman. Time-domain measurements of nanomagnet dynamics driven by spin-transfer torques. *Science*, 307(5707):228–231, 2005. URL http://www.sciencemag.org/content/307/5707/228.short.

[80] Sumito Tsunegi, Hitoshi Kubota, Kay Yakushiji, Makoto Konoto, Shingo Tamaru, Akio Fukushima, Hiroko Arai, Hiroshi Imamura, Eva Grimaldi, Romain Lebrun, Julie Grollier, Vincent Cros, and Shinji Yuasa. High emission power and Q factor in spin torque vortex oscillator consisting of FeB free layer. *Applied Physics Express*, 7(6):063009, June 2014. ISSN 1882-0778, 1882-0786. doi: 10.7567/APEX.7.063009. URL http://stacks.iop.org/1882-0786/7/i=6/a=063009?key=crossref.03332af14be6f463178a55848c9510cf.

[81] Arkady Pikovsky, Michael Rosenblum, and Jurgen Kurths. *A universal concept in nonlinear sciences*, volume 2 of *Cambridge University Press*. 2001. URL http://library.mpib-berlin.mpg.de/toc/ze_2006_1674.pdf.

[82] Shehzaad Kaka, Matthew R. Pufall, William H. Rippard, Thomas J. Silva, Stephen E. Russek, and Jordan A. Katine. Mutual phase-locking of microwave spin torque nano-oscillators. *Nature*, 437(7057):389–392, September 2005. ISSN 0028-0836, 1476-4679. doi: 10.1038/nature04035. URL http://www.nature.com/doifinder/10.1038/nature04035.

[83] J. Grollier, V. Cros, and A. Fert. Synchronization of spin-transfer oscillators driven by stimulated microwave currents. *Physical Review B*, 73(6):060409, February 2006. doi: 10.1103/PhysRevB.73.060409. URL http://link.aps.org/doi/10.1103/PhysRevB.73.060409.

[84] J. Persson, Yan Zhou, and Johan Akerman. Phase-locked spin torque oscillators: Impact of device variability and time delay. *Journal of Applied Physics*, 101(9):09A503, 2007. ISSN 00218979. doi: 10.1063/1.2670045. URL http://scitation.aip.org/content/aip/journal/jap/101/9/10.1063/1.2670045.

[85] Vasil Tiberkevich, Andrei Slavin, Elena Bankowski, and Grant Gerhart. Phase-locking and frustration in an array of nonlinear spin-torque nano-oscillators. *Applied Physics Letters*, 95(26):262505, 2009. ISSN 00036951. doi: 10.1063/1.3278602. URL http://scitation.aip.org/content/aip/journal/apl/95/26/10.1063/1.3278602.

[86] Dong Li, Yan Zhou, Changsong Zhou, and Bambi Hu. Global attractors and the difficulty of synchronizing serial spin-torque oscillators. *Physical Review B*, 82(14), October 2010. ISSN 1098-0121, 1550-235X. doi: 10.1103/PhysRevB.82.140407. URL http://link.aps.org/doi/10.1103/PhysRevB.82.140407.

[87] Andrei N. Slavin and Ilya N. Krivorotov. Spin-torque devices, March 2010. URL http://www.google.com/patents/US7678475. U.S. Classification 428/811, 428/811.1, 428/811.2, 257/421, 428/811.5, 360/324.2; International Classification G11B5/33; Cooperative Classification Y10T428/32, Y10T428/1114, H03B15/006, Y10T428/1107, Y10T428/325, B82Y25/00, H01L43/08, Y10T428/1143, G11C11/16, H01F10/325, H01F10/3254, H01F10/329, Y10T428/1121; European Classification B82Y25/00, H03B15/00B, G11C11/16, H01F10/32N2, H01L43/08, H01F10/32N4.

[88] R. Lebrun, A. Jenkins, A. Dussaux, N. Locatelli, S. Tsunegi, E. Grimaldi, H. Kubota, P. Bortolotti, K. Yakushiji, J. Grollier, A. Fukushima, S. Yuasa, and V. Cros. Understanding of Phase Noise Squeezing Under Fractional Synchronization of a Nonlinear Spin Transfer Vortex Oscillator. *Physical Review Letters*, 115(1), June 2015. ISSN 0031-9007, 1079-7114. doi: 10.1103/PhysRevLett.115.017201. URL http://link.aps.org/doi/10.1103/PhysRevLett.115.017201.

[89] S. Y. Martin, N. de Mestier, C. Thirion, C. Hoarau, Y. Conraux, C. Baraduc, and B. Diény. Parametric oscillator based on nonlinear vortex dynamics in low-resistance magnetic tunnel junctions. *Physical Review B*, 84(14):144434, October 2011. doi: 10.1103/PhysRevB.84.144434. URL http://link.aps.org/doi/10.1103/PhysRevB.84.144434.

[90] A. A. Tulapurkar, Y. Suzuki, A. Fukushima, H. Kubota, H. Maehara, K. Tsunekawa, D. D. Djayaprawira, N. Watanabe, and S. Yuasa. Spin-torque diode effect in magnetic tunnel junctions. *Nature*, 438(7066):339–342, November 2005. ISSN 0028-0836, 1476-4687. doi: 10.1038/nature04207. URL http://www.nature.com/doifinder/10.1038/nature04207.

[91] S. Miwa, S. Ishibashi, H. Tomita, T. Nozaki, E. Tamura, K. Ando, N. Mizuochi, T. Saruya, H. Kubota, K. Yakushiji, T. Taniguchi, H. Imamura, A. Fukushima, S. Yuasa, and Y. Suzuki. Highly sensitive nanoscale spin-torque diode. *Nature Materials*, 13(1): 50–56, October 2013. ISSN 1476-1122, 1476-4660. doi: 10.1038/nmat3778. URL http://www.nature.com/doifinder/10.1038/nmat3778.

[92] Inc. Herotek, 2015. URL http://www.herotek.com/datasheets/herote25.html.

[93] Weisheng Zhao and Guillaume Prenat. *Spintronics based Computing*. Springers edition, 2015. URL http://download.springer.com/static/pdf/788/bok%253A978-3-319-15180-9.pdf?originUrl=http%3A%2F%2Flink.springer.com%2Fbook%2F10.1007%2F978-3-319-15180-9&token2=exp=1438778347~acl=%2Fstatic%2Fpdf%2F788%2Fbok%25253A978-3-319-15180-9.pdf%3ForiginUrl%3Dhttp%253A%252F%252Flink.springer.com%252Fbook%252F10.1007%252F978-3-319-15180-9*~hmac=6386935abca71324e3bd31fbe35c809b905339d64b4fab30b5c8c8b4447472b5.

[94] A. S. Jenkins, R. Lebrun, E. Grimaldi, S. Tsunegi, P. Bortolotti, H. Kubota, K. Yakushiji, A. Fukushima, G. de Loubens, O. Klein, S. Yuasa, and V. Cros. Spin torque resonant vortex core expulsion for an efficient radio-frequency detection scheme. *arXiv:1505.05358 [cond-mat]*, May 2015. URL http://arxiv.org/abs/1505.05358.

[95] Bin Fang, Mario Carpentieri, Xiaojie Hao, Hongwen Jiang, Jordan A. Katine, Ilya N. Krivorotov, Berthold Ocker, Juergen Langer, Kang L. Wang, Baoshun Zhang, Bruno Azzerboni, Pedram Khalili Amiri, Giovanni Finocchio, and Zhongming Zeng. Giant spin-torque diode sensitivity at low input power in the absence of bias magnetic field. *arXiv:1410.4958 [cond-mat]*, October 2014. URL http://arxiv.org/abs/1410.4958.

[96] R. Wood, Mason Williams, A. Kavcic, and Jim Miles. The Feasibility of Magnetic Recording at 10 Terabits Per Square Inch on Conventional Media. *IEEE Transactions on Magnetics*, 45(2):917–923, February 2009. ISSN 0018-9464. doi: 10.1109/TMAG.2008.2010676.

[97] Robert L. White, R.M.H. Newt, and R.Fabian W. Pease. Patterned media: a viable route to 50 Gbit/in2 and up for magnetic recording? *IEEE Transactions on Magnetics*, 33(1): 990–995, January 1997. ISSN 0018-9464. doi: 10.1109/20.560144.

[98] K Mizushima, K Kudo, T Nagasawa, and R Sato. High-data-transfer-rate read heads composed of spin-torque oscillators. *Journal of Physics: Conference Series*, 266:012060, January 2011. ISSN 1742-6596. doi: 10.1088/1742-6596/266/1/012060. URL http://stacks.iop.org/1742-6596/266/i=1/a=012060?key=crossref.fcaf5234ae6d87606e4b65f43f3af778.

[99] P. M. Braganca, B. A. Gurney, A. G. F. Garcia, J. A. Katine, and J. R. Childress. Dependence of Nonlinearity and Spectral Linewidth on Bias Current in Large-Angle Spin-Torque Oscillators. *Physical Review Applied*, 4(1), July 2015. ISSN 2331-7019. doi: 10.1103/PhysRevApplied.4.014017. URL http://link.aps.org/doi/10.1103/PhysRevApplied.4.014017.

[100] P.K. Muduli, Y. Pogoryelov, F. Mancoff, and J. Akerman. Modulation of Individual and Mutually Synchronized Nanocontact-Based Spin Torque Oscillators. *IEEE Transactions on Magnetics*, 47(6):1575–1579, June 2011. ISSN 0018-9464. doi: 10.1109/TMAG.2010.2096463.

[101] Ezio Iacocca. *Strongly non-linear magnetization dynamics in nano-structures: perturbations, multi-mode generation, and topological droplets*. PhD thesis, Göteborgs universitet, 2014.

[102] Benoit Georges, Julie Grollier, Akio Fukushima, Vincent Cros, Bruno Marcilhac, Denis-Gérard Crété, Hitoshi Kubota, Kay Yakushiji, Jean-Claude Mage, Albert Fert, Shinji Yuasa, and Koji Ando. Frequency Converter Based on Nanoscale MgO Magnetic Tunnel Junctions. *Applied Physics Express*, 2(12):123003, December 2009. ISSN 1882-0778, 1882-0786. doi: 10.1143/APEX.2.123003. URL http://stacks.iop.org/1882-0786/2/123003.

[103] A. Yamaguchi, H. Miyajima, S. Kasai, and T. Ono. Self-homodyne rf demodulator using a ferromagnetic nanowire. *Applied Physics Letters*, 90(21):212505, 2007. ISSN 00036951. doi: 10.1063/1.2742588. URL http://scitation.aip.org/content/aip/journal/apl/90/21/10.1063/1.2742588.

[104] Robert A. Fishman. Origins of neuroscience: A history of explorations into brain function. By Stanley Finger, New York, Oxford University Press, 1994, 462 pp, illustrated, $75.00. *Annals of Neurology*, 36(5):807–807, November 1994. ISSN 1531-8249. doi: 10.1002/ana.410360532. URL http://onlinelibrary.wiley.com/doi/10.1002/ana.410360532/abstract.

[105] D. A. Dombeck, M. S. Graziano, and D. W. Tank. Functional Clustering of Neurons in Motor Cortex Determined by Cellular Resolution Imaging in Awake Behaving Mice.

Journal of Neuroscience, 29(44):13751–13760, November 2009. ISSN 0270-6474, 1529-2401. doi: 10.1523/JNEUROSCI.2985-09.2009. URL http://www.jneurosci.org/cgi/doi/10.1523/JNEUROSCI.2985-09.2009.

[106] Jae-eun Kang Miller, Inbal Ayzenshtat, Luis Carrillo-Reid, and Rafael Yuste. Visual stimuli recruit intrinsically generated cortical ensembles. *Proceedings of the National Academy of Sciences of the United States of America*, 111(38):E4053–4061, September 2014. ISSN 1091-6490. doi: 10.1073/pnas.1406077111.

[107] Yuriy V. Pershin and Massimiliano Di Ventra. Experimental demonstration of associative memory with memristive neural networks. *arXiv:0905.2935 [cond-mat, q-bio]*, May 2009. URL http://arxiv.org/abs/0905.2935.

[108] George I. Bourianoff and Dmitri E. Nikonov. Associative Memory Oscillator Array, April 2014. URL http://worldwide.espacenet.com/publicationDetails/biblio;jsessionid=HQNdPDrVBkFXUSZa3dgjRVuc.espacenet_levelx_prod_0?FT=D&date=20140403&DB=&locale=&CC=US&NR=2014092664A1&KC=A1&ND=1. CIB: G11C15/00; G11C27/00.

[109] D. Gusakova, M. Quinsat, J. F. Sierra, U. Ebels, B. Dieny, L. D. Buda-Prejbeanu, M.-C. Cyrille, V. Tiberkevich, and A. N. Slavin. Linewidth reduction in a spin-torque nano-oscillator caused by non-conservative current-induced coupling between magnetic layers. *Applied Physics Letters*, 99(5):052501–052501–3, August 2011. ISSN 00036951. doi: doi:10.1063/1.3615283. URL http://apl.aip.org/resource/1/applab/v99/i5/p052501_s1.

[110] K. Yu. Guslienko. Magnetic Vortex State Stability, Reversal and Dynamics in Restricted Geometries. *Journal of Nanoscience and Nanotechnology*, 8(7):3781–3789, July 2008. ISSN 15334880. doi: 10.1166/jnn.2008.003. URL http://openurl.ingenta.com/content/xref?genre=article&issn=1533-4880&volume=8&issue=7&spage=3781.

[111] N. A Usov. Magnetization curling in a fine cylindrical particle. *Journal of Magnetism and Magnetic Materials*, 118(3), 1993. ISSN 0304-8853. doi: 10.1016/0304-8853(93)90428-5.

[112] Ernst Feldtkeller and Harry Thomas. Struktur und Energie von Blochlinien in dünnen ferromagnetischen Schichten. *Physik der Kondensierten Materie*, 4(1):8–14, July 1965. ISSN 1434-6028, 1434-6036. doi: 10.1007/BF02423256. URL http://link.springer.com/10.1007/BF02423256.

[113] Yuri Gaididei, Volodymyr P. Kravchuk, and Denis D. Sheka. Magnetic vortex dynamics induced by an electrical current. *International Journal of Quantum Chemistry*, 110(1):83–97, January 2010. ISSN 1097-461X. doi: 10.1002/qua.22253. URL http://onlinelibrary.wiley.com/doi/10.1002/qua.22253/abstract.

[114] Nicolas Locatelli, Bruno Marccilhac, Jean-Claude Mage, Vincent Cros, Alexey Vasilyevich Khvalkovskiy, and Julie Grollier. Spintronic oscillator, and use thereof in radiofrequency devices, August 2014. URL http://www.google.com/patents/US20140218122. U.S. Classification 331/94.1; International Classification H03B15/00; Cooperative Classification H03B15/006, H03C3/0958.

[115] K. Yu Guslienko, B. A. Ivanov, V. Novosad, Y. Otani, H. Shima, and K. Fukamichi. Eigenfrequencies of vortex state excitations in magnetic submicron-size disks. *Journal of Applied Physics*, 91(10):8037–8039, May 2002. ISSN 00218979. doi: doi:10.1063/1.1450816. URL http://jap.aip.org/resource/1/japiau/v91/i10/p8037_s1.

[116] K. Yu. Guslienko, V. Novosad, Y. Otani, H. Shima, and K. Fukamichi. Field evolution of magnetic vortex state in ferromagnetic disks. *Applied Physics Letters*, 78(24):3848, 2001. ISSN 00036951. doi: 10.1063/1.1377850. URL http://scitation.aip.org/content/aip/journal/apl/78/24/10.1063/1.1377850.

[117] A. V. Khvalkovskiy, J. Grollier, A. Dussaux, Konstantin A. Zvezdin, and V. Cros. Vortex oscillations induced by spin-polarized current in a magnetic nanopillar: Analytical versus micromagnetic calculations. *Physical Review B*, 80(14):140401, October 2009. doi: 10.1103/PhysRevB.80.140401. URL http://link.aps.org/doi/10.1103/PhysRevB.80.140401.

[118] G. de Loubens, A. Riegler, B. Pigeau, F. Lochner, F. Boust, K. Y. Guslienko, H. Hurdequint, L. W. Molenkamp, G. Schmidt, A. N. Slavin, V. S. Tiberkevich, N. Vukadinovic, and O. Klein. Bistability of Vortex Core Dynamics in a Single Perpendicularly Magnetized Nanodisk. *Physical Review Letters*, 102(17):177602, May 2009. doi: 10.1103/PhysRevLett.102.177602. URL http://link.aps.org/doi/10.1103/PhysRevLett.102.177602.

[119] A. Dussaux, B. Georges, J. Grollier, V. Cros, A.V. Khvalkovskiy, A. Fukushima, M. Konoto, H. Kubota, K. Yakushiji, S. Yuasa, K.A. Zvezdin, K. Ando, and A. Fert. Large microwave generation from current-driven magnetic vortex oscillators in magnetic tunnel junctions. *Nat Commun*, 1:8, April 2010. doi: 10.1038/ncomms1006. URL http://dx.doi.org/10.1038/ncomms1006.

[120] M. Tsoi, A. G. M. Jansen, J. Bass, W.-C. Chiang, M. Seck, V. Tsoi, and P. Wyder. Excitation of a Magnetic Multilayer by an Electric Current. *Physical Review Letters*, 80

(19):4281–4284, May 1998. doi: 10.1103/PhysRevLett.80.4281. URL http://link.aps.org/doi/10.1103/PhysRevLett.80.4281.

[121] B. A. Ivanov and C. E. Zaspel. Excitation of spin dynamics by spin-polarized current in vortex state magnetic disks. *Physical review letters*, 99(24):247208, December 2007. ISSN 0031-9007.

[122] Q. Mistral, M. van Kampen, G. Hrkac, Joo-Von Kim, T. Devolder, P. Crozat, C. Chappert, L. Lagae, and T. Schrefl. Current-Driven Vortex Oscillations in Metallic Nanocontacts. *Physical Review Letters*, 100(25), June 2008. ISSN 0031-9007, 1079-7114. doi: 10.1103/PhysRevLett.100.257201. URL http://link.aps.org/doi/10.1103/PhysRevLett.100.257201.

[123] V. Sluka, A. Kákay, A. M. Deac, D. E. Bürgler, R. Hertel, and C. M. Schneider. Quenched Slonczewski windmill in spin-torque vortex oscillators. *Physical Review B*, 86(21), December 2012. ISSN 1098-0121, 1550-235X. doi: 10.1103/PhysRevB.86.214422. URL http://link.aps.org/doi/10.1103/PhysRevB.86.214422.

[124] Joo-Von Kim and Thibaut Devolder. Theory of the power spectrum of spin-torque nanocontact vortex oscillators. *arXiv:1007.3859 [cond-mat]*, July 2010. URL http://arxiv.org/abs/1007.3859.

[125] Nicolas Locatelli. *Dynamique par transfert de spin et synchronisation d'oscillateurs couplés à base de vortex magnétiques*. PhD thesis, Université Paris Sud, 2012. URL https://tel.archives-ouvertes.fr/tel-00801852/.

[126] S. S. Cherepov, B. C. Koop, A. Yu. Galkin, R. S. Khymyn, B. A. Ivanov, D. C. Worledge, and V. Korenivski. Core-Core Dynamics in Spin Vortex Pairs. *Physical Review Letters*, 109(9):097204, August 2012. doi: 10.1103/PhysRevLett.109.097204. URL http://link.aps.org/doi/10.1103/PhysRevLett.109.097204.

[127] J. F. Pulecio, P. Warnicke, S. D. Pollard, D. A. Arena, and Y. Zhu. Coherence and modality of driven interlayer-coupled magnetic vortices. *Nature Communications*, 5, April 2014. doi: 10.1038/ncomms4760. URL http://www.nature.com/ncomms/2014/140430/ncomms4760/full/ncomms4760.html.

[128] F. Boust and N. Vukadinovic. Micromagnetic Simulations of Vortex Resonances in Coupled Nanodisks. *IEEE Transactions on Magnetics*, 47(2):349–354, February 2011. ISSN 0018-9464. doi: 10.1109/TMAG.2010.2072915.

[129] N. Locatelli, V. Cros, and J. Grollier. Spin-torque building blocks. *Nat Mater*, 13(1):11–20, January 2014. ISSN 1476-1122. URL http://dx.doi.org/10.1038/nmat3823.

[130] Volker Sluka, Attila Kákay, Alina M. Deac, Daniel E. Bürgler, Riccardo Hertel, and Claus M. Schneider. Quenched Slonczewski-Windmill in Spin-Torque Vortex-Oscillators. *arXiv:1112.3163*, December 2011. URL http://arxiv.org/abs/1112.3163.

[131] D. Kumar, S. Barman, and A. Barman. Magnetic Vortex Based Transistor Operations. *Scientific Reports*, 4, February 2014. ISSN 2045-2322. doi: 10.1038/srep04108. URL http://www.ncbi.nlm.nih.gov/pmc/articles/PMC3925947/.

[132] Graham E. Rowlands, Jordan A. Katine, Juergen Langer, Jian Zhu, and Ilya N. Krivorotov. Time Domain Mapping of Spin Torque Oscillator Effective Energy. *Physical Review Letters*, 111(8):087206, August 2013. doi: 10.1103/PhysRevLett.111.087206. URL http://link.aps.org/doi/10.1103/PhysRevLett.111.087206.

[133] Kyung-Jin Lee, M. D. Stiles, Hyun-Woo Lee, Jung-Hwan Moon, Kyoung-Whan Kim, and Seo-Won Lee. Self-consistent calculation of spin transport and magnetization dynamics. *arXiv:1305.5087*, May 2013. URL http://arxiv.org/abs/1305.5087.

[134] M. Quinsat, V. Tiberkevich, D. Gusakova, A. Slavin, J. F. Sierra, U. Ebels, L. D. Buda-Prejbeanu, B. Dieny, M.-C. Cyrille, A. Zelster, and J. A. Katine. Linewidth of higher harmonics in a nonisochronous auto-oscillator: Application to spin-torque nano-oscillators. *Physical Review B*, 86(10):104418, September 2012. doi: 10.1103/PhysRevB.86.104418. URL http://link.aps.org/doi/10.1103/PhysRevB.86.104418.

[135] F. Sanches, V. Tiberkevich, K. Y. Guslienko, J. Sinha, M. Hayashi, O. Prokopenko, and A. N. Slavin. Current-driven gyrotropic mode of a magnetic vortex as a non-isochronous auto-oscillator. *Physical Review B*, 89(14), April 2014. ISSN 1098-0121, 1550-235X. doi: 10.1103/PhysRevB.89.140410. URL http://link.aps.org/doi/10.1103/PhysRevB.89.140410.

[136] L. Bianchini, S. Cornelissen, Joo-Von Kim, T. Devolder, W. van Roy, L. Lagae, and C. Chappert. Direct experimental measurement of phase-amplitude coupling in spin torque oscillators. *Applied Physics Letters*, 97(3):032502, 2010. ISSN 00036951. doi: 10.1063/1.3467043. URL http://scitation.aip.org/content/aip/journal/apl/97/3/10.1063/1.3467043.

[137] Yuki Kawada, Hiroshi Naganuma, Ahmet Serdar Demiray, Mikihiko Oogane, and Yasuo Ando. Mode change of vortex core oscillation induced by large direct current in 120 nm sized current perpendicular-to-plane giant magnetoresistance devices with a perpendicular polarizer. *Applied Physics Letters*, 105(5):052407, August 2014. ISSN 0003-6951, 1077-3118. doi: 10.1063/1.4892077. URL http://scitation.aip.org/content/aip/journal/apl/105/5/10.1063/1.4892077.

[138] E. Grimaldi, R. Lebrun, A. Jenkins, A. Dussaux, J. Grollier, V. Cros, A. Fert, H. Kubota, K. Yakushiji, A. Fukushima, R. Matsumoto, S. Yuasa, G. Cibiel, P. Bortolotti, and G. Pillet. Spintronic nano-oscillators: Towards nanoscale and tunable frequency devices. In *Frequency Control Symposium (FCS), 2014 IEEE International*, pages 1–6, May 2014. doi: 10.1109/FCS.2014.6859850.

[139] M. d'Aquino, C. Serpico, R. Bonin, G. Bertotti, and I. D. Mayergoyz. Micromagnetic analysis of injection locking in spin-transfer nano-oscillators. *Physical Review B*, 82(6), August 2010. ISSN 1098-0121, 1550-235X. doi: 10.1103/PhysRevB.82.064415. URL http://link.aps.org/doi/10.1103/PhysRevB.82.064415.

[140] Heng-Chia Chang. Stability analysis of self-injection-locked oscillators. *IEEE Transactions on Microwave Theory and Techniques*, 51(9):1989–1993, September 2003. ISSN 0018-9480. doi: 10.1109/TMTT.2003.815863.

[141] M. C. Cross. Improving the frequency precision of oscillators by synchronization. *Physical Review E*, 85(4), April 2012. ISSN 1539-3755, 1550-2376. doi: 10.1103/PhysRevE.85.046214. URL http://link.aps.org/doi/10.1103/PhysRevE.85.046214.

[142] K. Konishi, D. K. Dixit, A. A. Tulapurkar, S. Miwa, T. Nozaki, H. Kubota, A. Fukushima, S. Yuasa, and Y. Suzuki. Radio-frequency amplification property of the MgO-based magnetic tunnel junction using field-induced ferromagnetic resonance. *Applied Physics Letters*, 102(16):162409–162409–4, April 2013. ISSN 00036951. doi: doi:10.1063/1.4803050. URL http://apl.aip.org/resource/1/applab/v102/i16/p162409_s1.

[143] P. Dürrenfeld, E. Iacocca, J. Åkerman, and P. K. Muduli. Parametric excitation in a magnetic tunnel junction-based spin torque oscillator. *Applied Physics Letters*, 104 (5):052410, February 2014. ISSN 0003-6951, 1077-3118. doi: 10.1063/1.4864166. URL http://scitation.aip.org/content/aip/journal/apl/104/5/10.1063/1.4864166.

[144] P. K. Muduli, Ye. Pogoryelov, S. Bonetti, G. Consolo, Fred Mancoff, and Johan Åkerman. Nonlinear frequency and amplitude modulation of a nanocontact-based spin-torque oscillator. *Physical Review B*, 81(14), April 2010. ISSN 1098-0121, 1550-235X. doi: 10.1103/PhysRevB.81.140408. URL http://link.aps.org/doi/10.1103/PhysRevB.81.140408.

[145] Alexander A. Mitrofanov, Ansar R. Safin, and Nicolay N. Udalov. Phase Locked Loop of the Spin-Torque Nanooscillator. *arXiv preprint arXiv:1408.3868*, 2014. URL http://arxiv.org/abs/1408.3868.

[146] S. Tamaru, K. Yakushiji, B. Wang, A. Fukushima, and H. Kubota. Generation of highly stable 5 GHz microwave from a spin torque oscillator by phase locked loop referenced to

a 80 MHz clock. In *2015 IEEE Magnetics Conference (INTERMAG)*, pages 1–1, May 2015. doi: 10.1109/INTMAG.2015.7156842.

[147] Mark W. Keller, A. B. Kos, T. J. Silva, W. H. Rippard, and M. R. Pufall. Time domain measurement of phase noise in a spin torque oscillator. *Applied Physics Letters*, 94(19): 193105, 2009. ISSN 00036951. doi: 10.1063/1.3133356. URL http://scitation.aip.org/content/aip/journal/apl/94/19/10.1063/1.3133356.

[148] Heng-Chia Chang, Xudong Cao, Umesh K. Mishra, and Robert A. York. Phase noise in coupled oscillators: Theory and experiment. *Microwave Theory and Techniques, IEEE Transactions on*, 45(5):604–615, 1997. URL http://ieeexplore.ieee.org/xpls/abs_all.jsp?arnumber=575575.

[149] Kurt Wiesenfeld, Pere Colet, and Steven H. Strogatz. Synchronization Transitions in a Disordered Josephson Series Array. *Physical Review Letters*, 76:404–407, January 1996. ISSN 0031-9007. doi: 10.1103/PhysRevLett.76.404. URL http://adsabs.harvard.edu/abs/1996PhRvL..76..404W.

[150] Rafael Yuste. From the neuron doctrine to neural networks. *Nature Reviews Neuroscience*, 16(8):487–497, July 2015. ISSN 1471-003X, 1471-0048. doi: 10.1038/nrn3962. URL http://www.nature.com/doifinder/10.1038/nrn3962.

[151] A. Dussaux, A. V. Khvalkovskiy, P. Bortolotti, J. Grollier, V. Cros, and A. Fert. Field dependence of spin-transfer-induced vortex dynamics in the nonlinear regime. *Physical Review B*, 86(1):014402, July 2012. doi: 10.1103/PhysRevB.86.014402. URL http://link.aps.org/doi/10.1103/PhysRevB.86.014402.

[152] Lai Hong-ming. URL www.hk-phy.org/articles/swing/swing_e.html.

[153] Feng Guo, L. M. Belova, and R. D. McMichael. Parametric pumping of precession modes in ferromagnetic nanodisks. *Physical Review B*, 89(10), March 2014. ISSN 1098-0121, 1550-235X. doi: 10.1103/PhysRevB.89.104422. URL http://link.aps.org/doi/10.1103/PhysRevB.89.104422.

[154] P. Dürrenfeld, E. Iacocca, J. Åkerman, and P. K. Muduli. Modulation-mediated unlocking of a parametrically phase-locked spin torque oscillator. *Applied Physics Letters*, 105(25):252404, December 2014. ISSN 0003-6951, 1077-3118. doi: 10.1063/1.4904991. URL http://scitation.aip.org/content/aip/journal/apl/105/25/10.1063/1.4904991.

[155] Ye Pogoryelov, P. K. Muduli, S. Bonetti, E. Iacocca, Fred Mancoff, and Johan Åkerman. Frequency modulation of spin torque oscillator pairs. *Applied Physics Letters*, 98(19):

192501–192501–3, May 2011. ISSN 00036951. doi: doi:10.1063/1.3588218. URL http://apl.aip.org/resource/1/applab/v98/i19/p192501_s1.

[156] M. Manfrini, T. Devolder, Joo-Von Kim, P. Crozat, C. Chappert, W. Van Roy, and L. Lagae. Frequency shift keying in vortex-based spin torque oscillators. *Journal of Applied Physics*, 109(8):083940, 2011. ISSN 00218979. doi: 10.1063/1.3581099. URL http://scitation.aip.org/content/aip/journal/jap/109/8/10.1063/1.3581099.

[157] G. Finocchio, M. Carpentieri, A. Giordano, and B. Azzerboni. Non-Adlerian phase slip and nonstationary synchronization of spin-torque oscillators to a microwave source. *Physical Review B*, 86(1), July 2012. ISSN 1098-0121, 1550-235X. doi: 10.1103/PhysRevB.86.014438. URL http://link.aps.org/doi/10.1103/PhysRevB.86.014438.

[158] Vasil S. Tiberkevich, Roman S. Khymyn, Hong X. Tang, and Andrei N. Slavin. Sensitivity to external signals and synchronization properties of a non-isochronous auto-oscillator with delayed feedback. *Scientific Reports*, 4, January 2014. ISSN 2045-2322. doi: 10.1038/srep03873. URL http://www.nature.com/doifinder/10.1038/srep03873.

[159] A.S. Daryoush, T. Berceli, R. Saedi, P.R. Herczfeld, and A. Rosen. Theory of subharmonic synchronization of nonlinear oscillators. In *Microwave Symposium Digest, 1989., IEEE MTT-S International*, pages 735–738 vol.2, June 1989. doi: 10.1109/MWSYM.1989.38829.

[160] Xiangdong Zhang, X. Zhou, B. Aliener, and A.S. Daryoush. A study of subharmonic injection locking for local oscillators. *IEEE Microwave and Guided Wave Letters*, 2(3):97–99, March 1992. ISSN 1051-8207. doi: 10.1109/75.124911.

[161] Dong Li, Yan Zhou, Changsong Zhou, and Bambi Hu. Fractional locking of spin-torque oscillator by injected ac current. *Physical Review B*, 83(17), May 2011. ISSN 1098-0121, 1550-235X. doi: 10.1103/PhysRevB.83.174424. URL http://link.aps.org/doi/10.1103/PhysRevB.83.174424.

[162] Rie Matsumoto, André Chanthbouala, Julie Grollier, Vincent Cros, Albert Fert, Kazumasa Nishimura, Yoshinori Nagamine, Hiroki Maehara, Koji Tsunekawa, Akio Fukushima, and Shinji Yuasa. Spin-Torque Diode Measurements of MgO-Based Magnetic Tunnel Junctions with Asymmetric Electrodes. *Applied Physics Express*, 4(6):063001, May 2011. ISSN 1882-0778, 1882-0786. doi: 10.1143/APEX.4.063001. URL http://stacks.iop.org/1882-0786/4/063001.

[163] S. Sancho, F. Ramirez, and A. Suarez. Stochastic Analysis of Cycle Slips in Injection-Locked Oscillators and Analog Frequency Dividers. *IEEE Transactions on Microwave*

Theory and Techniques, 62(12):3318–3332, December 2014. ISSN 0018-9480. doi: 10.1109/TMTT.2014.2365798.

[164] S. Michotte, S. Matefi-Tempfli, L. Piraux, D. Y. Vodolazov, and F. M. Peeters. Condition of the occurrence of phase slip centers in superconducting nanowires under applied current or voltage. *Physical Review B*, 69(9), March 2004. ISSN 1098-0121, 1550-235X. doi: 10.1103/PhysRevB.69.094512. URL http://arxiv.org/abs/cond-mat/0309699.

[165] David Cohen-Tanugi, Austin Akey, and Nan Yao. Ultralow Superharmonic Resonance for Functional Nanowires. *Nano Letters*, 10(3):852–859, March 2010. ISSN 1530-6984, 1530-6992. doi: 10.1021/nl903302q. URL http://pubs.acs.org/doi/abs/10.1021/nl903302q.

[166] Olle Heinonen, Yan Zhou, and Dong Li. Mode coupling in spin torque oscillators. *arXiv:1310.6791 [cond-mat]*, October 2013. URL http://arxiv.org/abs/1310.6791.

[167] Sung Chul Lee, Ung Hwan Pi, Keewon Kim, Kwang Seok Kim, Jaikwang Shin, and U In Chung. Current Driven Magnetic Damping in Dipolar-Coupled Spin System. *Scientific Reports*, 2, July 2012. ISSN 2045-2322. doi: 10.1038/srep00531. URL http://www.ncbi.nlm.nih.gov/pmc/articles/PMC3404414/.

[168] Slobodianiuk. Transition from one- to two-mode generation regime in STNO mediated by thermal noise. *Condensed Matter Physics*, 17(1):13801, 2014. ISSN 1607324X. doi: 10.5488/CMP.17.13801. URL http://www.icmp.lviv.ua/journal/zbirnyk.77/13801/abstract.html.

[169] D. Gusakova, D. Houssameddine, U. Ebels, B. Dieny, L. Buda-Prejbeanu, M. C. Cyrille, and B. Delaët. Spin-polarized current-induced excitations in a coupled magnetic layer system. *Physical Review B*, 79(10):104406, March 2009. doi: 10.1103/PhysRevB.79.104406. URL http://link.aps.org/doi/10.1103/PhysRevB.79.104406.

[170] Ezio Iacocca, Philipp Dürrenfeld, Olle Heinonen, Johan Åkerman, and Randy K. Dumas. Mode-coupling mechanisms in nanocontact spin-torque oscillators. *Physical Review B*, 91 (10), March 2015. ISSN 1098-0121, 1550-235X. doi: 10.1103/PhysRevB.91.104405. URL http://link.aps.org/doi/10.1103/PhysRevB.91.104405.

[171] Hajime Okamoto, Adrien Gourgout, Chia-Yuan Chang, Koji Onomitsu, Imran Mahboob, Edward Yi Chang, and Hiroshi Yamaguchi. Coherent phonon manipulation in coupled mechanical resonators. *Nat Phys*, 9(8):480–484, August 2013. ISSN 1745-2473. URL http://dx.doi.org/10.1038/nphys2665.

[172] A. Yariv. Coupled-mode theory for guided-wave optics. *IEEE Journal of Quantum Electronics*, 9(9):919–933, September 1973. ISSN 0018-9197. doi: 10.1109/JQE.1973.1077767.

[173] B. Pigeau, C. Hahn, G. de Loubens, V. V. Naletov, O. Klein, K. Mitsuzuka, D. Lacour, M. Hehn, S. Andrieu, and F. Montaigne. Measurement of the Dynamical Dipolar Coupling in a Pair of Magnetic Nanodisks Using a Ferromagnetic Resonance Force Microscope. *Physical Review Letters*, 109(24), December 2012. ISSN 0031-9007, 1079-7114. doi: 10.1103/PhysRevLett.109.247602. URL http://link.aps.org/doi/10.1103/PhysRevLett.109.247602.

[174] Steven Lequeux, Joao Sampaio, Paolo Bortolotti, Thibaut Devolder, Rie Matsumoto, Kay Yakushiji, Hitoshi Kubota, Akio Fukushima, Shinji Yuasa, Kazumasa Nishimura, Yoshinori Nagamine, Koji Tsunekawa, Vincent Cros, and Julie Grollier. Increased magnetic damping of a single domain wall and adjacent magnetic domains detected by spin torque diode in a nanostripe. *arXiv:1508.04043 [cond-mat]*, August 2015. URL http://arxiv.org/abs/1508.04043.

[175] Hyunsung Jung, Ki-Suk Lee, Dae-Eun Jeong, Youn-Seok Choi, Young-Sang Yu, Dong-Soo Han, Andreas Vogel, Lars Bocklage, Guido Meier, Mi-Young Im, Peter Fischer, and Sang-Koog Kim. Tunable negligible-loss energy transfer between dipolar-coupled magnetic disks by stimulated vortex gyration. *Scientific Reports*, 1, August 2011. ISSN 2045-2322. doi: 10.1038/srep00059. URL http://www.ncbi.nlm.nih.gov/pmc/articles/PMC3216546/.

[176] Satoshi Sugimoto, Yasuhiro Fukuma, Shinya Kasai, Takashi Kimura, Anjan Barman, and YoshiChika Otani. Dynamics of Coupled Vortices in a Pair of Ferromagnetic Disks. *Physical Review Letters*, 106(19):197203, May 2011. doi: 10.1103/PhysRevLett.106.197203. URL http://link.aps.org/doi/10.1103/PhysRevLett.106.197203.

[177] P. S. Keatley, P. Gangmei, M. Dvornik, R. J. Hicken, J. Grollier, and C. Ulysse. Isolating the Dynamic Dipolar Interaction between a Pair of Nanoscale Ferromagnetic Disks. *Physical Review Letters*, 110(18), May 2013. ISSN 0031-9007, 1079-7114. doi: 10.1103/PhysRevLett.110.187202. URL http://link.aps.org/doi/10.1103/PhysRevLett.110.187202.

[178] Mogens Hϕgh Jensen, Per Bak, and Tomas Bohr. Transition to chaos by interaction of resonances in dissipative systems. I. Circle maps. *Physical Review A*, 30(4):1960–1969, October 1984. doi: 10.1103/PhysRevA.30.1960. URL http://link.aps.org/doi/10.1103/PhysRevA.30.1960.

[179] R. B. Karabalin, M. C. Cross, and M. L. Roukes. Nonlinear dynamics and chaos in two coupled nanomechanical resonators. *Physical Review B*, 79(16), April 2009. ISSN 1098-0121, 1550-235X. doi: 10.1103/PhysRevB.79.165309. URL http://link.aps.org/doi/10.1103/PhysRevB.79.165309.

[180] Z. Li, Y. Charles Li, and S. Zhang. Dynamic magnetization states of a spin valve in the presence of dc and ac currents: Synchronization, modification, and chaos. *Physical Review B*, 74(5), August 2006. ISSN 1098-0121, 1550-235X. doi: 10.1103/PhysRevB.74.054417. URL http://link.aps.org/doi/10.1103/PhysRevB.74.054417.

[181] Romain Lebrun, Nicolas Locatelli, Sumito Tsunegi, Julie Grollier, Vincent Cros, Flavio Abreu Araujo, Hitoshi Kubota, Kay Yakushiji, Akio Fukushima, and Shinji Yuasa. Nonlinear Behavior and Mode Coupling in Spin-Transfer Nano-Oscillators. *Physical Review Applied*, 2(6), December 2014. ISSN 2331-7019. doi: 10.1103/PhysRevApplied.2.061001. URL http://link.aps.org/doi/10.1103/PhysRevApplied.2.061001.

[182] M. Romera, E. Monteblanco, F. Garcia-Sanchez, B. Delaët, L. D. Buda-Prejbeanu, and U. Ebels. Non-linear mode interaction between spin torque driven and damped modes in spin torque nano-oscillators. *Applied Physics Letters*, 106(19):192405, May 2015. ISSN 0003-6951, 1077-3118. doi: 10.1063/1.4921097. URL http://scitation.aip.org/content/aip/journal/apl/106/19/10.1063/1.4921097.

[183] Andrei Slavin. Microwave sources: Spin-torque oscillators get in phase. *Nature nanotechnology*, 4(8):479–480, 2009. URL http://www.nature.com/articles/doi:10.1038%2Fnnano.2009.213.

[184] Henri de Bellescize. *La réception synchrone*. E. Chiron, Paris, 1932.

[185] A. A. Mitrofanov, A. R. Safin, and N. N. Udalov. Amplitude and phase noises of a spin-transfer nano-oscillator synchronized by a phase-lock loop. *Technical Physics Letters*, 41 (8):778–780, August 2015. ISSN 1063-7850, 1090-6533. doi: 10.1134/S1063785015080271. URL http://link.springer.com/10.1134/S1063785015080271.

[186] G. I. Bourianoff and D. E. Nikonov. *Associative Memory Oscillator Array*. Google Patents, 2014. URL http://www.google.com/patents/US20140092664.

[187] Jian Zhu, J. A. Katine, Graham E. Rowlands, Yu-Jin Chen, Zheng Duan, Juan G. Alzate, Pramey Upadhyaya, Juergen Langer, Pedram Khalili Amiri, Kang L. Wang, and Ilya N. Krivorotov. Voltage-Induced Ferromagnetic Resonance in Magnetic Tunnel Junctions. *Physical Review Letters*, 108(19), May 2012. ISSN 0031-9007, 1079-7114. doi: 10.1103/PhysRevLett.108.197203. URL http://link.aps.org/doi/10.1103/PhysRevLett.108.197203.

[188] M. J. Donahue and D. G. Porter. OOMMF User's Guide, Version 1.0, 1999.

[189] K. Yu Guslienko, K. S. Buchanan, S. D. Bader, and V. Novosad. Dynamics of coupled vortices in layered magnetic nanodots. *Applied Physics Letters*, 86(22):223112–223112–3, May 2005. ISSN 00036951. doi: doi:10.1063/1.1929078. URL http://apl.aip.org/resource/1/applab/v86/i22/p223112_s1.

[190] M. Pufall, W. Rippard, G. Csaba, D. Nikonov, G. Bourianoff, and W. Porod. Physical implementation of coherently-coupled oscillator networks. *IEEE Journal on Exploratory Solid-State Computational Devices and Circuits*, PP(99):1–1, 2015. ISSN 2329-9231. doi: 10.1109/JXCDC.2015.2468070.

[191] G. Csaba, M. Pufall, W. Rippard, and W. Porod. Modeling of coupled spin torque oscillators for applications in associative memories. In *2012 12th IEEE Conference on Nanotechnology (IEEE-NANO)*, pages 1–4, August 2012. doi: 10.1109/NANO.2012.6322201.

[192] A. Horvath, G. Csaba, and W. Porod. Dynamic coupling of spin torque oscillators for associative memories. In *2014 14th International Workshop on Cellular Nanoscale Networks and their Applications (CNNA)*, pages 1–2, July 2014. doi: 10.1109/CNNA.2014.6888662.

[193] R. Lebrun, S. Tsunegi, P. Bortolotti, H. Kubota, A. Jenkins, M. Romera, K. Yakushiji, A. Fukushima, J. Grollier, S. Yuasa, and year = 2016 Cros, V. Mutual synchronization of spin torque nano-oscillators through a non-local and tunable electrical coupling. *arXiv preprint arXiv:1601.01247*. URL http://arxiv.org/ftp/arxiv/papers/1601/1601.01247.pdf.

[194] A. Slavin and V. Tiberkevich. Theory of mutual phase locking of spin-torque nanosized oscillators. *Physical Review B*, 74(10), September 2006. ISSN 1098-0121, 1550-235X. doi: 10.1103/PhysRevB.74.104401. URL http://link.aps.org/doi/10.1103/PhysRevB.74.104401.

[195] A. D. Belanovsky, N. Locatelli, P. N. Skirdkov, F. Abreu Araujo, K. A. Zvezdin, J. Grollier, V. Cros, and A. K. Zvezdin. Non-Adlerian synchronization of dipolar coupled vortex Spin-Torque Nano-Oscillators. *arXiv preprint arXiv:1308.3811*, 2013. URL http://arxiv.org/abs/1308.3811.

[196] F. Abreu Araujo, A. D. Belanovsky, P. N. Skirdkov, K. A. Zvezdin, A. K. Zvezdin, N. Locatelli, R. Lebrun, J. Grollier, V. Cros, G. de Loubens, and O. Klein. Optimizing magnetodipolar interactions for synchronizing vortex based spin-torque nano-oscillators. *Physical Review B*, 92(4), July 2015. ISSN 1098-0121, 1550-235X. doi: 10.1103/PhysRevB.92.045419. URL http://link.aps.org/doi/10.1103/PhysRevB.92.045419.

[197] Yoshiki Kuramoto. Self-entrainment of a population of coupled non-linear oscillators. In Huzihiro Araki, editor, *International Symposium on Mathematical Problems in Theoretical Physics*, volume 39, pages 420–422. Springer-Verlag, Berlin/Heidelberg, 1975. ISBN 3-540-07174-1. URL http://www.springerlink.com/index/10.1007/BFb0013365.

[198] D. G. Aronson, G. B. Ermentrout, and N. Kopell. Amplitude response of coupled oscillators. *Physica D Nonlinear Phenomena*, 41:403–449, April 1990. ISSN 0167-2789. doi: 10.1016/0167-2789(90)90007-C. URL http://adsabs.harvard.edu/abs/1990PhyD...41..403A.

[199] A. S. Jenkins, E. Grimaldi, P. Bortolotti, R. Lebrun, H. Kubota, K. Yakushiji, A. Fukushima, G. de Loubens, O. Klein, S. Yuasa, and V. Cros. Controlling the chirality and polarity of vortices in magnetic tunnel junctions. *Applied Physics Letters*, 105(17): 172403, October 2014. ISSN 0003-6951, 1077-3118. doi: 10.1063/1.4900743. URL http://scitation.aip.org/content/aip/journal/apl/105/17/10.1063/1.4900743.

[200] Martin Collet, Xavier De Milly, Olivier D'Allivy-Kelly, Vladimir V. Naletov, Rozenn Bernard, Paolo Bortolotti, Vladislav Demidov, Sergej Demokritov, Jose Luis Prieto, Manuel Muñoz, Abdelmadjid Anane, Vincent Cros, Grégoire De Loubens, and Olivier Klein. Generation of coherent spin-wave modes in Yttrium Iron Garnet microdiscs by spin-orbit torque. *arXiv:1504.01512 [cond-mat]*, April 2015. URL http://arxiv.org/abs/1504.01512.

[201] Vladislav E. Demidov, Sergei Urazhdin, Henning Ulrichs, Vasyl Tiberkevich, Andrei Slavin, Dietmar Baither, Guido Schmitz, and Sergej O. Demokritov. Magnetic nano-oscillator driven by pure spin current. *Nature Materials*, October 2012. ISSN 1476-1122, 1476-4660. doi: 10.1038/nmat3459. URL http://www.nature.com/doifinder/10.1038/nmat3459.

[202] P. Nemec, E. Rozkotova, N. Tesarova, F. Trojanek, E. De Ranieri, K. Olejnik, J. Zemen, V. Novak, M. Cukr, P. Maly, and T. Jungwirth. Experimental observation of the optical spin transfer torque. *Nature Physics*, 8(5):411–415, April 2012. ISSN 1745-2473, 1745-2481. doi: 10.1038/nphys2279. URL http://arxiv.org/abs/1201.1436.

[203] C.-H. Lambert, S. Mangin, B. S. D. C. S. Varaprasad, Y. K. Takahashi, M. Hehn, M. Cinchetti, G. Malinowski, K. Hono, Y. Fainman, M. Aeschlimann, and E. E. Fullerton. All-optical control of ferromagnetic thin films and nanostructures. *Science*, 345(6202): 1337–1340, September 2014. ISSN 0036-8075, 1095-9203. doi: 10.1126/science.1253493. URL http://www.sciencemag.org/cgi/doi/10.1126/science.1253493.

[204] Ferran Macià, Andrew D Kent, and Frank C Hoppensteadt. Spin-wave interference patterns created by spin-torque nano-oscillators for memory and computation. *Nanotechnology*, 22(9):095301, March 2011. ISSN 0957-4484, 1361-6528. doi: 10.1088/0957-4484/22/9/095301. URL http://stacks.iop.org/0957-4484/22/i=9/a=095301?key=crossref.c62c38787aa97cb10712ebb5a7b77dc9.

[205] C. Moreau-Luchaire. Skyrmions at room temperature : From magnetic thin films to magnetic multilayers. *arXiv:1502.07853 [cond-mat]*, February 2015. URL http://arxiv.org/abs/1502.07853.

[206] J. Sampaio, V. Cros, S. Rohart, A. Thiaville, and A. Fert. Nucleation, stability and current-induced motion of isolated magnetic skyrmions in nanostructures. *Nature Nanotechnology*, 8(11):839–844, October 2013. ISSN 1748-3387, 1748-3395. doi: 10.1038/nnano.2013.210. URL http://www.nature.com/doifinder/10.1038/nnano.2013.210.

[207] Y. Zhou, E. Iacocca, A. A. Awad, R. K. Dumas, F. C. Zhang, H. B. Braun, and J. Åkerman. Dynamically stabilized magnetic skyrmions. *Nature Communications*, 6:8193, September 2015. doi: 10.1038/ncomms9193. URL http://www.nature.com/ncomms/2015/150909/ncomms9193/full/ncomms9193.html.

université
PARIS-SACLAY

Titre : Coupled vortex dynamics in spin-torque oscillators: From resonant excitation to mutual synchronization

Mots clés : vortex magnétique, mode couplés, électronique de spin, transfert de spin, excitation résonante et paramétrique, oscillateurs et détecteurs radiofréquences, bruit de phase, synchronisation mutuelle.

Résumé : La découverte de la magnétorésistance géante en 1988 est considérée comme la date de naissance d'un nouveau et dynamique champ de recherché appelé l'électronique de spin. La riche physique associée au transport de spin devrait révolutionner le futur de la nanoélectronique. Dans ce cadre les nano-oscillateurs à transfert de spin (STOs) se sont positionnés comme des candidats sérieux pour le développement d'une nouvelle génération de dispositifs rf basés sur l'électronique de spin.

Au début de ma thèse, l'important bruit de phase des STOs restait une contrainte majeure limitant les perspectives technologiques à ce type d'oscillateurs.

Dans cette thèse nous avons cherché à contrôler la dynamique des STOs et à réduire leur bruit phase en développant différentes stratégies : (i) l'optimisation des propriétés des matériaux magnétiques utilisés (ii) l'excitation de modes couplés dans des systèmes hybridés (iii) la stabilisation de la dynamique de la phase d'un STO avec un signal extérieur de référence (iv) la synchronisation mutuelle de différents oscillateurs pour améliorer la cohérence spectrale et la puissance des STOs. Nous focalisons en particulier sur le cas de STO à base de vortex magnétique qui présentent intrinsèquement des cohérences spectrales plus élevées que celles d'autres types d'oscillateurs.

Title : Vortex magnétiques couplés dans des oscillateurs à transfert de spin: De l'excitation résonante à la synchronisation mutuelle

Keywords : magnetic vortex, mode coupling, spintronic, spin-transfert, resonant and parametric excitation, radiofrequency oscillator and detector, phase noise, mutual synchronization.

Abstract : The discovery of the giant magnetoresistance in 1988 is considered as the birth date of a new and dynamic research field called spintronics. The rich physics associated with spin transport has created a breakthrough for the future of nano-electronics. In the magnetism roadmap, spin-torque oscillators (STOs) are candidates for future generation of spintronic based rf-devices.

At the beginning of this thesis, one major issue of spin-torque oscillators remained their poor spectral coherence.

To overcome this issue, we have investigated different approaches: (i) the development of magnetic materials with a low damping and large spin-polarization, (ii) the study of collective mode dynamics in hybridized magnetic systems (iii) the stabilization of the STO dynamics with a reference external signal (iv) the synchronization of multiple STOs to enhance both their power and spectral coherence. We focus our work on vortex based STOs which present higher spectral coherences than other kinds of STOs.

Université Paris-Saclay
Espace Technologique / Immeuble Discovery
Route de l'Orme aux Merisiers RD 128 / 91190 Saint-Aubin, France